

(6)

Calspan

Technical Report

ADA 029545

DDC

SEP 13 1976

B

AIR FORCE OFFICE OF TECHNOLOGICAL RESEARCH (AFOTR)
NOTICE OF TRANSFER OF DDC
THIS BOOK IS THE PROPERTY OF THE AIR FORCE OFFICE OF TECHNOLOGICAL RESEARCH (AFOTR)
AND IS LOANED TO YOU BY THE AIR FORCE OFFICE OF TECHNOLOGICAL RESEARCH (AFOTR)
IT IS TO BE RETURNED TO THE AIR FORCE OFFICE OF TECHNOLOGICAL RESEARCH (AFOTR)
ON THE DATE INDICATED ON THE LABEL
Technical Information Officer

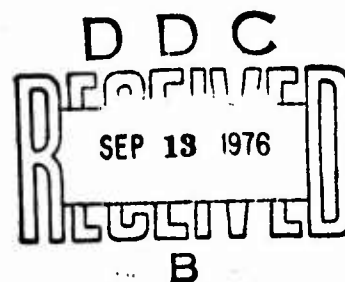
Calspan

ACCESSION for	
RTM	White Section <input checked="" type="checkbox"/>
DOC	Buff Section <input type="checkbox"/>
UNANNOUNCED	<input type="checkbox"/>
JUSTIFICATION	
BY	
DISTRIBUTION/AVAILABILITY CODES	
Dist.	AVAIL. and/or SPECIAL
A	

STUDIES OF TRANSITIONAL FLOW, UNSTEADY SEPARATION
PHENOMENA AND PARTICLE INDUCED AUGMENTATION
HEATING ON ABLATED NOSE TIPS

M.S. Holden
Calspan Report No. AB-5646-A-1
October 1975

Prepared For:
AIR FORCE OFFICE OF SCIENTIFIC RESEARCH
1400 WILSON BOULEVARD
ARLINGTON, VIRGINIA 22209
CONTRACT F44620-75-C-0019



CONDITIONS OF REPRODUCTION

Reproduction, translation, publication, use and disposal in whole or in part by or for the United States Government is permitted.

"Approved for public release; distribution unlimited."

Calspan Corporation
Buffalo, New York 14221

"Qualified requestors may obtain additional copies from the Defense Documentation Center, all others should apply to the National Technical Information Service."

PREFACE

The work described in this final report was performed by Calspan Corporation (formerly Cornell Aeronautical Laboratory, Inc.), Buffalo, New York, with the support of the U.S. Air Force under the Air Force Office of Scientific Research, 1400 Wilson Boulevard, Arlington, Virginia 22209, Contract No. F44620-75-C-0019. The contract monitor for this program, conducted during the period November 1974 to June 1975, was Mr. Milton Rogers.

The author would like to acknowledge many helpful discussions on this work which he has had with Mr. Milton Rogers of AFOSR, Lt. Taylor and Captain Jackson of SAMSO, Mr. Portenier, Drs. Taylor, Widhopf, Crowell and Victoria of the Aerospace Corporation, and Mr. Gustafson and Mr. Wilkinson of TRW.

SUMMARY

This report describes the results of two distinct studies of the aerodynamic heating of nose tips. In PART I of these studies we examined experimentally the development of laminar, transitional and turbulent boundary layers over ablated nose shapes at Mach numbers from 8 to 13 for Reynolds numbers up to 80×10^6 based on model diameter. Two groups of models were employed in this study, blunt elliptic, blunt biconic and triconic models were used in the first phase of this investigation where the greatest emphasis was placed on examining the length and structure of the transition region and the parameters which influence it. The second phase of this study was devoted to examining the flow over "highly ablated" nose shapes, over which flow separation and gross flow instabilities occurred. Here we studied how nose tip configuration, roughness and model incidence, as well as the Mach number and Reynolds number of the free stream, influenced the occurrence and structure of large scale periodic instabilities. These studies demonstrated the strong effect of pressure gradient and roughness on the length and characteristics of the transition region. In turn these parameters, along with nose tip geometry, strongly influence the occurrence of flow instabilities over highly-indented nose shapes.

In PART II of this investigation, we studied, in detail, the generation of disturbances in the stagnation region of the flow as a particle, which comes from the model surface, interacts with the bow shock. Here we were primarily interested in gaining a knowledge of the magnitude and mechanism of heating enhancement. These studies which were conducted at Mach 6 and 13, demonstrated that there was little heating enhancement as the particle (between 100 and 800 microns in size) transversed the shock layer; however heating levels between 3 and 10 times the stagnation point value can be generated as the particle penetrates the bow shock. Four distinctly different flow regimes were found to exist for different penetration distances and particle trajectories. Of these the most dramatic is one where a flow instability similar to that encountered over the highly indented nose shapes is observed.

TABLE OF CONTENTS

<u>Section</u>	PART 1	<u>Page</u>
	EXPERIMENTAL STUDIES OF TRANSITIONAL BOUNDARY LAYERS AND BOUNDARY LAYER SEPARATION WITH GROSS FLOW INSTABILITIES OVER ABLATED NOSE SHAPES.	1
1	INTRODUCTION.	2
2	STUDIES OF TRANSITION AND RE-LAMINARIZATION OVER MILDLY ABLATED NOSE SHAPES	5
	2.1 INTRODUCTION.	5
	2.2 EXPERIMENTAL STUDIES OF LAMINAR, TRANSITIONAL AND TURBULENT FLOWS, INCLUDING THE EFFECTS OF ROUGHNESS, ON ABLATED NOSE SHAPES.	14
3	FLOW SEPARATION AND THE DEVELOPMENT OF INSTABILITIES OVER ABLATED NOSE SHAPES.	62
	3.1 INTRODUCTION	62
	3.2 STUDIES OF LAMINAR FLOW OVER THE WIDHOPF 1 AND 2 NOSE SHAPES	69
	3.3 EXPERIMENTAL STUDIES OF THE STABLE AND OSCILLATORY FLOWS OVER THE "A" SERIES NOSE SHAPES	78
	3.4 DETAILED MEASUREMENTS ON THE AO CONFIGURATION	87
	3.5 DETAILED STUDIES ON THE PANT 1 CONFIGURATION	95
4	CONCLUSIONS	124

TABLE OF CONTENTS (Cont.)

<u>Section</u>	PART II	<u>Page</u>
	EXPERIMENTAL STUDIES OF PARTICLE ENHANCED HEATING OF NOSE TIPS.	126
1	INTRODUCTION.	127
2	EXPERIMENTAL PROGRAM.	131
	2.1 PROGRAM OBJECTIVES.	131
	2.2 MODEL AND INSTRUMENTATION	132
	2.3 EXPERIMENTAL FACILITIES	136
3	RESULTS AND DISCUSSION.	137
	3.1 PARTICLE-INDUCED VORTEX HEATING AUGMENTATION.	142
	3.2 HEATING AUGMENTATION RESULTING FROM SHOCK-SHOCK INTERACTION AND FLOW SEPARATION	143
	3.3 FLUID DYNAMIC MECHANISMS IN AUGMENTATION HEATING.	167
4	CONCLUSIONS AND RECOMMENDATIONS	168
APPENDIX		
A	EXPERIMENTAL FACILITIES AND MEASUREMENTS TECHNIQUES	171
	A.1 EXPERIMENTAL FACILITIES	171
	A.2 MODEL AND FLOW-FIELD INSTRUMENTATION.	173
	A.2.1 Introduction.	173
	A.2.2 Skin Friction Measurements.	176
	A.2.3 Heat Transfer Instrumentation	177
	A.2.4 Surface and Flow Field Pressure Measurements.	178
	A.2.5 Data Recording and Processing	181
	A.2.6 Single Frame and High Speed Motion Schlieren Photography	181
	CONCLUSIONS	182
	REFERENCES.	183

LIST OF ILLUSTRATIONS

<u>Figure</u>		<u>Page</u>
1	Correlation of Transition Measurements on Flat Plates and Cones in the Calspan Shock Tunnels with Ballistic and Downrange Measurements	6
2	Correlation of the Scale Length of the Transition Region on Flat Plates and Sharp Cones	8
3	Measurements of Transition Heating on a Blunt Biconic Configuration.	9
4a	Effect of Roughness on Transition and Relaminarisation Over the Biconic Configuration at Mach 13.	10
4b	Effect of Roughness on Transition and Relaminarisation Over the Biconic Configuration at Mach 11.	11
5	Schlieren Photograph Showing Boundary Layer Transition Over a Blunt Biconic Model at Mach 11	12
6	Heat Transfer Distribution in the Transition Region.	13
7	Models of the Mildly Ablated Nose Shapes Used in the Experimental Studies	15
8	Elliptic Nose Tip Mounted in 96" Shock Tunnel.	20
9	A Schlieren Photograph Typical of Those Obtained Over the Biconic Configurations	21
10a	Distribution of Heat Transfer Over the Blunt Biconic Configuration ($M = 12.6$, $Re_D = 2.1 \times 10^6$).	22
10b	Distribution of Heat Transfer Over the Blunt Biconic Configuration ($M = 13.0$ $Re/FT = 4.84 \times 10^6$).	23
10c	Distribution of Heat Transfer to the Blunt Biconic Configuration ($M = 10.8$ $Re/FT = 3 \times 10^6$)	24
10d	Distribution of Heat Transfer to the Blunt Biconic Configuration ($M = 11$, $Re/FT = 6.66 \times 10^6$)	25
10e	Distribution of Heat Transfer Over Blunt Biconic Configuration (Mach 11 $Re_D = 8 \times 10^6$).	26
10f	Distribution of Heat Transfer on the Blunt Biconic Configuration ($M = 11.2$ $Re/FT = 8.8 \times 10^6$)	27
10g	Distribution of Heat Transfer on the Blunt Biconic Configuration ($M = 7.8$ $Re/FT = 6.6 \times 10^7$)	28
11a	Typical Pressure Distribution on Biconic Configuration at Mach 13	29
11b	Typical Pressure Distribution on Biconic Configuration at Mach 11	30

LIST OF ILLUSTRATIONS (Cont.)

<u>Figure</u>		<u>Page</u>
11c	Typical Pressure Distribution on the Biconic Nose at Mach 8	31
12	Schlieren Photograph of the Flow Over the Elliptic Nose Tip. .	32
13a	Measurements of Heat Transfer on the Elliptic Nose at Mach 12.8.	33
13b	Measurements of Heat Transfer of the Elliptic Nose at Mach 11.	34
13c	Measurements of Heat Transfer on the Elliptic Nose at Mach 7.8	35
14a	A Typical Distribution of Pressure on the Elliptic Nose at Mach 13.	36
14b	A Typical Distribution of Pressure on the Elliptic Nose at Mach 7.8	37
15a	A Schlieren Photograph of the Flow Over the Triconic Configuration with Boundary Layer Separation Over the Second Surface	38
15b	Schlieren Photograph Showing Boundry Layer Separation for Transition Flow Over the Model	39
15c	Schlieren Photograph for Turbulent Flow Over Model	40
16a	Heat Transfer Distribution Over the Triconic Model at Mach 12.8	41
16b	Heat Transfer Distribution Over the Triconic Model at Mach 11.	42
16c	Heat Transfer Distribution Over the Triconic Model at Mach 7.8	43
17a	Distribution of Pressure Over the Biconic Configuration at Mach 12.8.	44
17b	Pressure Distribution Over the Triconic Configuration at Mach 11.	45
18	Comparison Between Theory and Experiment for the Biconic Configuration at Mach 12.5	47
19	Comparison Between Theory and Experiment for the Biconic Configuration at Mach 11	48
20	Comparison Between Theory and Experiment for Laminar Heating to the Elliptic Nose Tip	49

LIST OF ILLUSTRATIONS (Cont.)

<u>Figure</u>		<u>Page</u>
21	Measurements of Transition Heating on the Biconic Configuration.	50
22	Comparison Between Simple Theory and Experimental Measurements for Transitional Flow Over the Biconic Configuration.	52
23	Comparison Between the Shock Shape Determined by the Godunov Code and the Experimental Measurements	53
24	Heat Transfer Measurements Demonstrating the Effect of 5 Mil Roughness on Transition and the Character of the Transitional and Relaminarization Regions	54
25	Heat Transfer Measurements Demonstrating the Effect of 5 Mil Roughness on Transition and the Character of the Transitional and Relaminarization Regions	56
26	Heat Transfer Measurements Demonstrating the Effect of 5 Mil Roughness on Transition and the Character of the Transitional and Relaminarization Regions	57
27a	Comparison Between the Heat Transfer to the Biconic Configuration with 5 Mil Roughness and the Theory Developed by Crowell Incorporating POWARS Roughness Model.	59
27b	Comparison Between the Experimental Measurements and Theoretical Solution Obtained by Crowell for Transition Flow Over a Smooth Biconic	60
28	Slender Equilibrium Shape Developed Under Purely Turbulent Boundary Layer Conditions (From REF. 10)	63
29	Variation of Profile Shape with Time for Axisymmetric Camphor Models	63
30	The Development of Ablated Nose Shapes Over Which Flow Instabilities can Occur (Ref. 16).	64
31a	Biconic Representation for Ablated Nose Shape.	65
31b	Tri-radius Representation for Ablated Nose Shape	65
32	Typical Highly-Indented Ablated Shape	65
33	Longitudinal Oscillations, Type E Over Spiked Bodies	67
34	"D" Oscillation Over Spiked Body	68
35	Stability Boundary for E Oscillation on Biconic Configurations	70

LIST OF ILLUSTRATIONS (Cont.)

<u>Figure</u>		<u>Page</u>
36	Widhopf Configurations 1 and 2	71
37	Comparison Between Theory and Experiment for the Widhopf 1 Configuration (1-10-10).	74
38	Schlieren Photograph of Flow Over Widhopf 1 Configuration. . .	75
39a	Schlieren Photographs of Flow Over Widhopf 2 Configuration . .	75
39b	Schlieren Photographs of Flow Over Widhopf 2 Configuration . .	75
40a	Heat Transfer and Pressure Measurements on the Widhopf 2 Configuration	76
40b	Heat Transfer and Pressure Measurements on the Widhopf 2 Configuration	77
41	The "A" Configurations Used in the Calspan Test Matrix	79
42	The "D" Oscillation Over the A1 Configuration	82
43	Mini "E" Oscillation Over the A2 Configuration	84
44	Steady Flow Over the A3 Configuration	85
45	Mini "E" Oscillation Over the A4 Configuration	86
46	Oscillation Boundaries on Highly Indented Nose Shapes	88
47	Two of the Models from the "A" Series Test Program	89
48	"E" Oscillation on A0 Configuration at Zero Angle of Attack. .	91
49a	Heat Transfer Measurements on the A0 Configuration at Mach 13	92
49b	Pressure Transfer Measurements on the A0 Configuration at Mach 13	94
50	Typical Heat Transfer Records from Thin Film Gage on the A0 Configuration	96
51a	Heat Transfer Measurements on the A0 Configuration at Mach 11	97
51b	Pressure Transfer Measurements on the A0 Configuration at Mach 11	99
52a	Effects of Roughness on the Heat Transfer Measurements on the A0 Configuration at Mach 13	100
52b	Effects of Roughness on the Pressure Transfer Measurements on the A0 Configuration at Mach 13.	102

LIST OF ILLUSTRATIONS (Cont.)

<u>Figure</u>		<u>Page</u>
53	Asymmetric Oscillation on the AO Configuration at 3.5° Angle of Attack	103
54a	Effects of Angle-of-Attack on the Heat Transfer Measurements on the AO Configuration at Mach 13	105
54b	Effects of Angle-of-Attack on the Pressure Transfer Measurements on the AO Configuration at Mach 13	107
55	Pant 1 Configuration	110
56	Full E Oscillation Over Smooth Pant 1 Configuration.	112
57	"D" Oscillation Over Pant 1 Configuration with Roughness	113
58	Flow Asymmetries in the Flow About Rough Pant Shape.	114
59a	Heat Transfer Measurements for the E Mode Oscillation Over the Pant 1 Configuration at Mach 13.0	115
59b	Pressure Measurements for the E Mode Oscillation Over the Pant 1 Configuration at Mach 13	116
60a	Heat Transfer Measurements for the E Mode Oscillations Over the Pant 1 Configuration at Mach 11	117
60b	Pressure Measurements for the E Mode Oscillation Over the Pant 1 Configuration at Mach 11.	118
61a	Heat Transfer Measurements for the "D" Mode Flow Oscillation on a Rough (5 Mil) Pant 1 Configuration at Mach 11	119
61b	Pressure Measurements for the "D" Mode Flow Oscillation on a Rough (5 Mil) Pant 1 Configuration at Mach 11	120
62a	Heat Transfer Measurements Over a Smooth Pant 1 Configuration for a 1° Angle of Attack at Mach 11	121
62b	Pressure Measurements Over a Smooth Pant 1 Configuration for a 1° Angle of Attack at Mach 11.	122
63	Shock-Particle Interaction Over a Blunt Ellipsoid.	128
64	Shock-Particle Interaction Over a Blunted Cone	129
65	Vortex Generation Resulting From Particle Rebound, a Sequence Taken in the Boeing Mach 6 Tunnel	130
66	Impact Particle Launcher	134

LIST OF ILLUSTRATIONS (Cont.)

<u>Figure</u>		<u>Page</u>
67	Model Assembly & Instrumentation Nose Tip Heating (SAMSO/AFOSR).	135
68	Heating Augmentation Associated with Particle-Induced Ring Vortex Interaction.	144
69	"Stable" Flow Resulting from Small Penetration	145
70	Particle-Induced Large Scale Oscillation (E) of Flow Field (Mach 13).	147
71	Particle-Induced Large Scale Oscillation (E) (Mach 6.5).	150
72	Typical Heat Transfer Record from Thin Film Gages.	155
73	Heat Transfer Distribution to the Face of the Disc for a Fully Oscillating Flow Over the Model.	156
74	Typical Pressure Oscillogram, Run 3.	157
75	Heat Transfer Rate Distribution, Run 15.	158
76	Heat Transfer Rate Distribution, Run 18.	160
77	Non-Oscillatory Flow Resulting from Off-Axis Particle Trajectory	161
78	Heat Transfer Rate Distribution, Run 20.	164
79	Weak Oscillatory Flow Resulting from Small Penetration and Off-Axis Trajectory.	165
80a	Wave Diagram for Tailored-Interface Shock Tunnel	172
80b	Test Time Available for Tailored-Interface Operation of 48-Inch Shock Tunnel	172
81	Calspan Hypersonic Shock Tunnel Performance.	174
82	Minimum Transition Distance on Sharp Flat Plate Models for Calspan Hypersonic Shock Tunnels	175
83	Drawing of Section Through Skin Friction Transducer.	179
84	High-Frequency Pressure Mounting	179
85	Models Showing Typical Heat Transfer Gage Installation	180

LIST OF TABLES

<u>Table</u>		<u>Page</u>
1	Test Conditions for Tests of Mildly Indented Nose Shapes [See Figure 7].	16
2	Test Conditions for Widhopf 1 and 2 Configurations	72
3	Test Conditions for the A Configurations	80
4	Test Conditions for Fully Instrumented AO Configurations	90
5	Test Conditions for Pant 1 Tests	111
6	Test Matrix for Calspan Program.	138
7	Test Conditions for Heating Enhancement Program.	139

PART I
EXPERIMENTAL STUDIES OF TRANSITIONAL BOUNDARY LAYERS
AND BOUNDARY LAYER SEPARATION WITH GROSS FLOW
INSTABILITIES OVER ABLATED NOSE SHAPES

Section 1

INTRODUCTION

To develop a reliable and accurate re-entry system employing slender high β vehicles, it is necessary to understand and formulate methods to analyze the changes which occur to the ablative nose tip and the associated viscous and inviscid flow field in which it is enveloped during re-entry. Small changes to the shape of a nose tip can change significantly the drag and moment coefficients of the vehicle, particularly if such shape changes are asymmetric in character. While measurements from ablation tests have suggested that nose shapes develop equilibrium or self-preserving profiles^{*} under fixed free stream conditions, complex non-equilibrium shapes can develop as the vehicle descends through the atmosphere, and its boundary layer undergoes a transition from laminar to turbulent characteristics. The flow fields over such "non-equilibrium" shapes are complex, involving regions of shock wave-boundary layer interaction, and shock-shock interaction. The large localized heating rates associated with such interactions can ultimately create nose shapes over which flow instabilities resulting from the alternate formation and collapse of embedded separated regions can occur. The dynamic forces which result from such instabilities seriously degrade the performance of the vehicle. Experimental studies have demonstrated that small asymmetries in surface roughness or ablated shape for these configurations can result in flow asymmetries of dramatic proportions. A small angle of incidence can result in flow asymmetries of comparable magnitudes.

The movement of the transition point from the conical surface onto the face of a nosetip begins a process which, because of resultant localized increase in heating, may create an indented nose shape. The formation of an imbedded shock over this configuration results in a significant increase in heating at the base of the shock (resulting from shock wave-boundary layer interaction) which drives the ablating nose into a shape with a more concave form. On these shapes, the shock-shock interaction can also cause intense heating at the reattachment point of the shear layer which is generated at the

^{*} Discussed in Section 3.

intersection between the bow shock and embedded shock. In many cases nose tips do not ablate symmetrically and the asymmetric flow field which results can impress a pressure distribution on the nose which can cause asymmetric forces of significant proportions. These side forces are of greatest magnitude when a separated region is induced on one side of the nose tip while the flow remains attached on the other. This situation can also arise on symmetric highly-ablated nose shapes when they are pitched at angle of attack.

The development, through ablation, of nose shapes over which gross aerodynamic instabilities occur, has been demonstrated in ablation tests using camphor models and inferred from downrange observation of full scale flight missions. Regions of gross instability on nose shapes in hypersonic flow were first studied in detail over "spiked bodies". For a certain class of configurations, where a spike pierces the bow shock and yet is of insufficient length to permit an equilibrium separated region to be formed, a flow oscillation is observed in which there is a periodic formation and collapse of the separated region. A similar oscillation is observed over bi-conic configurations; and studies have been performed to define the geometries over which these oscillations occur. Most of the studies which were conducted in hypersonic flow were at low Reynolds numbers; however the recent high Reynolds number studies at Calspan have demonstrated that transition to turbulence on the nose of the vehicle can significantly inhibit such oscillations. Nose tip roughness, which is an inherent feature of ablating nose shapes, was also found to play an important role in the oscillation onset. The detailed heat transfer, pressure and skin friction measurements made in the Calspan study identified the importance of shock-boundary layer interaction and shock-shock interaction as the basic mechanisms which cause large heating rates driving an indented shape toward shapes over which flow instabilities occur. Perhaps the most important finding from these studies is the large sensitivity of the oscillating flow fields to angle of attack. The large asymmetric pressure forces and heat transfer rates generated under these conditions tend to drive the nose region into an asymmetric form and the vehicle to increasing angle of incidence. The oscillations generated under these conditions differ significantly from those observed at zero incidence.

In this study we investigated two aspects of the aerodynamics of the non-equilibrium ablation of nose tips. In the first of these studies we obtained detailed heat transfer and pressure measurements on blunt elliptic, blunt biconic and triconic models at Mach number from 8 to 13 for Reynolds numbers up to 80×10^6 . Here, while we sought information on the laminar heat transfer distribution over these nose shapes, we were primarily interested in examining the length and structure of the transition region and the parameters which influenced it. In the second study we examined the flow over highly ablated nose shapes over which flow separation and gross flow instabilities occurred. Here our studies were devoted to examining how nose tip configuration, surface roughness and model incidence, as well as Mach number and Reynolds number of the inviscid flow influenced the occurrence and structure of large-scale periodic aerodynamic instabilities which can develop over these shapes.

Section 2

STUDIES OF TRANSITION AND RE-LAMINARIZATION OVER MILDLY ABLATED NOSE SHAPES

2.1 INTRODUCTION

The development of computer codes to describe accurately the shape change of a nose-tip of a slender RV as it descends through the atmosphere revolves about an accurate description of the boundary layer and its interaction with the ablation material. While the description of the development of nose tip shapes in laminar flows may be considered to be relatively accurate, the complexities in the fluid mechanics which arise when transition begins on the bodies has yet to be fully understood or successfully described in an analytical or numerical framework. It is clear that, at this time, in order to assist in understanding the origins and development of turbulence over complex nose shapes, we require an insight through experimental measurements. The problem of predicting the position of boundary layer transition on ablating nose shapes has yet to be solved. While this problem is difficult enough for smooth bodies, on nose tips we are faced with understanding the influence of ablation and roughness. While recent analytical studies have used linearized stability theory (Ko)¹ and turbulent energy methods (Wilcox² and Finson³) in attempts to describe this process with some success, each employs some degree of empiricism in their approaches. In correlating measurements of transition made in wind tunnels, we are faced with the problem of evaluating the influence of tunnel noise on this process, and some theories (e.g., Wilcox's) attempt to account for this. Aerotherm have suggested from their studies that transition can be correlated in the form $Re_{\theta} \left(\frac{T_{edge}}{T_{wall}} \frac{k}{\theta} \right)^{0.7} = 215$. Where k is the roughness height and θ the momentum thickness at the beginning of transition. While this criteria is simple, it has the merit of being in relatively good agreement with measurements made by Aerotherm at Mach 5. Measurements of transition over sharp flat plates and cones in the Calspan Shock Tunnels at high Mach numbers have been found to be in remarkably good agreement in the ballistic range and correlations of flight data as shown with measurements in Figure 1.

While the beginning of transition may be influenced by tunnel noise, the characteristics of the transitional region and the turbulent boundary layer which developed downstream of it does not exhibit this sensitivity. The length and characteristics of the transition region, however, do depend strongly on the pressure and entropy gradients in the inviscid flow and the roughness of the

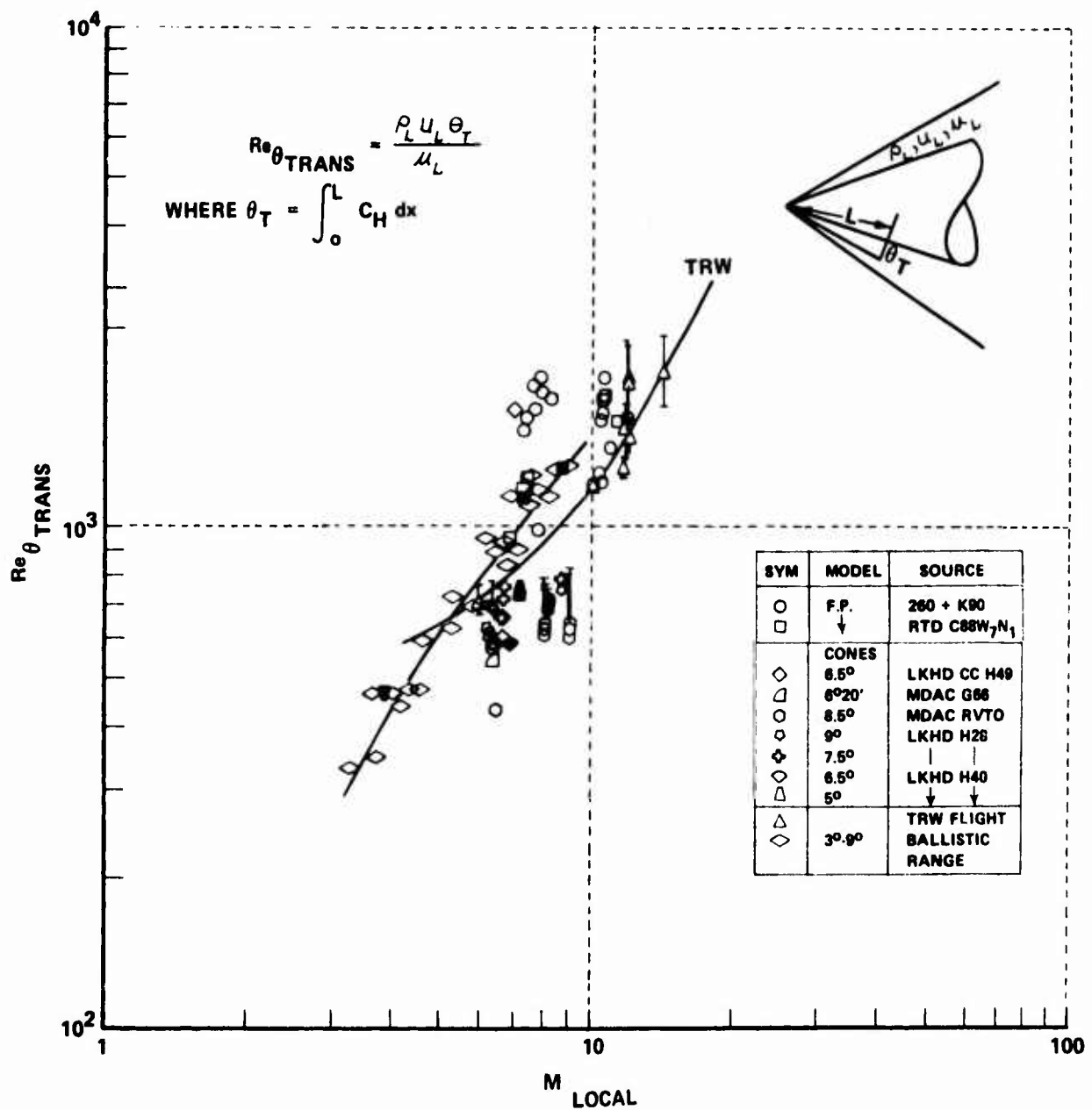


Figure 1 CORRELATION OF TRANSITION MEASUREMENT ON FLAT PLATES AND CONES IN THE CALSPAN SHOCK TUNNELS WITH BALLISTIC AND DOWNRANGE MEASUREMENTS (REF. 6)

surface. For constant pressure, high speed boundary layers in the absence of entropy gradient, the length of the transition region can be related to the length of the laminar run as shown in correlations of measurements on flat plate and cones made at Calspan presented in Figure 2. However, as shown in Figure 3, the length of the transition region on blunted nose tips cannot be related simply due to the length of laminar run. Adding roughness not only increases the level of heating, but also significantly modifies the length and characteristics of the transition region as shown in Figure 4. The photographs obtained in the experimental studies on bi-conic configurations, show on Figure 5 indicate a wave-like structure in the boundary layer close to the transition point. This structure has also been observed in experimental studies conducted by Demetriades.⁴ The records of the heat transfer in the transition region on this bi-conic configuration in the present studies show distinctive bursts in heating which raise the local heat transfer rate to close to the turbulent value. These bursts appear to be convected downstream over adjacent gages. This result is not inconsistent with Emmons' spot theory in which the heat transfer to the wall is related to an intermittency parameter and through the relationship

$$C_{H_{TRANS}} = \gamma C_{H_{TURB}} + (1 - \gamma) C_{H_{LAMINAR}}$$

where γ is the fraction of time the boundary layer exhibits turbulent characteristics, and $C_{H_{TURB}}$ and $C_{H_{LAM}}$ are the heat transfer coefficients for full turbulent or laminar flow respectively. Clearly, γ assumes values from 0 to 1 through the transition region and can be related to the position in the transition region by the expression $\gamma = \frac{1 - e^{-A\xi^2}}{1 - e^{-A}}$ as shown in Figure 6. A is a parameter chosen from correlation of the experimental data. While this general approach has been used with some success to describe the distribution of heat transfer to the wall in the transition region, it is clear it must be modified, based on experimental measurements, when transition is influenced by roughness, vorticity, entropy and pressure gradients. It is of interest to note that while the Emmons' theory⁵ is in relatively good agreement with the mean values of heat transfer in the transition region at high Mach numbers, the fluctuation measurements of heat transfer made under these conditions do not display the intermittent laminar and turbulence character upon which this theory is based.

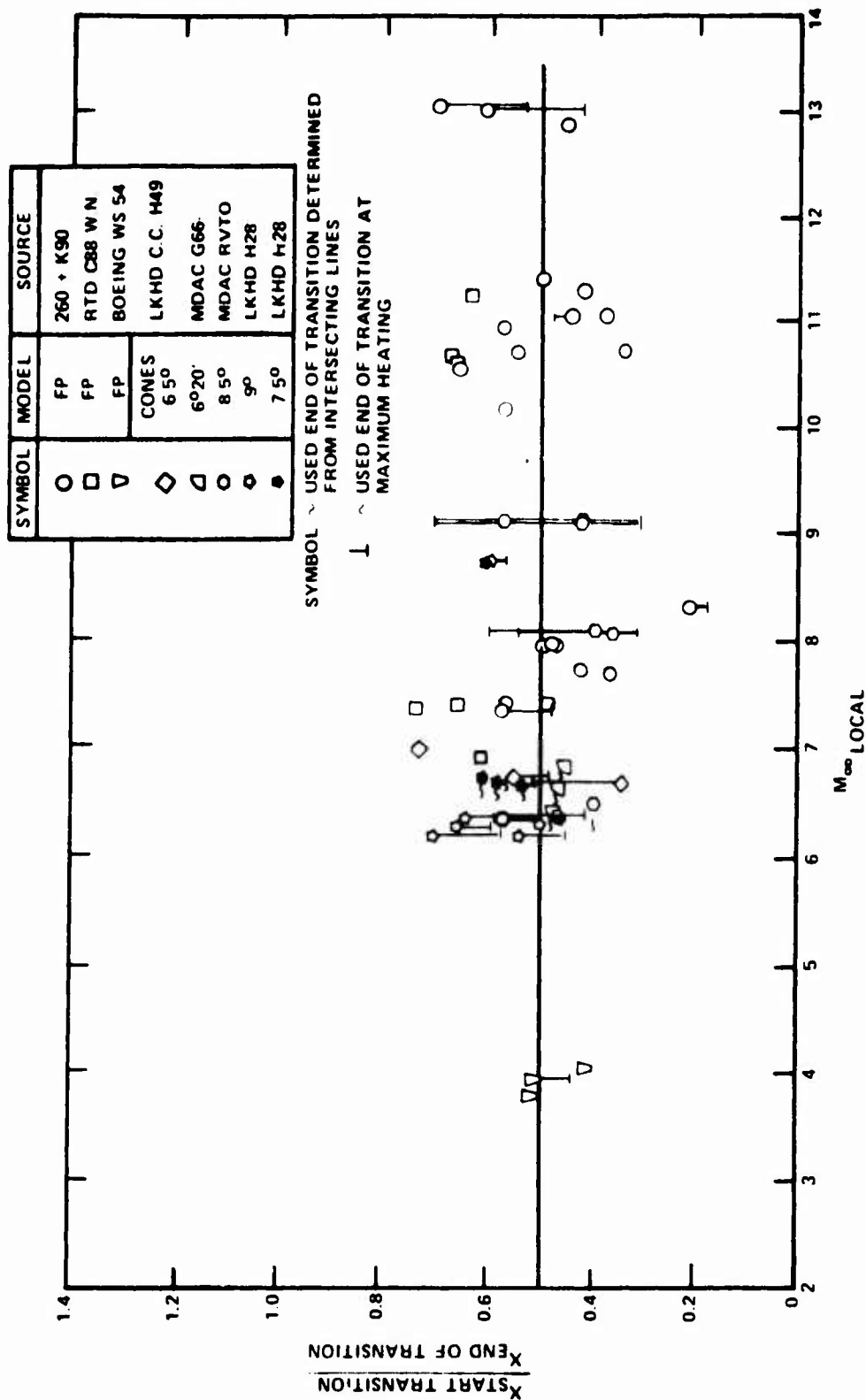


Figure 2 CORRELATION OF THE SCALE LENGTH OF THE TRANSITION REGION ON FLAT PLATES AND SHARP CONES (REF. 6)

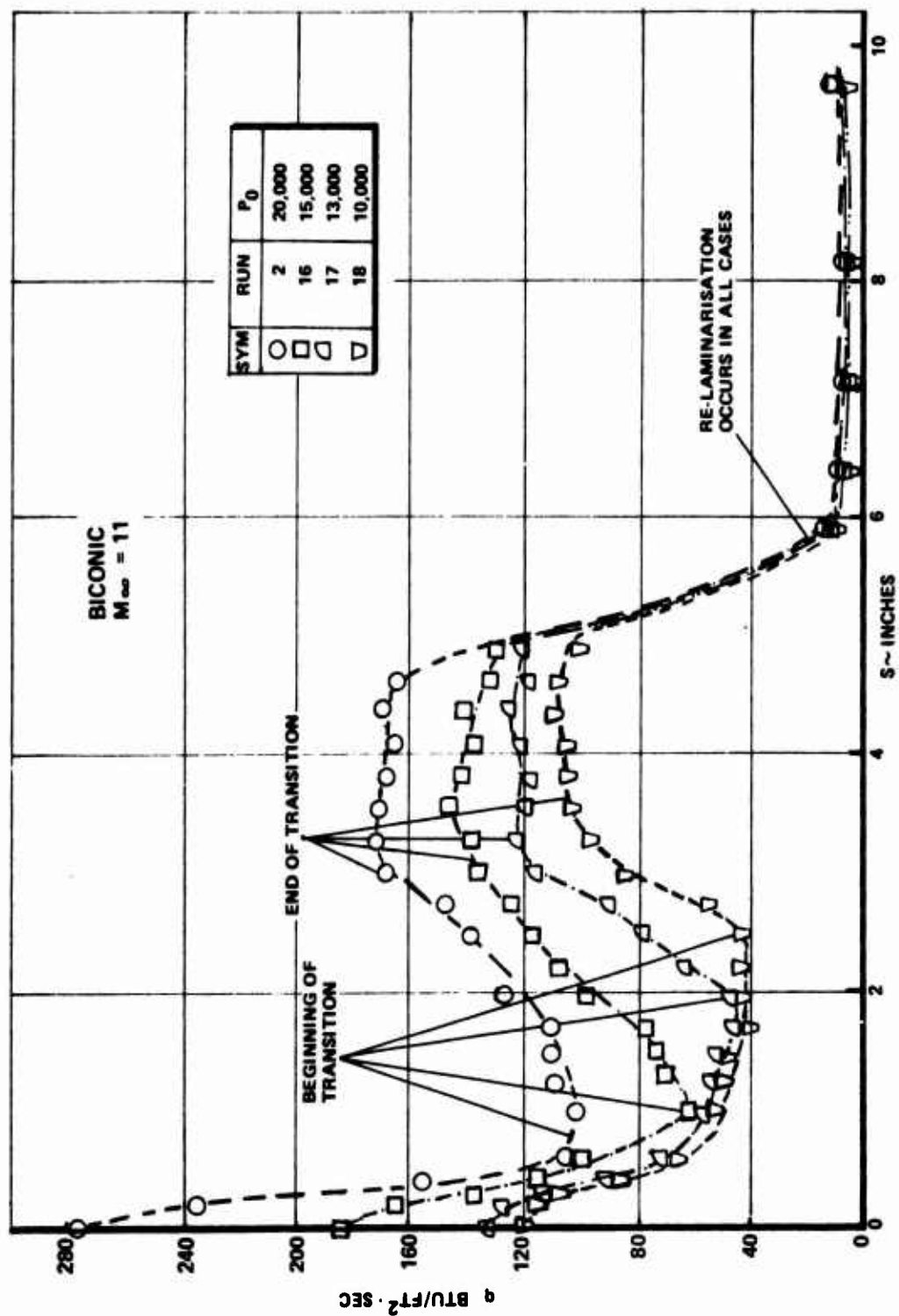


Figure 3 MEASUREMENTS OF TRANSITION HEATING ON A BLUNT BICONIC CONFIGURATION

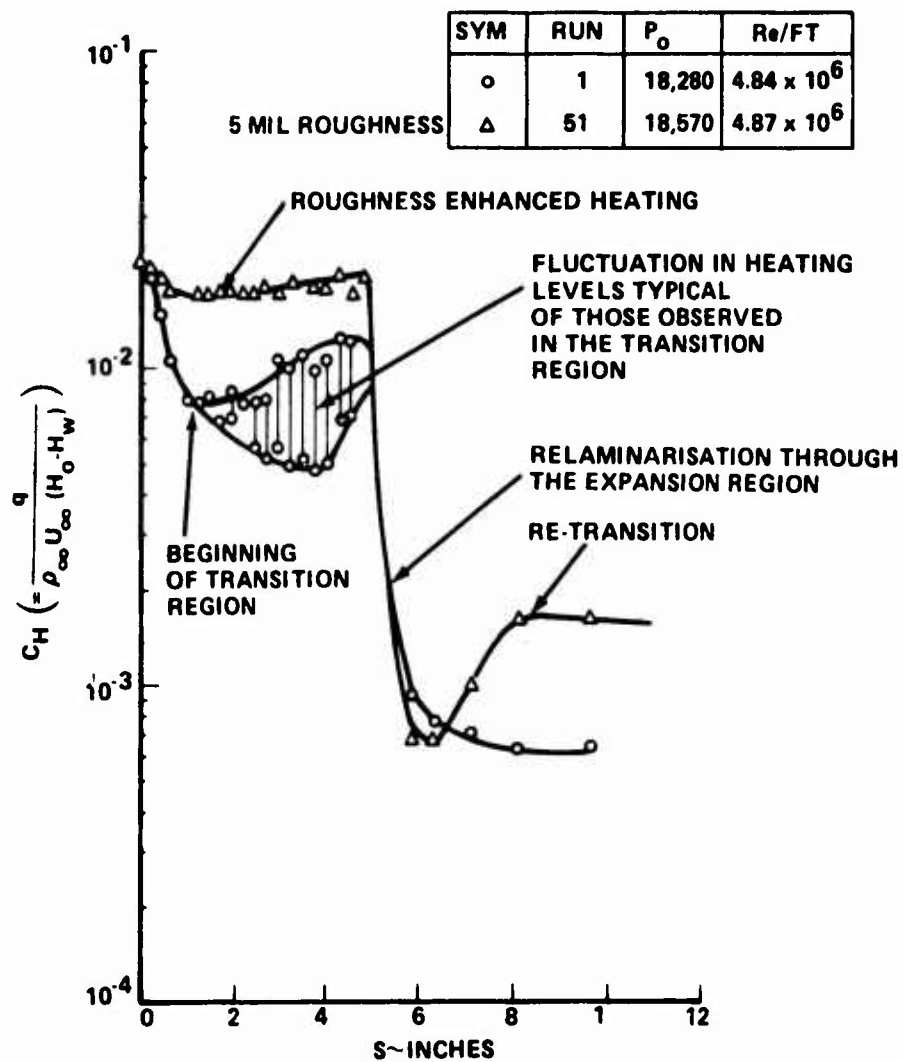


Figure 4a EFFECT OF ROUGHNESS ON TRANSITION AND RELAMINARISATION OVER THE BICONIC CONFIGURATION AT MACH 13

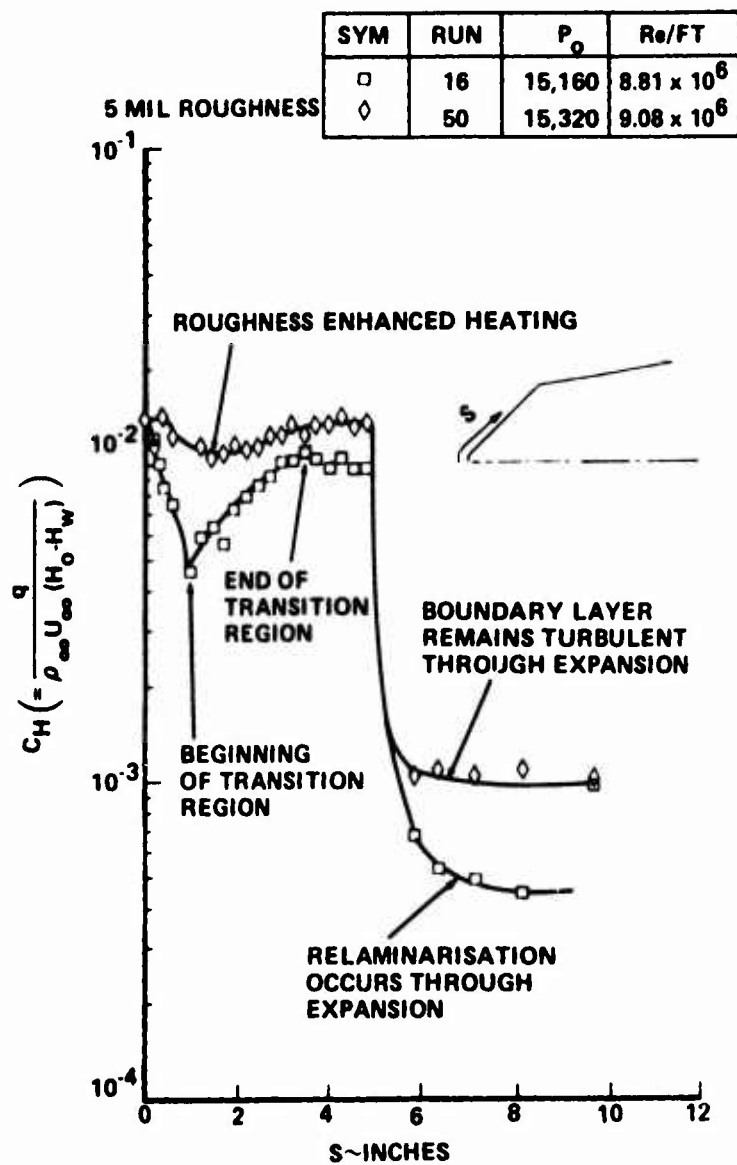


Figure 4b EFFECT OF ROUGHNESS ON TRANSITION AND RELAMINARISATION OVER THE BICONIC CONFIGURATION AT MACH 11

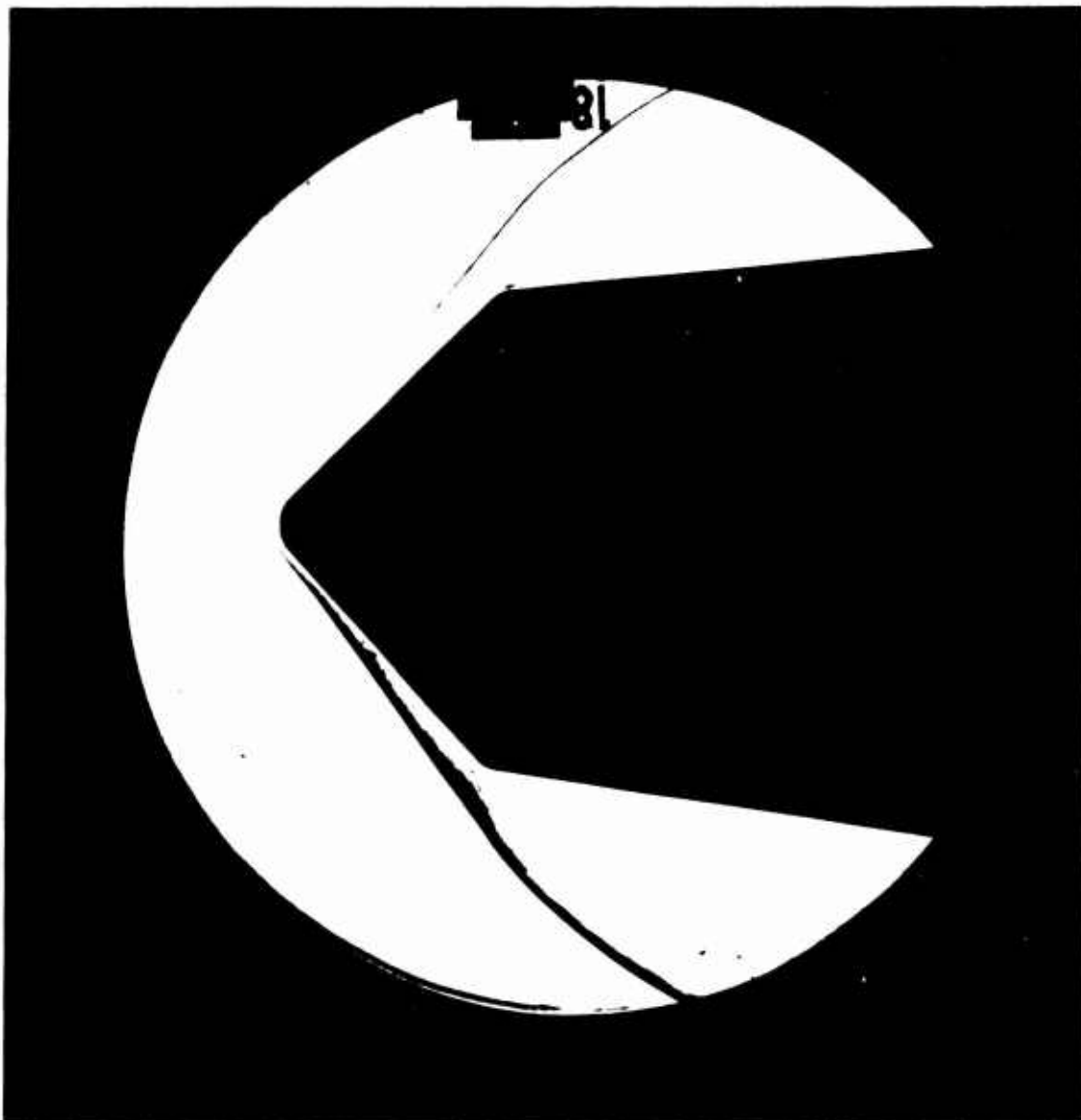


Figure 5 SCHLIEREN PHOTOGRAPH SHOWING BOUNDARY LAYER TRANSITION OVER A BLUNT BICONIC MODEL AT MACH 11

$$C_H = \gamma C_{H_{TURB}} + (1-\gamma) C_{H_{LAM}}$$

$$\text{WHERE } \gamma = \frac{1 - e^{-A\xi^2}}{1 - e^{-A}}$$

$$\text{AND } \xi = \frac{x - x_{LAM}}{x_{TURB} - x_{LAM}}$$

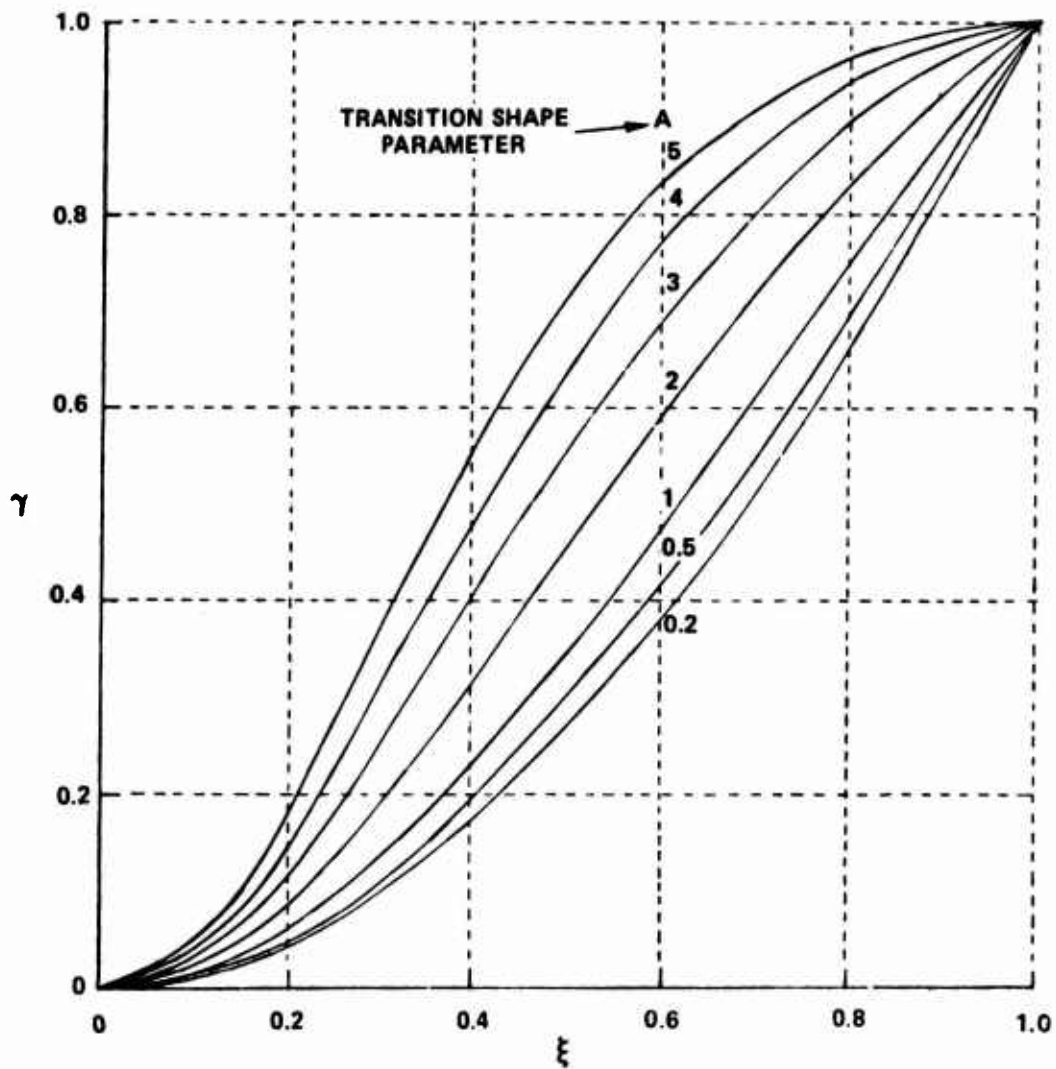
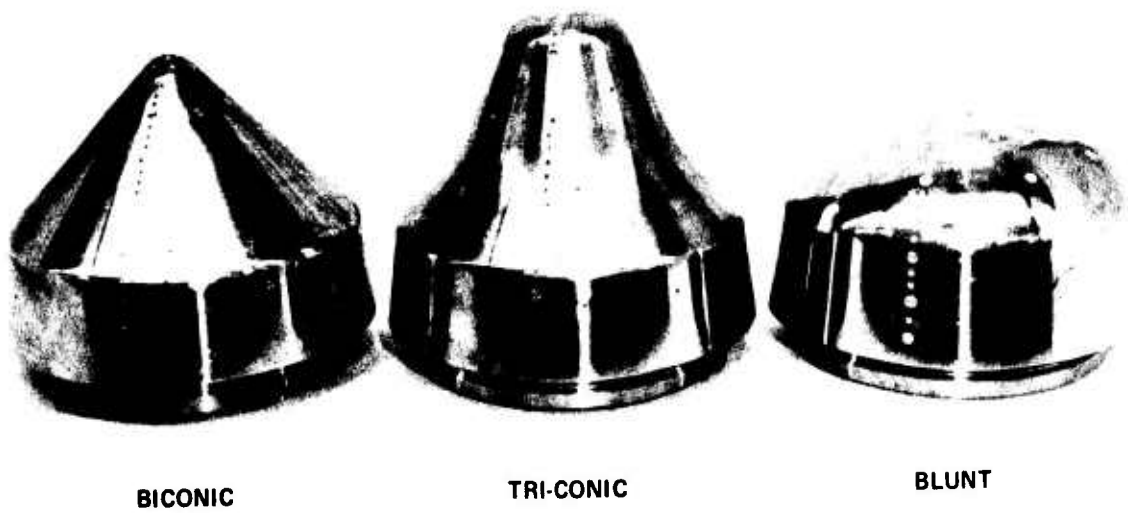


Figure 6 HEAT TRANSFER DISTRIBUTION IN THE TRANSITION REGION

One characteristic of the transition region which is important in nose tip technology is the "heat transfer overshoot" which occurs close to the end of the transition process. The generation of turbulence in the transition region is such that the turbulent scale size larger than that for a corresponding fully turbulent boundary layer is generated, and this results in increased heating levels. This "low Reynolds" number turbulent structure is influenced by viscosity and eventually dissipation drives the turbulent scale sizes toward the local equilibrium values. However, this relaxation process can occur over a region as long as 50 boundary layers thicknesses, as shown by Holden⁶ and Bushnell.⁷ While this low Reynolds number effect causes heating rates of only 125% in excess of the equilibrium turbulent levels, sophisticated shape change codes which are now being developed should be formulated in such a way that the flow downstream of transition is modelled correctly. Again experimental measurements are needed to inspire and evaluate such models.

2.2 EXPERIMENTAL STUDIES OF LAMINAR, TRANSITIONAL AND TURBULENT FLOWS, INCLUDING THE EFFECTS OF ROUGHNESS, ON ABLATED NOSE SHAPES

The three models used in the investigation of transition on ablated nose shapes, chosen as representative of those that might be found in flight, are shown in Fig. 7. These models were highly instrumented with heat transfer and pressure gages to provide the spatial and temporal resolution required to define accurately the characteristics of the transition and relaminarisation region. Figure 8 shows the model with the elliptic nose shape installed in the 96" Shock Tunnel. Schlieren photographs typical of those obtained in the studies are shown in Figs. 9, 12 and 15. The distributions of heat transfer over the biconic, elliptic and tri-conic configurations at Mach numbers from 8 to 13 for a range of Reynolds numbers from 10^6 to 80×10^6 are shown in Figures 10, 13 and 16. The pressure distributions over the bi-conic and elliptic configurations varied little with Mach number and Reynolds number, and typical distributions obtained on these configurations are shown in Figs. 11 and 14. The pressure measurements obtained on the tri-conic configuration are shown in Fig. 17. Here the variations of pressure or heating distribution with Mach number and Reynolds number reflects changes in the structure of the regions of viscous interaction and flow separation over the convex surface of the model.



**Figure 7 MODELS OF THE MILDLY ABLATED NOSE SHAPES
USED IN THE EXPERIMENTAL STUDIES**

Table 1
TEST CONDITIONS FOR TESTS OF ABLATED
NOSE SHAPES [SEE FIGURE 7]

RUN NO.	ATTACK	DEGREES	1	2	3	4	6	7	b
YAW	DEGREES	0.0	0.0	0.0	0.0	0.0	0.0	0.0	0.0
ROLL	DEGREES	0.0	0.0	0.0	0.0	0.0	0.0	0.0	0.0
M(I)	-	3.720E+00	3.339E+00	3.509E+00	3.600E+00	3.600E+00	3.308E+00	3.299E+00	3.609E+00
P(O)	PSIA	1.828E+04	1.765E+04	1.765E+04	1.765E+04	1.765E+04	1.765E+04	1.765E+04	1.765E+04
H(O)	FT LBS/SLUGS	2.128E+07	1.943E+07	1.777E+07	2.038E+07	2.038E+07	1.769E+07	1.741E+07	2.025E+07
T(O)	OR	3.241E+03	3.020E+03	2.737E+03	3.069E+03	3.069E+03	2.780E+03	2.687E+03	3.070E+03
M	-	1.297E+01	1.115E+01	1.060E+01	1.255E+01	1.255E+01	1.125E+01	1.062E+01	1.256E+01
U	FT/SEC	6.432E+03	6.115E+03	5.841E+03	6.288E+03	6.288E+03	5.837E+03	5.782E+03	6.268E+03
T	OR	1.023E+02	1.251E+02	1.216E+02	1.044E+02	1.044E+02	1.120E+02	1.186E+02	1.035E+02
P	PSIA	7.902E-02	2.216E-01	7.770E-02	3.675E-02	3.675E-02	2.239E-01	7.545E-02	3.648E-02
Q	SLUGS/FT ³	9.310E+00	1.929E+01	6.350E+00	4.054E+00	4.054E+00	1.985E+01	6.196E+00	4.258E+00
RHO	SLUGS/FT ³	6.481E-05	1.486E-04	5.361E-05	2.952E-05	2.952E-05	1.678E-04	5.338E-05	3.121E-05
MU	SLUGS/FT SEC	8.608E-08	1.052E-07	1.023E-07	8.787E-08	8.787E-08	9.420E-08	9.973E-08	8.705E-08
RE/FT.	-	4.843E+06	6.639E+06	3.662E+06	2.113E+06	2.113E+06	1.040E+07	3.095E+06	2.247E+06
PITQT	PSIA	1.730E+01	3.579E+01	1.176E+01	7.527E+00	7.527E+00	3.676E+01	1.147E+01	7.905E+00
T*	OR	9.491E+02	9.016E+02	8.480E+02	9.236E+02	9.236E+02	8.451E+02	8.360E+02	9.178E+02
MU*	SLUGS/FT SEC	5.783E-07	5.586E-07	5.356E-07	5.678E-07	5.678E-07	5.343E-07	5.204E-07	5.653E-07
SQRT.C*	-	8.511E-01	8.586E-01	8.666E-01	8.546E-01	8.546E-01	8.671E-01	8.686E-01	8.557E-01
H(W)	FT LBS/SLUG	3.171E+06	3.195E+06	3.177E+06	3.189E+06	3.189E+06	3.207E+06	3.177E+06	3.171E+06
T(W)	OR	5.260E+02	5.320E+02	5.290E+02	5.310E+02	5.310E+02	5.340E+02	5.290E+02	5.260E+02
P(TS)	PSI	9.670E-05	7.736E-05	8.670E-05	3.668E-05	3.668E-05	7.736E-05	1.934E-05	3.868E-05

Table 1
TEST CONDITIONS FOR TESTS OF ABLATED
NOSE SHAPES [SEE FIGURE 7] (CONTINUED)

RUN NO.	12	13	16	17	18	19	20
ATTACK	0.0	0.0	0.0	0.0	0.0	0.0	0.0
YAW	0.0	0.0	0.0	0.0	0.0	0.0	0.0
ROLL	0.0	0.0	0.0	0.0	0.0	0.0	0.0
M(I)	3.419E+00	3.609E+00	3.420E+00	3.282E+00	3.275E+00	3.265E+00	3.674E+00
P(O)	5.041E+03	7.596E+03	1.516E+04	1.298E+04	1.120E+04	1.089E+04	1.519E+04
H(O)	1.658E+07	2.032E+07	1.749E+07	1.693E+07	1.715E+07	1.688E+07	2.093E+07
T(O)	2.571E+03	3.080E+03	2.741E+03	2.652E+03	2.673E+03	2.634E+03	3.182E+03
M	1.082E+01	1.255E+01	1.115E+01	1.110E+01	1.104E+01	1.105E+01	1.288E+01
U	5.642E+03	6.279E+03	5.803E+03	5.708E+03	5.744E+03	5.698E+03	6.377E+03
T	1.131E+02	1.042E+02	1.127E+02	1.100E+02	1.125E+02	1.106E+02	1.019E+02
P	6.919E-02	3.727E-02	1.935E-01	1.690E-01	1.471E-01	1.422E-01	1.019E+02
U	5.674E+00	4.110E+00	1.682E+01	1.458E+01	1.257E+01	1.222E+01	7.740E+00
RHO	5.133E-05	3.002E-05	1.439E-04	1.299E-04	1.097E-04	1.084E-04	5.461E-05
MU	9.513E-08	8.762E-08	5.478E-08	9.256E-08	9.462E-08	9.300E-08	8.577E-08
RE/FT.	3.045E+06	2.152E+06	8.410E+06	7.949E+06	6.660E+06	6.642E+06	4.075E+06
PITOT	1.050E+01	7.632E+00	3.116E+01	2.700E+01	2.327E+01	2.262E+01	1.438E+01
T*	8.079E+02	9.207E+02	8.268E+02	8.166E+02	8.263E+02	8.158E+02	9.387E+02
MU*	5.179E-07	5.666E-07	5.507E-07	5.219E-07	5.261E-07	5.214E-07	5.740E-07
SQRT.C*	8.731E-01	6.553E-01	6.684E-01	8.716E-01	8.701E-01	8.717E-01	8.526E-01
H(W)	3.165E+06	3.177E+06	3.177E+06	3.153E+06	3.177E+06	3.159E+06	3.177E+06
T(W)	5.270E+02	5.290E+02	5.290E+02	5.250E+02	5.290E+02	5.260E+02	5.290E+02
P(TSI)	5.802E-05	5.868E-05	9.670E-05	5.802E-05	3.863E-05	3.868E-05	3.868E-05

Table 1
TEST CONDITIONS FOR TESTS OF ABLATED
NOSE SHAPES [SEE FIGURE 7] (CONTINUED)

RUN NO.	ATTACK	DEGREES	21	23	44	25	2c	2e	30
YAW	DEGREES	0.0	0.0	0.0	0.0	0.0	0.0	0.0	0.0
ROLL	DEGREES	0.0	0.0	0.0	0.0	0.0	0.0	0.0	0.0
M(I)	-	3.664E+00	3.290E+00	3.522E+00	3.318E+00	2.552E+00	2.477E+00	2.534E+00	2.534E+00
P(O)	PSIA	1.139E+04	1.509E+04	1.385E+04	1.681E+04	1.670E+04	1.546E+04	1.674E+04	1.674E+04
H(O)	FT LBS/SLUGS	4.110E+07	1.749E+07	1.741E+07	1.753E+07	1.098E+07	1.068E+07	1.111E+07	1.111E+07
T(O)	OR	3.196E+03	2.741E+03	2.719E+03	2.754E+03	1.824E+03	1.770E+03	1.841E+03	1.841E+03
M	-	1.272E+01	1.117E+01	1.112E+01	1.121E+01	7.781E+00	7.775E+00	7.787E+00	7.787E+00
U	FT/SEC	6.410E+02	5.802E+02	5.788E+02	5.809E+02	4.506E+02	4.444E+02	4.533E+02	4.533E+02
T	OR	1.056E+02	1.144E+02	1.127E+02	1.117E+02	1.395E+02	1.359E+02	1.409E+02	1.409E+02
P	PSIA	5.428E+00	1.895E+01	1.770E+01	2.123E+01	2.868E+00	2.601E+00	2.854E+00	2.854E+00
J	SLUGS/FT ³	4.153E-05	1.417E-04	1.533E+01	1.869E+01	1.217E+02	1.102E+02	1.213E+02	1.213E+02
RHO	SLUGS/FT SEC	8.487E-05	4.436E-08	9.475E-08	9.391E-08	1.726E-03	1.606E-03	1.700E-03	1.700E-03
MU	-	2.995E+06	8.715E+06	6.053E+06	9.870E+06	6.643E+07	6.258E+07	6.516E+07	6.516E+07
RE/FT.	PSIA	1.101E+01	3.069E+01	2.860E+01	3.463E+01	2.240E+02	2.028E+02	2.233E+02	2.233E+02
PITOT	OR	4.464E+02	8.384E+02	6.332E+02	8.379E+02	6.434E+02	6.356E+02	6.508E+02	6.508E+02
T*	SLUGS/FT SEC	5.760E-07	5.214E-07	5.291E-07	5.312E-07	4.400E-07	4.360E-07	4.437E-07	4.437E-07
MU*	-	8.512E-01	8.681E-01	8.690E-01	8.692E-01	9.026E-01	9.039E-01	9.013E-01	9.013E-01
SQRT.C*	FT LBS/SLUG	3.195E+06	3.201E+06	3.165E+06	3.153E+06	3.153E+06	3.183E+06	3.189E+06	3.189E+06
H(W)	OR	5.320E+02	5.330E+02	5.270E+02	5.300E+02	5.250E+02	5.300E+02	5.310E+02	5.310E+02
T(W)	PSI	3.668E-05	3.668E-05	5.102E-05	5.802E-05	7.736E-05	5.802E-05	5.802E-05	5.802E-05

Table 1
TEST CONDITIONS FOR TESTS OF ABLATED
NOSE SHAPES [SEE FIGURE 7] (CONTINUED)

RUN NO.	31	35	40	49	50	51
ATTACK	0.0	0.0	0.0	0.0	0.0	0.0
YAW	0.0	0.0	0.0	0.0	0.0	0.0
ROLL	0.0	0.0	0.0	0.0	0.0	0.0
M(I)	2.512E+00	3.350E+00	3.358E+00	3.295E+00	3.324E+00	3.715E+00
P(O)	1.609E+04	1.555E+04	1.566E+04	1.150E+04	1.532E+04	1.657E+04
H(O)	1.024E+07	1.751E+07	1.776E+07	1.727E+07	1.734E+07	2.138E+07
T(O)	1.798E+03	2.742E+03	2.780E+03	2.684E+03	2.719E+03	3.255E+03
M	7.779E+00	1.116E+01	1.116E+01	1.104E+01	1.115E+01	1.296E+01
U	4.476E+03	5.805E+03	5.850E+03	5.763E+03	5.777E+03	6.448E+03
T	1.377E+02	1.125E+02	1.143E+02	1.132E+02	1.117E+02	1.026E+02
P	2.736E+00	1.966E-01	1.984E-01	1.506E-01	1.964E-01	7.964E-02
Q	1.160E+02	1.733E+01	1.731E+01	1.284E+01	1.711E+01	9.407E+00
RWD	1.668E-03	1.461E-04	1.457E-04	1.116E-04	1.476E-04	6.516E-05
MU	1.156E-07	9.462E-08	9.609E-08	9.523E-08	9.391E-08	8.628E-08
RE/FT.	6.457E+07	9.087E+06	6.870E+06	6.766E+06	9.082E+06	4.870E+06
PI TOT	4.126E+02	3.210E+01	3.207E+01	2.568E+01	3.169E+01	1.746E+01
T*	6.399E+02	6.352E+02	6.455E+02	6.296E+02	6.303E+02	9.534E+02
MU*	4.382E-07	5.300E-07	5.345E-07	5.275E-07	5.278E-07	5.801E-07
SQRT.C*	9.032E-01	6.666E-01	6.670E-01	8.095E-01	8.694E-01	8.504E-01
H(W)	3.171E+06	3.153E+06	3.171E+06	3.171E+06	3.159E+06	3.183E+06
T(W)	5.280E+02	5.250E+02	5.280E+02	5.260E+02	5.260E+02	5.300E+02
P(TS)	5.802E-05	1.547E-04	1.741E-04	2.901E-04	1.354E-04	2.901E-04

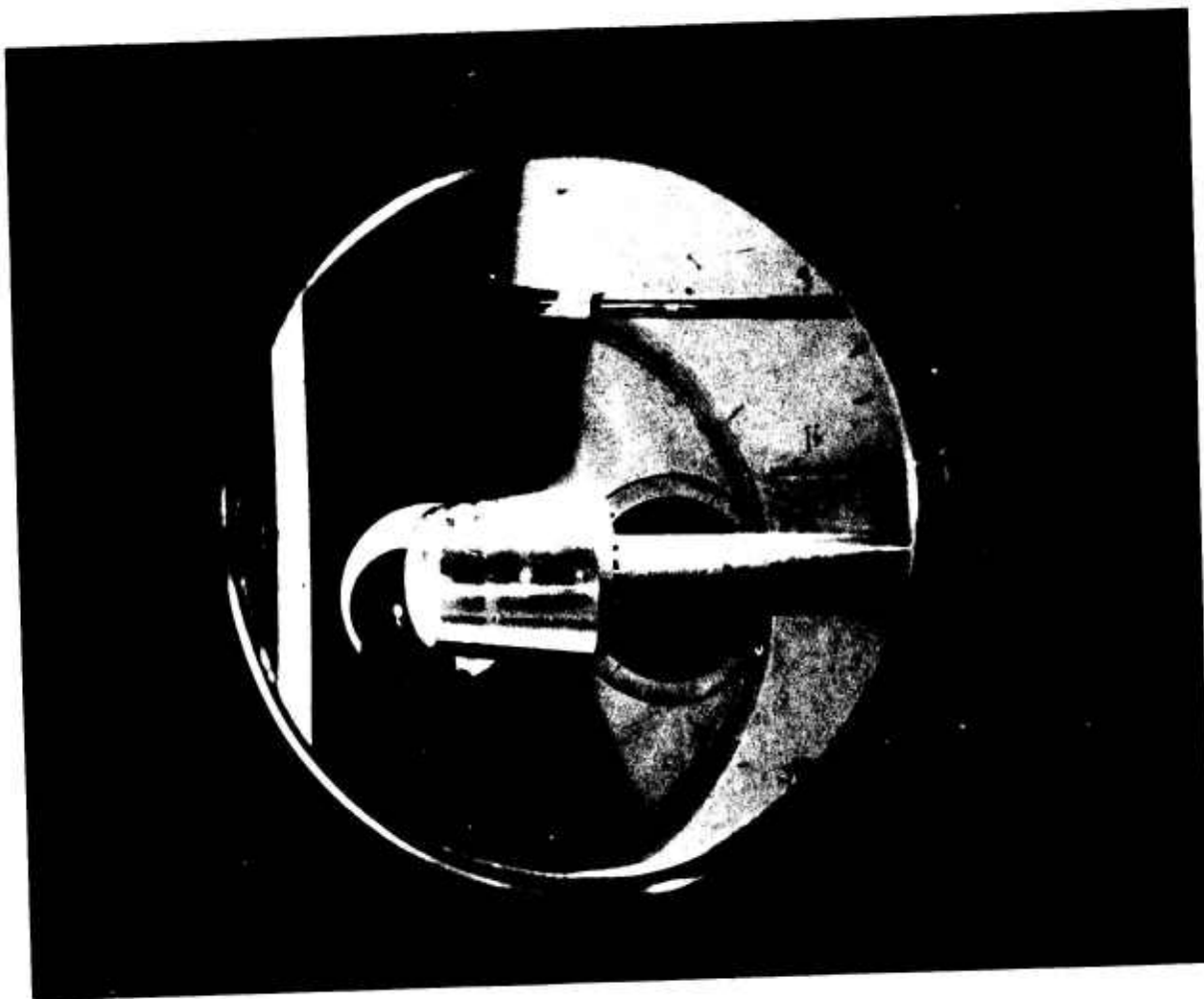


Figure 8 ELLIPTIC NOSE TIP MOUNTED IN 96" SHOCK TUNNEL

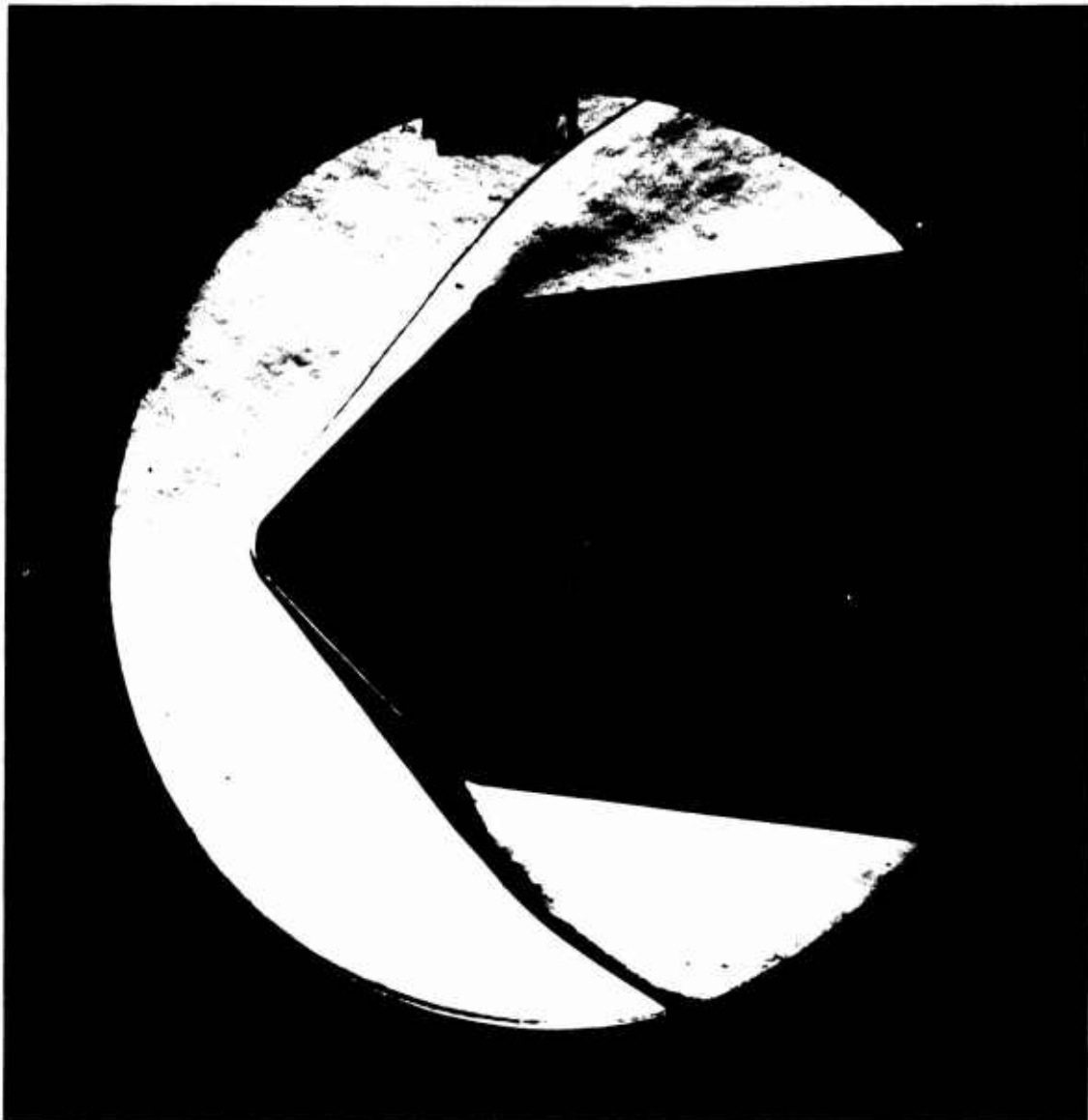


Figure 9 A SCHLIEREN PHOTOGRAPH TYPICAL OF THOSE OBTAINED OVER
THE BICONIC CONFIGURATIONS ($M = 11$)

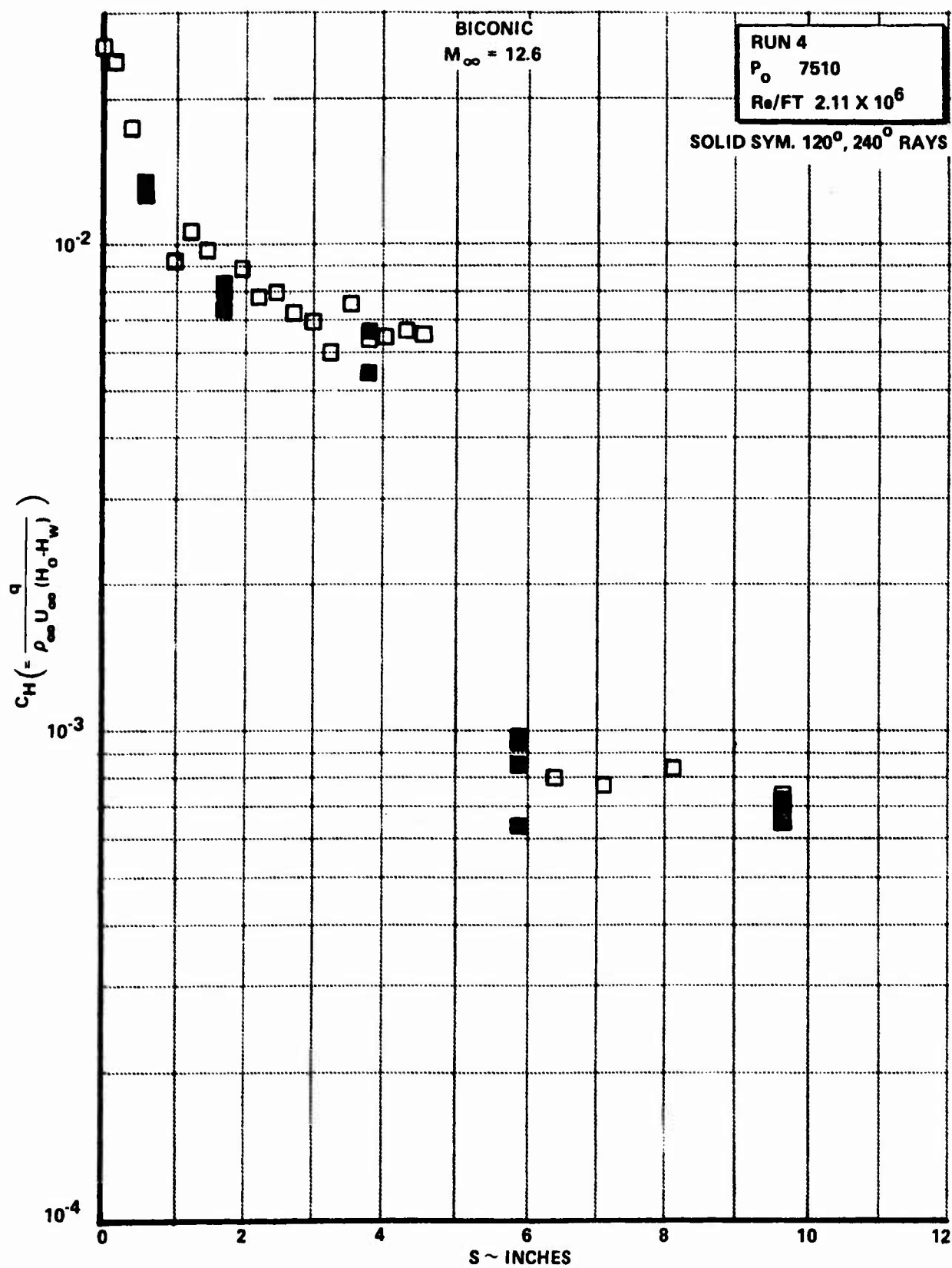


Figure 10a

DISTRIBUTION OF HEAT TRANSFER OVER THE BLUNT BICONIC CONFIGURATION
 $(M = 12.6, Re_D = 2.1 \times 10^6)$

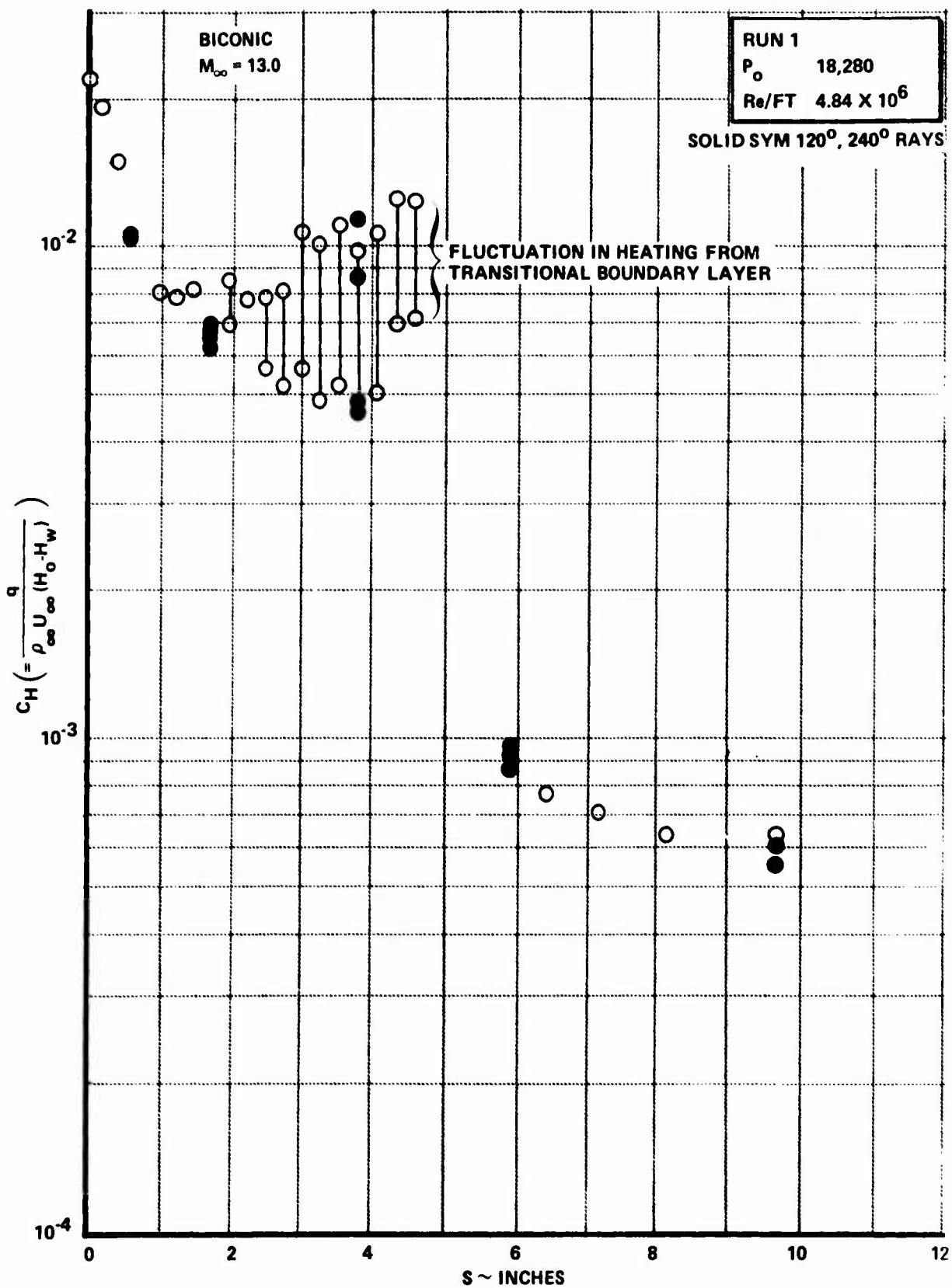


Figure 10b DISTRIBUTION OF HEAT TRANSFER OVER THE BLUNT BICONIC CONFIGURATION
($M_{\infty} = 13.0$ $Re/FT = 4.84 \times 10^6$)

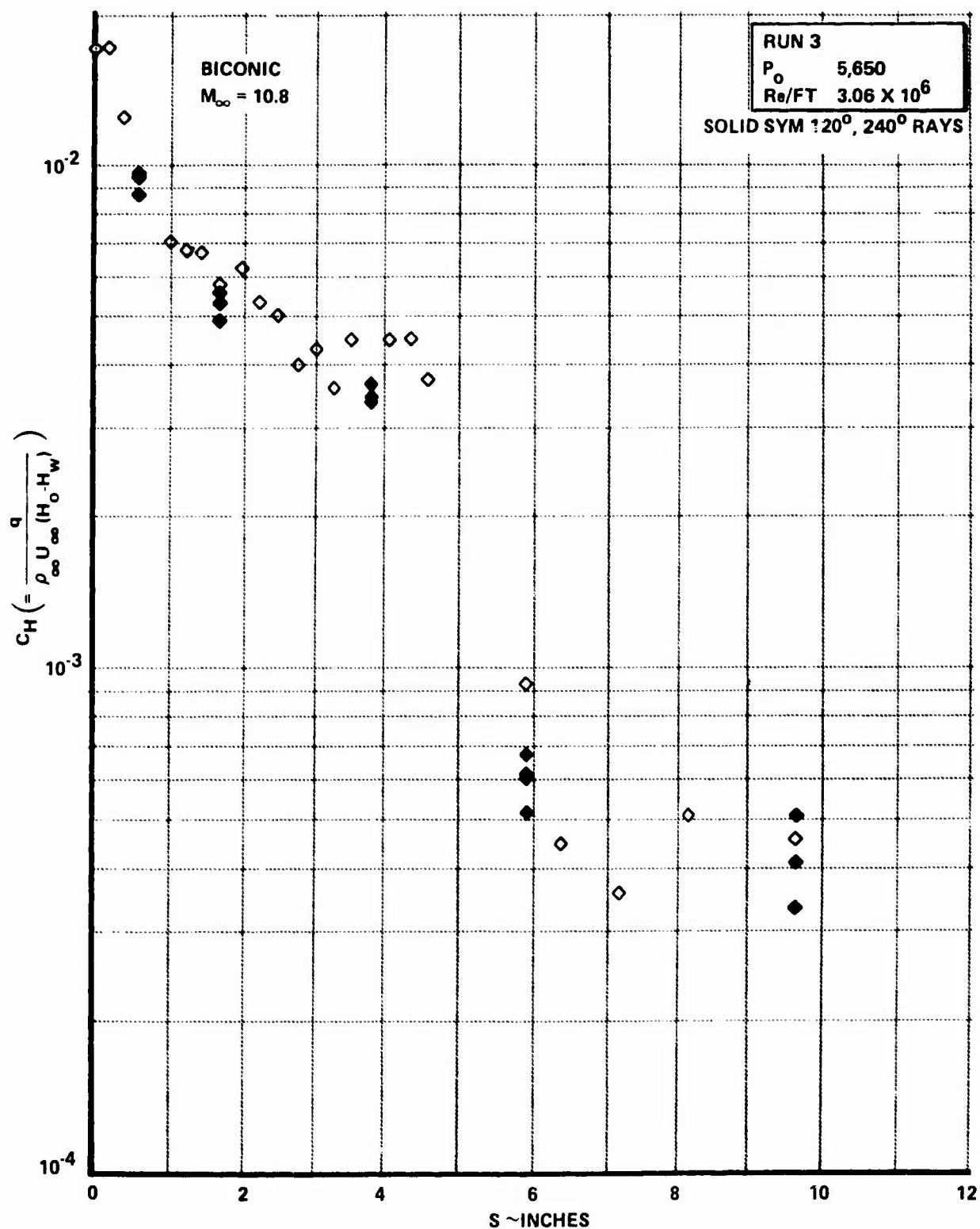


Figure 10c DISTRIBUTION OF HEAT TRANSFER TO THE BLUNT BICONIC CONFIGURATION
($M = 10.8$ $Re/FT = 3 \times 10^6$)

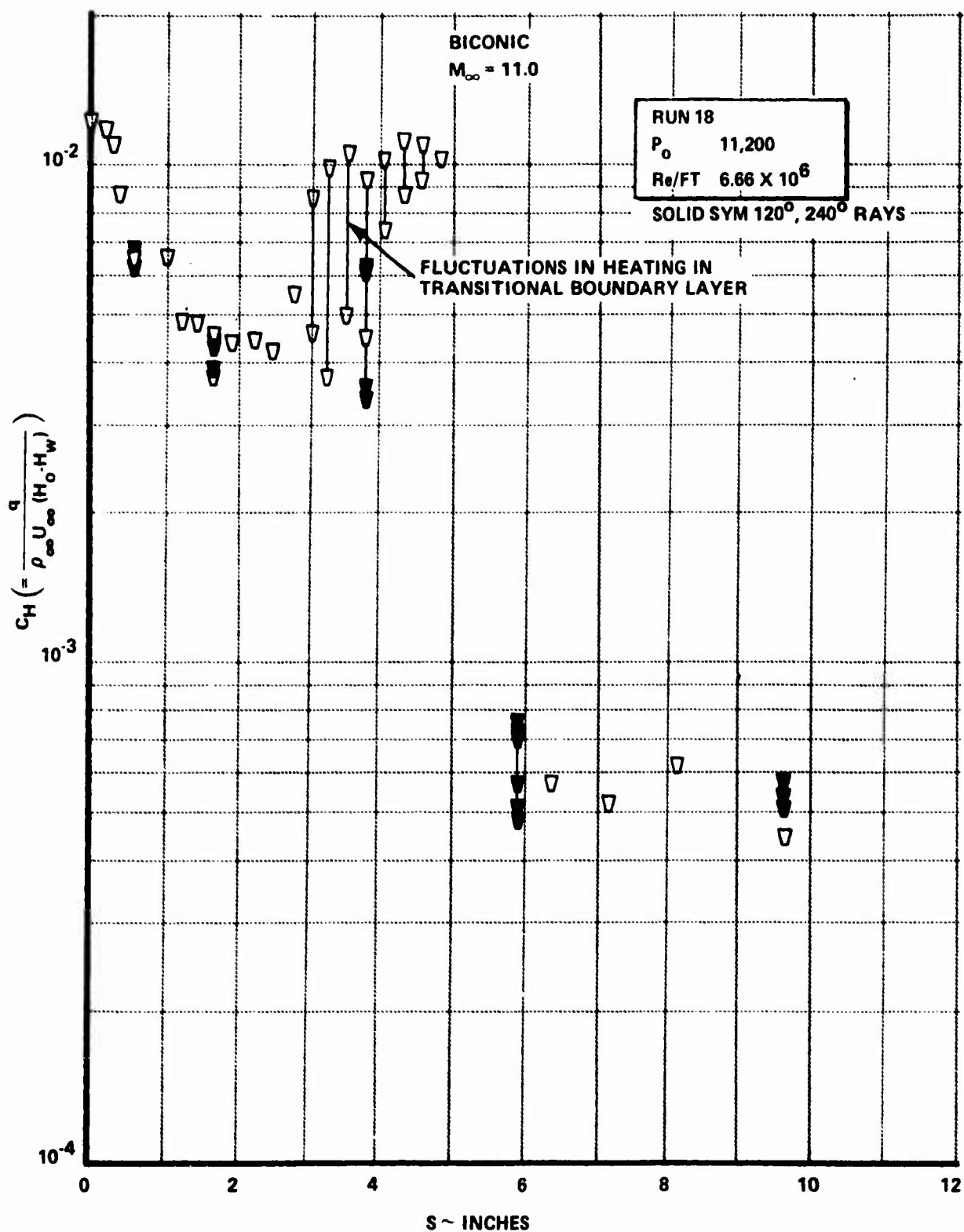


Figure 10d

DISTRIBUTION OF HEAT TRANSFER TO THE BLUNT BICONIC CONFIGURATION
 $(M = 11, Re/FT 6.66 \times 10^6)$

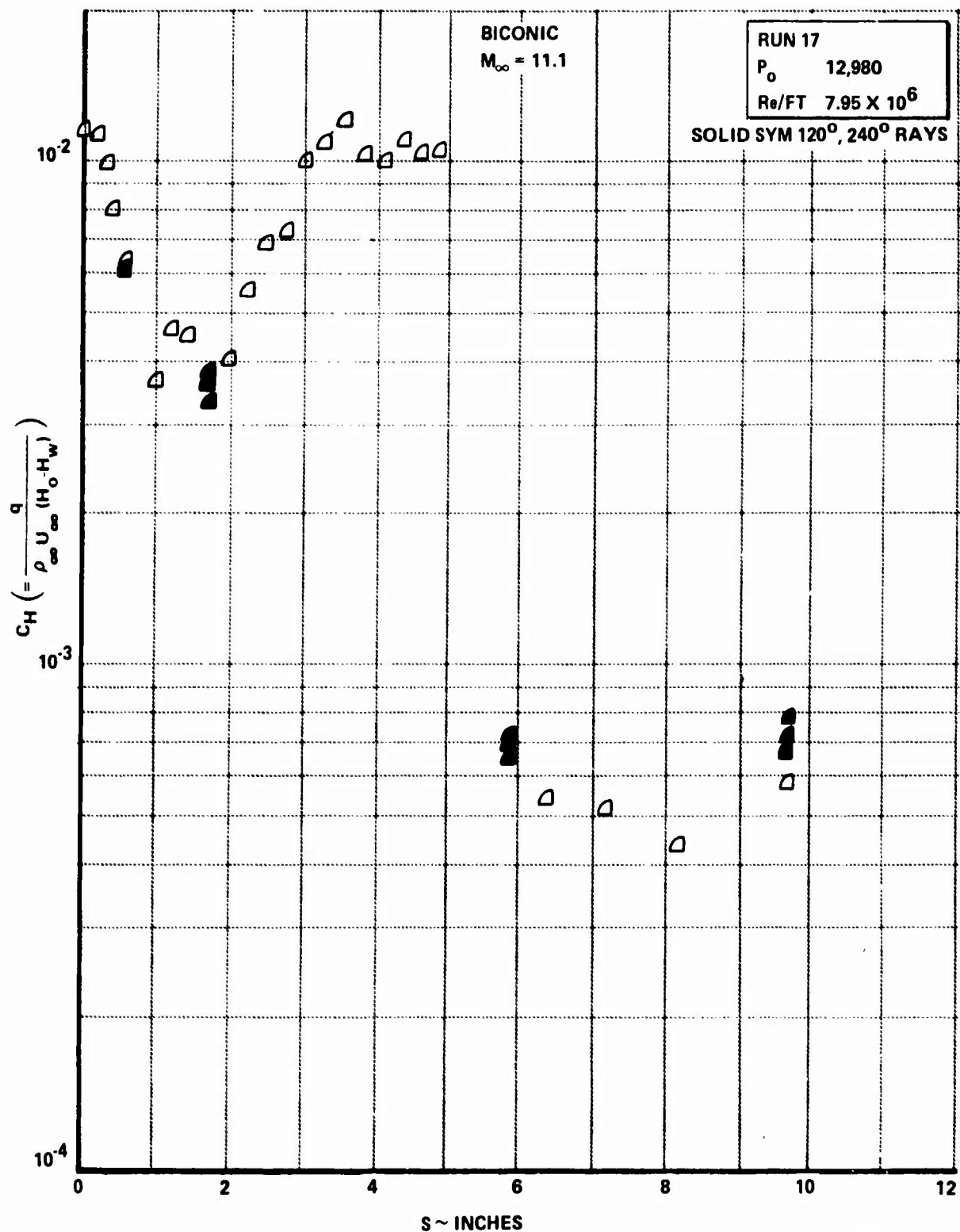


Figure 10e DISTRIBUTION OF HEAT TRANSFER OVER BLUNT BICONIC CONFIGURATION
(MACH 11 $Re_D = 8 \times 10^6$)

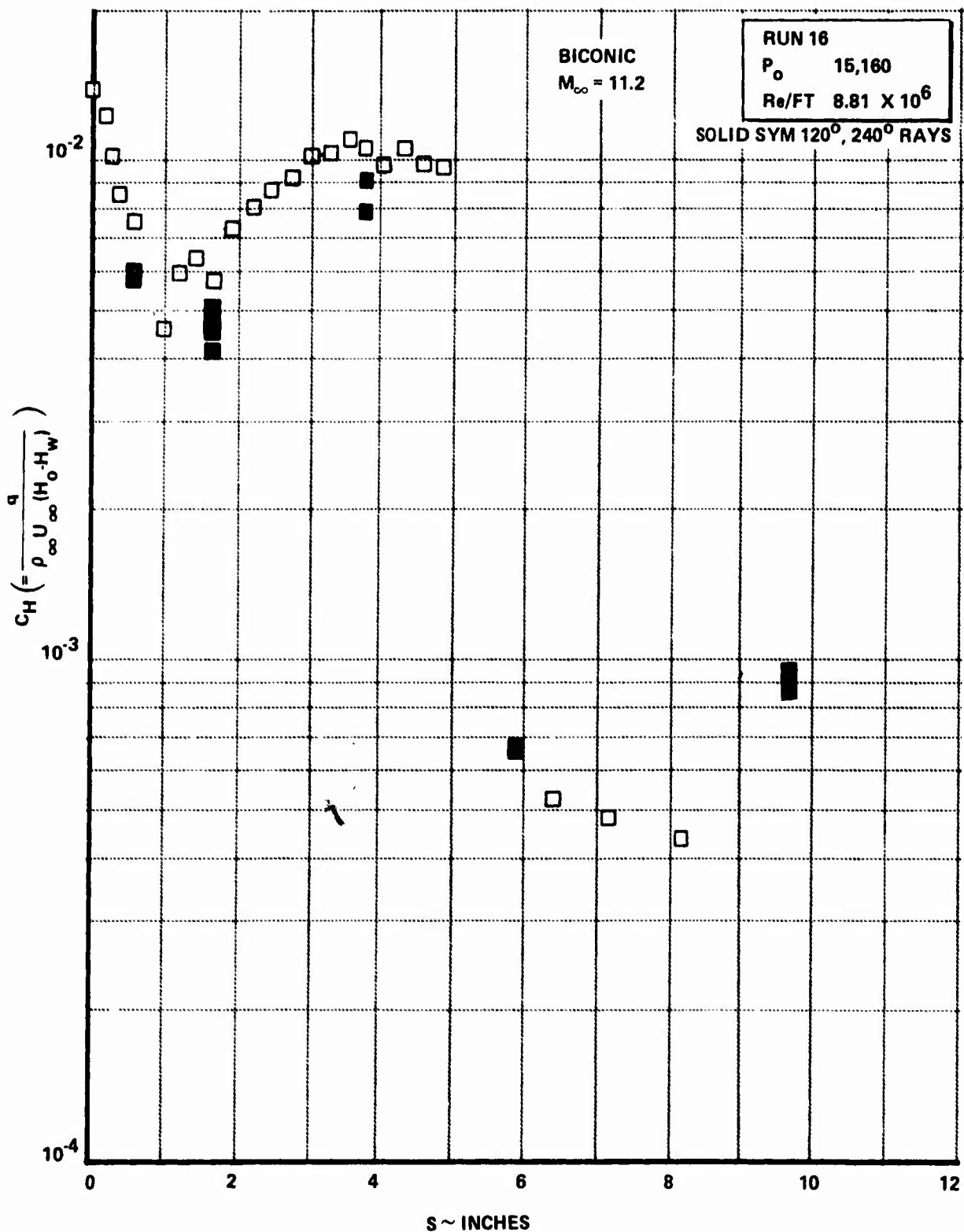


Figure 10f DISTRIBUTION OF HEAT TRANSFER ON THE BLUNT BICONIC CONFIGURATION
($M = 11.2$ $Re/FT = 8.8 \times 10^6$)

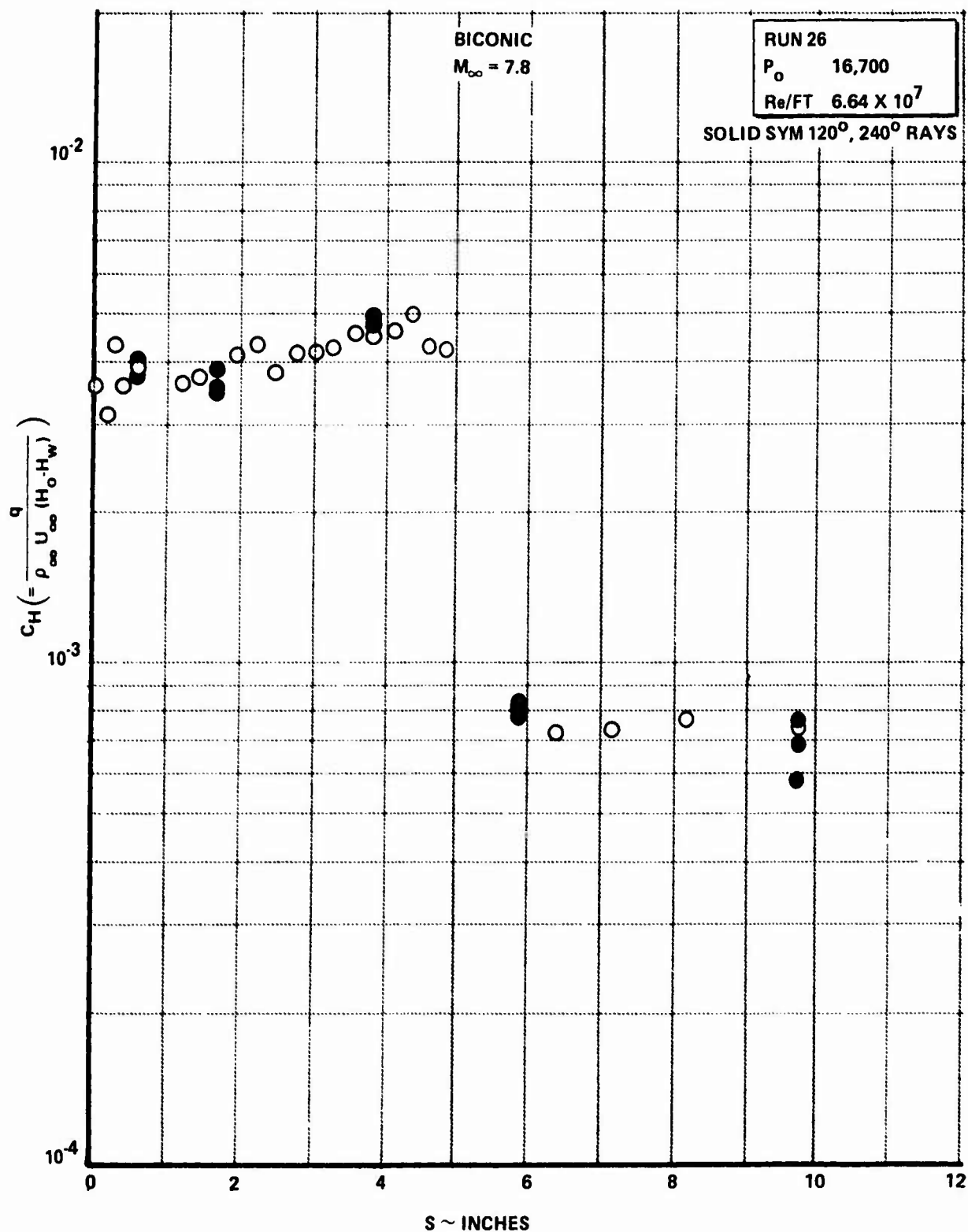


Figure 10g DISTRIBUTION OF HEAT TRANSFER ON THE BLUNT BICONIC CONFIGURATION
($M = 7.8$ $Re/FT = 6.6 \times 10^7$)

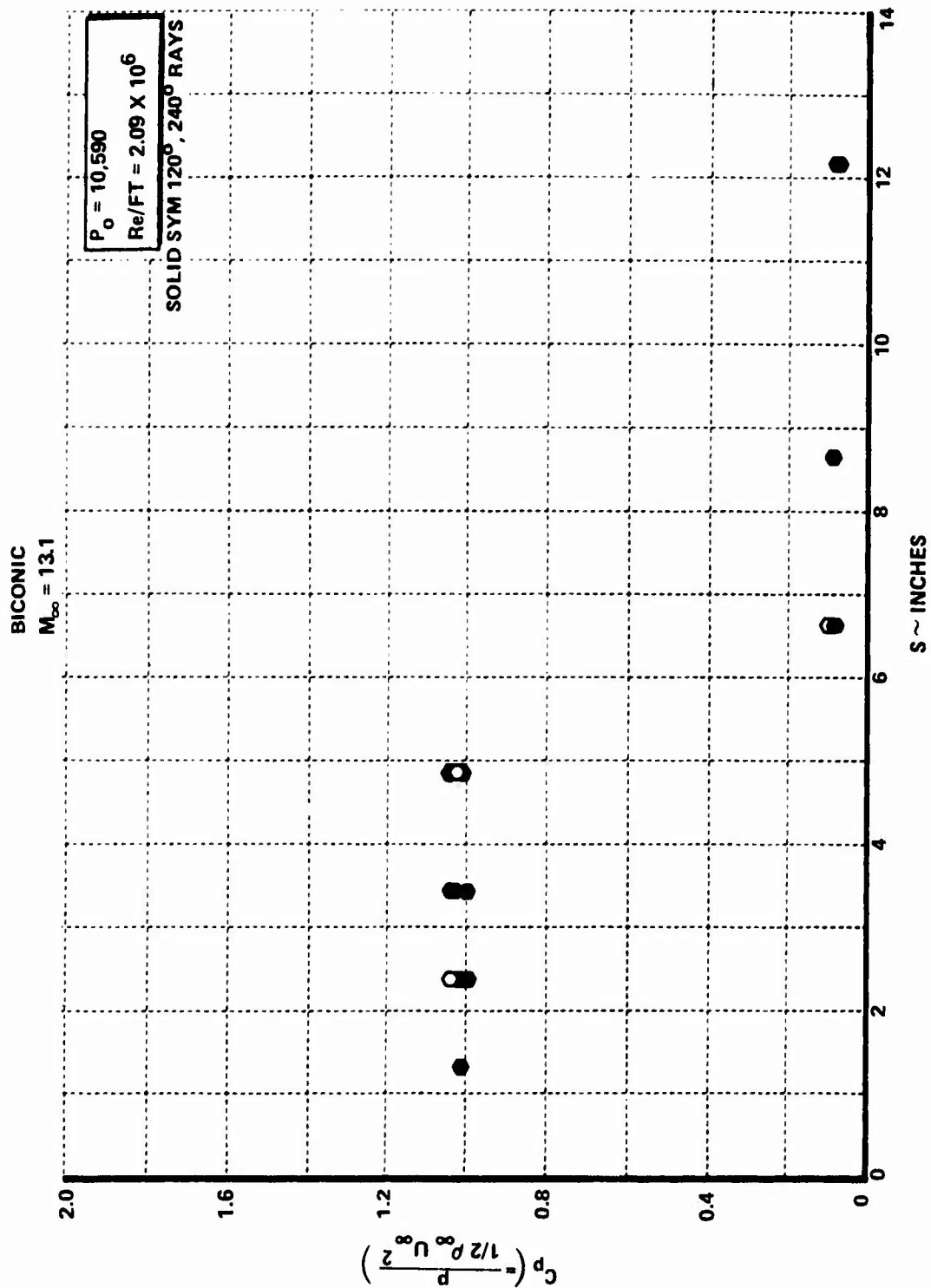


Figure 11a TYPICAL PRESSURE DISTRIBUTION ON BICONIC CONFIGURATION AT MACH 13

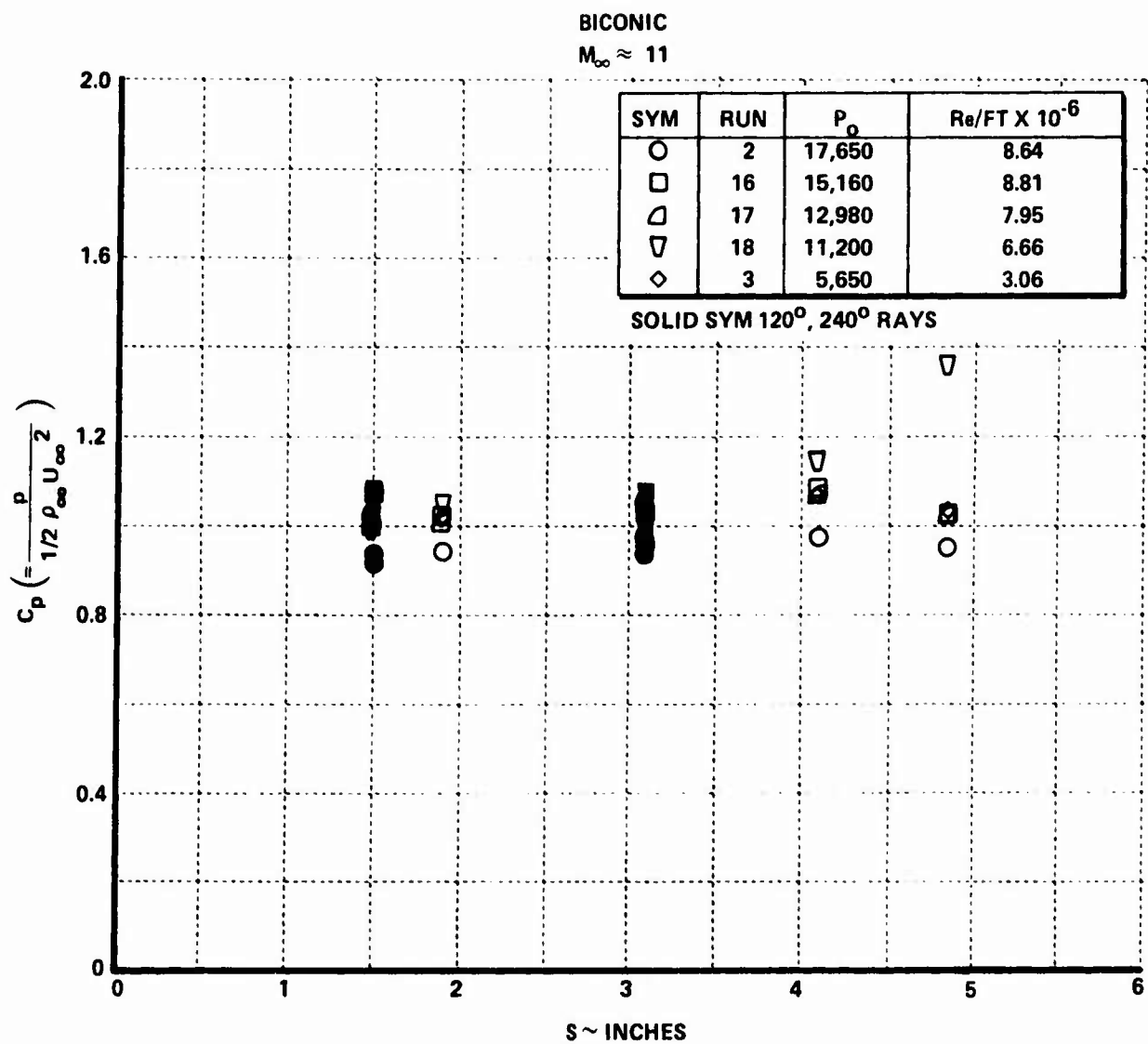


Figure 11b TYPICAL PRESSURE DISTRIBUTION ON BICONIC CONFIGURATION AT MACH 11

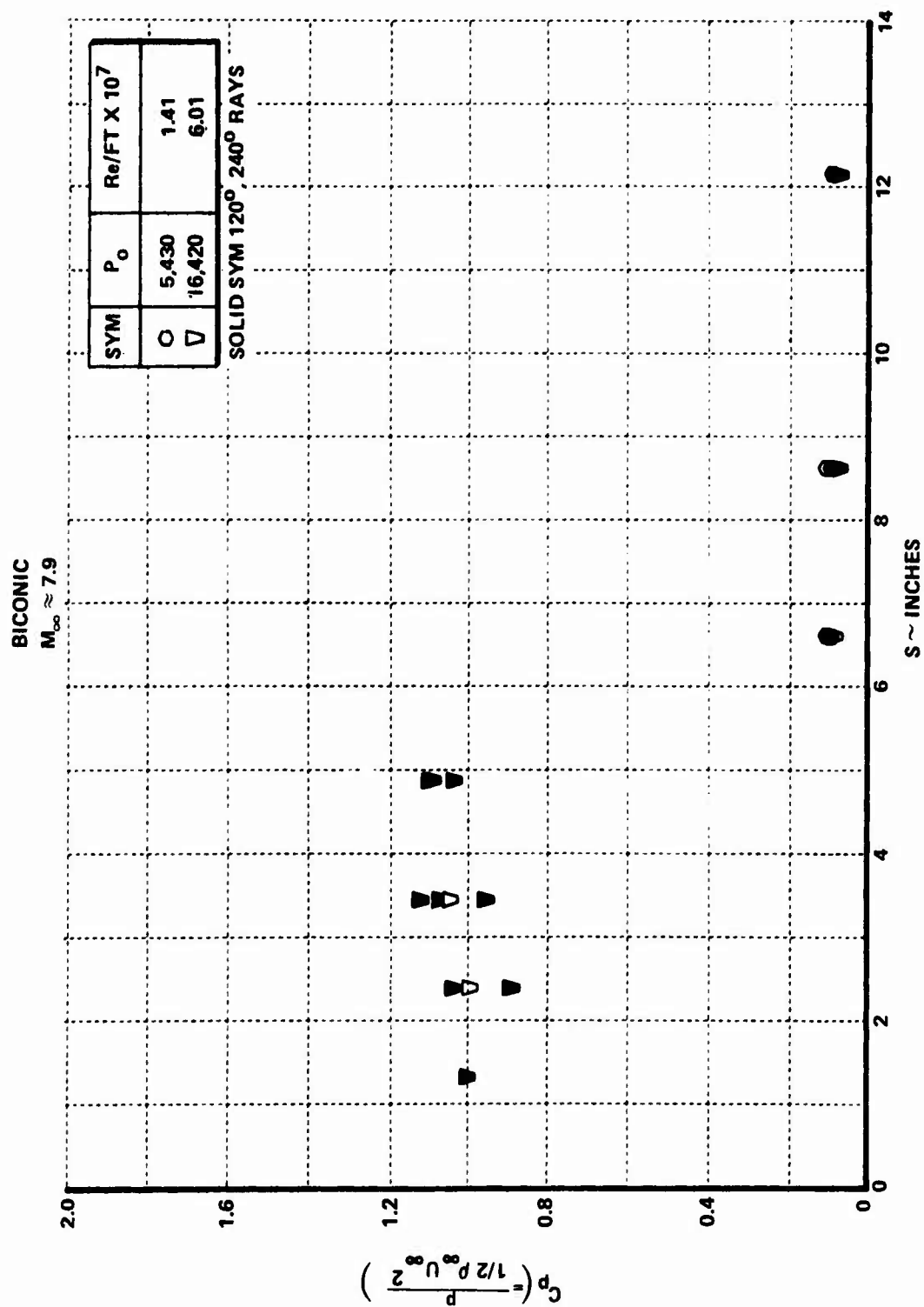


Figure 11c TYPICAL PRESSURE DISTRIBUTION ON BICONIC NOSE AT MACH 8



Figure 12 SCHLIEREN PHOTOGRAPH OF THE FLOW OVER THE ELLIPTIC NOSE TIP
($M = 13$)

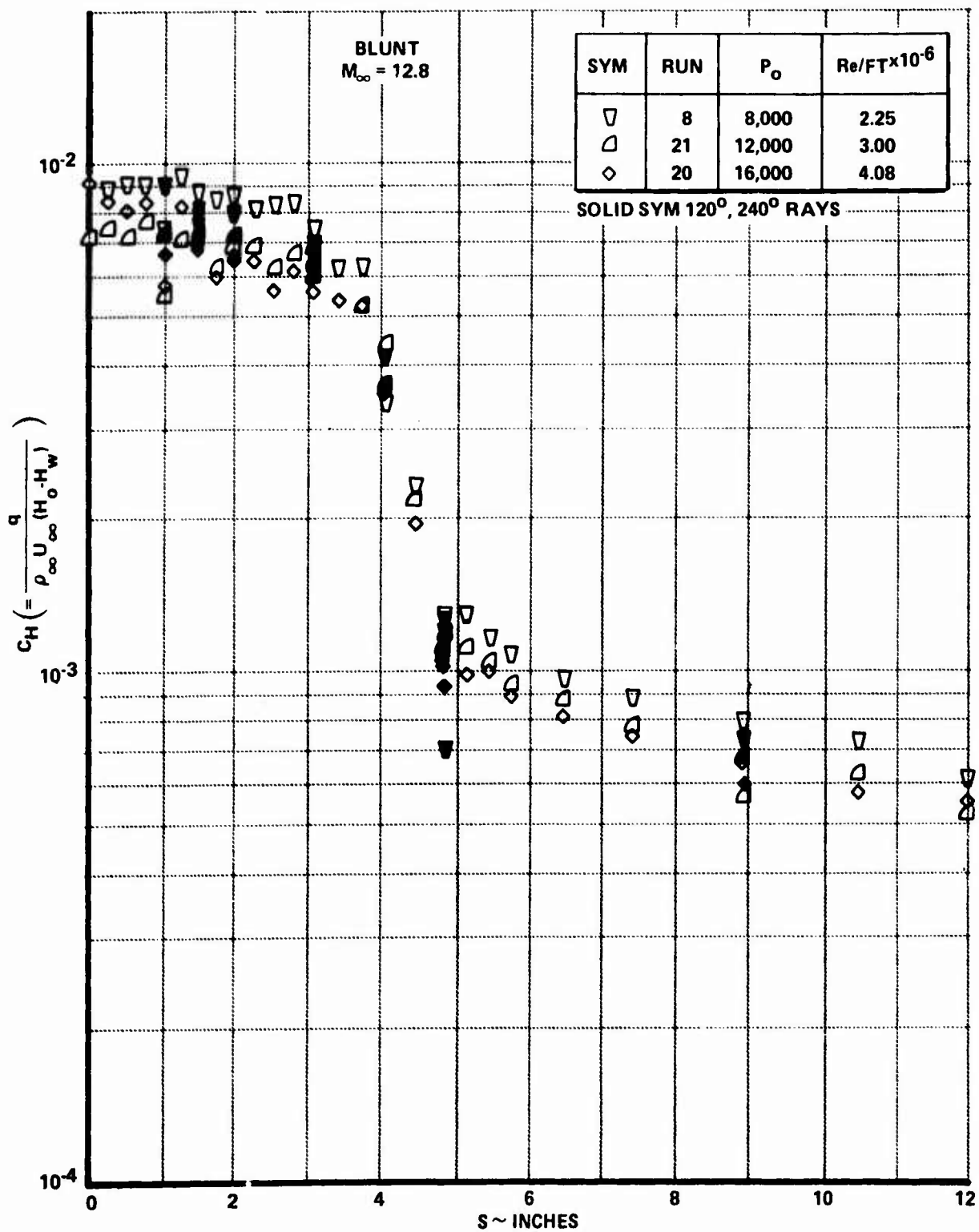


Figure 13a MEASUREMENTS OF HEAT TRANSFER ON THE ELLIPTIC NOSE AT MACH 12.8

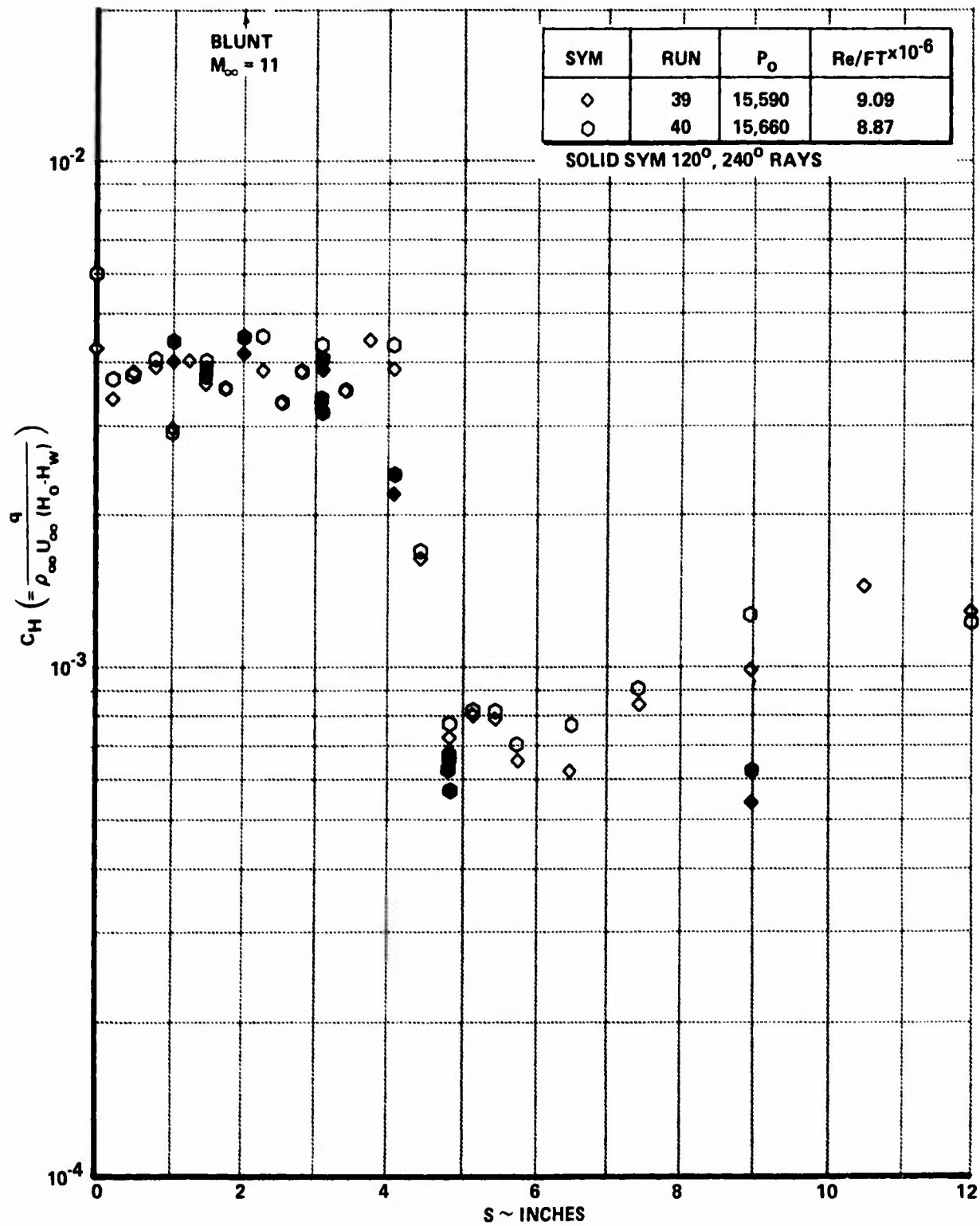


Figure 13b MEASUREMENTS OF HEAT TRANSFER OF THE ELLIPTIC NOSE AT MACH 11

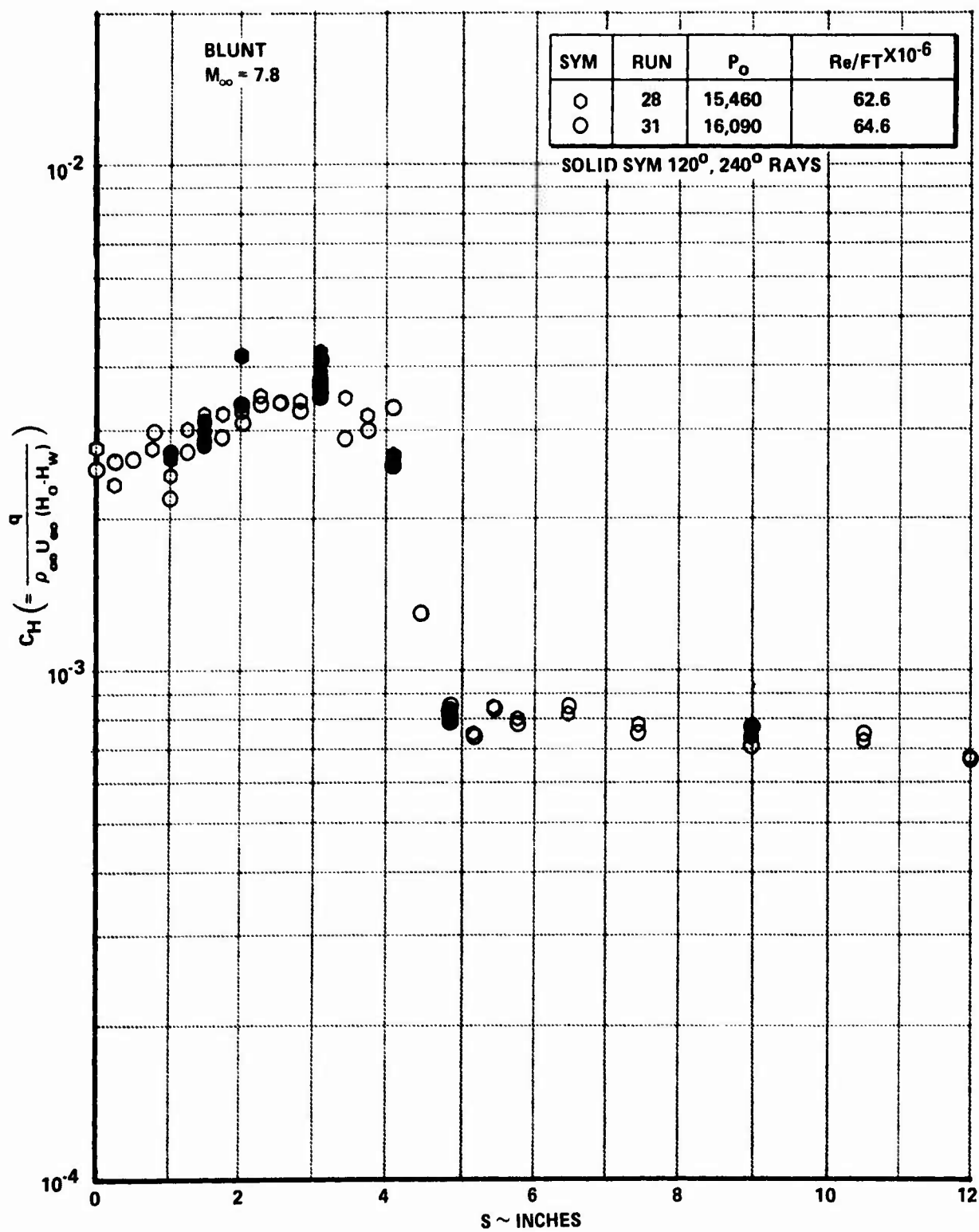


Figure 13c MEASUREMENTS OF HEAT TRANSFER ON THE ELLIPTIC NOSE AT MACH 7.8

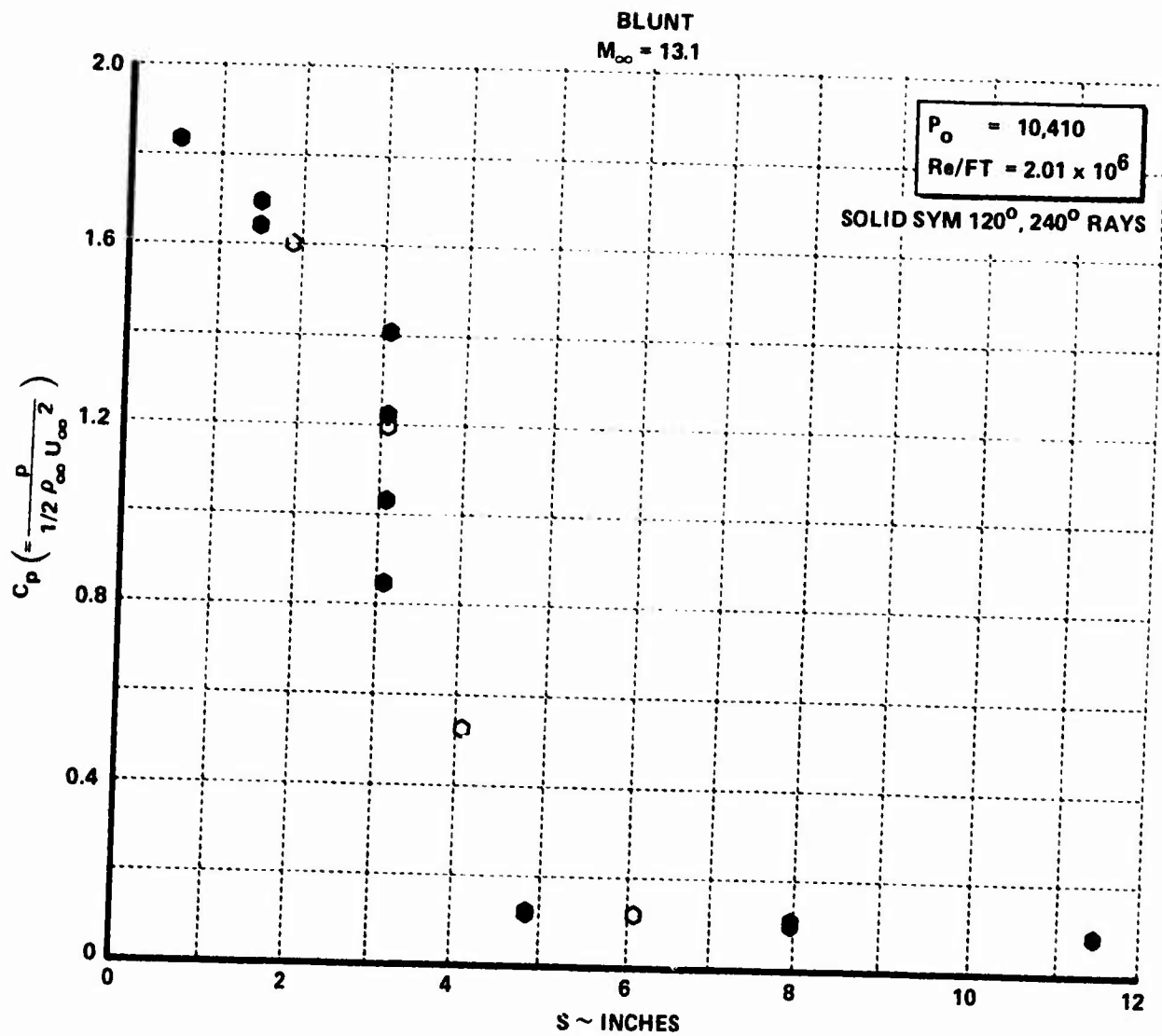


Figure 14a A TYPICAL DISTRIBUTION OF PRESSURE ON THE ELLIPTIC NOSE AT MACH 13

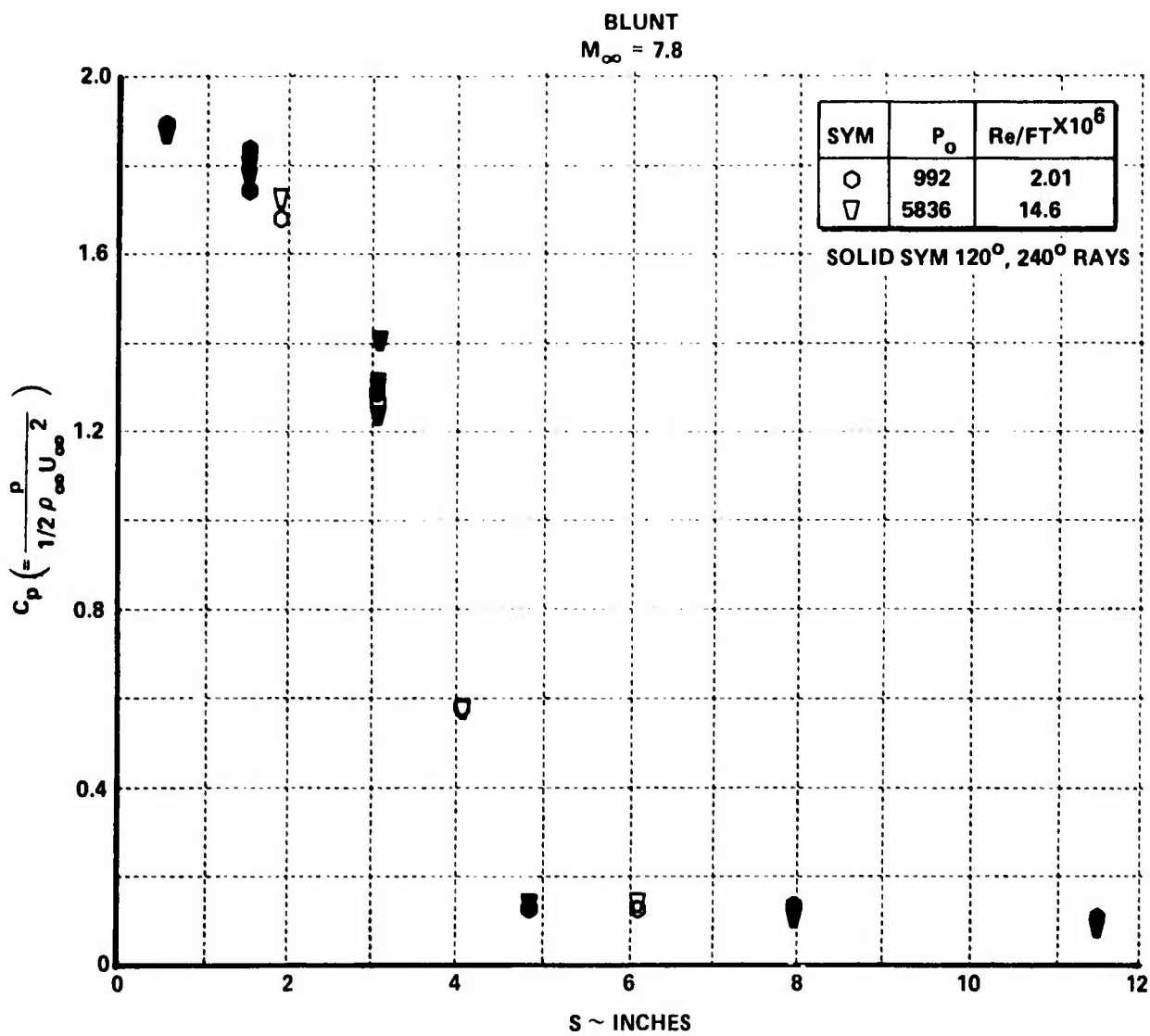


Figure 14b A TYPICAL DISTRIBUTION OF PRESSURE ON THE ELLIPTIC NOSE AT MACH 7.8



Figure 15a A SCHLIEREN PHOTOGRAPH OF THE FLOW OVER THE TRI-CONIC CONFIGURATION WITH BOUNDARY LAYER SEPARATION OVER THE SECOND SURFACE ($M = 13$)



Figure 15b SCHLIEREN PHOTOGRAPH SHOWING BOUNDARY LAYER SEPARATION FOR
TRANSITION FLOW OVER THE TRI-CONIC MODEL ($M = 11$)



Figure 15c SCHLIEREN PHOTOGRAPH FOR TURBULENT FLOW OVER
THE TRI-CONIC MODEL ($M = 11$)

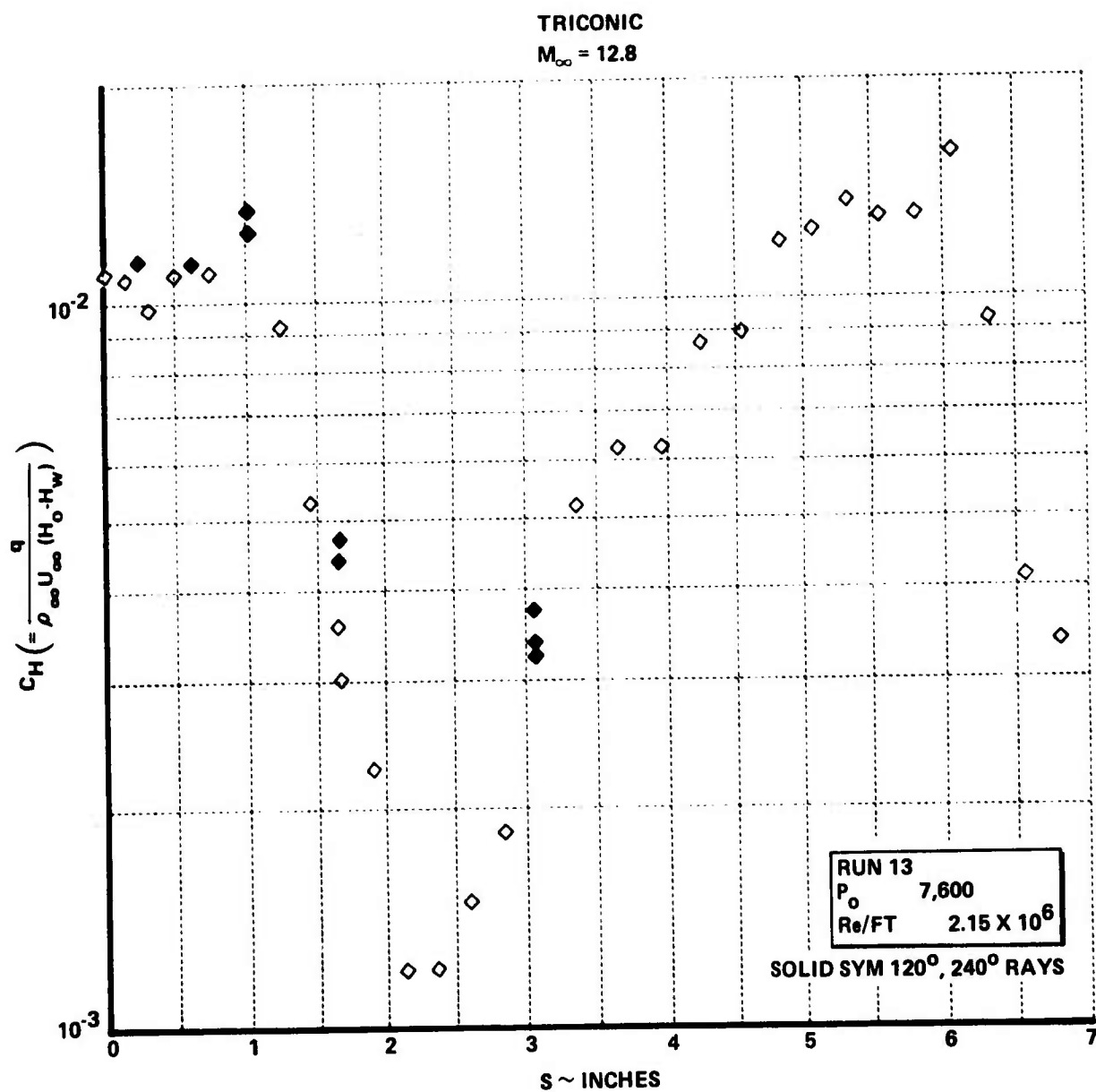


Figure 16a HEAT TRANSFER DISTRIBUTION OVER THE TRICONIC MODEL AT MACH 12.8

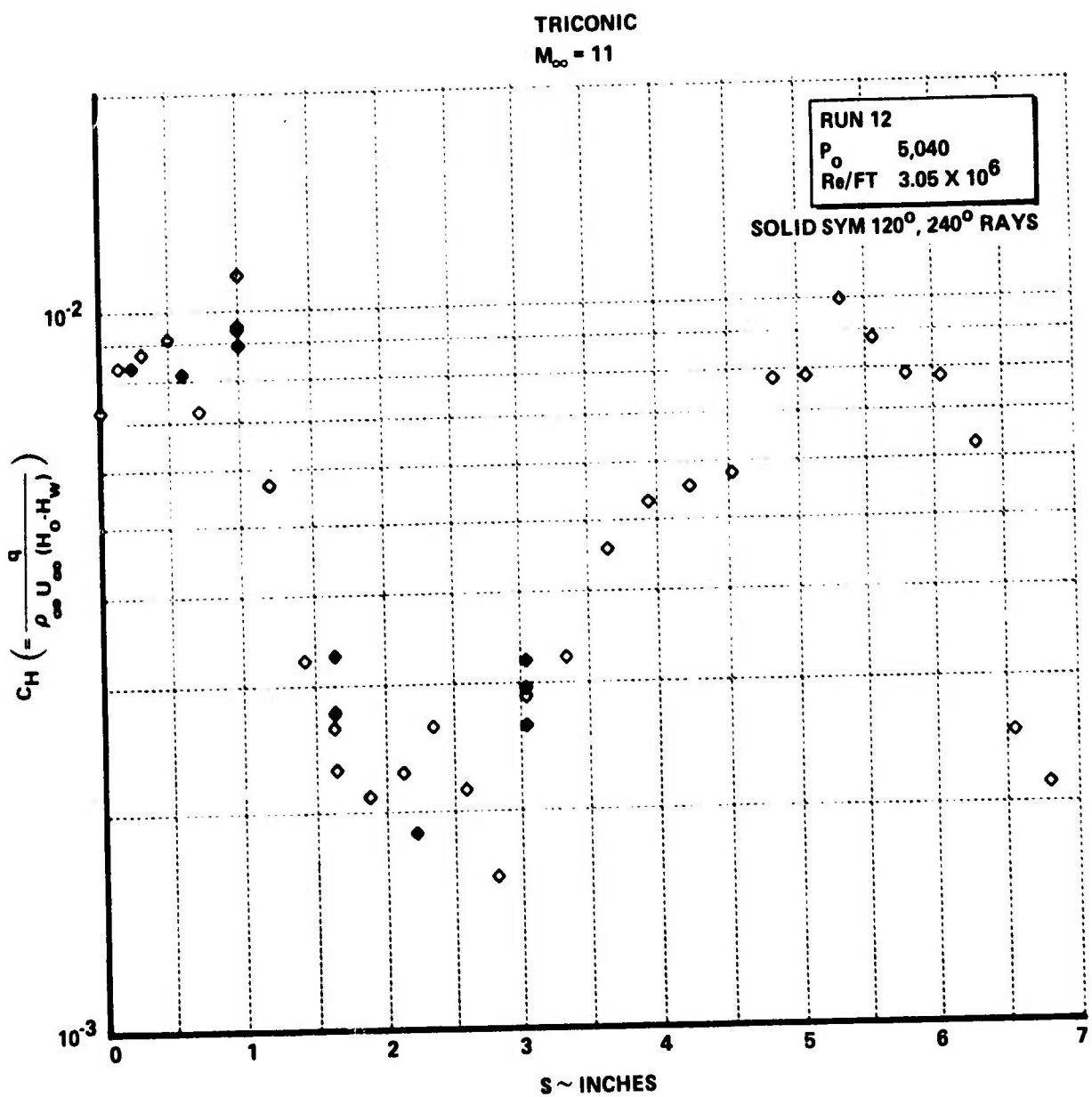


Figure 16b HEAT TRANSFER DISTRIBUTION OVER THE TRI-CONIC MODEL AT MACH 11

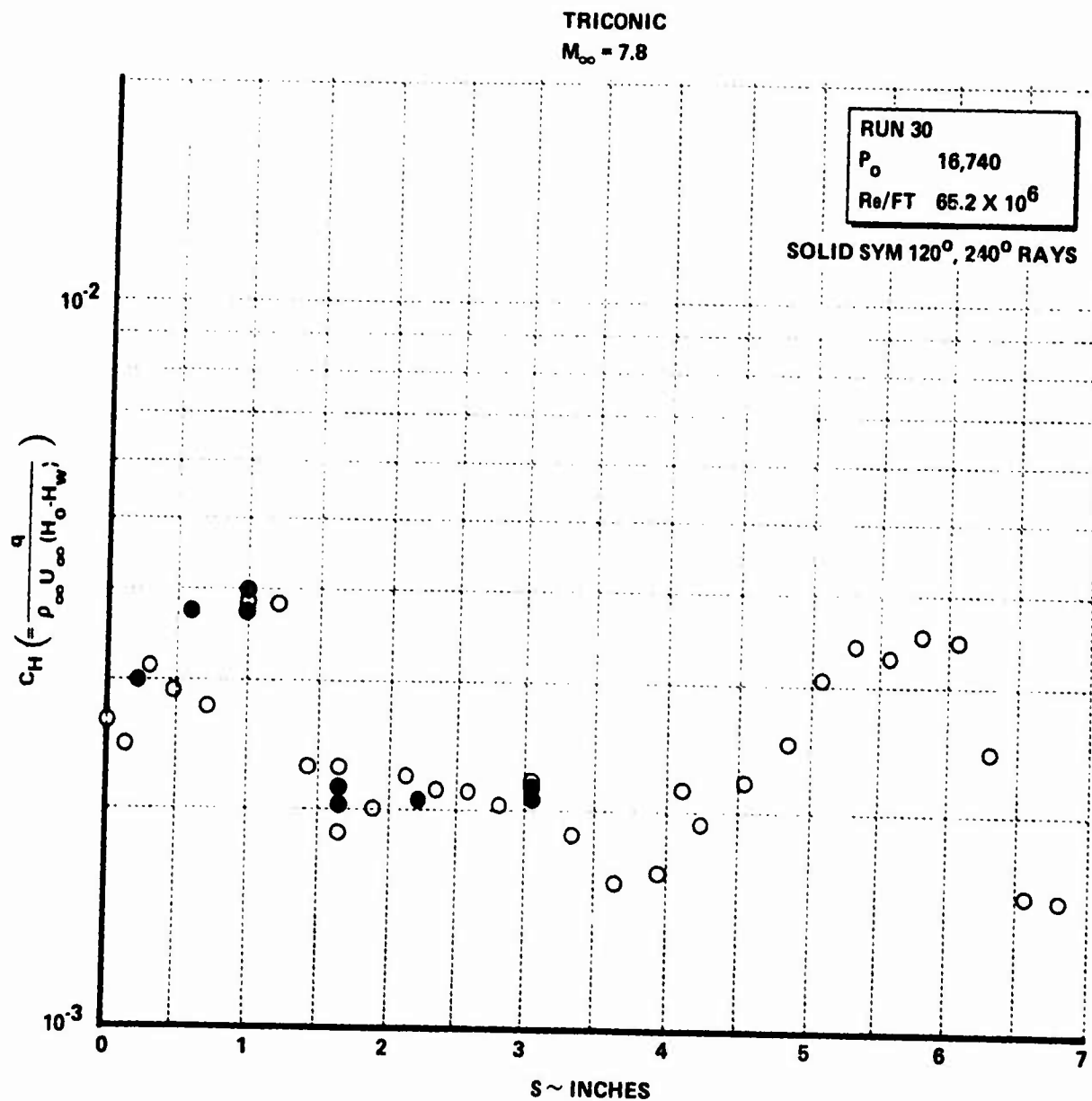


Figure 16c HEAT TRANSFER DISTRIBUTION OVER THE TRICONIC MODEL AT MACH 7.8

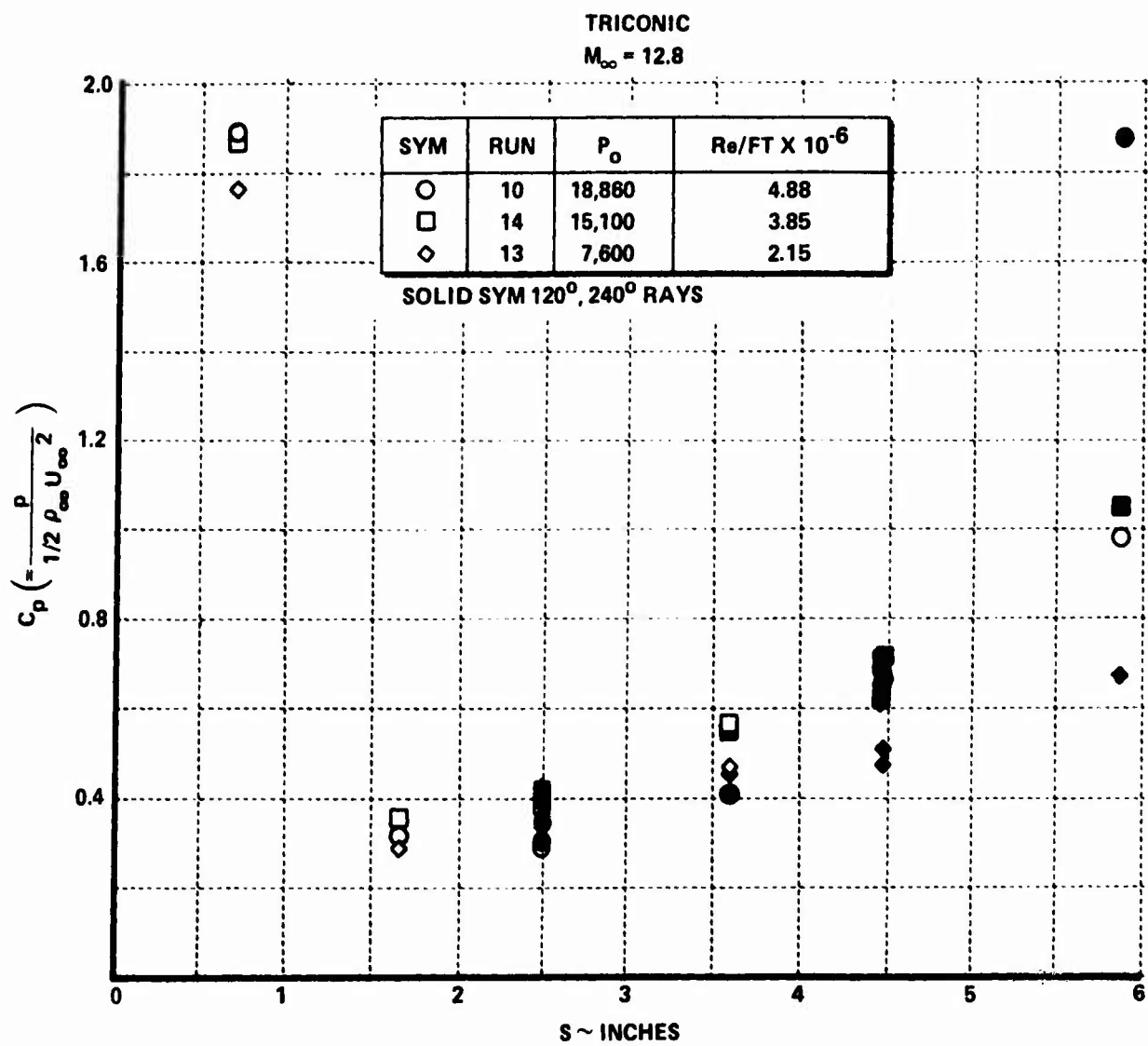


Figure 17a DISTRIBUTION OF PRESSURE OVER THE BI-CONIC CONFIGURATION AT MACH 12.8

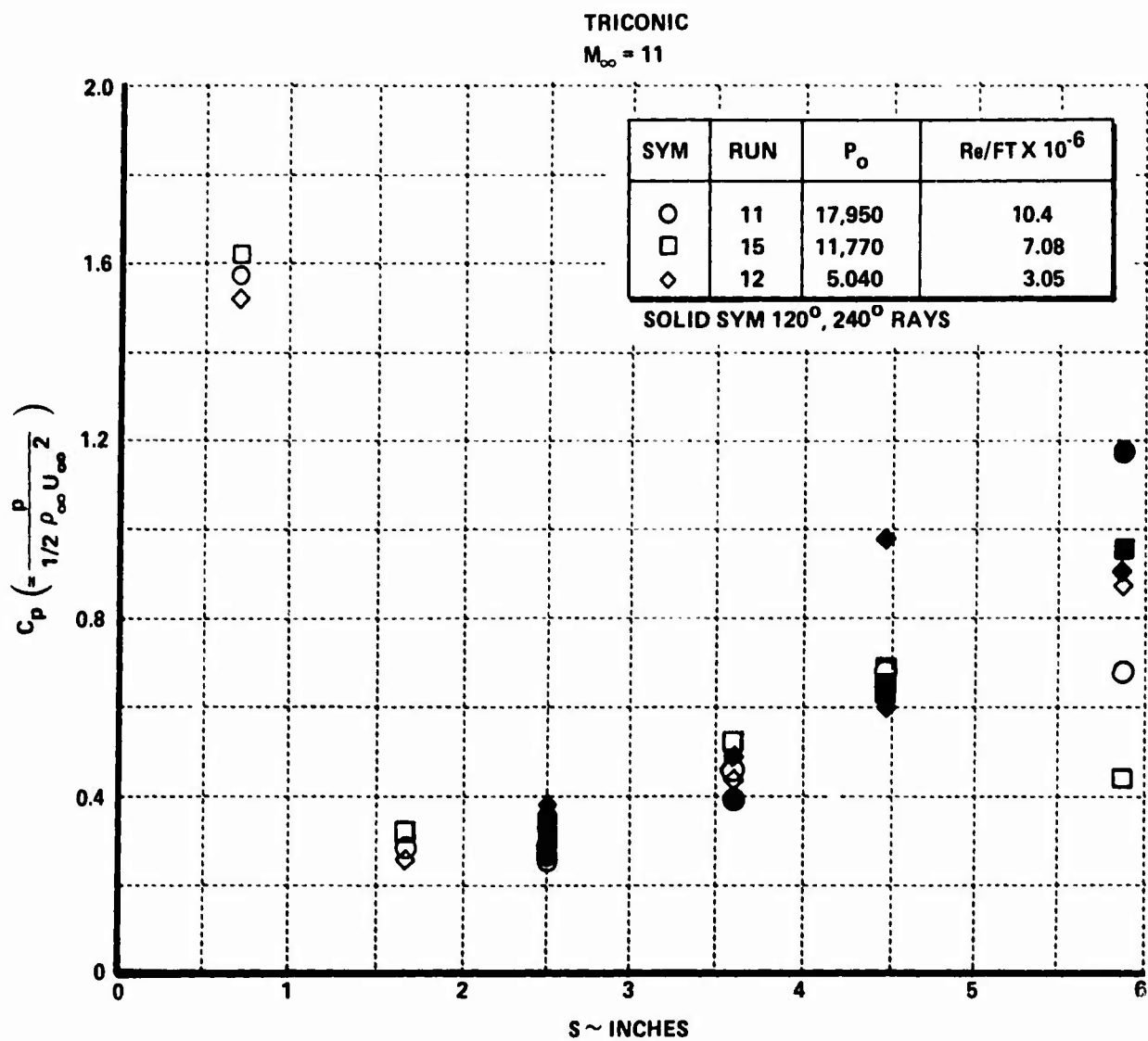


Figure 17b PRESSURE DISTRIBUTION OVER THE TRI-CONIC CONFIGURATION AT MACH 11

The experimental program was conducted at Mach numbers from 8 to 13 for a range of Reynolds numbers such that laminar, transitional and turbulent flows were obtained over the model nose shapes. Emphasis was placed on obtaining measurements which would assist in attempts to evaluate the models, in particular those of the transitional and relaminarization regions, which are used in the shape change codes. We performed simple calculations to determine laminar and the heat transfer distributions over the biconic and elliptic configurations using the modified Lees equation^{8,9}

$$\frac{q}{q_{\text{STAG}}} = \sqrt{\frac{f}{\beta(j+1)}} \left[\frac{P_c U_c Y^j}{\int_0^S P_c U_c Y^{2j} ds} \right]$$

where $j = 0$ (2 dimensional), $j = 1$ (axi-symmetric); $\beta = \sqrt{\frac{\gamma-1}{\gamma}}$ for spherical nose and 2 for 2:1 elliptic nose. In this expression $P_c = P_e/P_o$, $U_c = U_e/U_\infty$, $Y = rb/a$ and $S = S/a$, where a is a reference length ($a = R_N$ for a spherical nose and $R_N/4$ for the 2:1 elliptic nose). The stagnation point heat transfer was determined using the Fay-Riddell method. For turbulent flow we use the relationships developed by Mirels (REF 12)

$$q_T/q_{\text{REF}} = \frac{P_c U_c}{S^{0.2}}$$

$$\text{where } q_{\text{REF}} = \left(\frac{0.03}{P_r^{2/3}} \frac{k \Delta H \mu_o}{a^{0.2}} \right) \left(\frac{P_o U_\infty}{\mu_o} \right)_a^{0.8}$$

and $\Delta H = H_o - H_w$, k = Mirels' roughness coefficient and P_R is the Prandtl number. The three comparisons which are shown in Figs. 18, 19 and 20 demonstrate relatively good agreement between theory and experiment, and indicate the flow remains completely laminar to the end of the afterbody.

The characteristics of the transition region over the bi-conic configuration were explored by progressively increasing the unit Reynolds number of the free stream, thereby moving transition first onto the conical surface and then toward the hemispherical nose tip. Typical distributions of heating obtained from these studies are shown in Fig. 21. Here we see that the length of the transition region is not simply related to length of the laminar run

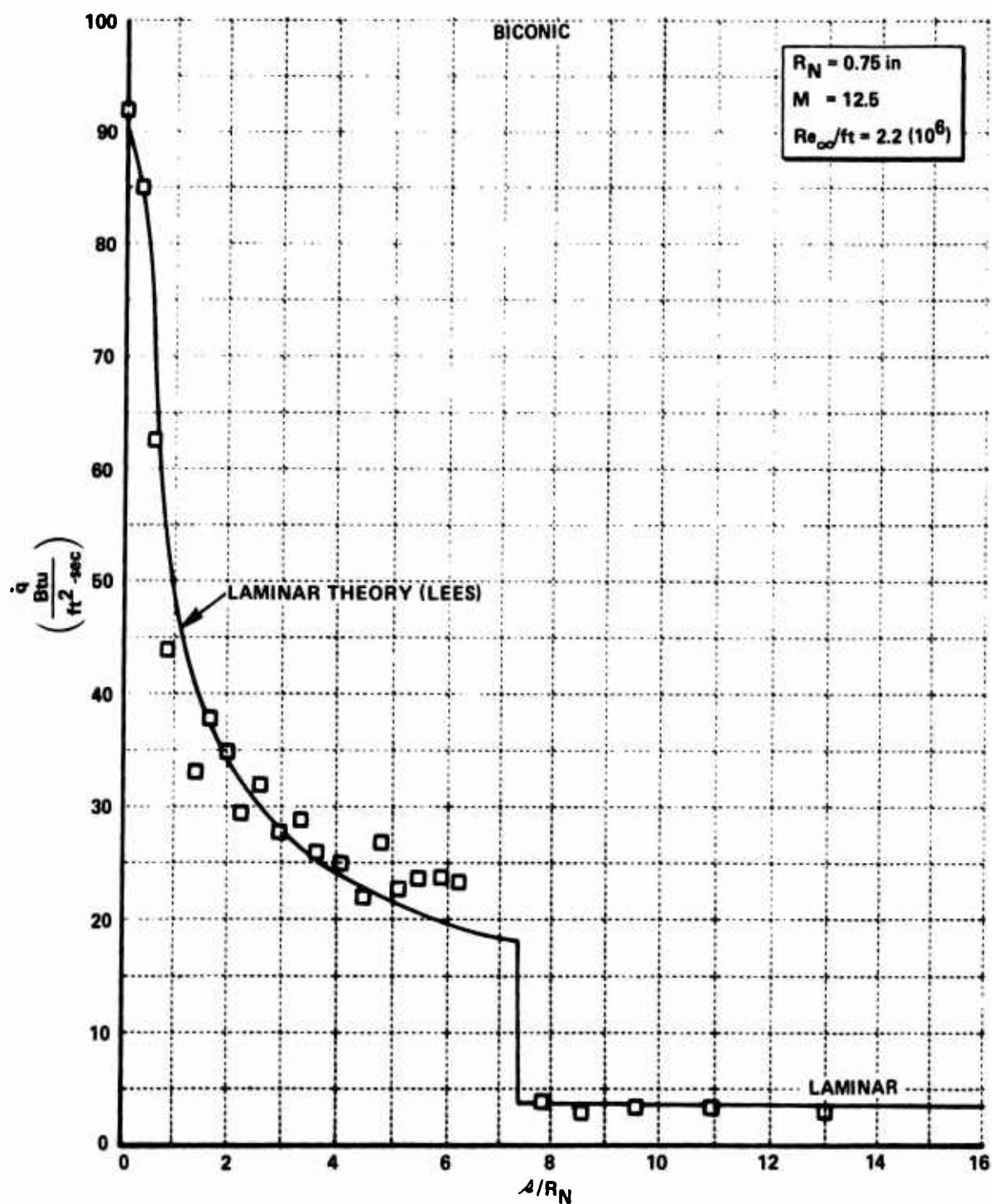


Figure 18 COMPARISON BETWEEN THEORY AND EXPERIMENT
FOR THE BICONIC CONFIGURATION AT MACH 12.5

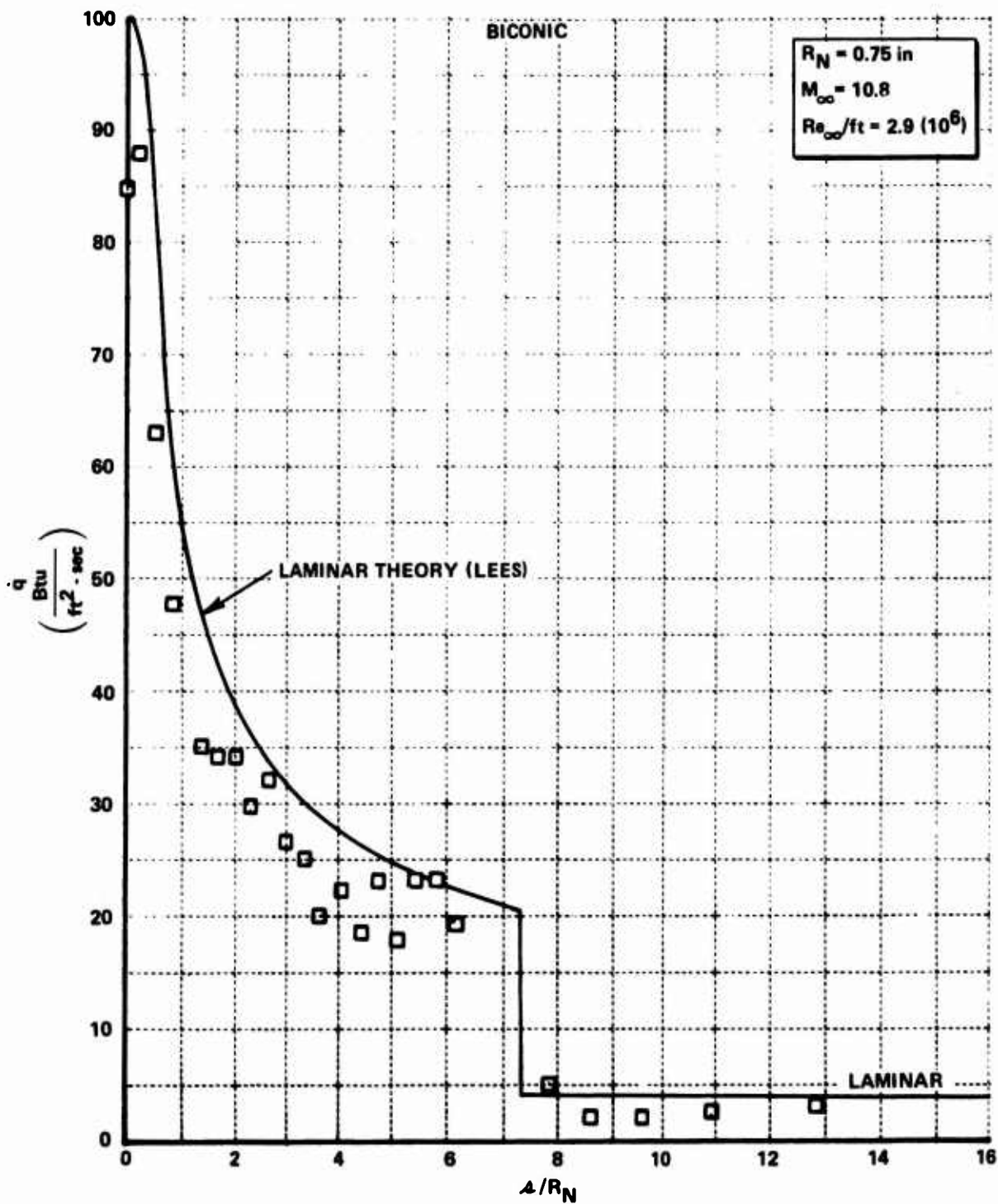


Figure 19 COMPARISON BETWEEN THEORY AND EXPERIMENT FOR THE BI-CONIC CONFIGURATION AT MACH 11

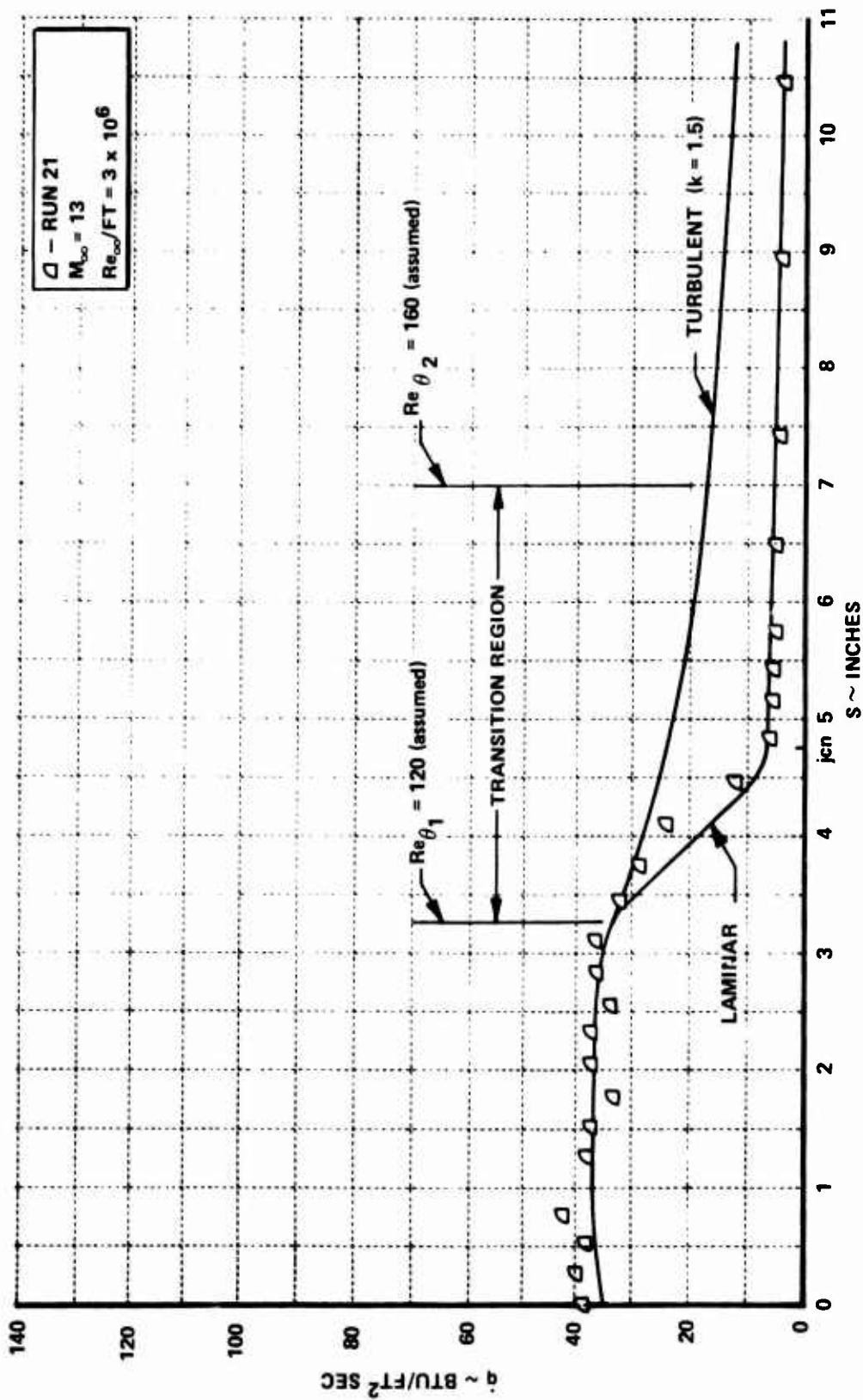


Figure 20 COMPARISON BETWEEN THEORY AND EXPERIMENT FOR LAMINAR HEATING TO THE ELLIPTIC NOSE TIP

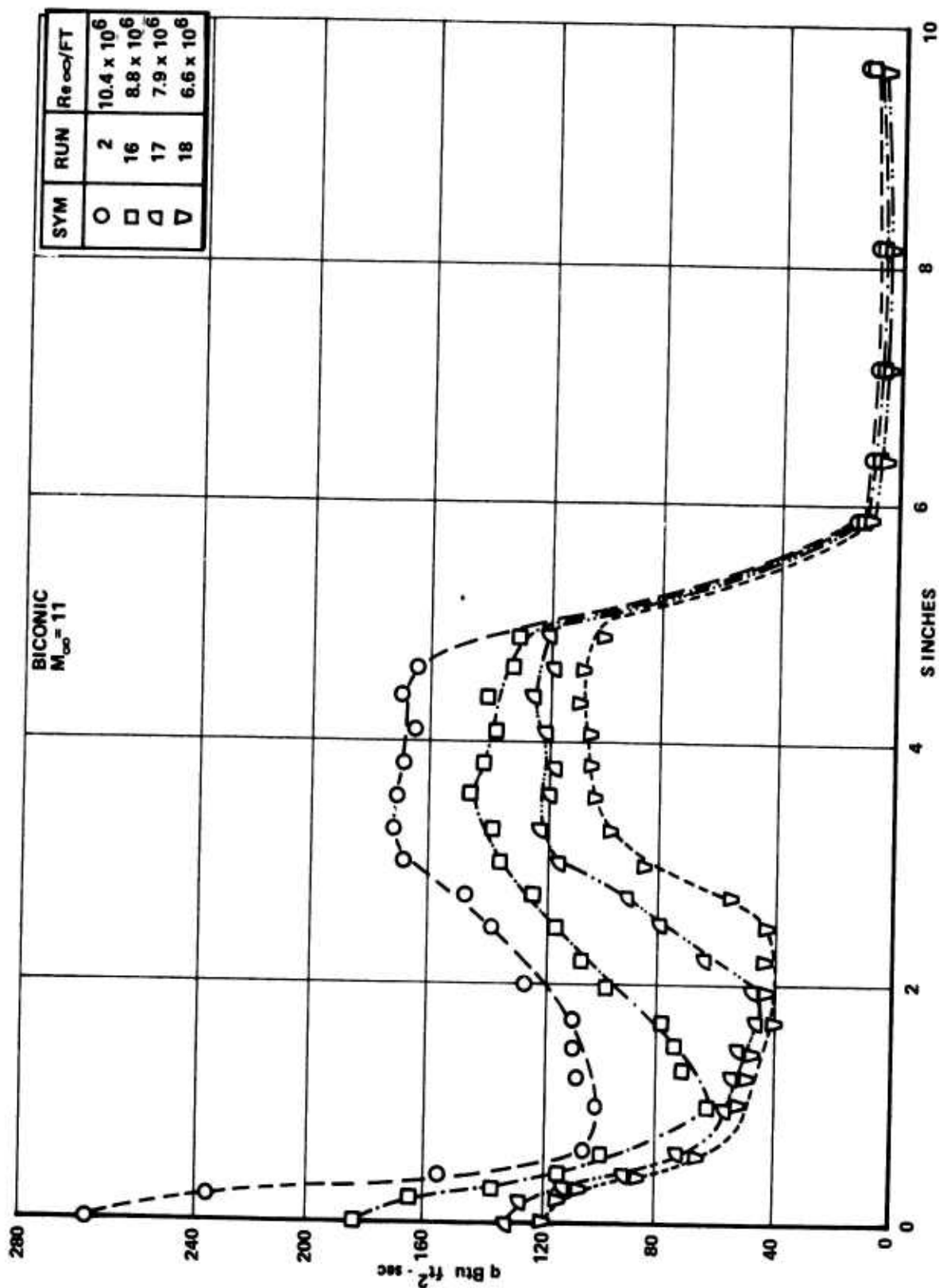


Figure 21 MEASUREMENTS OF TRANSITION HEATING ON THE BICONIC CONFIGURATION

ahead of transition or momentum thickness at the beginning of the transition process. Our measurements indicated that the transition process was strongly influenced by the local pressure gradient on the inviscid flow and the entrainment of the highly non-homogeneous, rotational inviscid flow - the entropy layer originating in the stagnation region. If however the length of the transition region is defined from experiment, then the distribution of heat transfer through this region can be predicted with reasonable accuracy using the intermittency relationships $C_{H\text{TRANS}} = \gamma C_{H\text{TURB}} + (1-\gamma) C_{H\text{LAM}}$ where γ was defined earlier. The comparison between the simple theory and experiment shown in Fig. 22 demonstrates that the mean heat transfer rate increases monotonically through the transition region. In fact the temporal variation of heating at a specific point in the transition region is such that the intermittency model, in which it is assumed that the surface experiences alternating laminar and turbulent conditions, is supported by the present set of experimental measurements.

To perform accurate calculations of the boundary layer flow over the bi-conic configuration it is necessary to model the entrainment of the entropy layer into the boundary layer, i.e. account for entropy layer swallowing. A further refinement would be to include the effects of vorticity generated in the entropy layer into the model of the boundary layer development. To assess the effects of entropy swallowing it is desirable to perform calculations to determine the characteristics of the inviscid flow. Such calculations have been performed by Crowell¹¹ who has used the Godunov method to determine the inviscid flow over the elliptic and bi-conic configurations. The Godunov method was used by Crowell to determine the shock shape and pressure distribution over the elliptic and bi-conic configurations. The comparisons between the measured and computed shock shape shown in Fig. 23 demonstrate that the theoretical method is in excellent agreement with the experimental measurements.

Model roughness had a significant effect on the magnitude and distribution of heating over bi-conic nose shapes, particularly where transition was observed on the "smooth" configuration. The increase in heating which resulted from introducing 0.005 roughness on the 45° bi-conic nose shape at Mach 13 is shown in Fig. 24. On the smooth configuration transition began

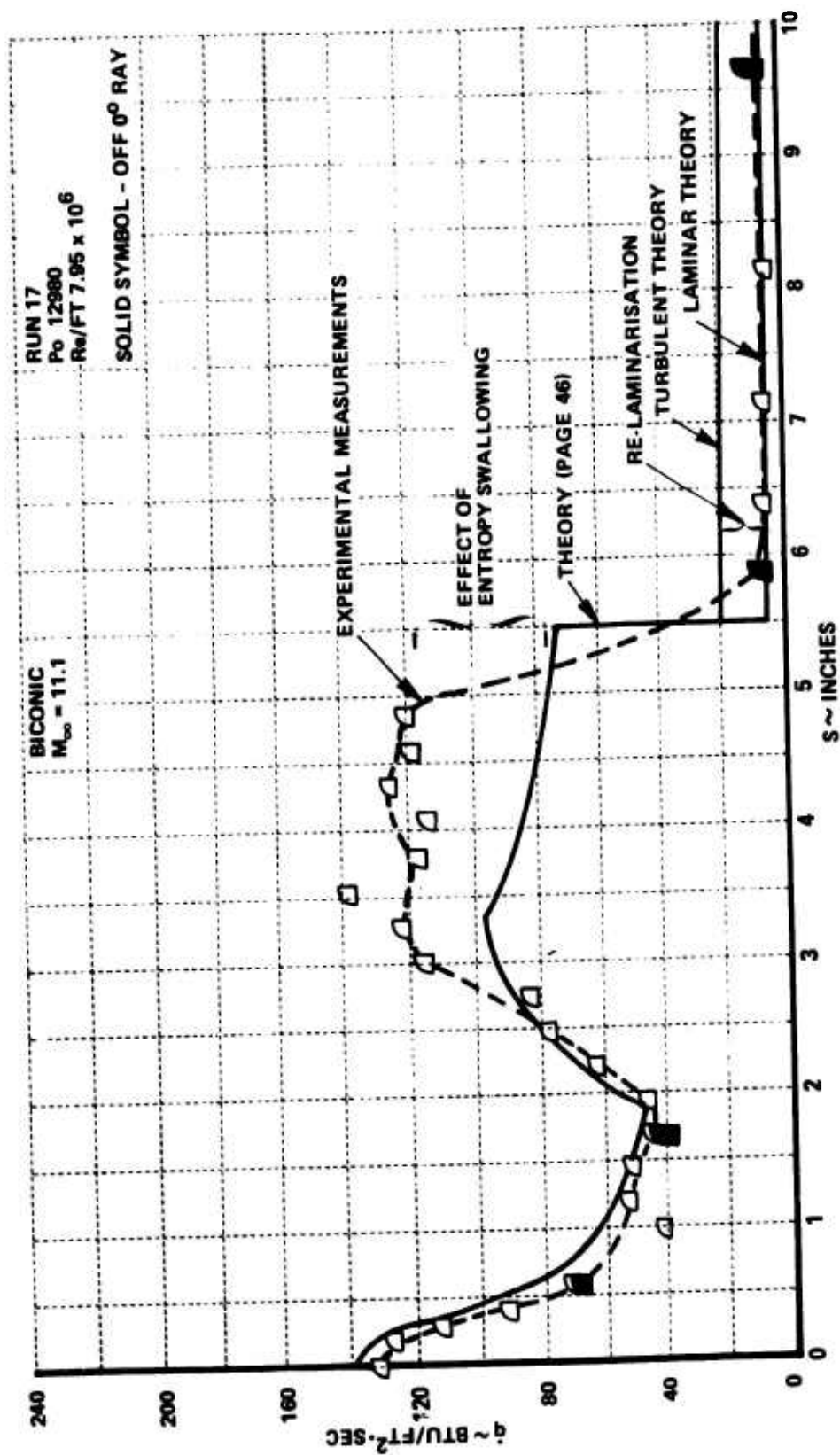


Figure 22 COMPARISON BETWEEN SIMPLE THEORY AND EXPERIMENTAL MEASUREMENTS FOR TRANSITIONAL FLOW OVER THE BICONIC CONFIGURATION

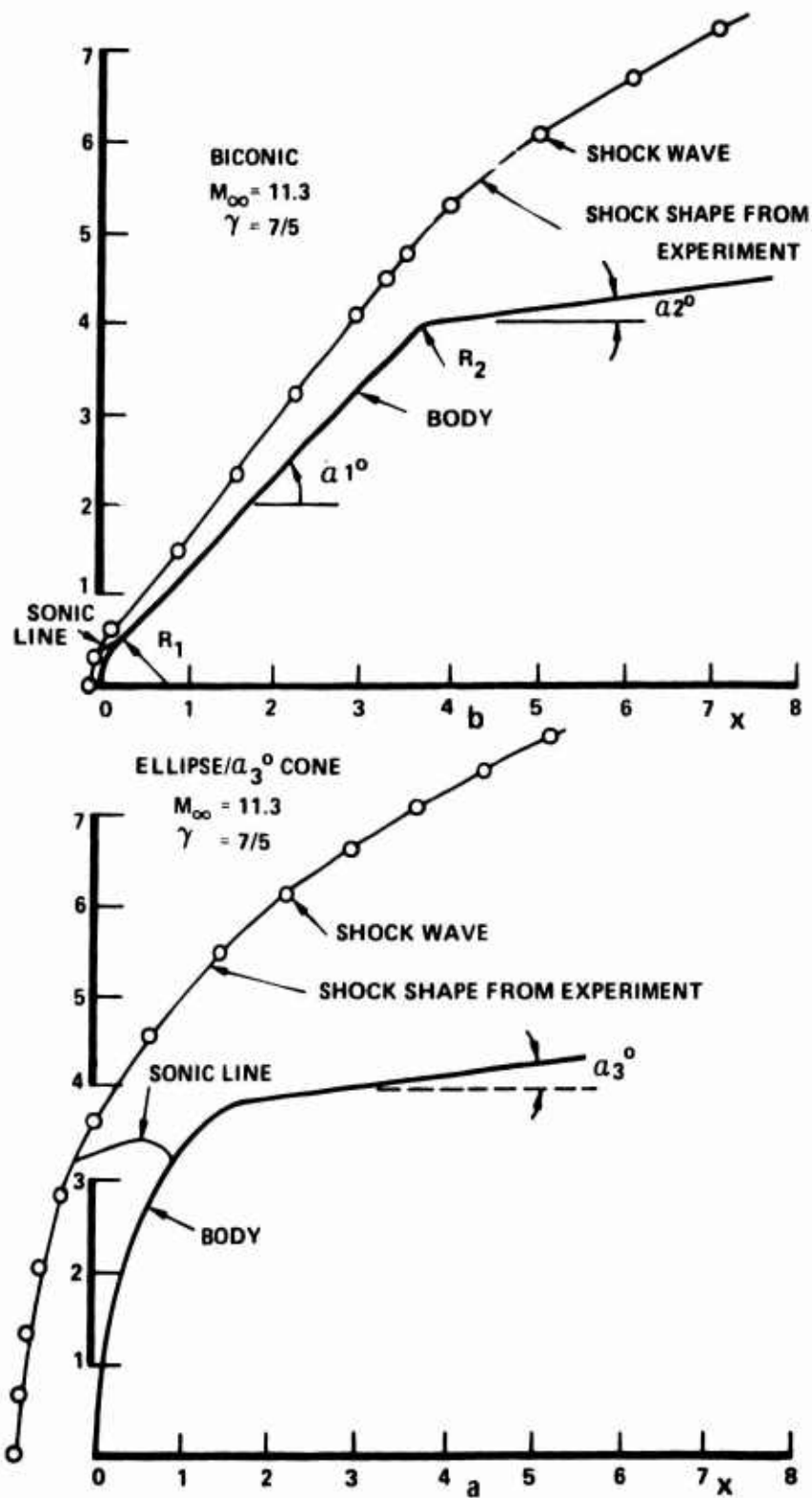


Figure 23 COMPARISON BETWEEN THE SHOCK SHAPE DETERMINED BY THE GODUNOV CODE AND THE EXPERIMENTAL MEASUREMENTS

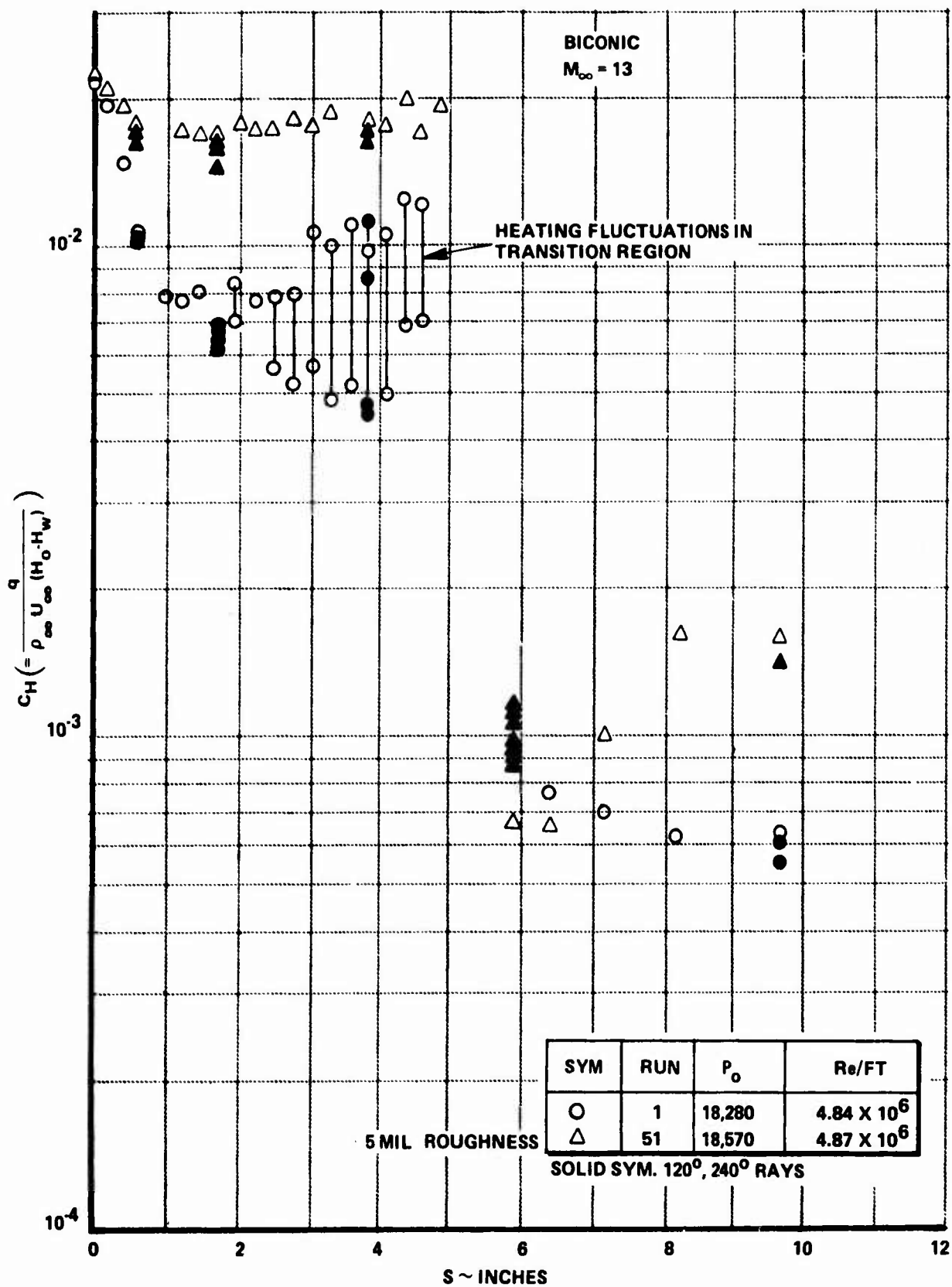


Figure 24 HEAT TRANSFER MEASUREMENTS DEMONSTRATING THE EFFECT OF 5 MIL ROUGHNESS ON TRANSITION AND THE CHARACTER OF THE TRANSITIONAL AND RELAMINARIZATION REGIONS

on the conical surface approximately 2 inches from the stagnation point and was complete by the cone-cone junction. The output from the heat transfer gages in the transition region exhibited an output typical of the intermittent character of the turbulence in this region, where the timewise variation in heat transfer spanned the local laminar and turbulent values (See Fig. 24). Introducing roughness moved transition forward to a point just downstream of the sphere-cone junction with the heat transfer on the conical surface exhibiting a fully turbulent character. Our measurements demonstrated that transition and the heating rates in the turbulent flow were symmetrically positioned on the cone surface. It is clear from the measurements that re-laminarization takes place at the cone-cone junction on both the smooth and rough body. However while re-transition takes place on the rough body, the flow over the afterbody on the smooth model remains laminar. Clearly re-laminarization and the effect of roughness on re-laminarization are phenomena of significant importance in nose-tip technology.

The effect of roughness on the transition process and the heat transfer levels downstream of transition was also investigated at Mach 11 for free stream conditions which caused the beginning of transition to be located close to the midpoint of the 45° bi-conic surface, and at the junction of this surface with the hemispherical nose-cap. These measurements are shown in Figures 25 and 26. We observe that roughness has moved the transition point well forward for the tests conducted at a λRe_D of 6×10^6 , and in each case has inhibited the re-laminarization process which occurred at the sphere-cone junction on the smooth bodies. While relaminarization occurred on the afterbody downstream of the cone-cone junction over the smooth bodies at both Reynolds numbers the flow at the highest Reynolds number on the rough body remained turbulent through this expansion region. We observe from the measurements made on both the smooth and rough nose tips that transition, relaminarization and the distribution of heat transfer occurs symmetrically over the model surface.

While the conventional shape change codes do not incorporate features which enable the position of re-laminarization or the heat transfer distribu-

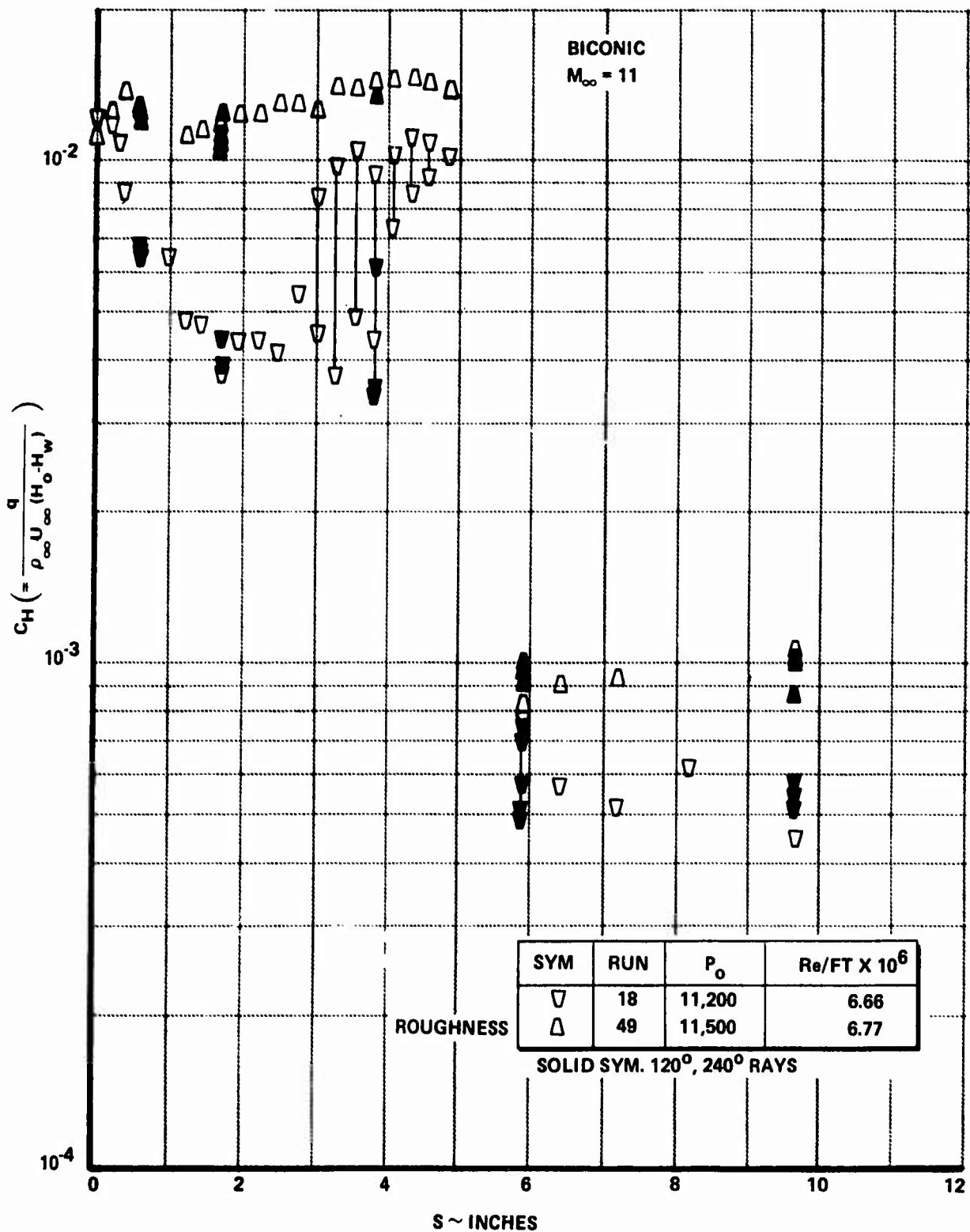


Figure 25 HEAT TRANSFER MEASUREMENTS DEMONSTRATING THE EFFECT OF 5 MIL ROUGHNESS ON TRANSITION AND THE CHARACTER OF THE TRANSITIONAL AND RELAMINARIZATION REGIONS

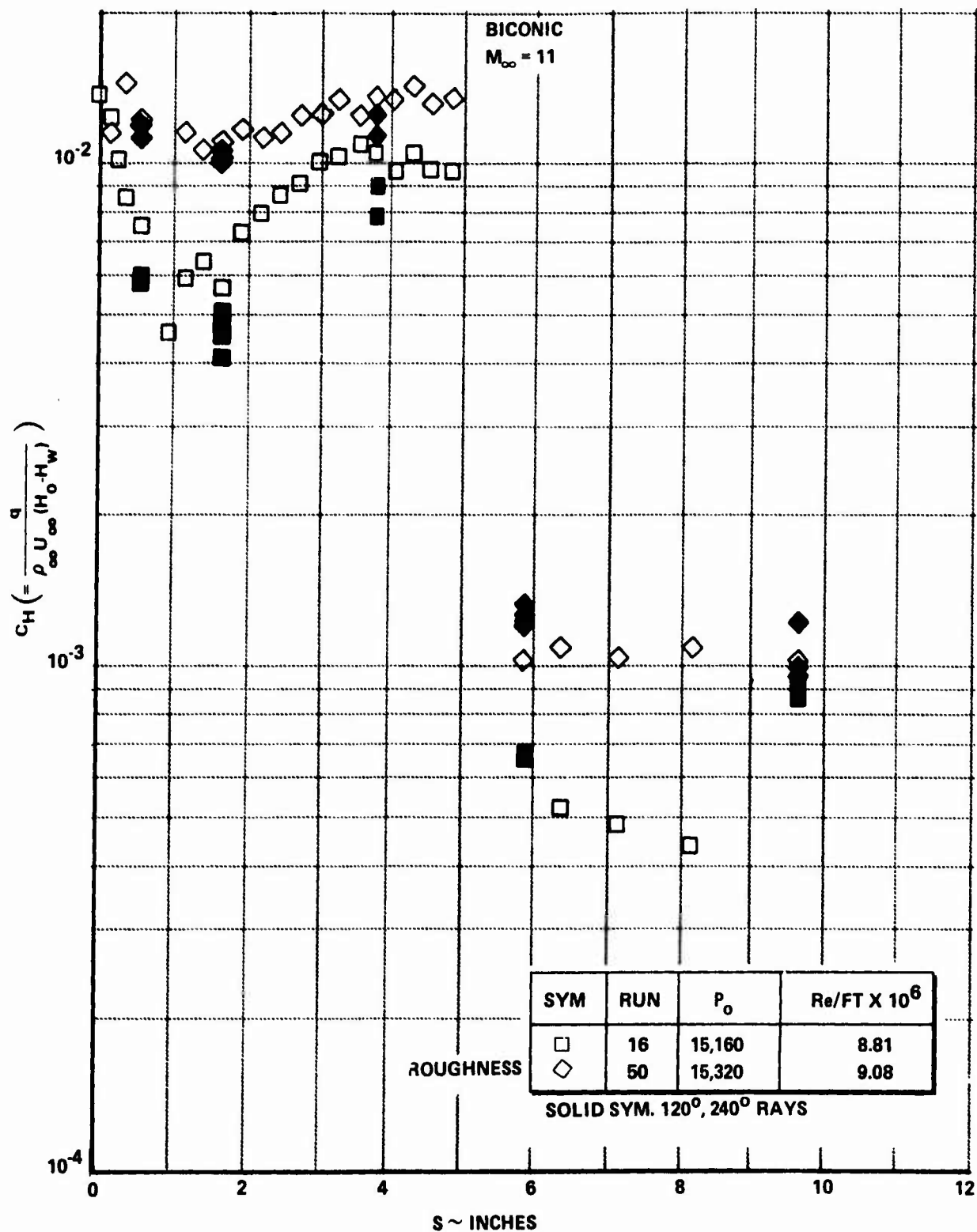


Figure 26 HEAT TRANSFER MEASUREMENTS DEMONSTRATING THE EFFECT OF 5 MIL ROUGHNESS ON TRANSITION AND THE CHARACTER OF THE TRANSITIONAL AND RELAMINARIZATION REGIONS

tion within these regions to be calculated, the effects of roughness has been incorporated in a semi-empirical technique. Crowell, using the Powars¹⁴ roughness heating formulation together with shock shape and pressure distributions from the Godunov code obtained the calculations shown in Fig. 27a for the heat transfer to the biconic nose. These solutions were obtained employing normal shock and entropy layer swallowing models to establish the local properties outside the boundary layer. We see that while the solution employing the more attractive entropy layer swallowing technique overpredicts the heating, that based on the normal shock approach underestimates the heating levels. It should also be noted that the roughness induced augmentation is based on measurements¹⁴ made at Mach 5, and the good agreement between the measurements and the theory in the absence of roughness shown in Fig. 27b suggests that the roughness modelling is in question. Clearly the mechanics of roughness induced transition and heating enhancement and wall heating in regions of transition and re-laminarization remain to be understood. Experiments are required on smooth and rough nose-tips over a range of bluntness ratios and free stream conditions so that we can isolate the relative effects of entropy layer swallowing, roughness induced turbulence and transition.

The relaminarization of a turbulent or transitional boundary layer when subjected to a strong streamwise favorable pressure gradient has been observed in both ground and flight tests and is clearly an important phenomena. Relaminarization not only causes a decrease in the heating levels, but creates a situation in which the boundary layer can be more easily separated by an adverse pressure gradient. This latter feature is of critical importance in the development of flows over highly ablated nose shapes where boundary layer separation and flow instabilities are observed to occur. The large decrease in the heating levels associated with re-laminarization were observed in the measurements made on the bi-conic configurations at Calspan and are shown in Figures 25 and 26. For flows without roughness, the heat transfer gages on the conical frustrum always give mean and fluctuating heat transfer values which were in close agreement to those for fully laminar flow, irrespective of the position of transition on the fore-body. Only by severely tripping the boundary layer with roughness is one able to preserve their turbulent character-

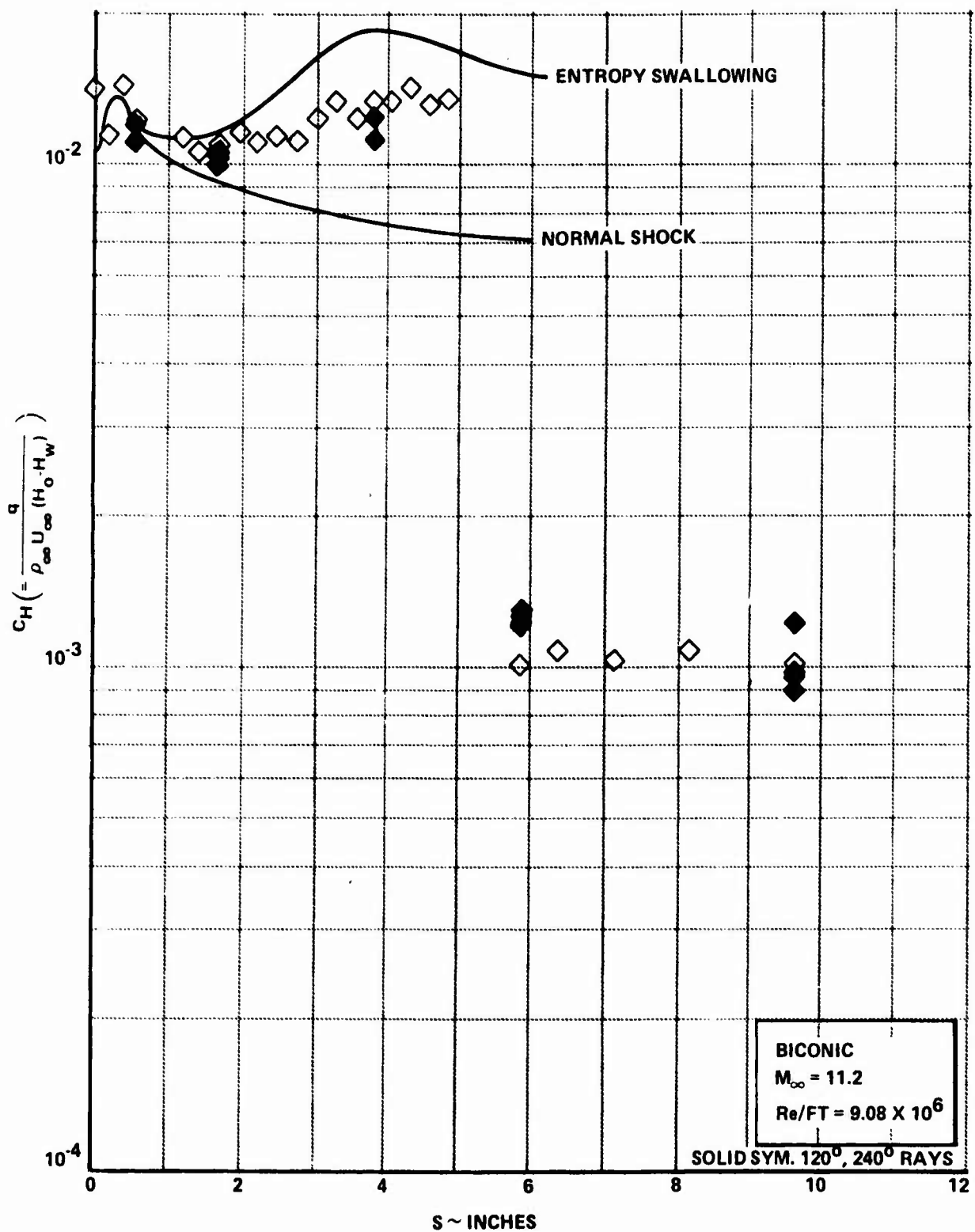


Figure 27a COMPARISON BETWEEN THE HEAT TRANSFER TO THE BI-CONIC CONFIGURATION WITH 5 MIL ROUGHNESS AND THE THEORY DEVELOPED BY CROWELL INCORPORATING POWARS ROUGHNESS MODEL

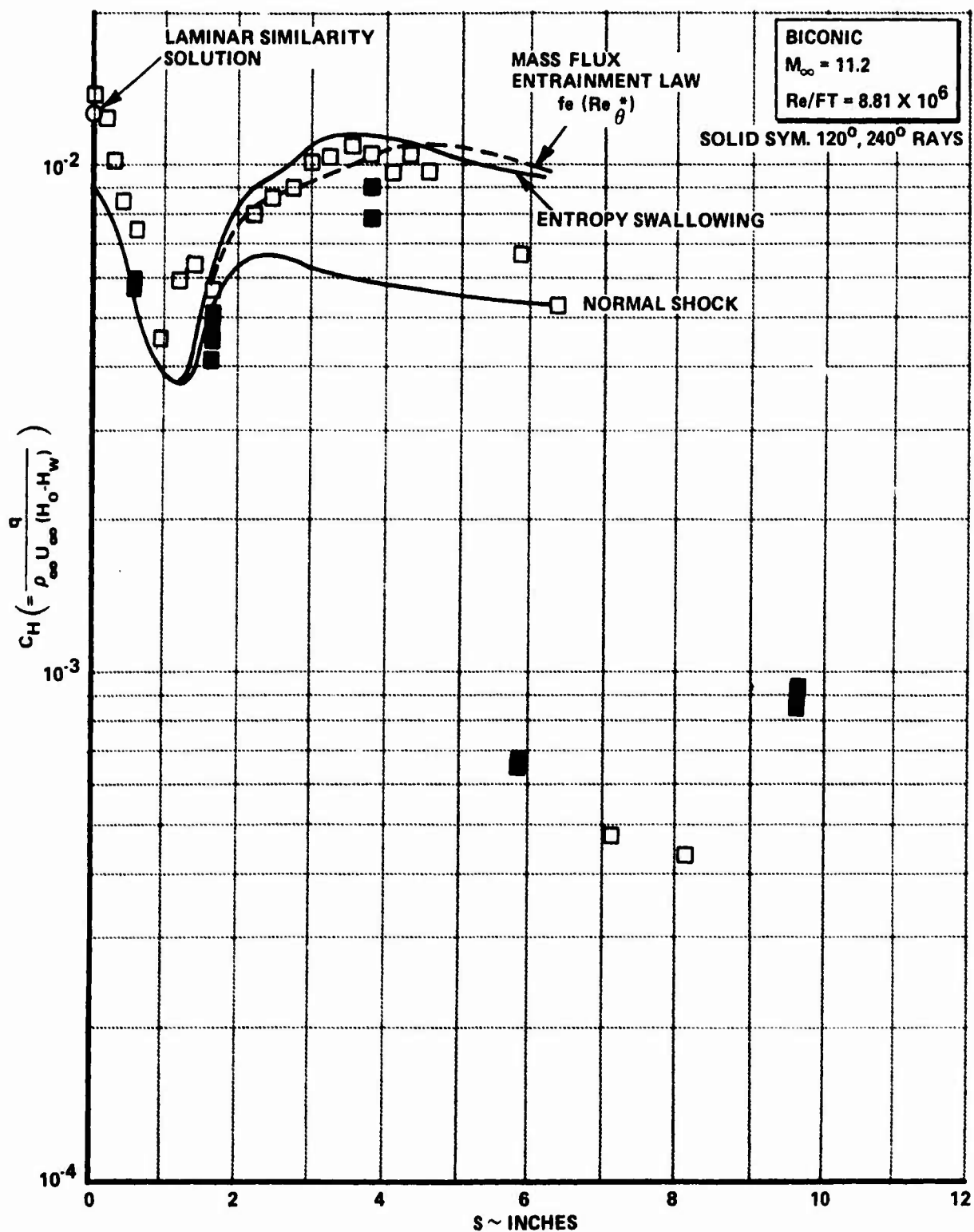


Figure 27b COMPARISON BETWEEN THE EXPERIMENTAL MEASUREMENTS AND THEORETICAL SOLUTION OBTAINED BY CROWELL FOR TRANSITION FLOW OVER A SMOOTH BI-CONIC

istics through the expansion region, as shown in Figure 25. While some criteria have been developed to suggest the conditions under which boundary layers will re-laminarize in subsonic flow, no such criteria exist for the supersonic regime with roughness. Relaminarization, which is most easily understood in terms of the turbulent energy approach, can be described as a process in which strong dissipation of the turbulence energy takes place while turbulence production is reduced because the favorable pressure gradient decreases the velocity gradient in the production region of the boundary layer. While it may be possible to obtain numerical solutions to the turbulent energy equations to determine the development of turbulent energy in highly expanding flows, experimental measurements are required to provide or validate the numerical constants used in such an approach.

Section 3
FLOW SEPARATION AND THE DEVELOPMENT OF INSTABILITIES
OVER ABLATED NOSE SHAPES

3.1 INTRODUCTION

Wind tunnel studies using ablating models have demonstrated that "slender" concave nose shapes, over which gross flow instabilities are observed, can be formed under certain free stream conditions and nose-tip properties. While an explanation of this behavior using sophisticated shape change codes awaits the development of accurate models of regions of transition and relaminarisation, the simple equilibrium solutions obtained by Welsh¹⁵ provide an important insight into the development of ablated nose shapes. Welsh's analysis, predicts the occurrence of the well known "blunt" self-preserving nose shape for fully laminar or fully turbulent boundary layers; however for flows where transition occurs ahead of the sonic point on the nose tip (and under certain fully turbulent conditions) this approach predicts the occurrence of slender nose shapes similar to those shown in Fig. 28. This result has been verified in wind tunnel tests of camphor models where shapes similar to those shown on Figure 29 can be developed under transitional conditions. The existence of slender ablated nose shapes have been demonstrated in many experimental studies however in general these shapes exhibit marked asymmetric characteristics. Asymmetric nose shapes are believed to result from asymmetric transition; whatever the cause such shapes can give rise to large de-stabilizing moments and side forces. Under certain conditions, highly indented nose shapes, similar to that shown in Fig. 30 were generated on camphor models, and over such shapes, the viscous and inviscid flow fields interact in such a way that the flow became oscillatory.

In studies of ablated nose shapes, it has become customary to describe the nose tip geometry in terms of the BI-CONIC or TRI-RADIUS configuration. Schematic representations of these shapes are shown in Figure 31. A highly ablated nose shape the form of which is to be characterised by these models is shown in Fig. 32. Bi-conic configurations with $R_n = Q_1 = 0$ are spiked bodies, and it was on these bodies that gross instabilities described above

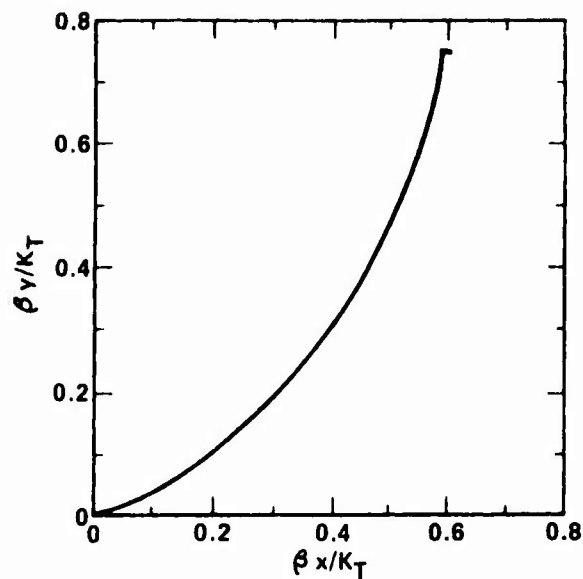


Figure 28 SLENDER EQUILIBRIUM SHAPE DEVELOPED UNDER PURELY TURBULENT BOUNDARY LAYER CONDITIONS (FROM REF. 10)

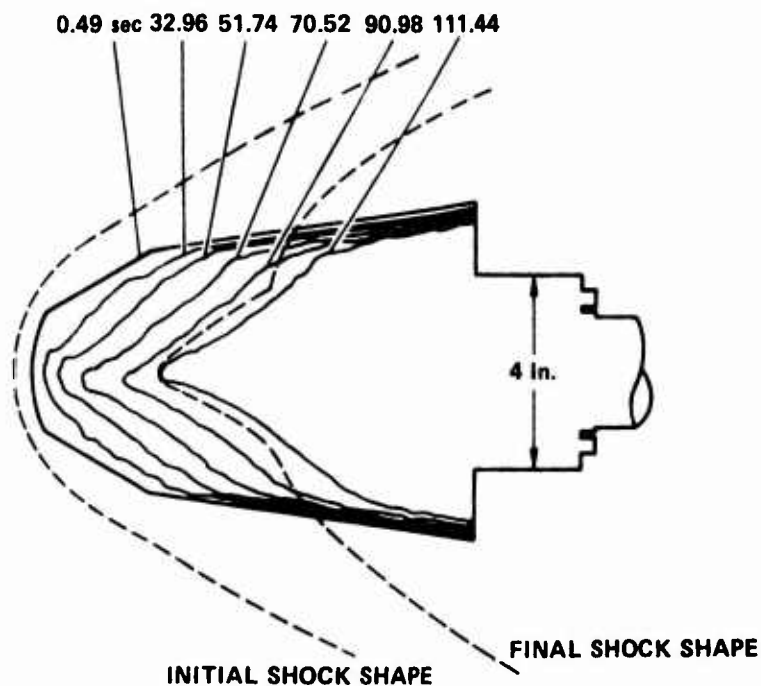


Figure 29 VARIATION OF PROFILE SHAPE WITH TIME FOR AXISYMMETRIC CAMPHOR MODELS

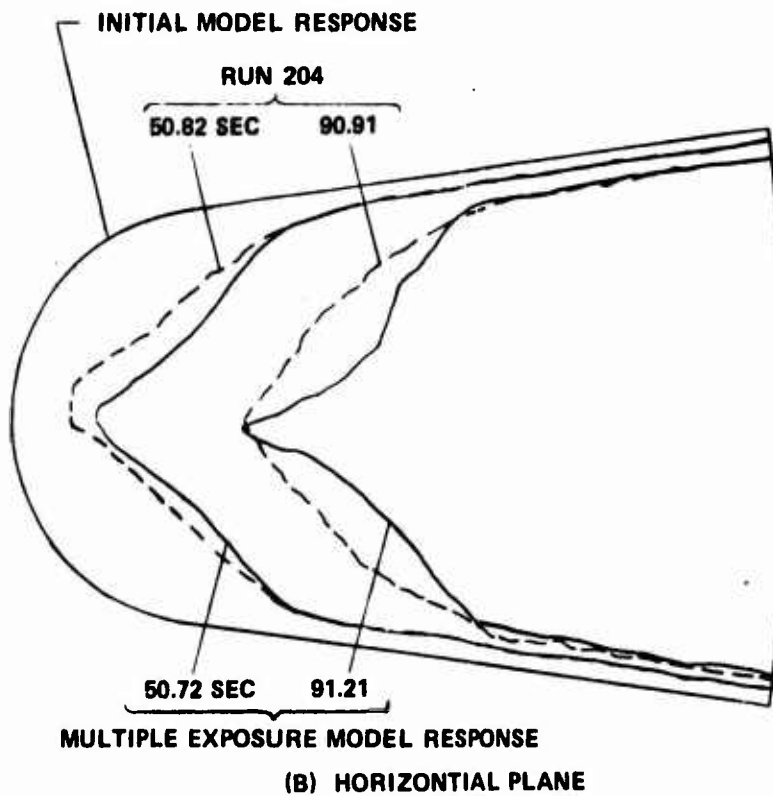
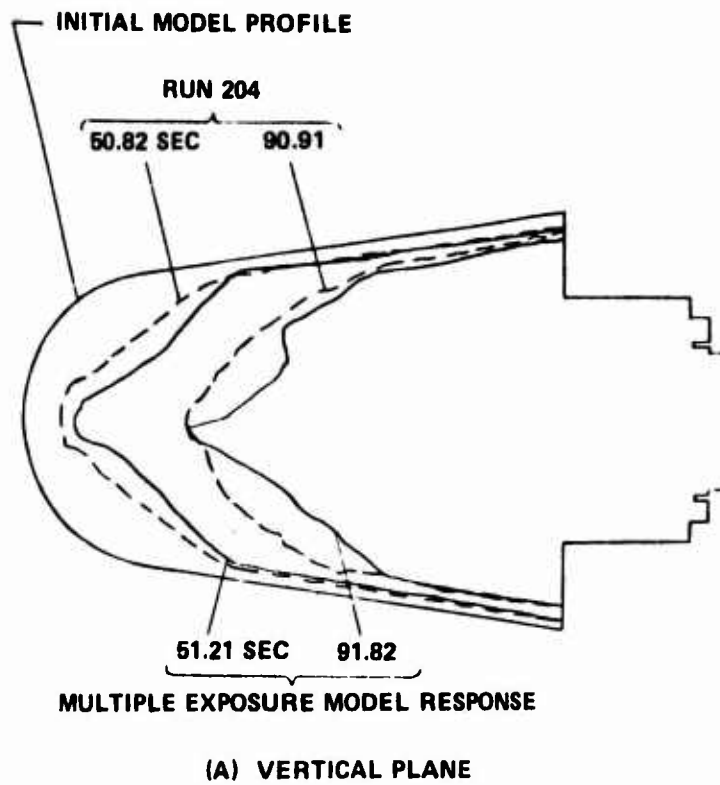


Figure 30 THE DEVELOPMENT OF ABLATED NOSE SHAPES OVER WHICH FLOW INSTABILITIES CAN OCCUR (REF. 16)

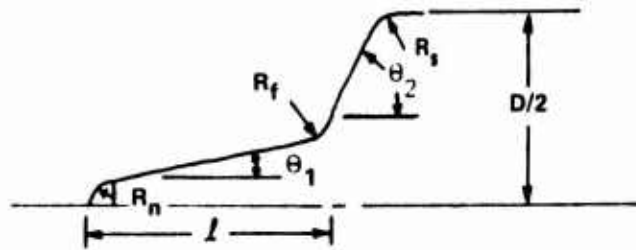


Figure 31a BI-CONIC REPRESENTATION FOR ABLATED NOSE SHAPE

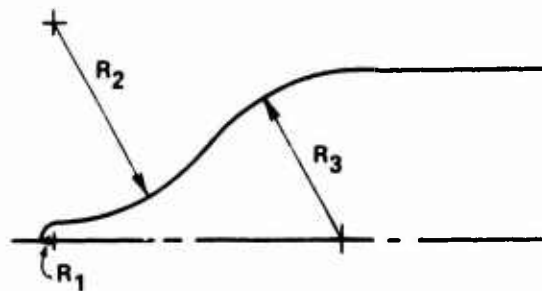


Figure 31b TRI-RADIUS REPRESENTATION FOR ABLATED NOSE SHAPE

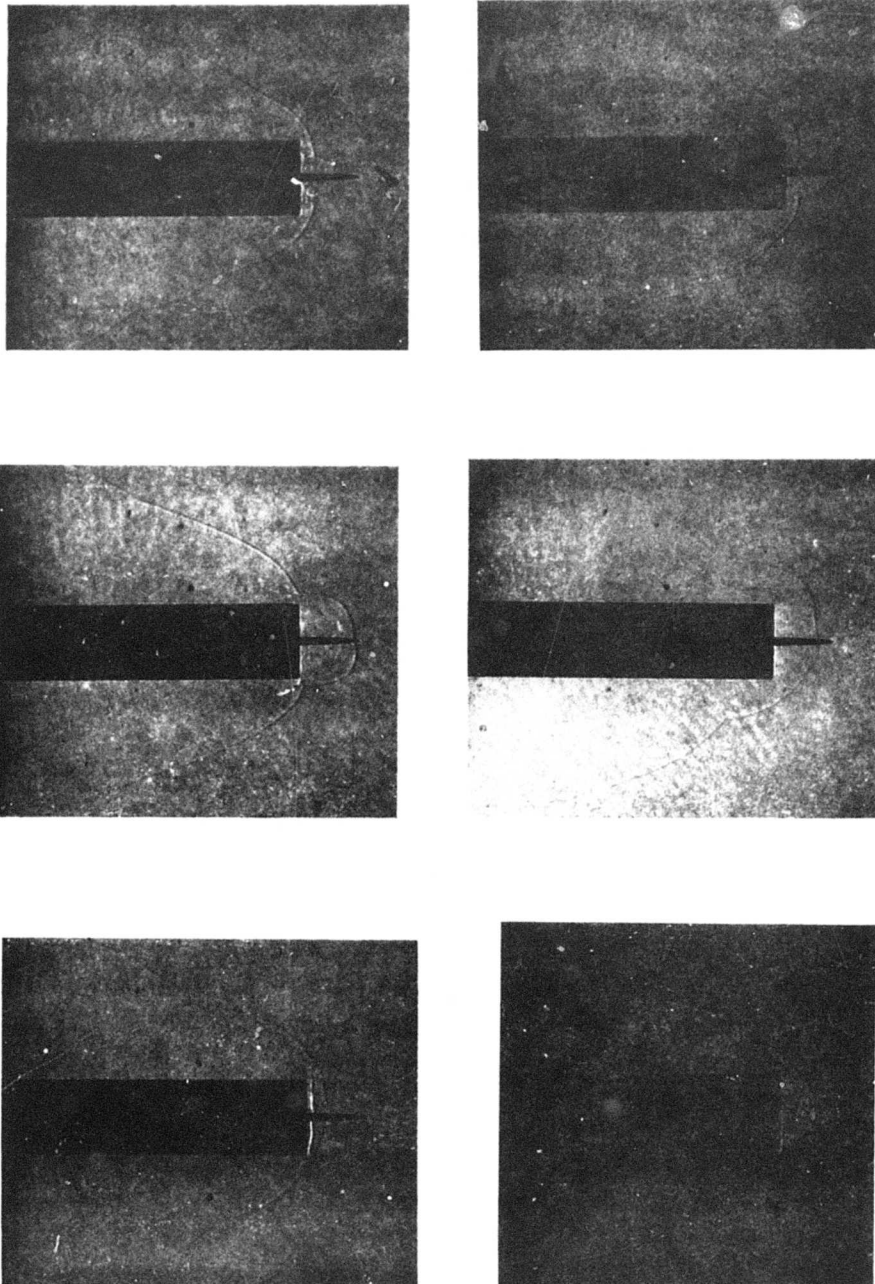


Figure 32 TYPICAL HIGHLY INDENTED ABLATED SHAPE

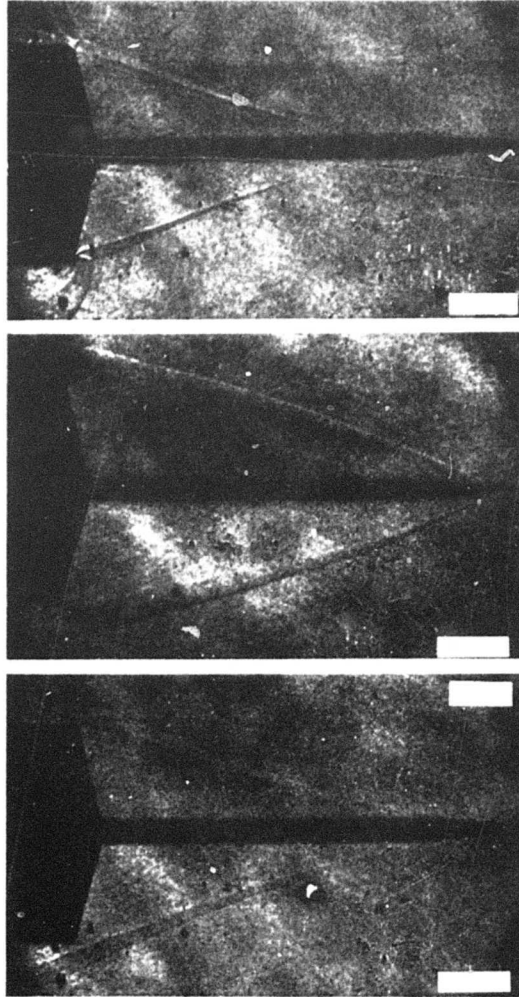
were first studied in hypersonic flow by Maull,¹⁷ Wood¹⁸ and Holden.²⁰ Maull and Wood, studied the flow over spiked flat-ended cylinders and cones and found (using high speed schlieren photography) the range of geometries for which gross axial pulsations of the flow are observed (see Figure 33). This flow instability, termed the "E" oscillation, occurs on a blunt body* when the spike pierces the bow shock and yet is of insufficient length to permit an equilibrium separated region to be established. While Maull and Wood used only schlieren photography to detect flow oscillations, Holden with the aid of high frequency thin film gages was able to detect two additional modes as well as the variation of heat transfer levels which occurred during these oscillations. The D oscillation arises from the symmetrical radial enlargement and contraction of the separated region as depicted in Figure 34. The D oscillation has a frequency slightly larger than the E oscillation. On configurations which were close to the E oscillation boundary, Holden observed a marked "lateral" (L) oscillation which appeared insensitive to model incidence. It was speculated that this motion was a circumferential oscillation resulting from an inability of this flow to generate a stable reattachment point. Again, this oscillation had a frequency larger than the longitudinal E instability. Each of these oscillations were accompanied by large variations in the heating rate to the face of the model. A common feature of the E oscillations observed in these tests, in which only laminar flows were studied, was that the Strouhal number ($\frac{fD}{V}$) appeared independent of Mach number and model geometry.

One of the most interesting results from the Pant series I tests¹⁶ in which flow oscillations were observed on ablating camphor models in ground tests was that these instabilities appeared to be predominately of the D and L type, although the E oscillation was also observed. Seldom was a completely symmetric ablation shape observed; in general, flow instabilities occurred on one side of the model and enhanced the asymmetry. An ablated nose shape typical of one where oscillations were observed is shown in Figure 30. It is clear that this shape could be defined in terms of either a Bi-Conic or Tri-Radius configuration. The former representation, however, lends itself to a

* A body which will support a detached shock in the absence of a spike.



LONGITUDINAL OSCILLATION IN TYPE E OVER SPIKED BODIES Figure 33



"D" OSCILLATION OVER SPIKED BODY

Figure 34

similar treatment to that used to define the oscillation boundaries for spiked-body flows. Figure 35 shows the oscillation boundaries determined from the spiked body studies and tests on Bi-Conic configurations performed by Aerotherm¹⁶. The results from the latter study reinforce the conclusions from the studies by Wood and Holden that θ_2 and $1/D$ are the major parameters controlling the occurrence of the E oscillation. The oscillation boundaries determined by Aerotherm for turbulent flow, fall within those found for laminar flows for Wood and Holden. Increasing θ_1 , R_N/D , R_S/D decreases the range of the θ_2 and $1/D$ for which flow pulsations are observed. The effects of Mach number and roughness were not included on the Aerotherm study. Limited variation in Reynolds number was included, but most of the data were for the higher Reynolds number, turbulent flow condition. While the studies referenced above reported that the E pulsations for highly indented nose shapes had a Strouhal frequency of close to 0.2, there is strong evidence that instabilities other than this oscillation; namely, the D and L modes have frequencies which are larger and influenced by the model geometry. From the studies performed by Calspan during the past year, it is clear that the Mach number and Reynolds number and roughness are important parameters which, through their effect on transition and boundary layer separation, influence the occurrence of separation and the boundaries between the D and E oscillation.

3.2 STUDIES OF LAMINAR FLOW OVER THE WIDHOPF 1 AND 2 NOSE SHAPES

The majority of the studies conducted at Calspan were performed for conditions such that the boundary layers over the models of ablated nose shapes were transitional or turbulent in character. However, we studied the laminar flow over two ablated nose shapes for which Widhopf and Victoria²⁰ obtained detailed numerical solutions to the complete flow field using the time-dependent Navier-Stokes equations. These nose shapes termed the 1-10-10 and 1-10-1 in the tri-radius terminology (or the Widhopf 1 and 2) are shown in Figure 36. Detailed heat transfer and pressure measurements were made over both of these configurations at Mach 10 for a Reynolds number (Re_N) of 300. The instrumentation and recording equipment were designed to enable frequencies up to 1 Mz to be recorded with little attenuation. Widhopf's calculations for

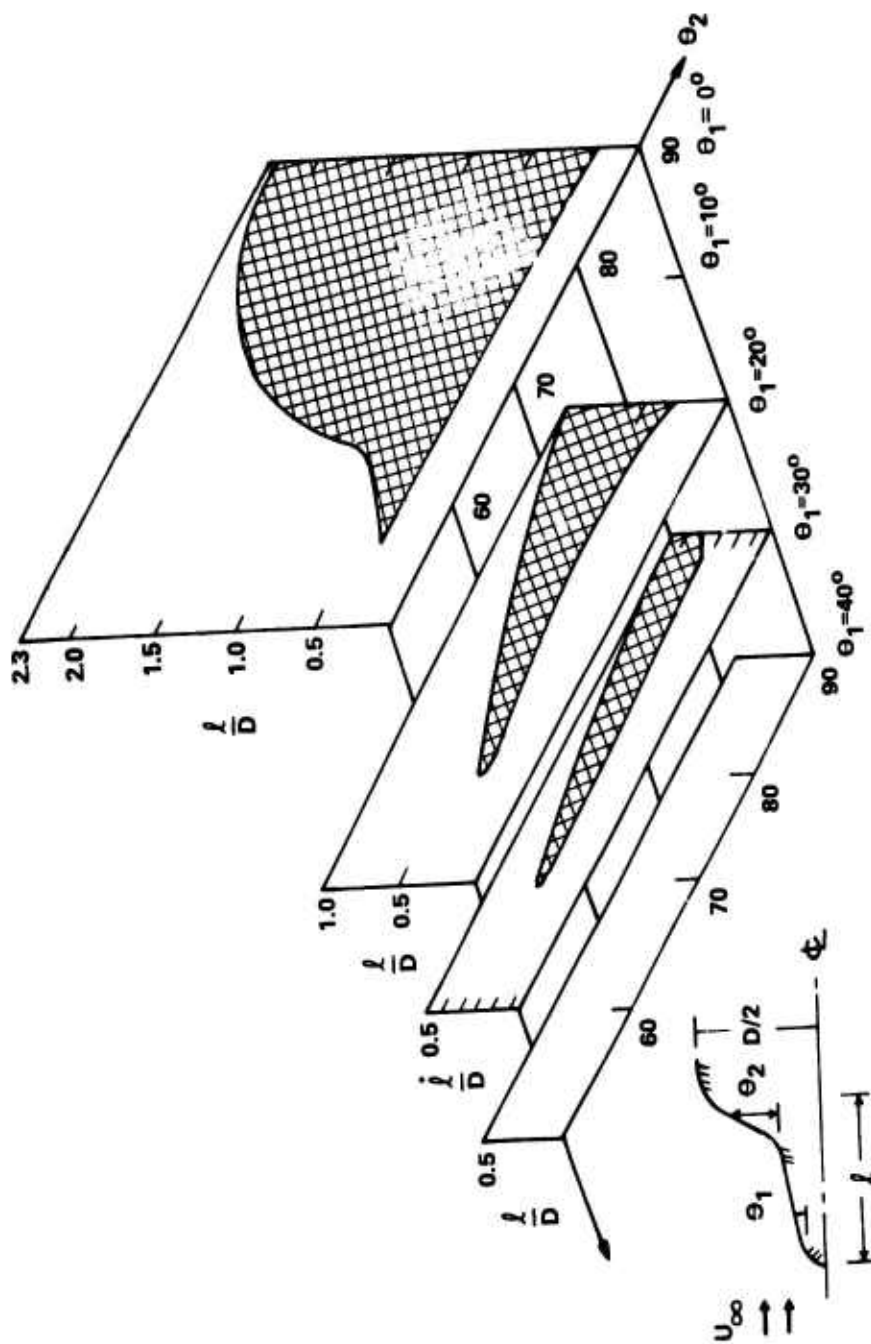


Figure 35 STABILITY BOUNDARY FOR E OSCILLATION ON BICONIC CONFIGURATIONS

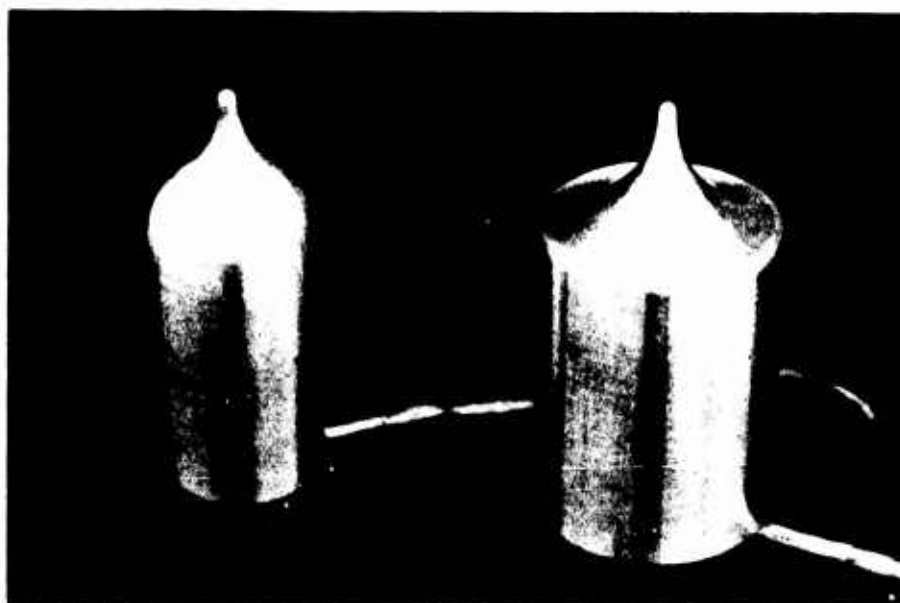
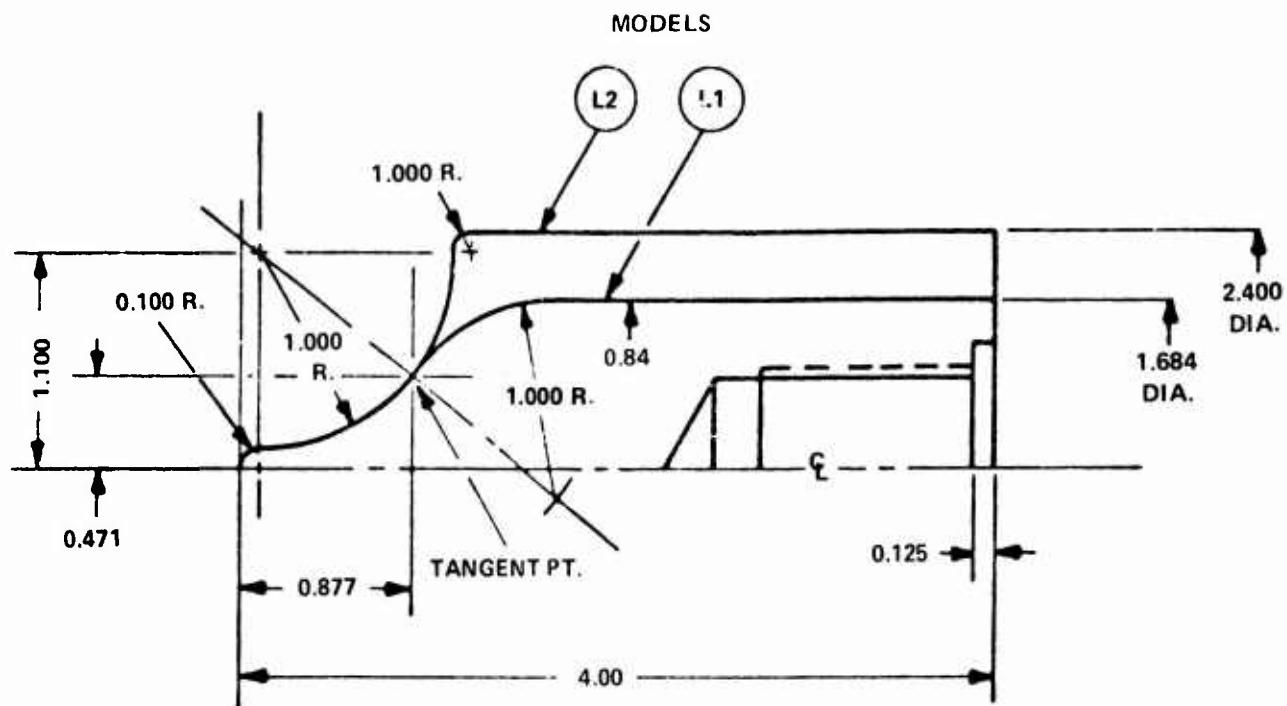


Figure 36 WIDHOPF CONFIGURATIONS 1 AND 2

Table 2
TEST CONDITIONS FOR WIDHOPF 1 AND 2 CONFIGURATIONS

RUN NO.	1	2	3	4	5
M(I)	5.310E+00	5.487E+00	5.431E+00	5.423E+00	5.511E+00
P(Q)	3.132E+02	3.082E+02	3.194E+02	3.168E+02	3.157E+02
H(O)	4.059E+07	4.319E+07	4.229E+07	4.203E+07	4.321E+07
T(O)	5.423E+03	5.683E+03	5.592E+03	5.564E+03	5.679E+03
M	9.970E+00	9.910E+00	1.091E+01	9.890E+00	9.795E+00
U	8.796E+03	9.066E+03	9.014E+03	8.947E+03	9.068E+03
T	3.237E+02	3.552E+02	2.839E+02	3.403E+02	3.564E+02
P	4.192E-03	4.336E-03	2.257E-03	4.334E-03	4.485E-03
Q	2.920E-01	2.924E-01	1.882E-01	2.970E-01	3.015E-01
RHO	1.087E-06	1.025E-06	6.672E-07	1.069E-06	1.056E-06
MU	2.578E-07	2.789E-07	2.298E-07	2.691E-07	2.796E-07
KE/FT.	3.708E+04	3.331E+04	2.617E+04	3.553E+04	3.424E+04
PITOT	5.492E-01	5.506E-01	3.543E-01	5.590E-01	5.678E-01
H(W)	3.186E+06	3.195E+06	3.189E+06	3.183E+06	3.183E+06
T(W)	5.305E+02	5.320E+02	5.310E+02	5.300E+02	5.300E+02

the 1-10-10 configuration showed a high frequency instability occurred in the flow field close to the point of surface inflexion on this body. This localized oscillation was predicted to have a major frequency of approximately 600 KHz. Thus, the heat transfer gages were constructed so that their physical dimensions were smaller than the wavelength of the oscillation. The heat transfer distribution to this body is shown in Figure 37 together with the predictions from the Navier-Stokes solutions of Widhopf. Although the measurements are in good agreement with the mean values from these calculations, we were unable to detect the flow instabilities observed by Widhopf in his numerical solutions. Measurements were made at a different Mach number and Reynolds number to determine whether an oscillation could be induced at slightly different flow conditions, but again we found a stable flow. However, one of the most interesting aspects of the aerodynamics of this configuration is the large heating rates generated at the inflexion of the concave surface at the base of the embedded shock (see Figure 38). Studies of shock wave-turbulent boundary layer interaction on concave bodies suggest that an even larger increase in heat transfer would occur on the 1-10-10 configuration if the boundary layer were transitional or turbulent. An ablating body upon which these heating levels were impressed would tend to become more highly indented and possibly develop onto the shape of the 1-10-1 configuration.

Heat transfer, pressure and schlieren records from measurements made on the 1-10-1 configuration at Mach 10 demonstrate that the flow is fully pulsating in the E oscillation mode. The schlieren photographs, shown in Figure 39, indicate the oscillation is symmetric with a frequency which gives a Strouhal number ($\frac{f v}{D}$) of 0.19. The heat transfer and pressure to the model (shown in Fig. 40) undergoes a cyclic variation with the heat transfer varying between a value which is approximately equal that to the stagnation point on a flat faced cylinder with the same body diameter, to a level six times as large. This latter condition is attained during the part of the cycle where the separated shear layer impinges onto the almost vertical face of the afterbody. A small angle of attack can induce a second asymmetric oscillational mode during which a circumferential movement of the separated region occurs. This mode, which

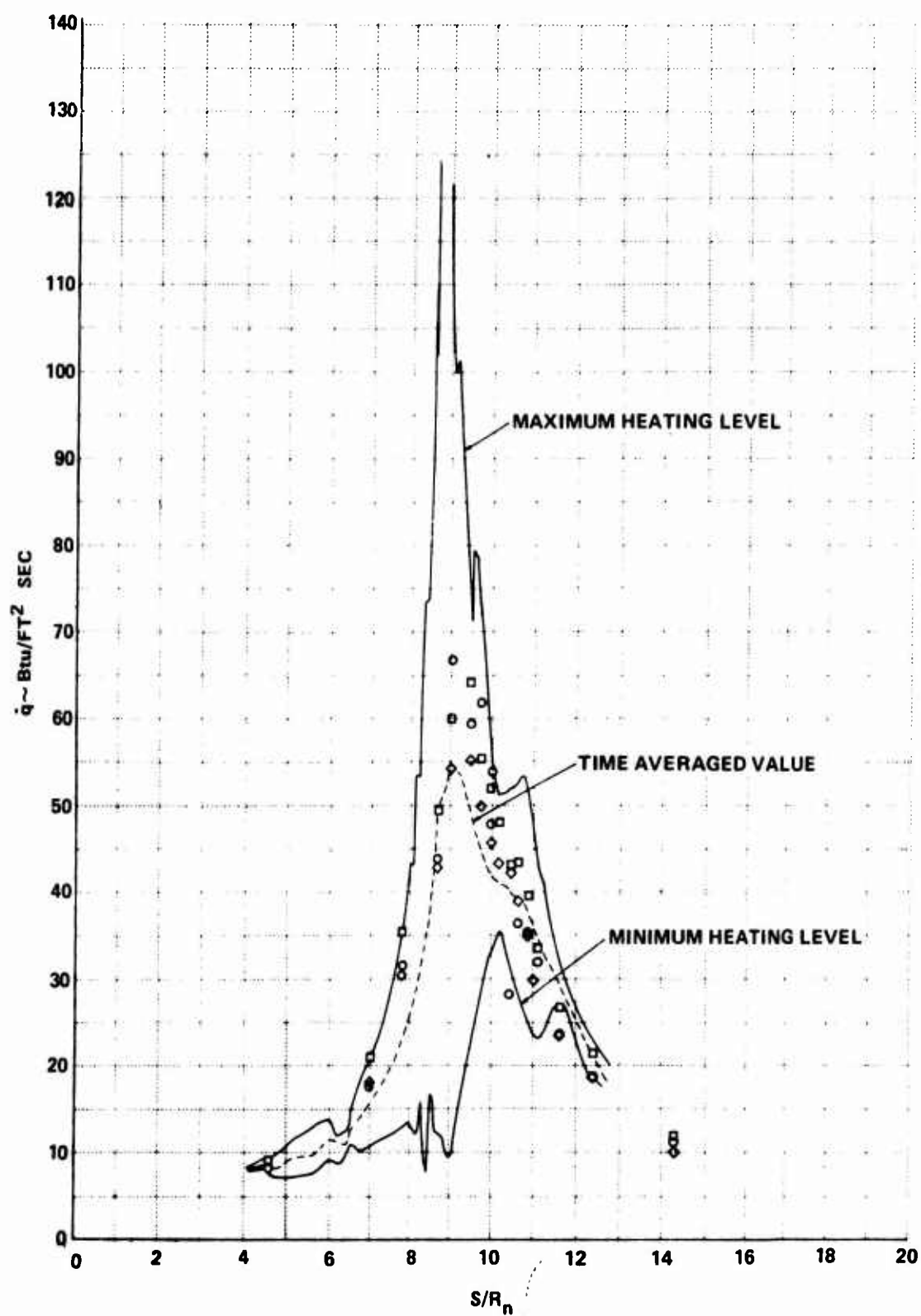


Figure 37 COMPARISON BETWEEN THEORY AND EXPERIMENT FOR THE WIDHOPF 1 CONFIGURATION (1-10-10)

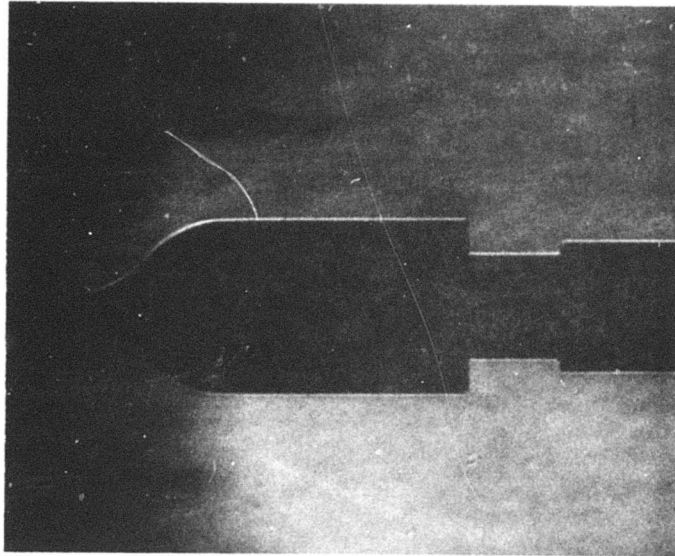


Figure 38 SCHLIEREN PHOTOGRAPH OF FLOW OVER WIDHOPF 1 CONFIGURATION

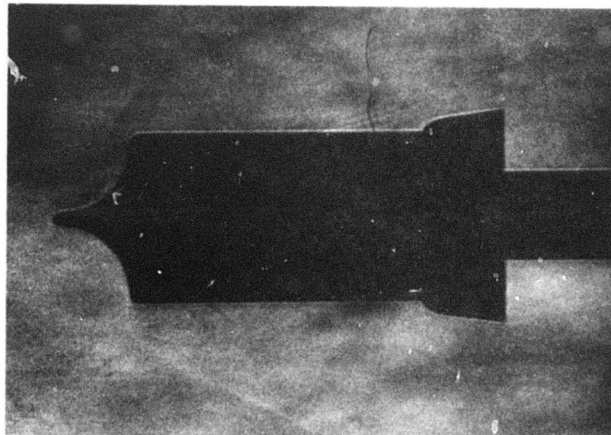


Figure 39a SCHLIEREN PHOTOGRAPH OF FLOW OVER WIDHOPF 2 CONFIGURATION

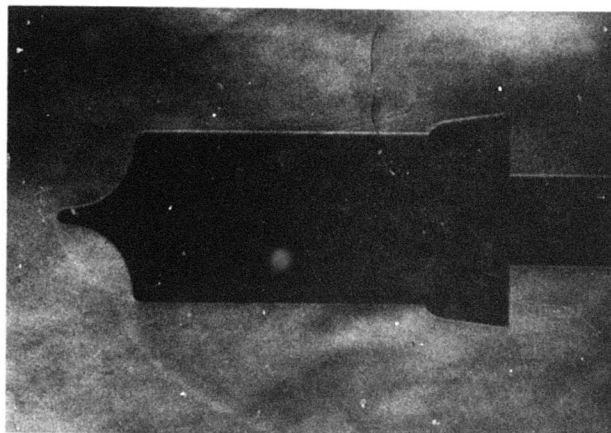


Figure 39b SCHLIEREN PHOTOGRAPH OF FLOW OVER WIDHOPF 2 CONFIGURATION

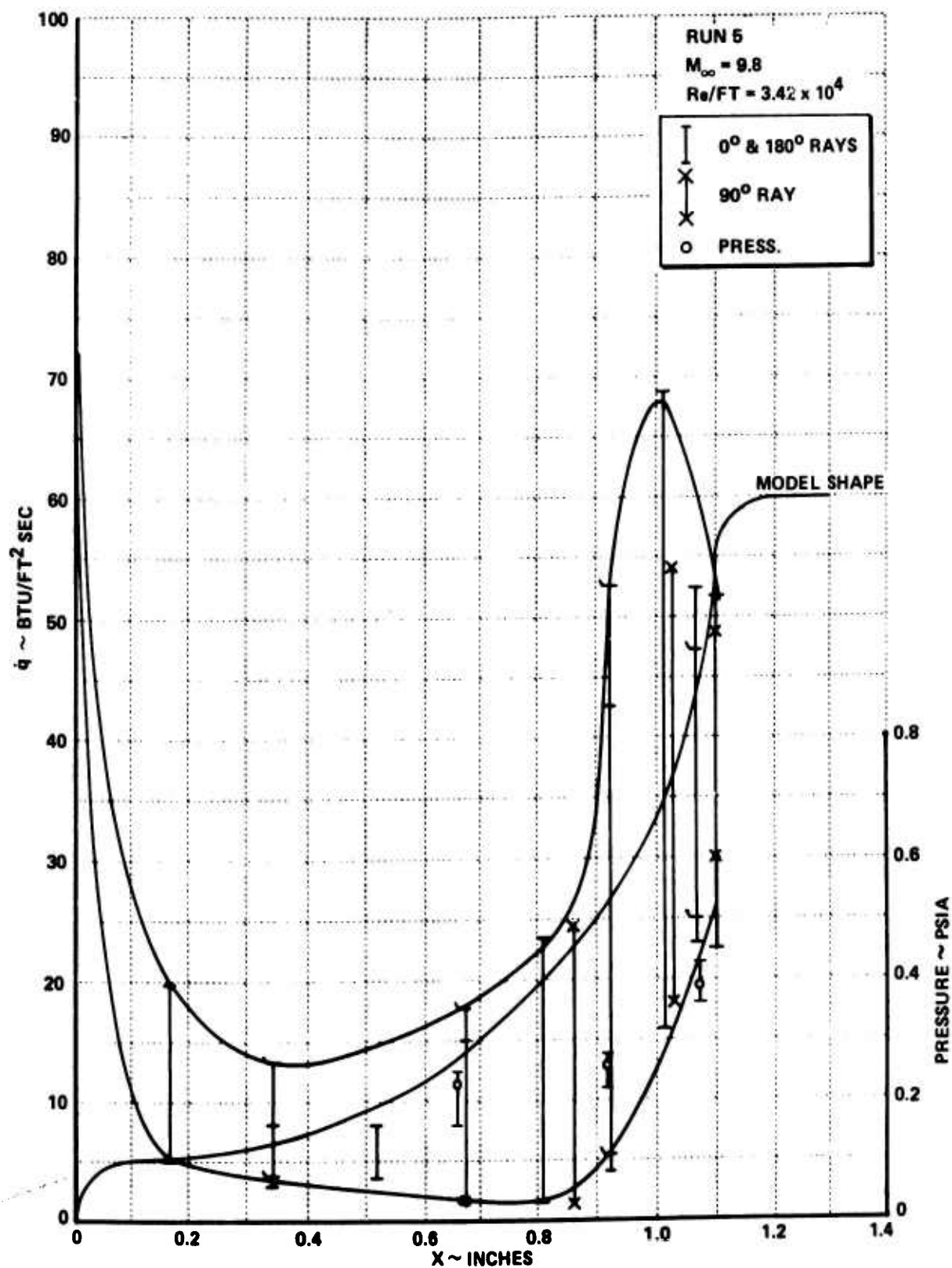


Figure 40a HEAT TRANSFER AND PRESSURE MEASUREMENTS ON THE WIDHOPF 2 CONFIGURATION

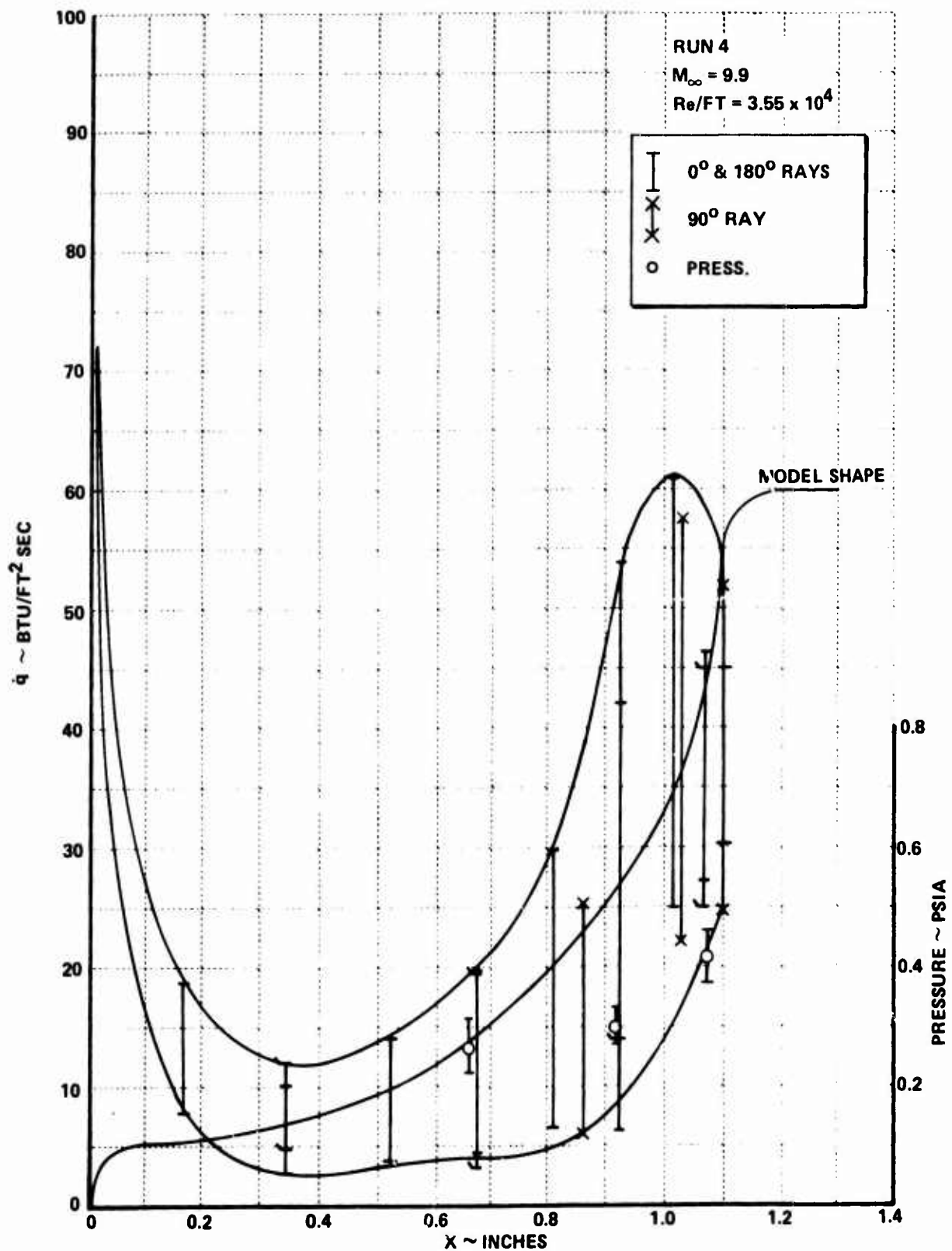


Figure 40b HEAT TRANSFER AND PRESSURE MEASUREMENTS ON THE WIDHOPF 2 CONFIGURATION

will be discussed in greater detail as it occurs both on the "A" shapes and the Pant I configurations, induces higher harmonics of the basic E oscillation, and causes asymmetric loading of significant proportions. While the basic frequency of the E oscillational mode and the higher harmonics appear to be little influenced by the Mach number or Reynolds number of the free stream or the roughness of the model when a highly ablated nose shape is tested, for configurations which are close to the oscillation boundaries these effects do become of importance. Such is the case for a series of "A" nose shapes tested in our recent experimental program.

3.3 EXPERIMENTAL STUDIES OF THE STABLE AND OSCILLATORY FLOWS OVER THE "A" SERIES NOSE SHAPES

The "A" series nose shapes were developed from observations made on flight and ground tests to establish the shape of ablated nose configurations on which pulsations are observed. The configuration labeled A0 in Figure 41 was the nose shape originally chosen by AVCO as representative of a configuration achieved in flight. This shape was tested under laminar flow conditions and shown to exhibit unsteady flow characteristics. However, configuration A1 was, in fact, constructed by AVCO to be tested at AEDC. This later shape was tested at Calspan where we found that an absence of E pulsations for high Reynolds number conditions at Mach 11 and 13. The shapes A2, A3 and A4 were selected for preliminary studies at Calspan to provide information to determine how AVCO could make simple modifications to the A1 configuration to obtain an E oscillation, as well as obtaining basic information on how the oscillation boundaries are modified by body geometry, Mach number, Reynolds number and roughness.

The characteristics of the flow field over the A1 configuration can be seen with the aid of the high speed movie sequence shown in Figure 42. A full scale E oscillation is not observed on this configuration; instead, the D oscillation occurs. Here, there is a periodic growth and collapse of the separated region, however, the separation point remains close to the tip of the nose rather than moving from the tip to the base as observed for the E

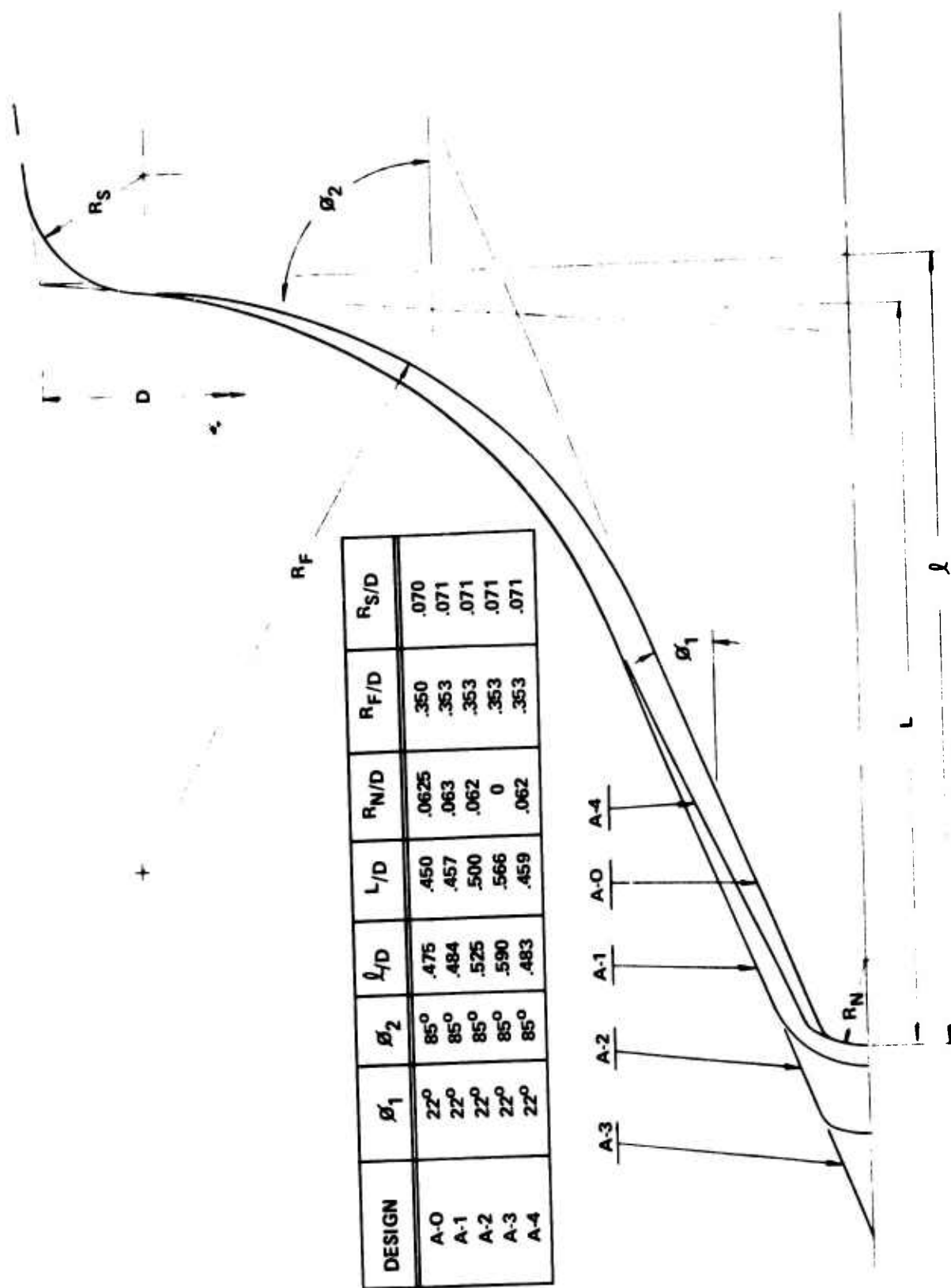


Figure 41 THE "A" CONFIGURATIONS USED IN THE CALSPAN TEST MATRIX

Table 3
TEST CONDITIONS FOR THE A CONFIGURATIONS

RUN NO.	35	36	37	38	41	42
ATTACK	0.0	0.0	0.0	0.0	0.0	0.0
YAW	0.0	0.0	0.0	0.0	0.0	0.0
ROLL	0.0	0.0	0.0	0.0	0.0	0.0
M(I)	3.343E+00	3.792E+00	3.335E+00	3.350E+00	3.296E+00	3.170E+00
P(I)	1.533E+04	1.905E+04	1.837E+04	1.537E+04	1.755E+04	1.597E+04
H(O)	1.790E+07	2.169E+07	1.754E+07	1.731E+07	1.674E+07	1.586E+07
T(O)	2.708E+03	3.290E+03	2.758E+03	2.714E+03	2.645E+03	2.519E+03
M	1.123E+01	1.294E+01	1.133E+01	1.123E+01	1.132E+01	1.132E+01
U	5.871E+03	6.494E+03	5.813E+03	5.774E+03	5.679E+03	5.527E+03
T	1.156E+02	1.047E+02	1.095E+02	1.099E+02	1.047E+02	9.914E+01
P	1.841E-01	8.330E-02	2.216E-01	1.879E-01	2.155E-01	1.953E-01
Q	1.628E+01	9.773E+00	1.993E+01	1.661E+01	1.934E+01	1.754E+01
RHO	1.360E-04	6.674E-05	1.098E-04	1.435E-04	1.727E-04	1.653E-04
MU	9.554E-08	8.811E-08	9.212E-08	9.244E-08	8.607E-08	8.341E-08
RE/FT.	8.359E+06	4.919E+06	1.072E+07	9.964E+06	1.114E+07	1.096E+07
PITOT	3.017E+01	1.817E+01	3.691E+01	3.076E+01	3.580E+01	3.244E+01
T*	8.510E+02	9.606E+02	8.366E+02	8.268E+02	8.071E+02	7.797E+02
MU*	5.369E-07	5.830E-07	5.306E-07	5.263E-07	5.175E-07	5.052E-07
SQRT.C*	6.661E-01	8.494E-01	8.684E-01	8.699E-01	8.731E-01	8.776E-01
H(W)	3.195E+06	3.147E+06	3.171E+06	3.135E+06	3.129E+06	3.147E+06
T(W)	5.320E+02	5.240E+02	5.280E+02	5.220E+02	5.210E+02	5.240E+02
P(TS)	2.321E-04	2.901E-04	2.708E-04	3.288E-04	3.288E-04	1.354E-04
RE(STAG)	5.743E+04	2.832E+04	7.156E+04	6.063E+04	7.283E+04	6.975E+04
POP4TH	8.763E-01	9.458E-01	9.059E-01	8.728E-01	8.946E-01	9.081E-01

Table 3 (Continued)

TEST CONDITIONS FOR THE A CONFIGURATIONS

RUN NO.	43	44	45	46	52	53
ATTACK						
YAW	0.0	0.0	0.0	0.0	0.0	0.0
ROLL	0.0	0.0	0.0	0.0	0.0	0.0
M(I)	3.167E+00	3.313E+00	3.303E+00	3.273E+00	3.701E+00	3.299E+00
P(O)	1.583E+04	1.735E+04	1.739E+04	1.690E+04	1.777E+04	1.774E+04
H(O)	1.543E+07	1.708E+07	1.719E+07	1.661E+07	2.100E+07	1.715E+07
T(O)	2.493E+03	2.693E+03	2.709E+03	2.626E+03	3.204E+03	2.703E+03
M	1.132E+01	1.131E+01	1.131E+01	1.131E+01	1.296E+01	1.131E+01
U	5.496E+03	5.737E+03	5.755E+03	5.656E+03	6.390E+03	5.748E+03
T	9.808E+01	1.071E+02	1.077E+02	1.040E+02	1.011E+02	1.073E+02
P	1.945E-01	2.112E-01	2.110E-01	2.073E-01	7.717E-02	2.116E-01
Q	1.745E+01	1.895E+01	1.891E+01	1.857E+01	9.086E+00	1.898E+01
RHC	1.664E-04	1.659E-04	1.645E-04	1.672E-04	6.408E-05	1.654E-04
MU	8.251E-08	9.007E-08	9.056E-08	8.753E-08	8.502E-08	9.027E-08
RE/FT.	1.108E+07	1.056E+07	1.045E+07	1.060E+07	4.816E+06	1.053E+07
PITOT	3.227E+01	3.509E+01	3.502E+01	3.437E+01	1.688E+01	3.514E+01
T*	7.727E+02	6.198E+02	8.248E+02	8.033E+02	9.396E+02	8.234E+02
MU*	5.020E-07	5.232E-07	5.254E-07	5.158E-07	5.745E-07	5.248E-07
SQRT.C*	6.787E-01	6.710E-01	8.702E-01	8.737E-01	8.524E-01	8.705E-01
H(W)	3.132E+06	3.147E+06	3.165E+06	3.135E+06	3.165E+06	3.165E+06
T(W)	5.215E+02	5.240E+02	5.270E+02	5.220E+02	5.270E+02	5.270E+02
P(TS)	4.835E-04	2.901E-04	2.901E-04	2.901E-04	2.708E-04	2.901E-04
RE(STAG)	7.022E+04	6.902E+04	6.934E+04	7.049E+04	2.709E+04	6.974E+04
POP4TH	9.032E-01	8.713E-01	8.809E-01	8.784E-01	9.094E-01	8.869E-01

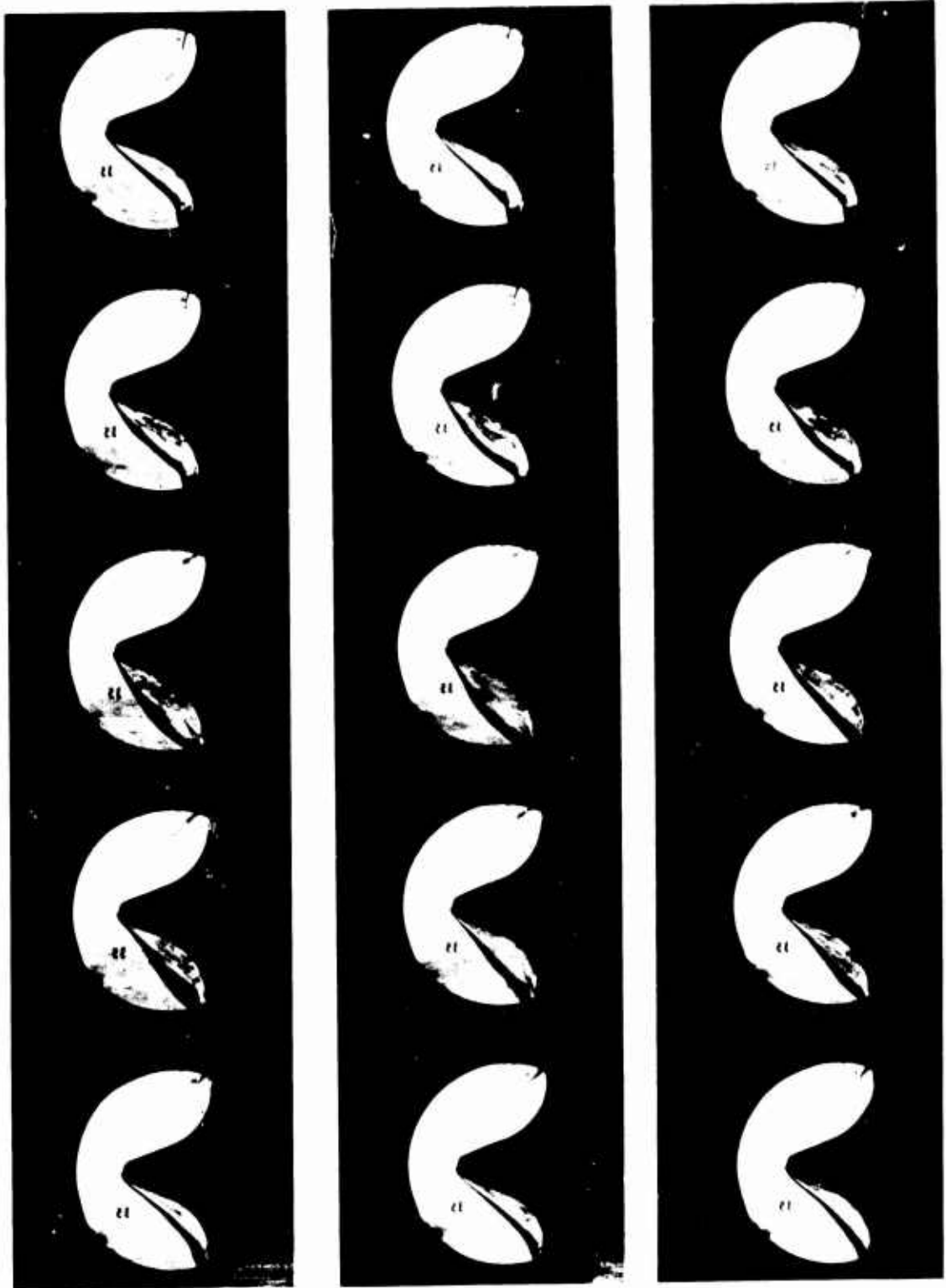


Figure 42 THE "D" OSCILLATION OVER THE A1 CONFIGURATION

oscillation. The mass entrained into the separated region is partially shed as the reattachment point in the separated shear layer moves from the shoulder of the nose shape. The movement of the shear layer toward the axis accompanies the subsequent partial collapse of the recircular region. As this occurs, the shear layer sweeps across the face of the nose producing heat transfer rates in excess of five times that to the stagnation point of a sphere with the same base diameter as the nose tip. During this oscillation, the pressure to the nose tip undergoes a cyclic variation between a value just greater than the pitot pressure to approximately one third this value, while the nose tip drag varies by a factor of approximately two. Further measurements with the A1 configuration suggested that the D oscillation could be stabilized with increased model roughness, Mach number and Reynolds number. The interesting feature of the D oscillation, however, is that a Strouhal number of 0.30 characterizes the frequency, which is close to double the oscillation frequency observed for the basic E mode oscillation. In fact, our measurements suggest the D mode may form the first harmonic when a strong E oscillation is observed.

Following our discovery that an E oscillation could not be induced over the A1 configuration, studies were conducted on configurations A2, A3 and A4, which were shapes derived by changing the tip configuration of the A1 shape. A2 has the same bluntness ratio as A0 but a slightly larger L/D. We found that although an E oscillation was generated over this configuration (see Figure 43), this oscillation had a lower non-dimensional frequency than observed earlier and appeared close to establishing a steady separated flow. In fact, extending the nose to a sharp point, the A3 configuration, generated a steady attached flow (as shown in Figure 44), although one cycle of the E mode was observed just before flow breakdown. Here we believe the boundary layer ahead of the corner radius (R_F) was fully turbulent and for this reason the flow did not separate or oscillate. If a laminar flow were to be established over the tip of the A3 nose shape, we believe an E oscillation would result. This configuration we believe would be sensitive to roughness effects. Finally, our studies of the flow over the A4 configuration, a configuration where θ_1 was modified to achieve approximately the same bluntness ratio as the A0 configuration was found to be just unstable in the E mode, as shown in Figure 45.

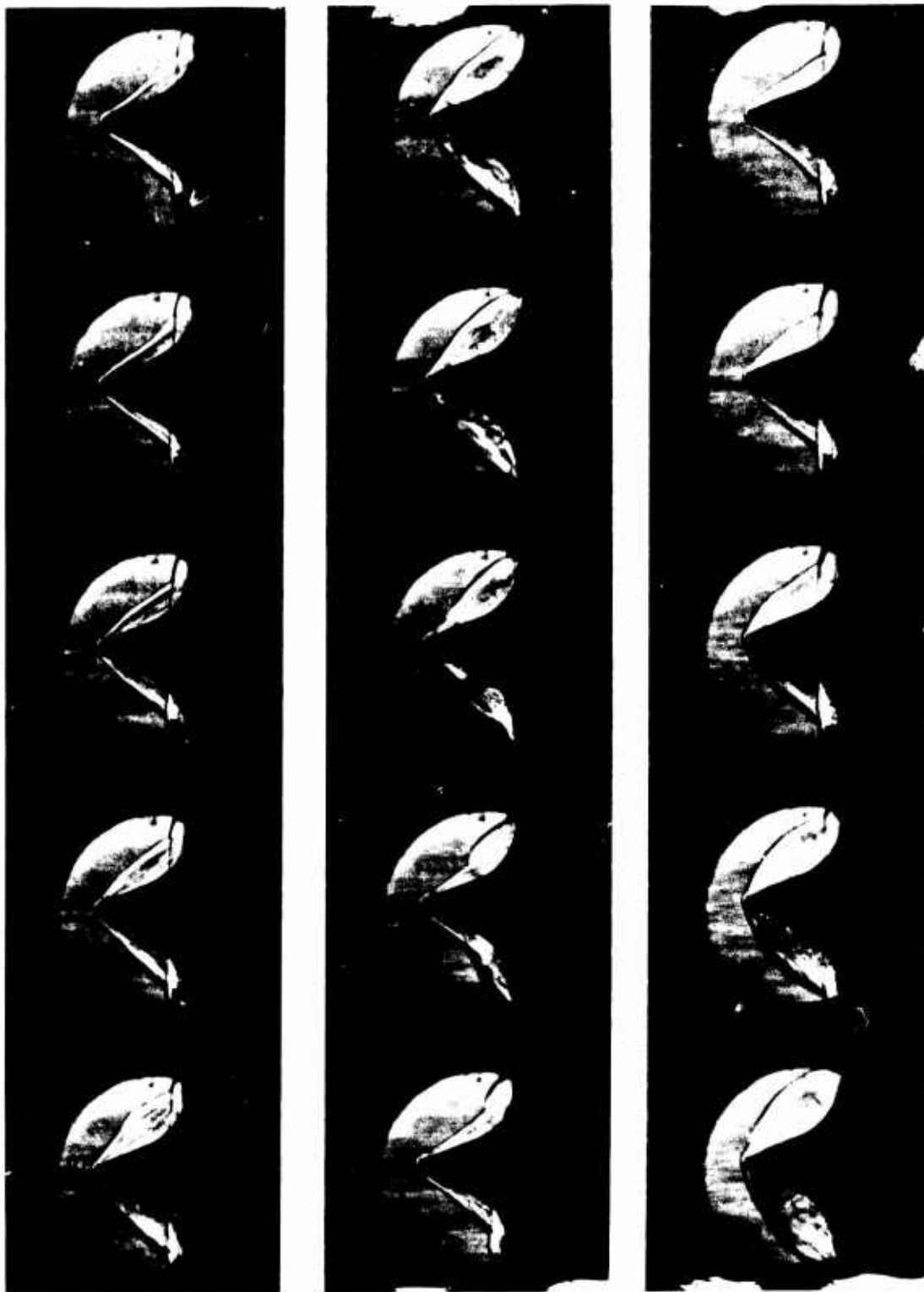


Figure 43 MINI "E" OSCILLATION OVER THE A2 CONFIGURATION



Figure 44 STEADY FLOW OVER THE A3 CONFIGURATION

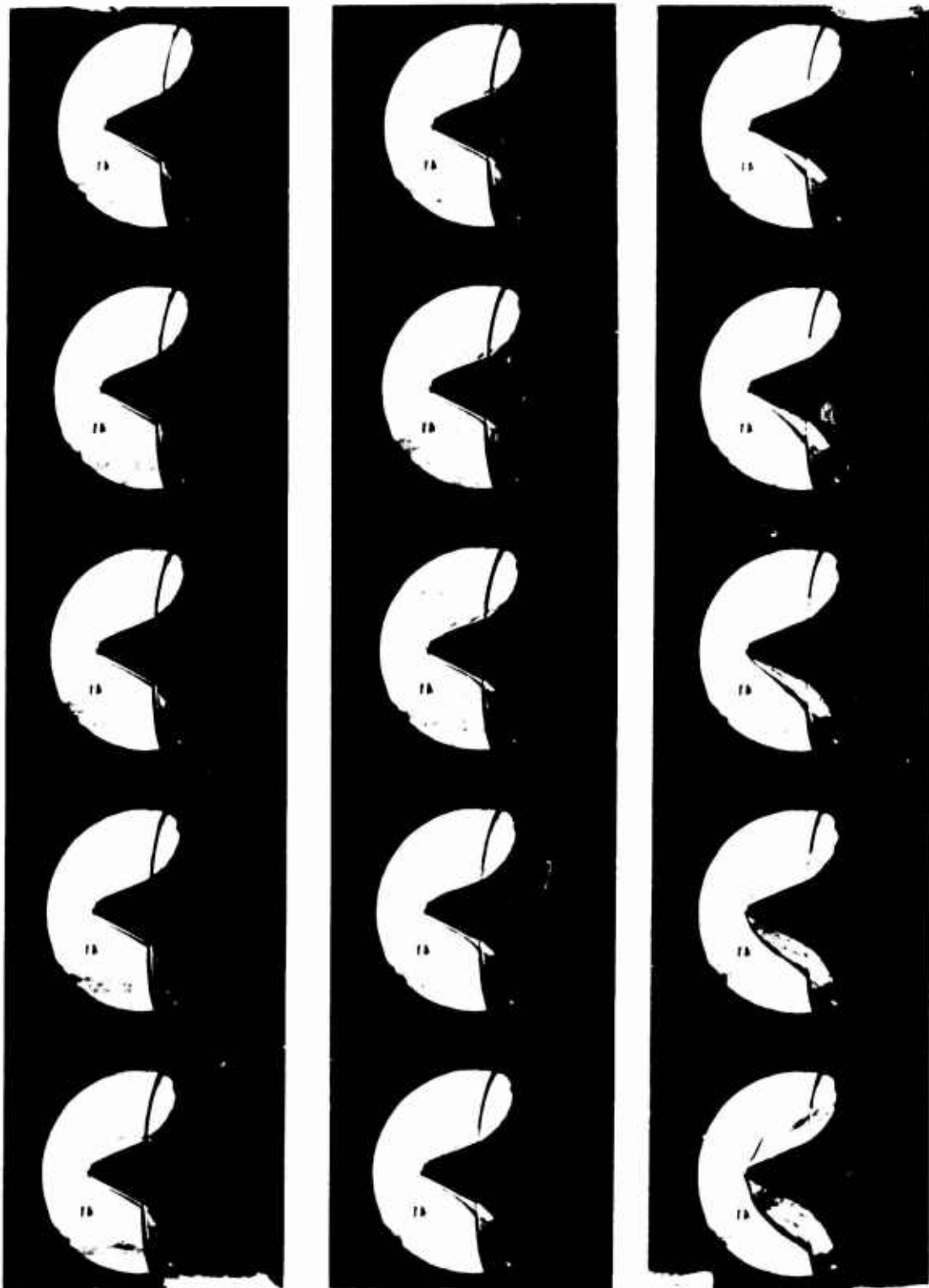


Figure 45 MINI "E" OSCILLATION OVER THE A4 CONFIGURATION

Thus, nose tip configuration A1, A2, A3 and A4 have geometries which induce flow fields which lie close to the oscillation boundaries as shown in Figure 25. However, the flow over the A0 configuration is fully pulsating in the E mode, and this is the configuration over which detailed heat transfer and pressure measurements were obtained.

3.4 DETAILED MEASUREMENTS ON THE A0 CONFIGURATION

The A0 configuration was fully instrumented with high frequency response pressure and heat transfer gages. In addition to placing a high density of instrumentation along the 0° ray, measurements of heat transfer and pressure were made on rays inclined at 120 and 240 degrees to this principal axis, as shown in Figure 47. In this way, we were able to effectively investigate flow asymmetries which result from asymmetric transition or angle of attack effects. A photographic sequence showing the flow over the A0 configuration at zero angle of attack is shown in Figure 48. Here we see the sequence of events in which the bow shocks from the tip and the afterbody intersect at the tip-afterbody junction producing a pressure rise which the boundary layer cannot sustain without separation taking place. The separation point moves forward to the nose tip and, because it is impossible to establish an equilibrium separated shear layer between the tip and the shoulder of the model, the separation point overshoots the nose. The resulting flow field is one with a large bow shock standing off the entire configuration. This bow shock collapses back to the model surface causing the entire sequence to be repeated. Extremely large heat transfer rates are generated by shock-boundary layer interaction and shock-shock interaction which occur at the junction between the fore- and after-body. During the initial formation of the separated region at a time when a strong oblique shock is formed at the forebody-afterbody junction, see Figures 48 and 49 severe heating is observed at the base of this shock. As the separated region grows, we observe the formation of a shear layer at the intersection between the fore-body and after-body shocks. The heat transfer rates which are generated in the region where this shear layer attaches to the surface of the

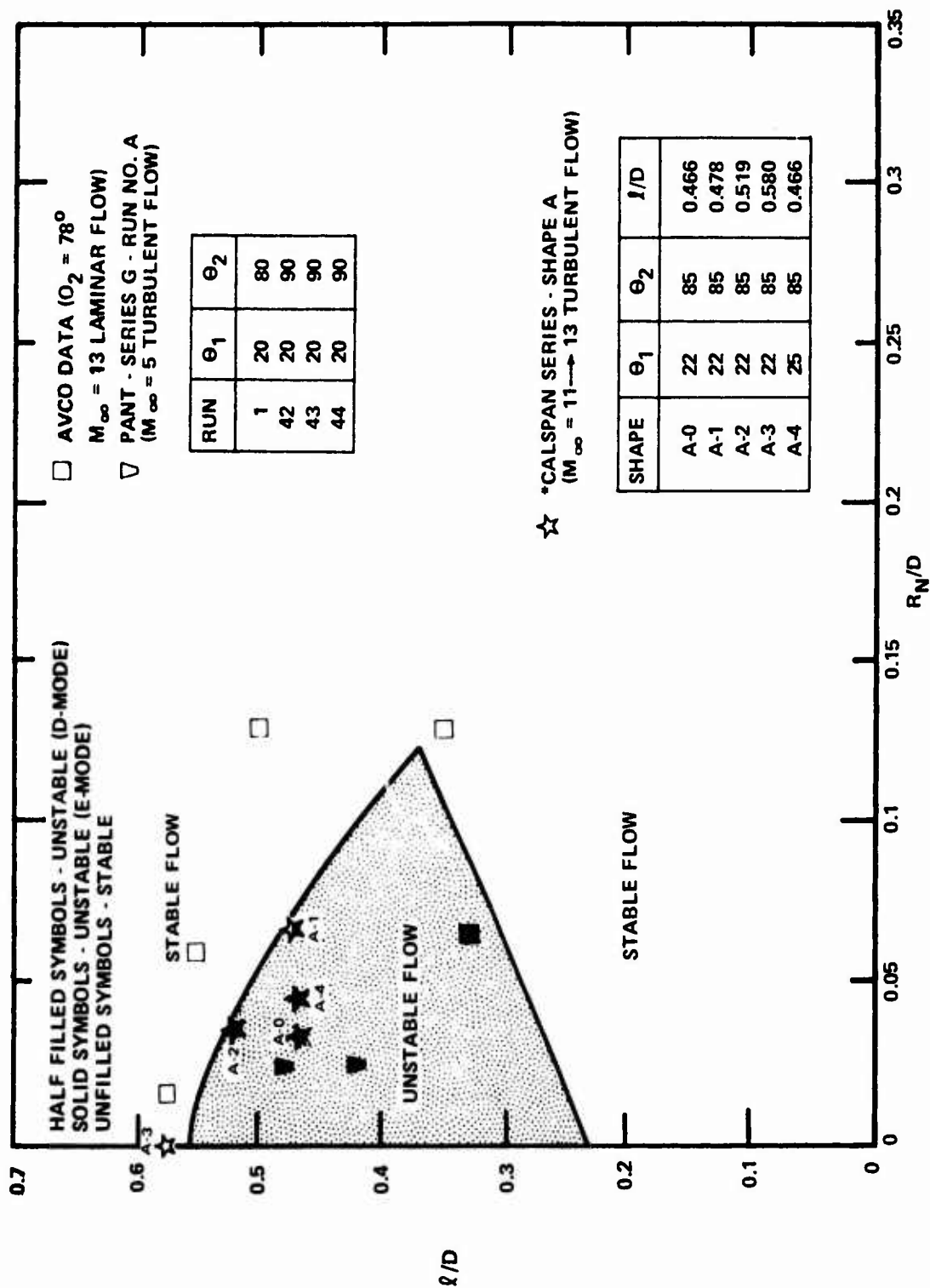
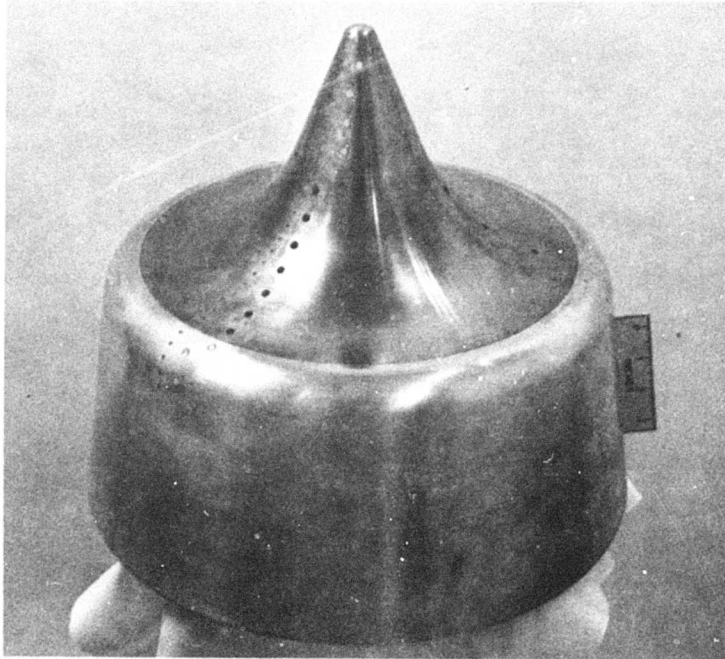


Figure 46 OSCILLATION BOUNDARIES ON HIGHLY INDENTED NOSE SHAPES



(a) AO CONFIGURATION



(b) A1 CONFIGURATION

Figure 47 TWO OF THE MODELS FROM THE "A" SERIES TEST PROGRAM

Table 4
TEST CONDITIONS FOR FULLY INSTRUMENTED AO CONFIGURATIONS

RUN NO.	1	2	3	4	5	6	7
M(I)	3.776E+00	3.665E+00	3.386E+00	3.268E+00	3.702E+00	3.663E+00	3.494E+00
P(O)	1.653E+04	1.608E+04	6.067E+03	1.704E+04	1.867E+04	1.839E+04	1.618E+04
H(O)	2.192E+07	2.089E+07	1.646E+07	1.739E+07	2.126E+07	2.125E+07	1.979E+07
T(O)	3.326E+03	3.159E+03	2.633E+03	2.737E+03	3.238E+03	3.240E+03	3.046E+03
M	1.293E+01	1.300E+01	1.049E+01	1.131E+01	1.300E+01	1.302E+01	1.306E+01
U	6.528E+03	6.374E+03	5.955E+03	5.789E+03	6.429E+03	6.428E+03	6.204E+03
T	1.060E+02	9.992E+01	1.244E+02	1.089E+02	1.017E+02	1.014E+02	9.362E+01
P	8.031E-02	7.739E-02	7.868E-02	2.039E-01	7.985E-02	7.761E-02	6.753E-02
Q	9.412E+00	9.169E+00	6.538E+00	1.829E+01	9.453E+00	9.216E+00	8.073E+00
RHD	6.360E-05	6.499E-05	5.309E-05	1.572E-04	6.586E-05	6.423E-05	6.040E-05
ML	8.914E-06	6.407E-06	1.045E-07	9.153E-09	8.559E-08	8.531E-08	7.693E-08
RE/FT.	4.658E+06	4.928E+06	3.025E+06	9.943E+06	4.947E+06	4.840E+06	4.748E+06
PITOT	1.750E+01	1.703E+01	1.212E+01	3.387E+01	1.757E+01	1.712E+01	1.498E+01
T*	9.706E+02	9.370E+02	6.721E+02	8.352E+02	9.492E+02	9.514E+02	9.057E+02
MU*	5.871E-07	5.734E-07	5.460E-07	5.300E-07	5.784E-07	5.793E-07	5.603E-07
SQRT.C*	8.480E-01	8.526E-01	8.631E-01	8.686E-01	8.510E-01	8.507E-01	8.575E-01
H(W)	3.177E+06	3.177E+06	3.201E+06	3.213E+06	3.163E+06	3.213E+06	3.231E+06
T(W)	5.290E+02	5.290E+02	5.330E+02	5.350E+02	5.300E+02	5.350E+02	5.380E+02

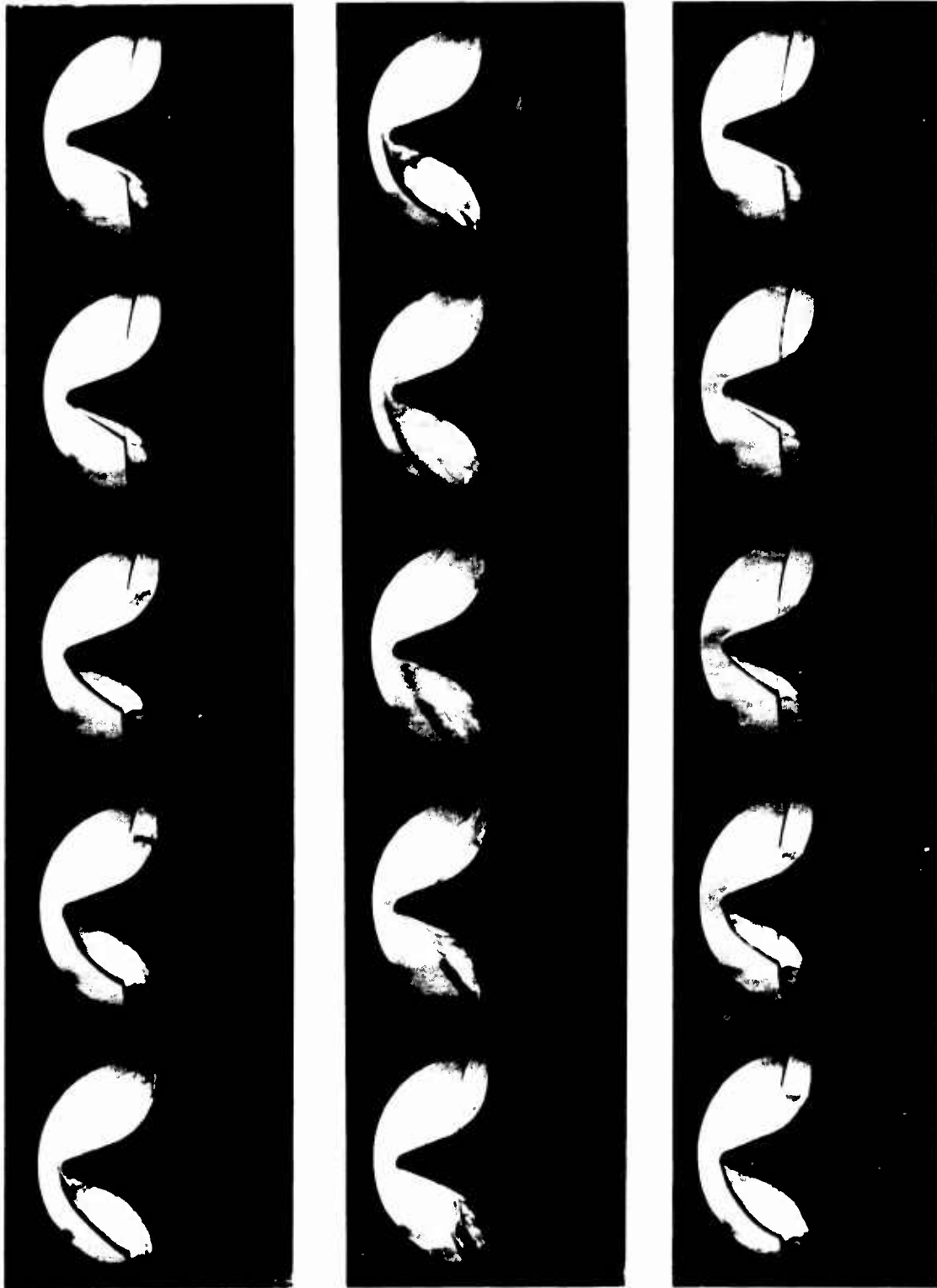


Figure 48 "E" OSCILLATION ON AO CONFIGURATION AT ZERO ANGLE OF ATTACK

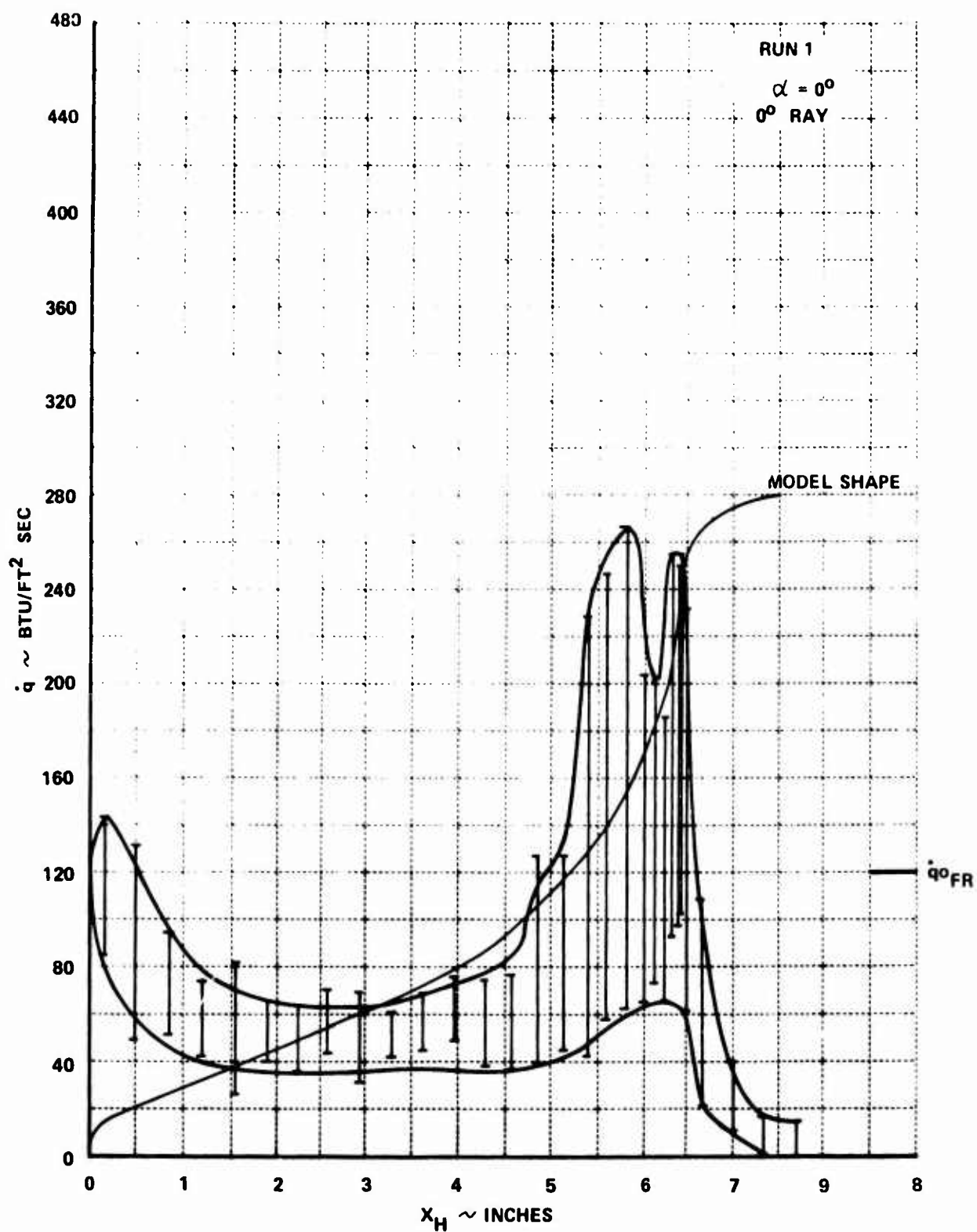


Figure 49a HEAT TRANSFER MEASUREMENTS ON THE AO CONFIGURATION AT MACH 13

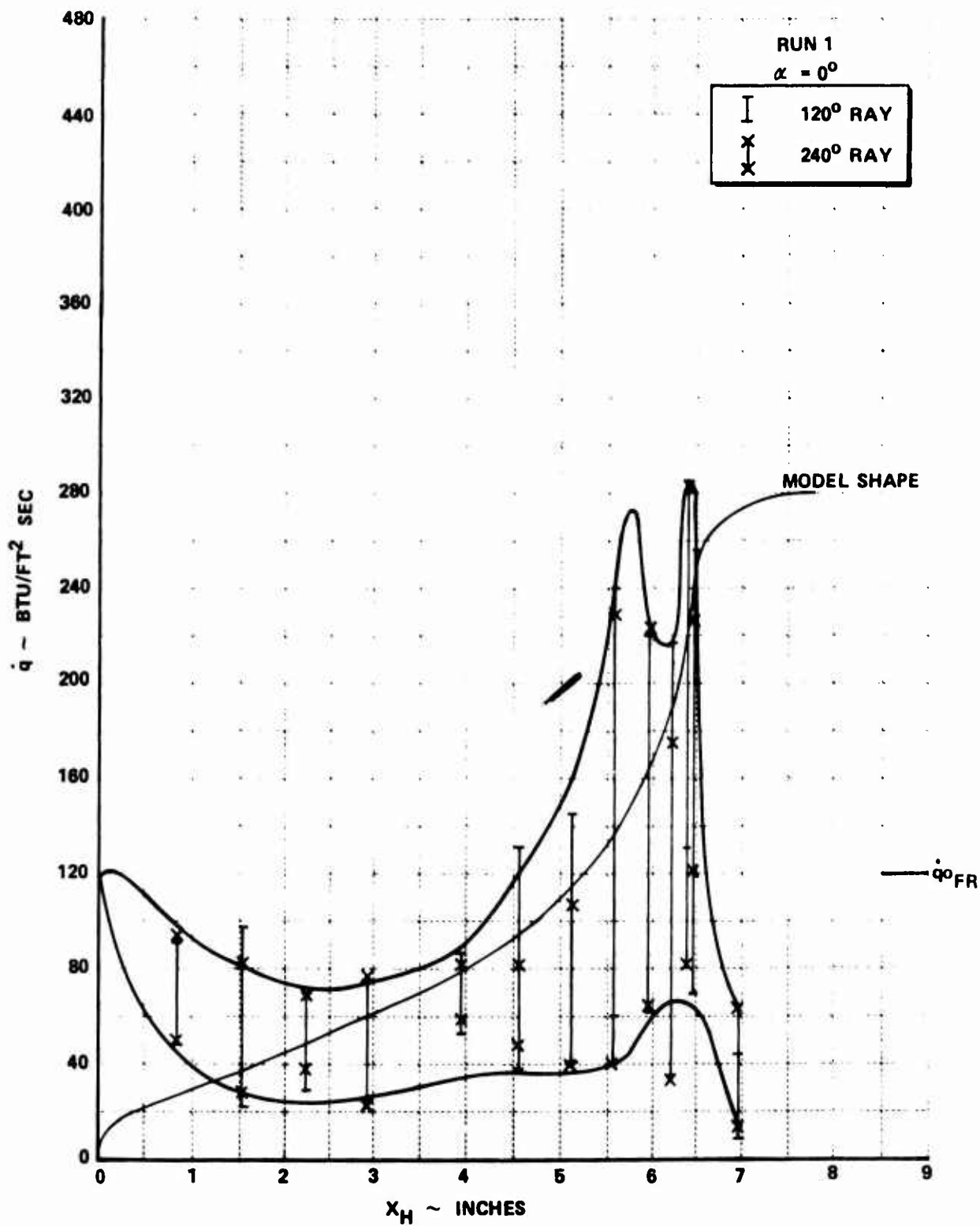


Figure 49a HEAT TRANSFER MEASUREMENTS ON THE AO CONFIGURATION AT MACH 13 (Continued)

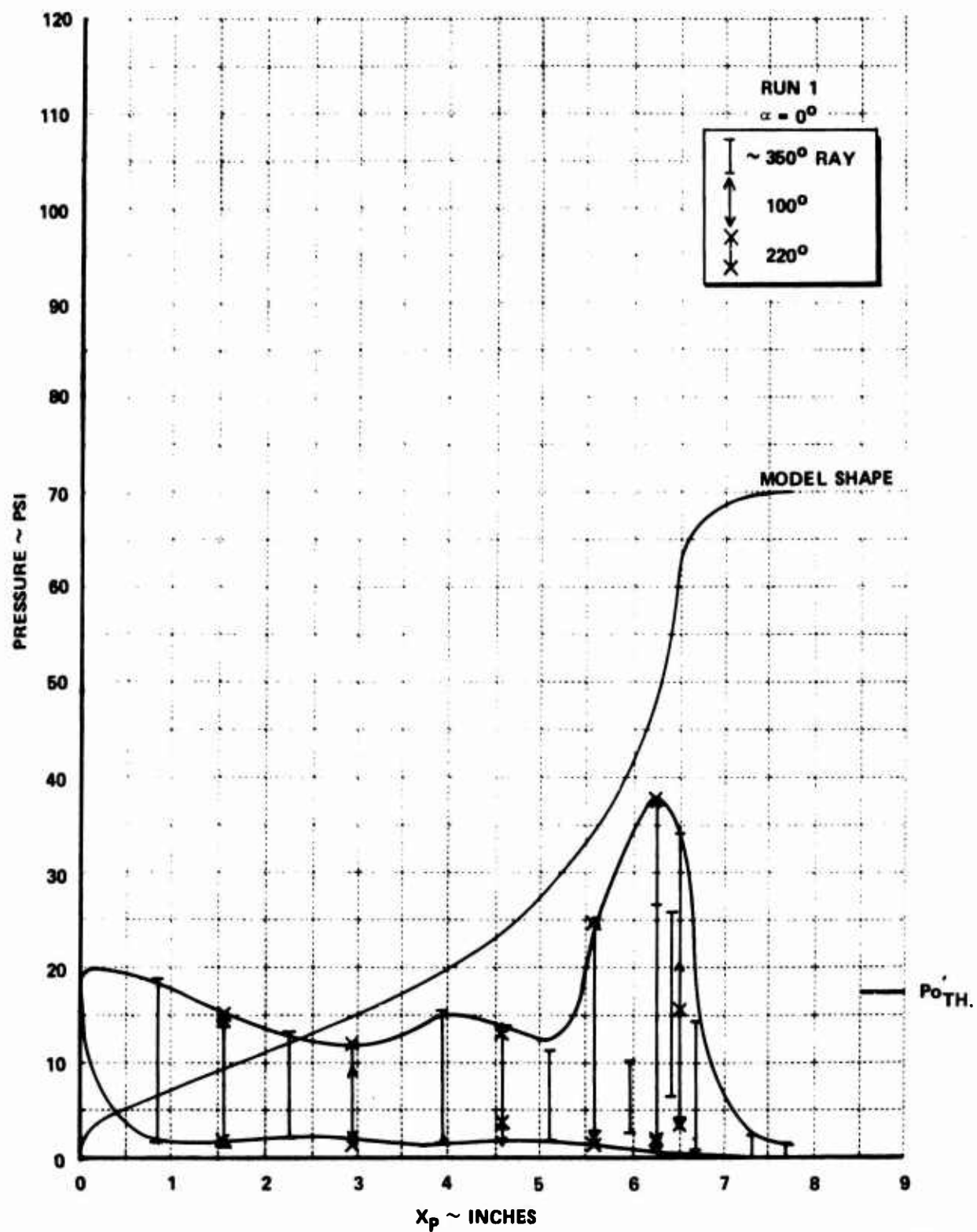


Figure 49b PRESSURE TRANSFER MEASUREMENTS ON THE AO CONFIGURATION AT MACH 13

nose tip exceed those to the stagnation region of a sphere with the same diameter as the nose and after-body by factors of 3 and 5 respectively. The typical outputs of heat transfer and pressure gages positioned in the junction region are shown in Fig. 50. We see the heat transfer rate varies between a peak value resulting from the shock-boundary layer and shock-shock interaction to a minimum value corresponding to the flow configuration where the bow shock is standing off the nose tip. Further distribution of heating and pressure over the AO configuration at a series of times during one cycle of the E oscillation is illustrated in Figs. 51 and 52. It is clear that the very large heating rates at the center section of the model would lead to large non-equilibrium distortions in the shape of an ablating nose tip. The structure and frequency of the oscillatory flow field over the AO configuration showed little sensitivity to Reynolds number or Mach number although introducing 5 mil roughness did slightly modify its amplitude. However the supporting of this model at an angle of attack induced a flow oscillation which was asymmetric in character and exhibited two distinct modes of oscillation.

The asymmetric flow about the AO configuration at an angle of attack of 4.5° is shown in Fig. 53. We see that the basic mode is a relatively symmetric E oscillation, however, during the period when the flow on the windward side of the nose tip undergoes one cycle, the flow on the windward side undergoes two such cycles. Thus, one asymmetric E cycle occurs during every symmetric E cycle. Significant asymmetric pressure and heating loads are created by the oscillation as indicated by the distributions shown in Fig. 54. This asymmetry is a maximum at the time when the flow on the windward side is attached and the bow shock has been forced to move just beyond the tip by flow separation on the leeward side. Thus, considerable side forces are generated which in addition to causing a pitching momentum at the nose tip, exerts severe bending moments which could possibly lead to nose tip fracture.

3.5 DETAILED STUDIES ON THE PANT 1 CONFIGURATION

While high speed movies and isolated pressure measurements were made

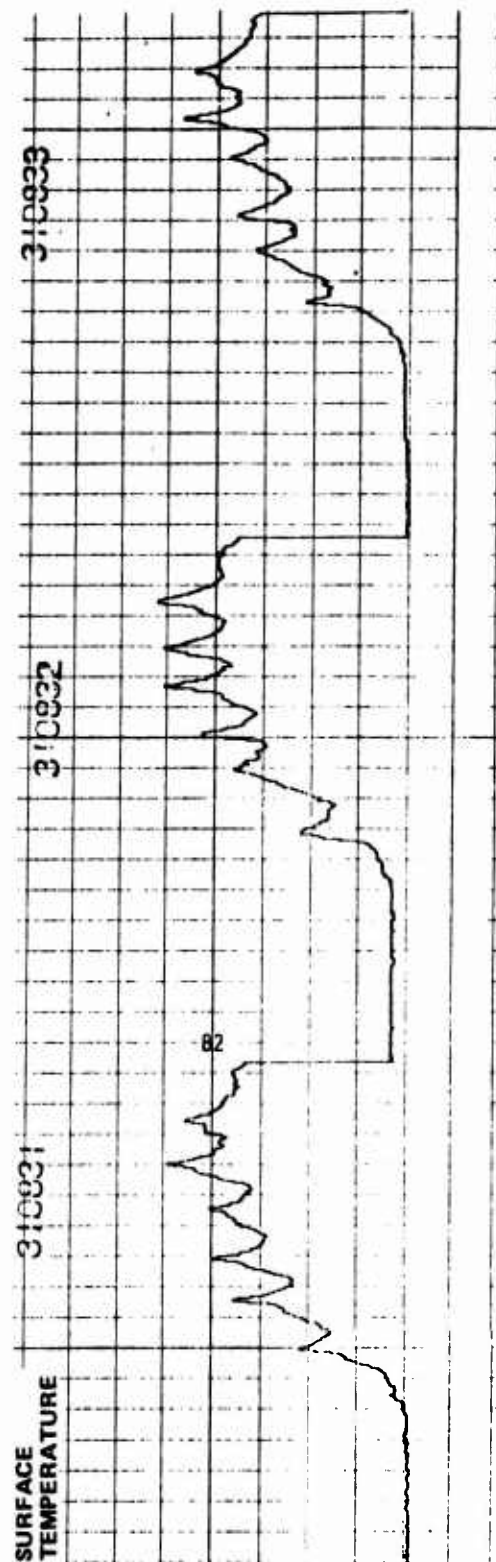
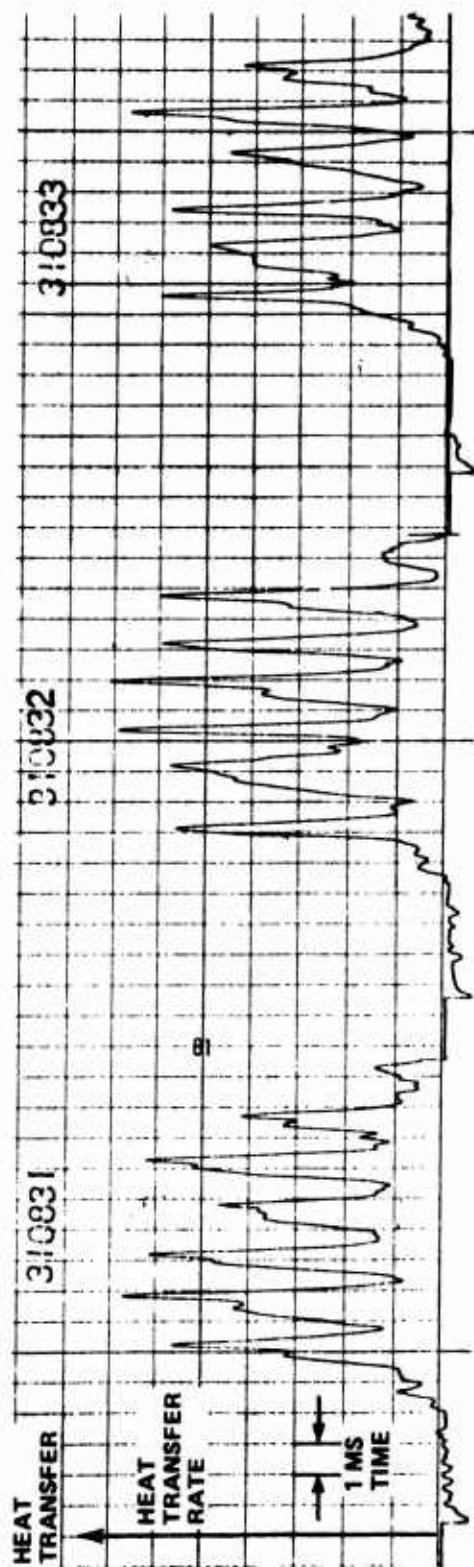


Figure 50 TYPICAL HEAT TRANSFER RECORDS FROM THIN FILM GAGE ON THE AO CONFIGURATION

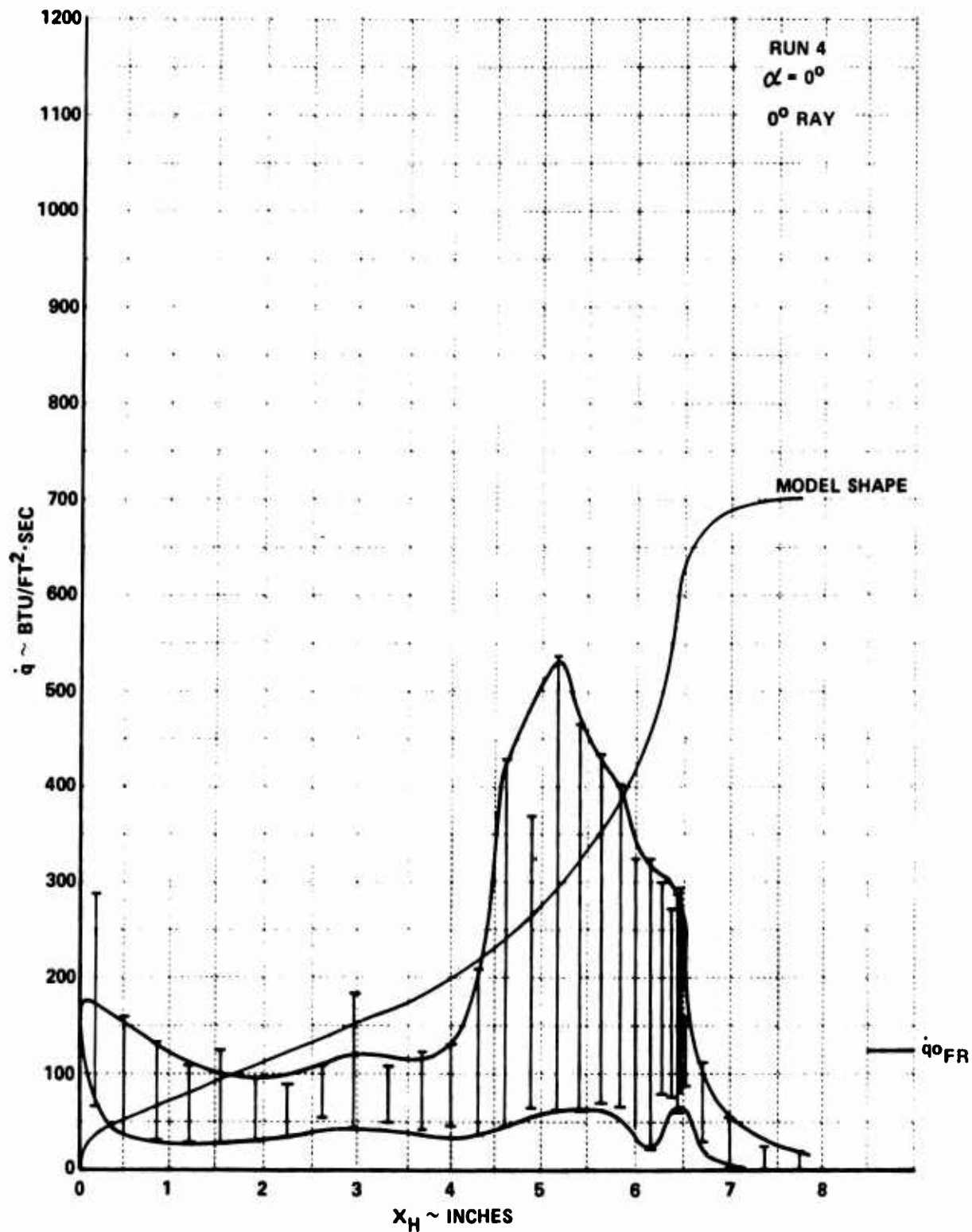


Figure 51a HEAT TRANSFER MEASUREMENTS ON THE AO CONFIGURATION AT MACH 11

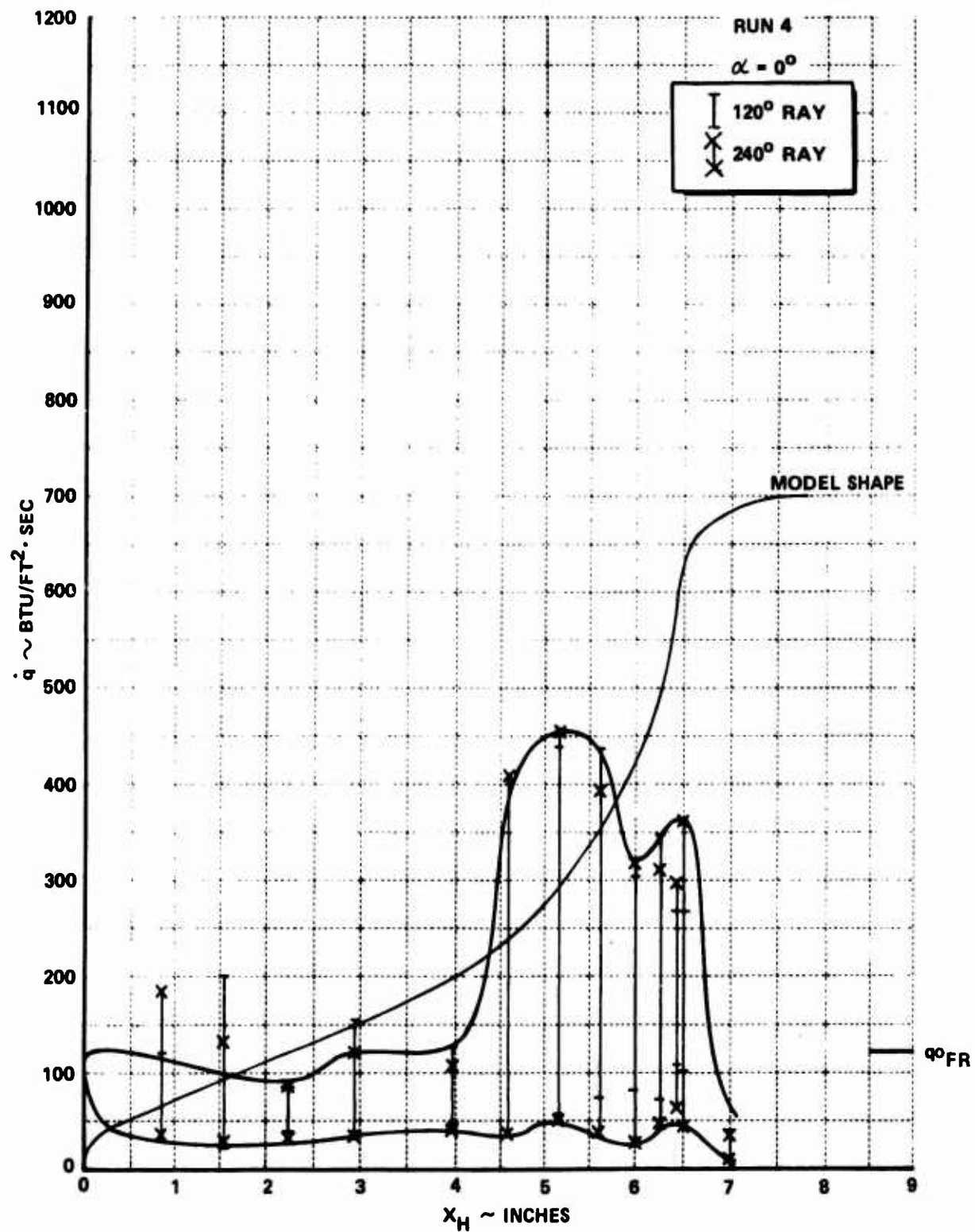


Figure 51a HEAT TRANSFER MEASUREMENTS ON THE AO CONFIGURATION AT MACH 11
 (Continued)

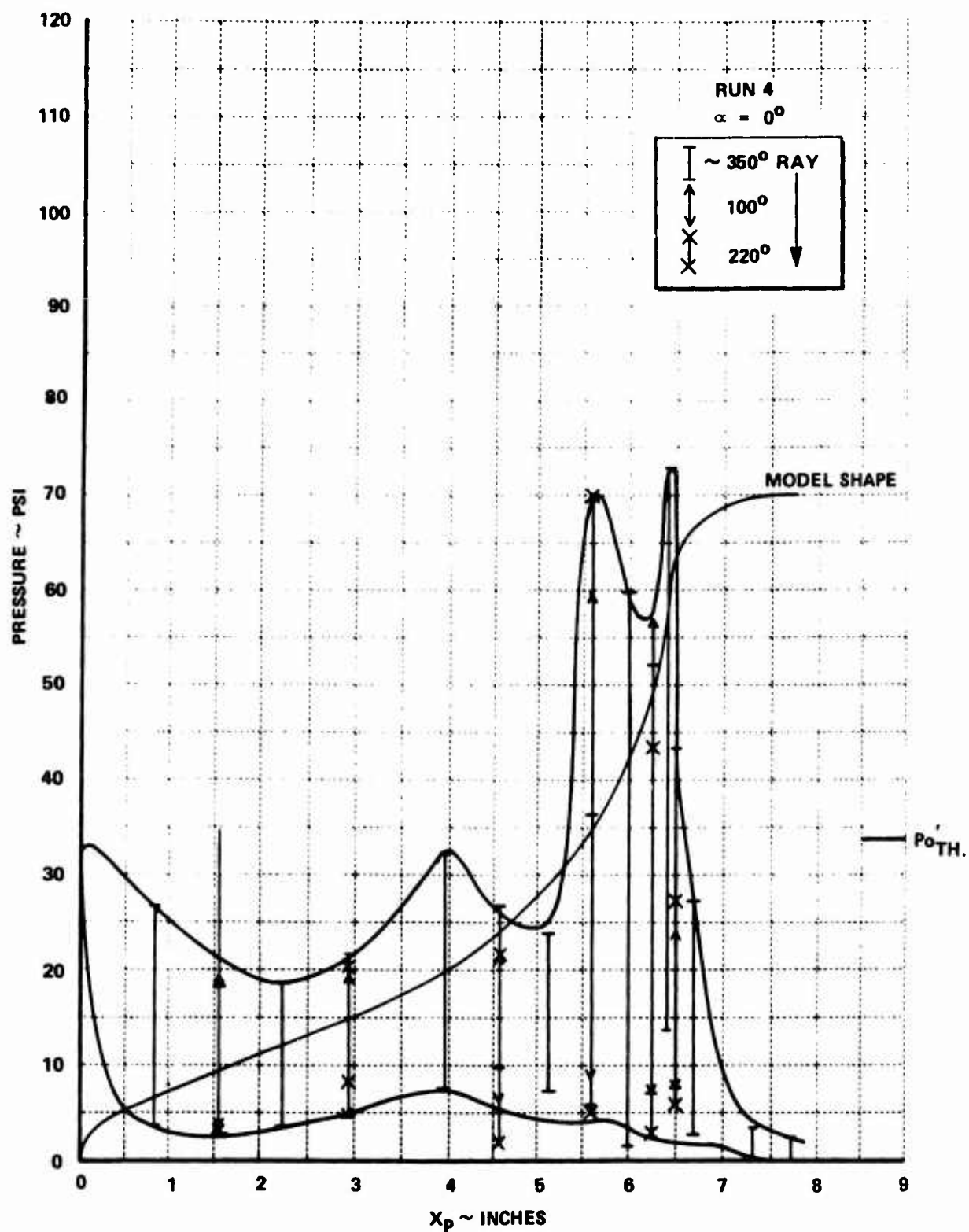


Figure 51b PRESSURE TRANSFER MEASUREMENTS ON THE AO CONFIGURATION AT MACH 11

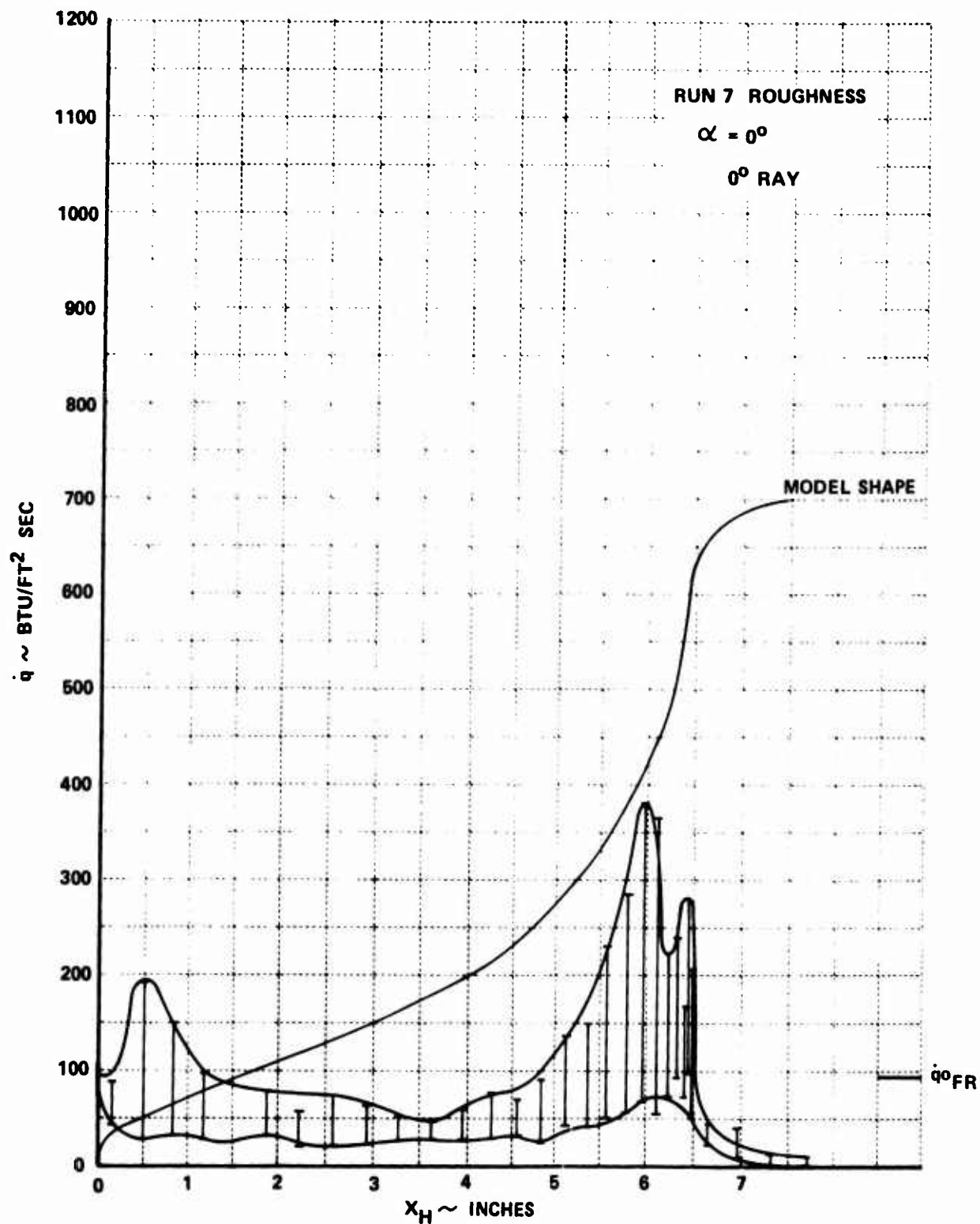


Figure 52a EFFECTS OF ROUGHNESS ON THE HEAT TRANSFER MEASUREMENTS ON THE AO CONFIGURATION AT MACH 13

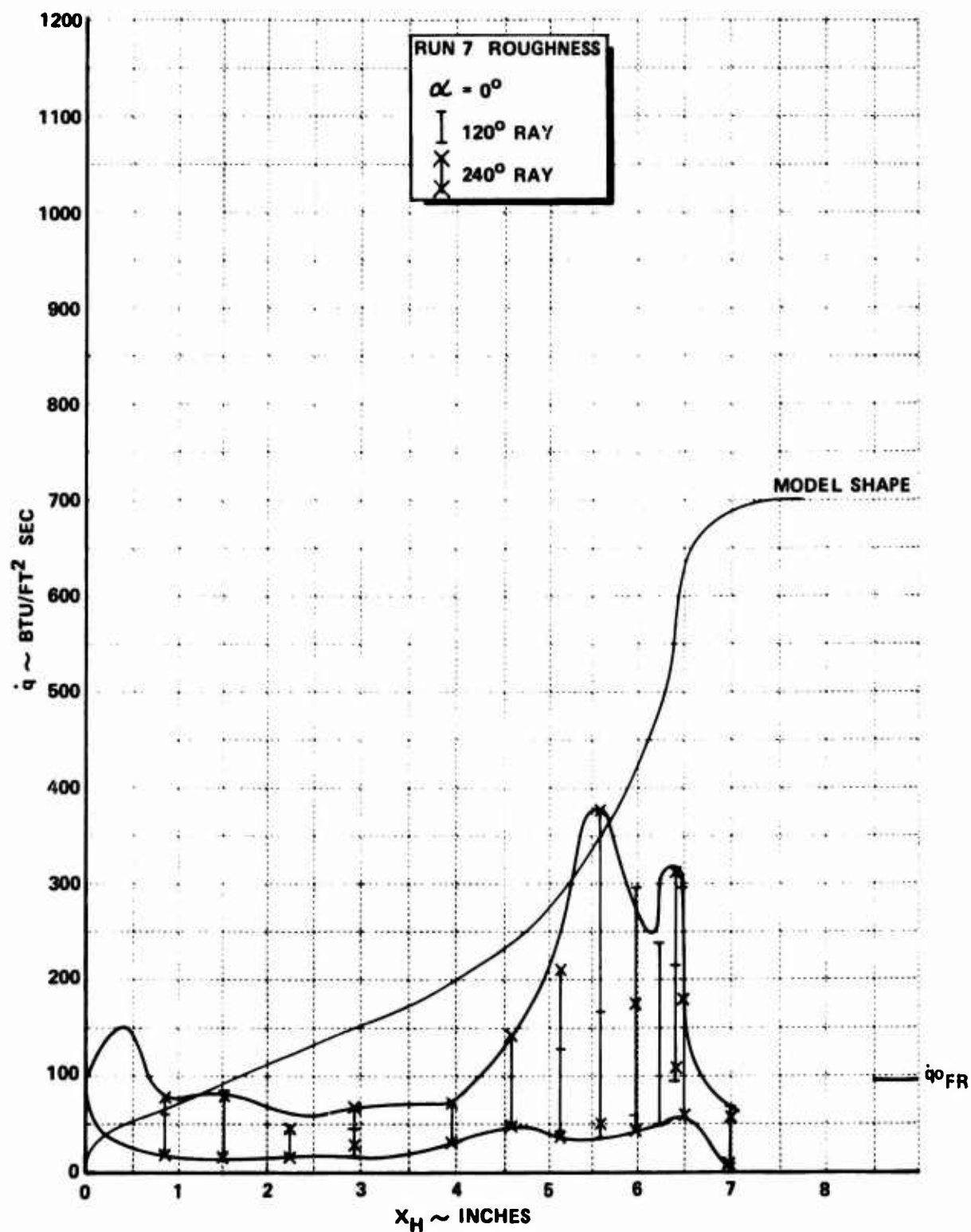


Figure 52a EFFECTS OF ROUGHNESS ON THE HEAT TRANSFER MEASUREMENTS ON THE AO CONFIGURATION AT MACH 13 (Continued)

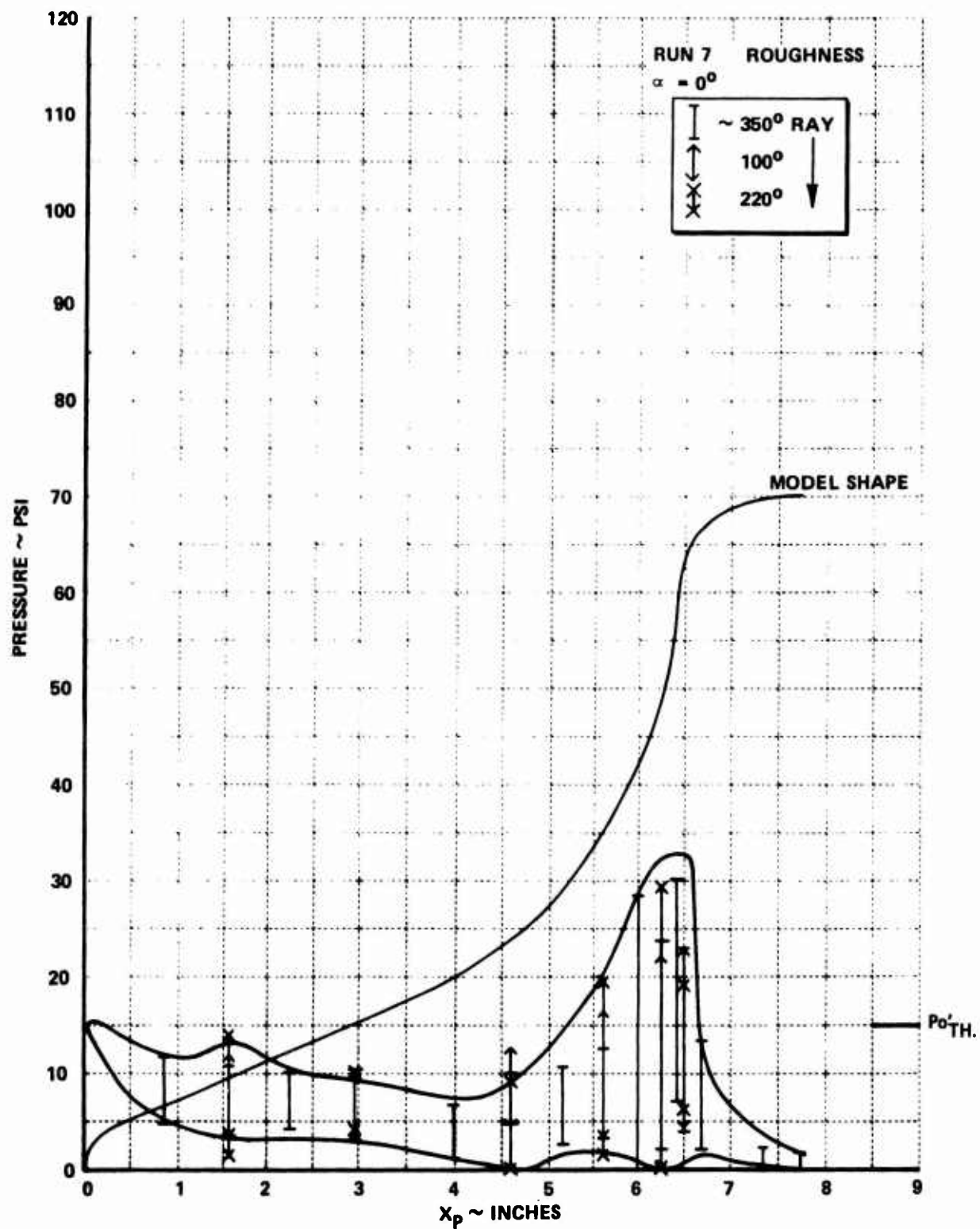


Figure 52b EFFECTS OF ROUGHNESS ON THE PRESSURE TRANSFER MEASUREMENTS ON THE AO CONFIGURATION AT MACH 13



Figure 53 ASYMMETRIC OSCILLATION ON THE AO CONFIGURATION AT
3.5° ANGLE OF ATTACK



Figure 53 (Continued)

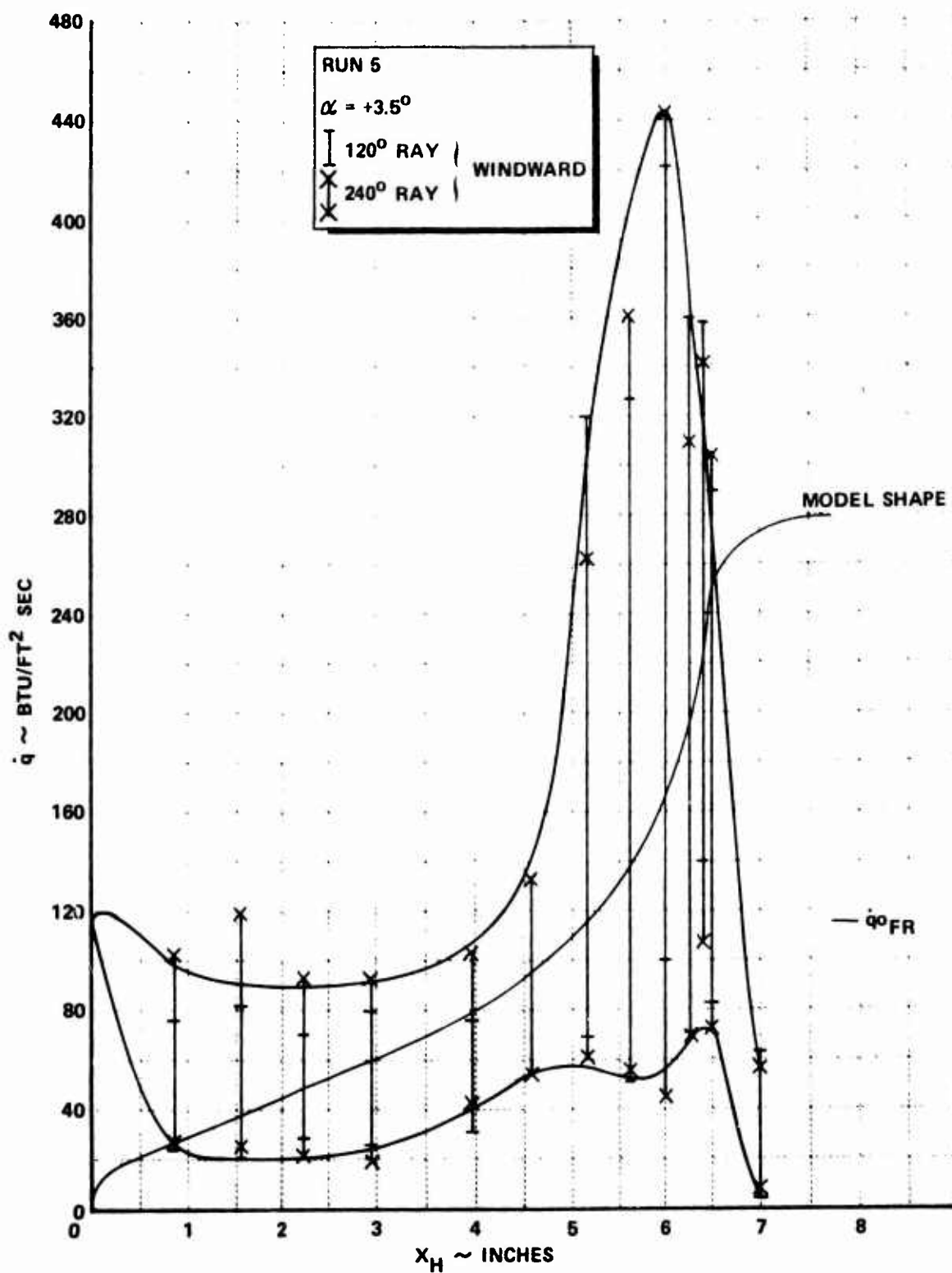


Figure 54a EFFECTS OF ANGLE-OF-ATTACK ON THE HEAT TRANSFER MEASUREMENTS ON THE AO CONFIGURATION AT MACH 13

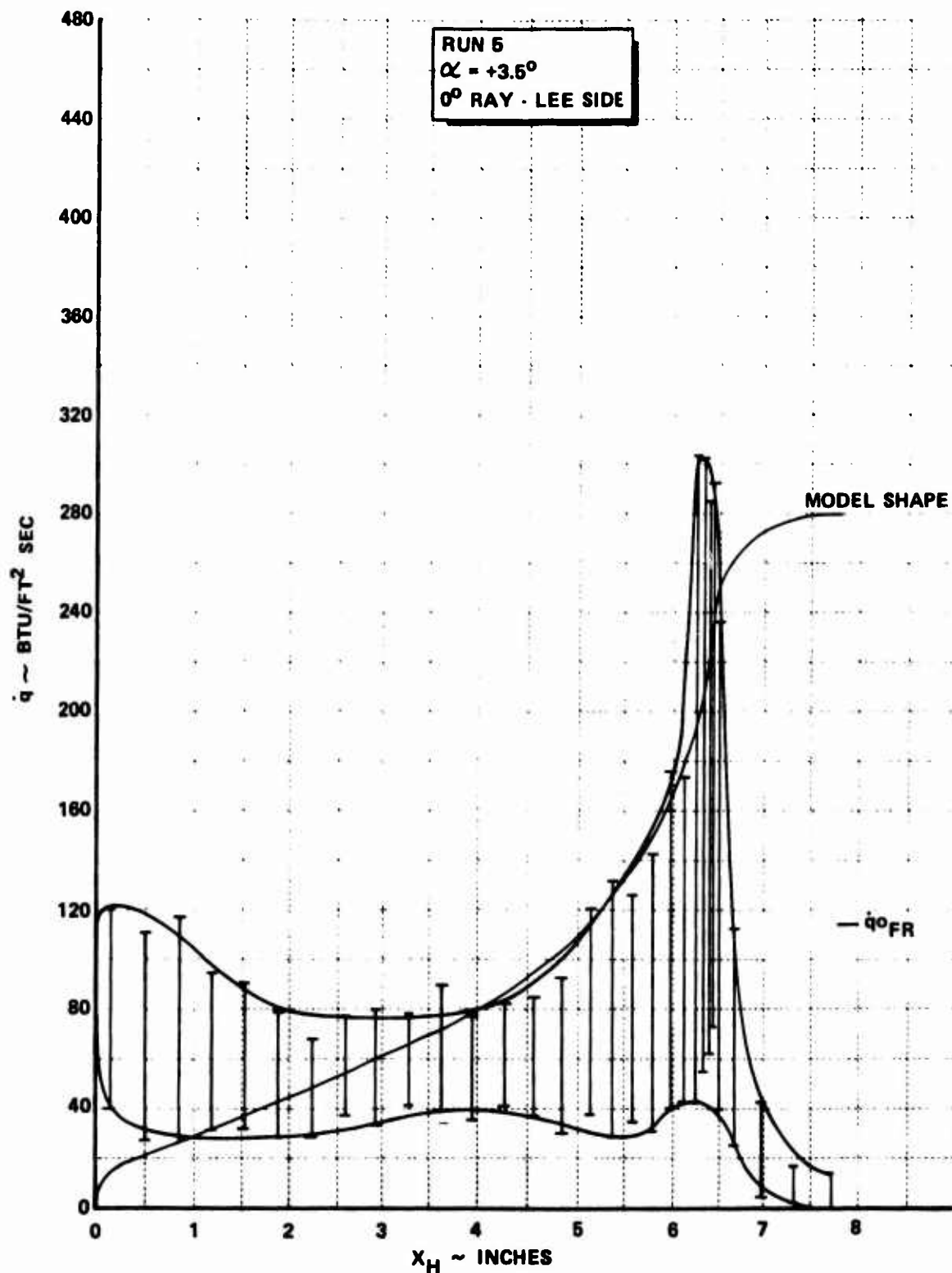


Figure 54a EFFECTS OF ANGLE-OF-ATTACK ON THE HEAT TRANSFER MEASUREMENTS ON THE AO CONFIGURATION AT MACH 13 (Continued)

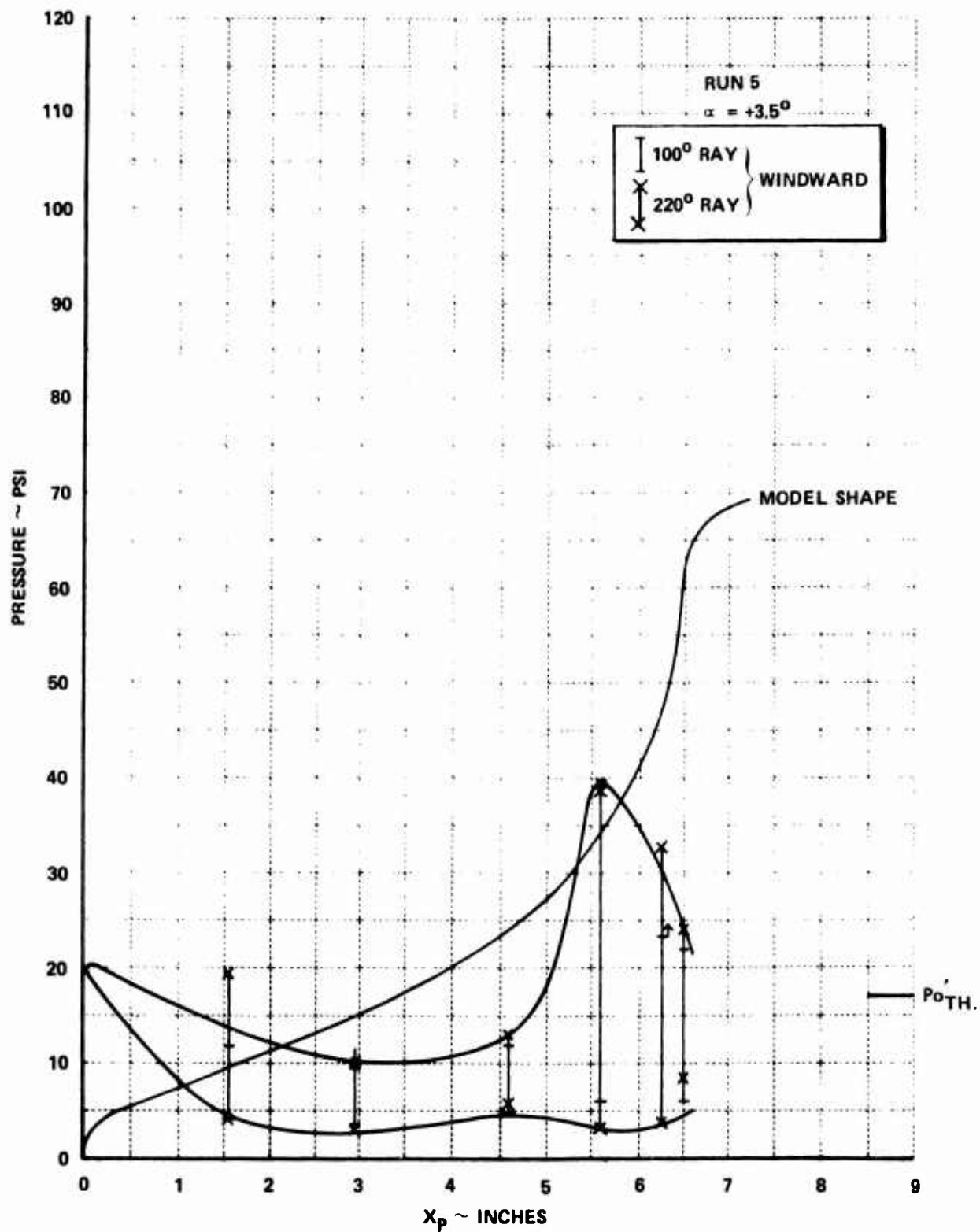


Figure 54b EFFECTS OF ANGLE-OF-ATTACK ON THE PRESSURE TRANSFER MEASUREMENTS ON THE AO CONFIGURATION AT MACH 13

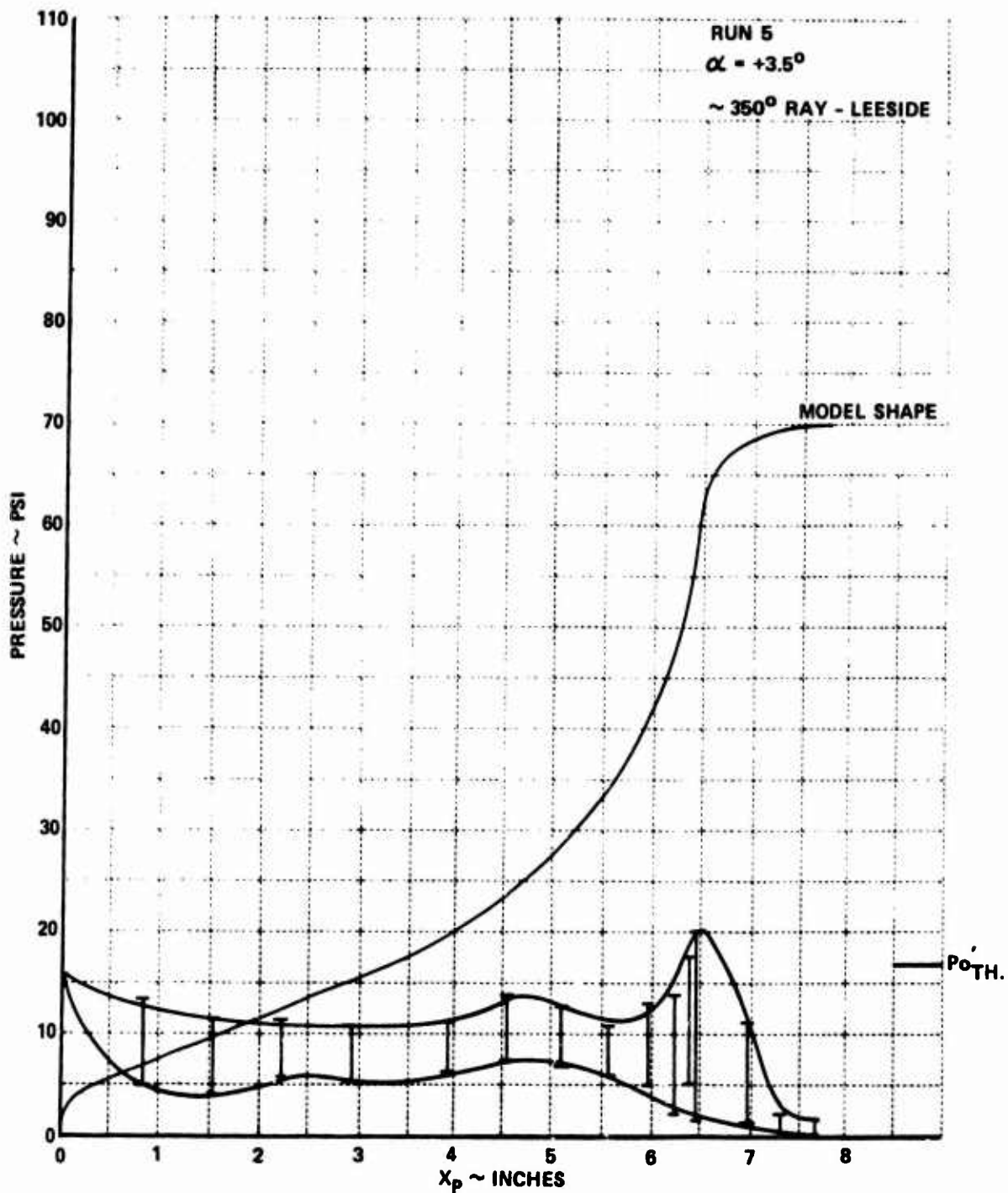


Figure 54b EFFECTS OF ANGLE-OF-ATTACK ON THE PRESSURE TRANSFER MEASUREMENTS
 ON THE AO CONFIGURATION AT MACH 13 (Continued)

during the PANT test series conducted by Aerotherm there were no detailed measurements of the heat transfer and pressure obtained. Of the various blunted bi-conic configurations studies in the PANT test matrix, the PANT 1 configuration perhaps best represents the geometry of highly ablated nose shapes obtained in ablation studies where gross instabilities were observed in the inviscid flow. Preliminary studies at Calspan had also revealed that under some circumstances significant flow asymmetries can develop over the PANT 1 configuration similar to those described above, for the A0 configuration at angle of attack. To detect flow asymmetries, pressure and heat transfer instrumentation was placed around the model circumference as well as along one major instrumentation ray. A photograph of the model and instrumentation is shown in Fig. 55. The studies over this configuration were conducted at Mach 11 and 13 over a range of Reynolds numbers so that laminar, transitional and turbulent flows could be investigated. A sequence of photographs taken from movies of the flow at Mach 11 & 13 are shown in Figs. 56, 57 and 58. We observe a full E oscillation for conditions where we believe the boundary layer is transitional over the body. Adding roughness did not markedly affect the major features of the oscillation, although some degree of flow asymmetry is induced presumably by asymmetric transition. The major fluid dynamic mechanisms responsible for the large heating rates observed on the model can be visualized with the aid of Figs. 56-62, the shock-shock interaction between the bow shocks from the forebody and the afterbody creates a shear layer which impinges on the face of the model. Originating close to the cone-afterbody junction, this shear layer is swept outward as the recirculation region formed over the cone drives the cone shock away from the surface. Finally the shear layer is driven to the afterbody shoulder and the air trapped in recirculation region formed between it and the now bulbous cone shock escapes rapidly. The bow shock collapses back to the afterbody surface and the entire sequence begins again. While at Mach 13 this sequence of events is not significantly modified by roughness, at Mach 11 introducing 5 mil roughness causes the separation point to be fixed close to the tip of the forebody. The flow instability which is observed under this condition resembled a strong "D" type oscillation similar but more violent than the flow oscillation over the A1 configuration. Again, we observe that the frequencies associated with

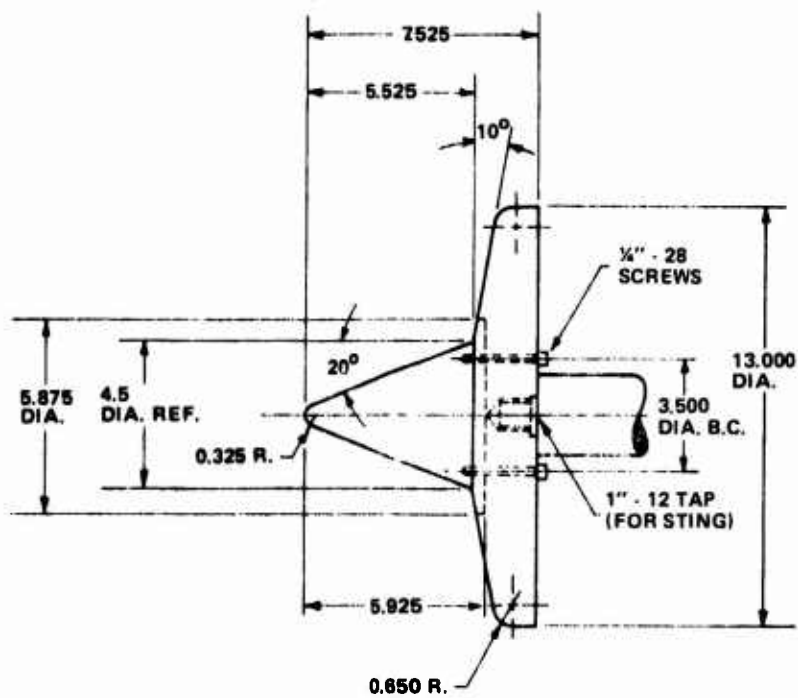
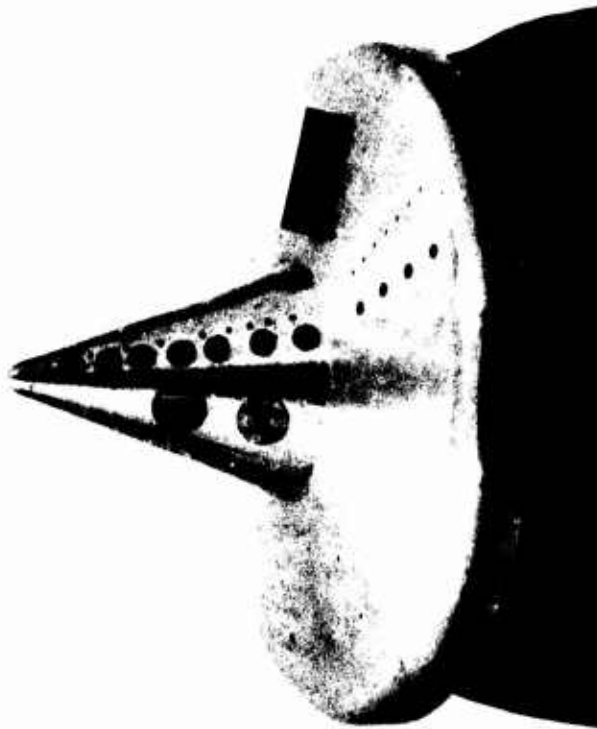


Figure 55 PANT 1 CONFIGURATION

Table 5
TEST CONDITIONS FOR PANT 1 TESTS

RUN NO.	54	55	56	57	58	59
ATTACK	0.0	0.0	0.0	0.0	1.000E+00	0.0
YAW	0.0	0.0	0.0	0.0	0.0	0.0
ROLL	0.0	0.0	0.0	0.0	0.0	0.0
M(I)	2.746E+00	3.705E+00	3.331E+00	5.286E+00	3.335E+00	3.554E+00
P(O)	1.894E+04	1.869E+04	1.792E+04	1.667E+04	1.771E+04	3.571E+03
H(O)	2.130E+07	2.129E+07	1.743E+07	1.723E+07	1.780E+07	1.965E+07
T(O)	3.241E+03	3.243E+03	2.743E+03	2.715E+03	2.795E+03	2.984E+03
M	1.297E+01	1.300E+01	1.132E+01	1.130E+01	1.131E+01	1.227E+01
U	6.435E+03	6.434E+03	5.796E+03	5.762E+03	5.856E+03	6.170E+03
T	1.023E+04	1.019E+02	1.091E+02	1.081E+02	1.115E+02	1.051E+02
P	8.220E-02	7.498E-02	2.170E-01	2.037E-01	2.124E-01	1.921E-02
Q	9.694E+00	9.465E+00	1.947E+01	1.823E+01	1.903E+01	2.028E+00
RHO	6.743E-05	6.585E-05	1.669E-04	1.582E-04	1.598E-04	1.534E-05
MU	8.606E-08	8.574E-08	9.177E-08	9.091E-08	9.381E-08	8.840E-08
RE/FT.	5.042E+00	4.942E+00	1.054E+07	1.003E+07	9.975E+00	1.071E+06
PITOT	1.801E+01	1.759E+01	3.605E+01	3.376E+01	3.525E+01	3.763E+00
T*	9.481E+02	9.503E+02	6.328E+02	8.277E+02	8.473E+02	8.994E+02
MU*	5.779E-07	5.788E-07	5.284E-07	5.267E-07	5.353E-07	5.576E-07
SQRT.C*	8.512E-01	8.509E-01	8.490E-01	8.491E-01	8.667E-01	8.581E-01
H(W)	3.153E+00	3.183E+06	3.165E+06	3.182E+06	3.195E+06	3.165E+06
T(W)	5.250E+02	5.300E+02	5.270E+02	5.300E+02	5.320E+02	5.270E+02
P(TS)	1.434E-04	1.354E-04	1.547E-04	1.547E-04	1.934E-04	9.670E-05

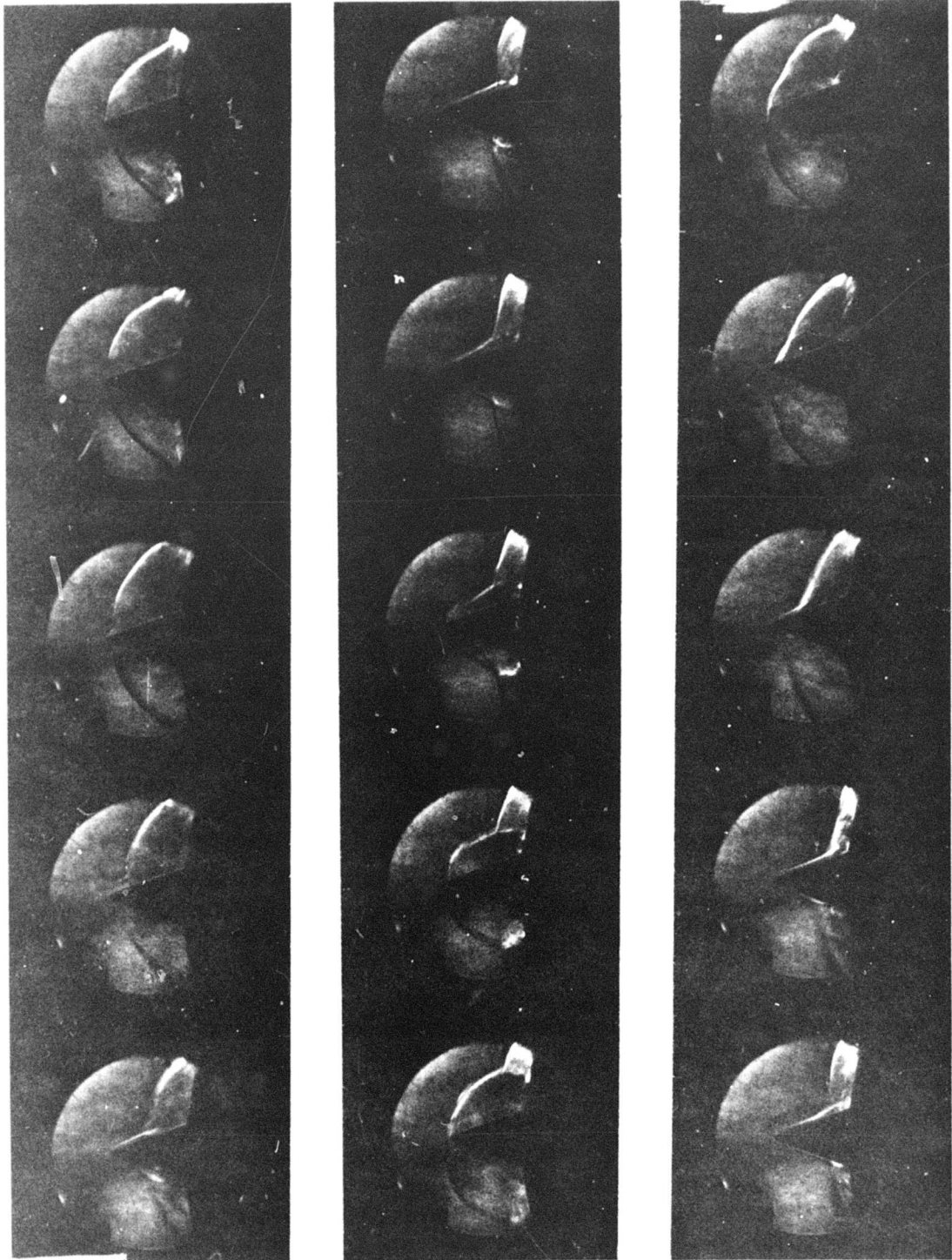


Figure 56 FULL E OSCILLATION OVER SMOOTH PANT 1 CONFIGURATION

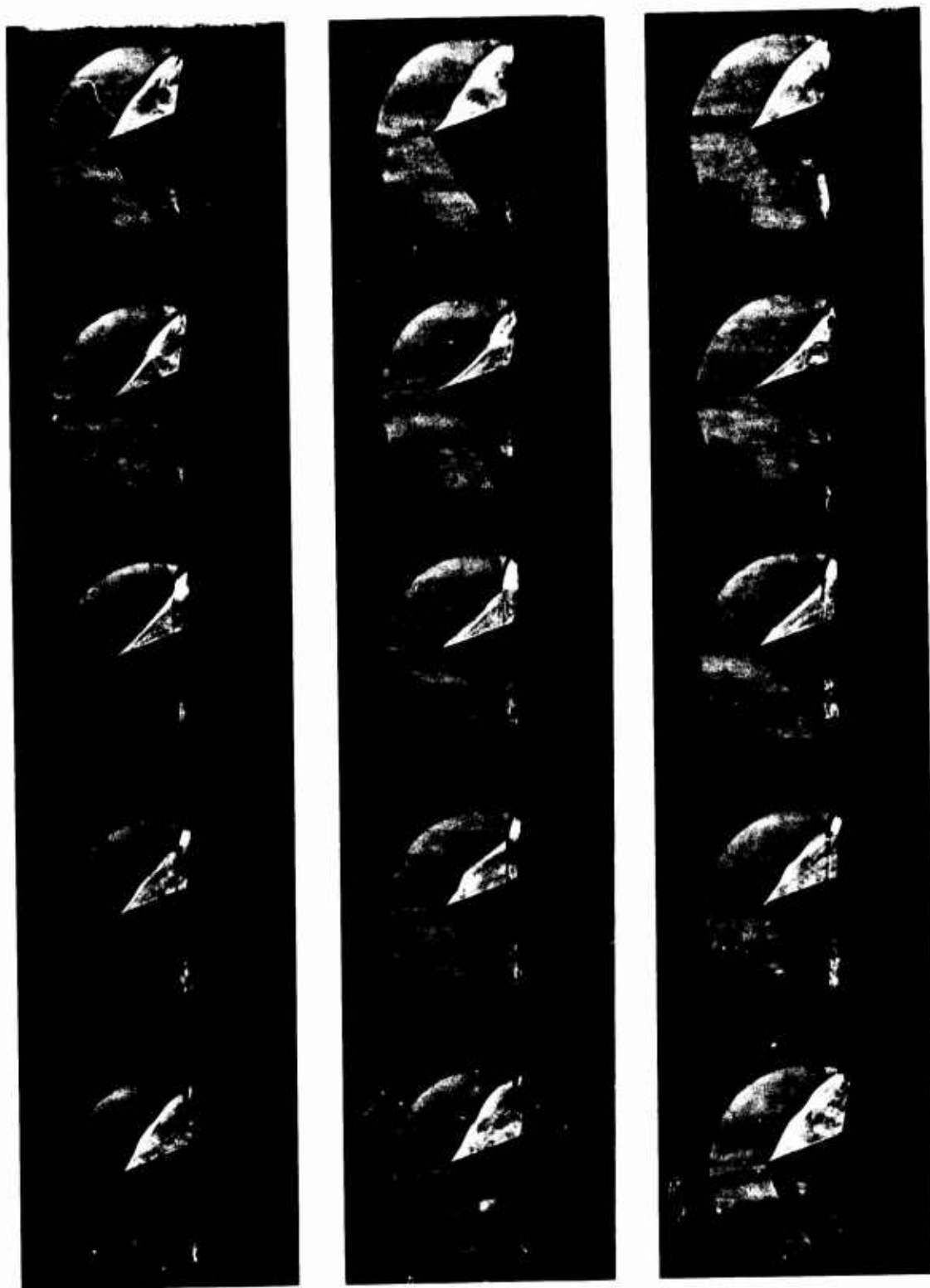


Figure 57 "D" OSCILLATION OVER PANT 1 CONFIGURATION WITH ROUGHNESS



Figure 58 FLOW ASYMMETRIES IN THE FLOW ABOUT ROUGH PANT SHAPE

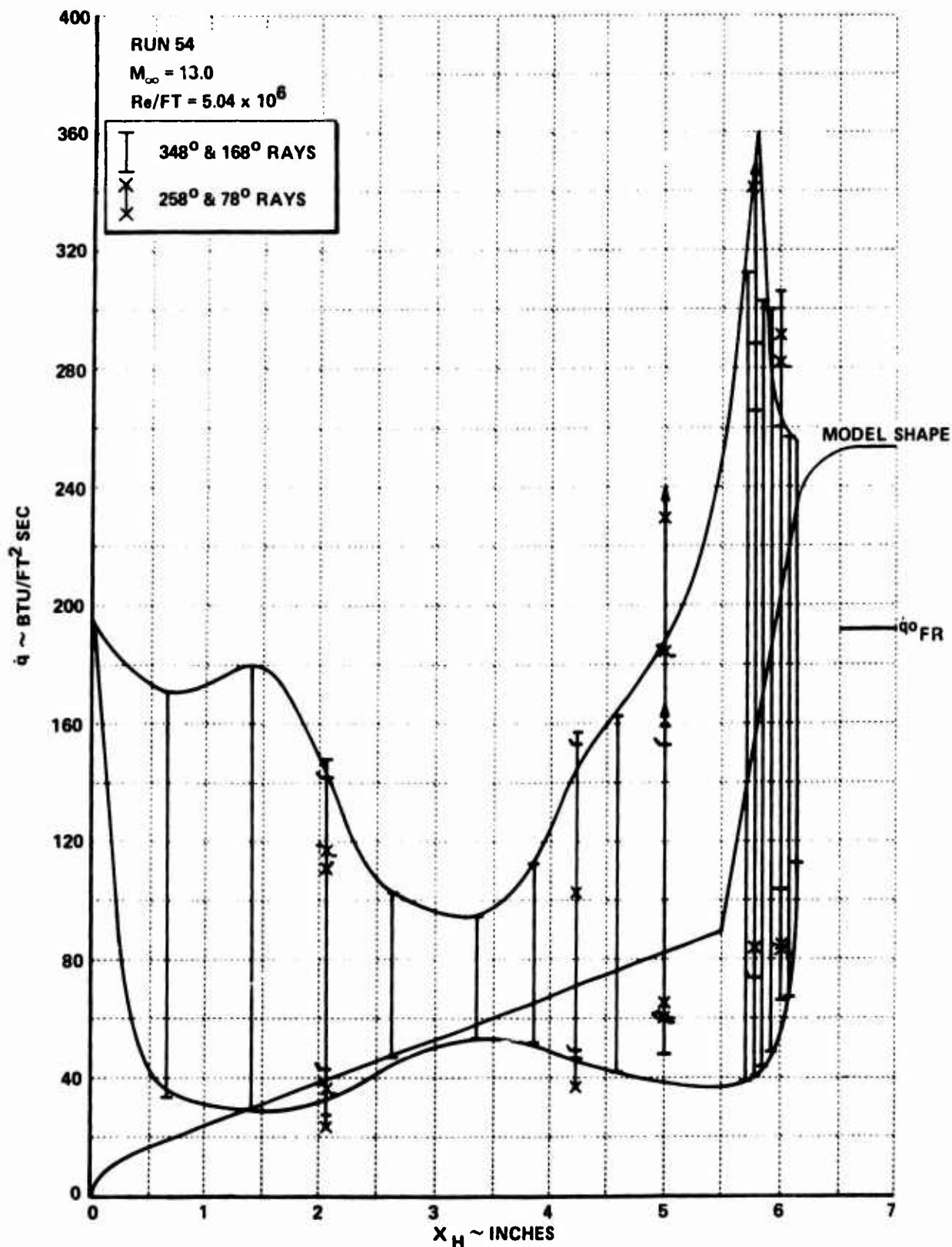


Figure 59a HEAT TRANSFER MEASUREMENTS FOR THE E MODE OSCILLATION OVER THE PANT 1 CONFIGURATION AT MACH 13.0

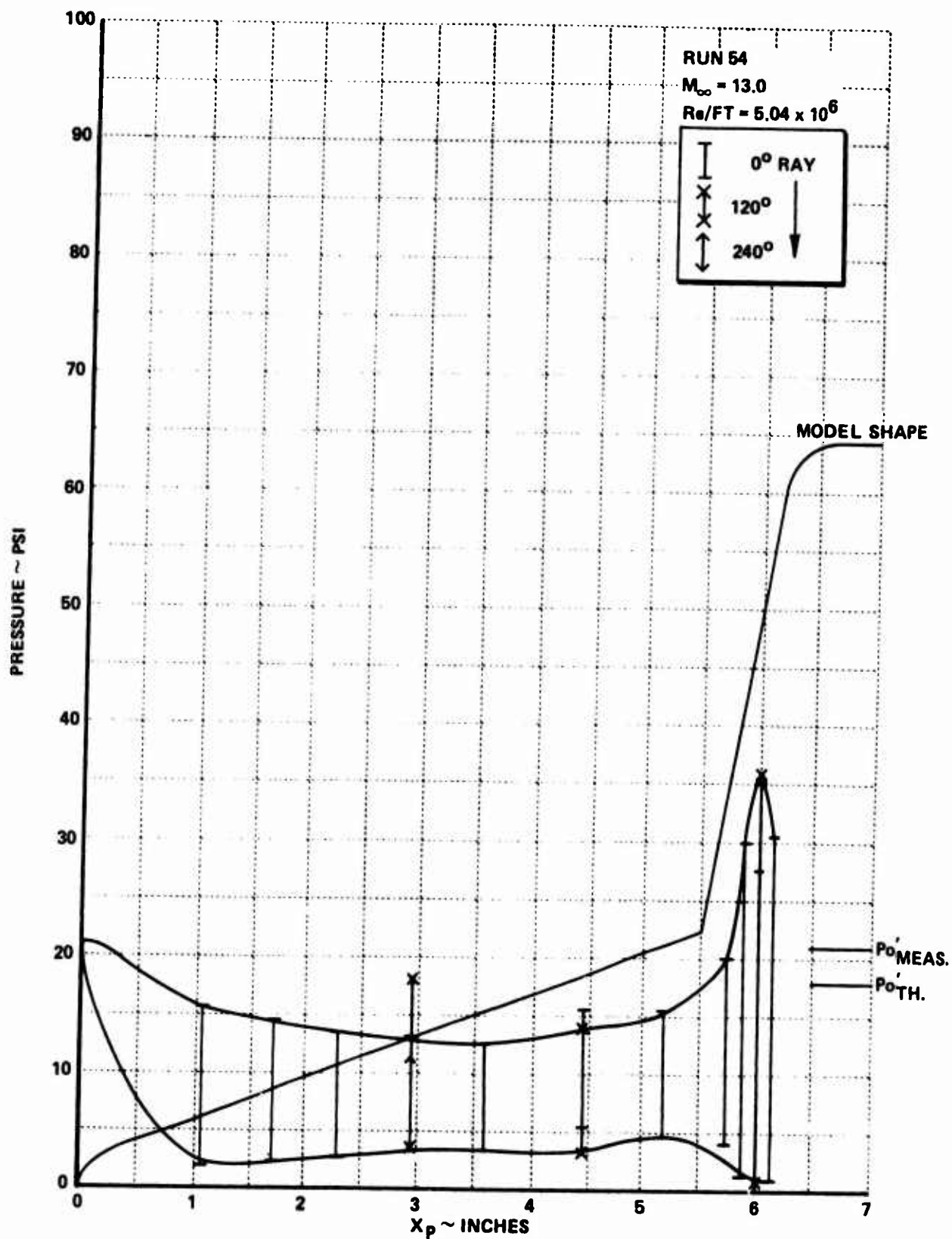


Figure 59b PRESSURE MEASUREMENTS FOR THE E MODE OSCILLATION OVER THE PANT 1 CONFIGURATION AT MACH 13

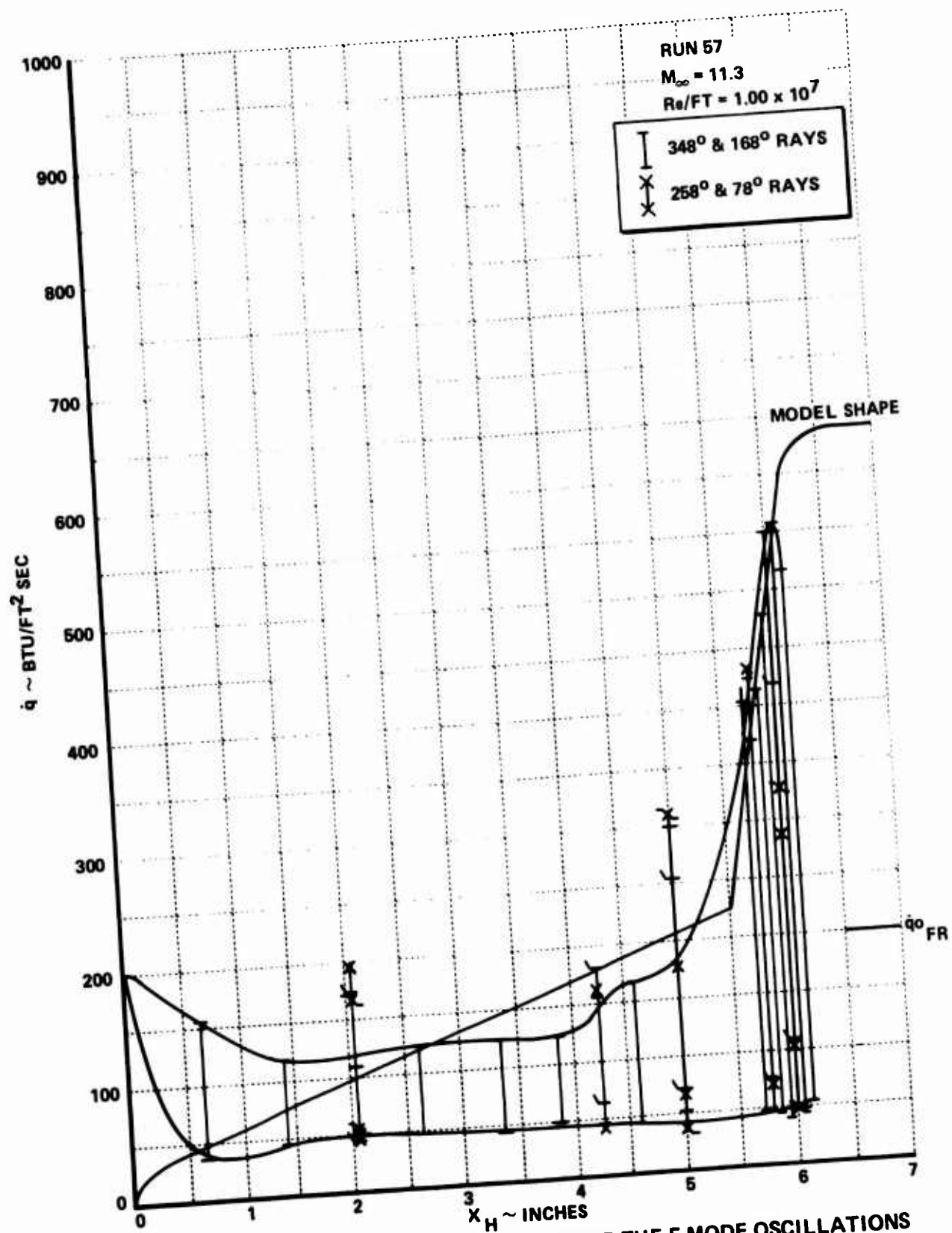


Figure 60a HEAT TRANSFER MEASUREMENTS FOR THE E MODE OSCILLATIONS OVER THE PANT 1 CONFIGURATION AT MACH 11

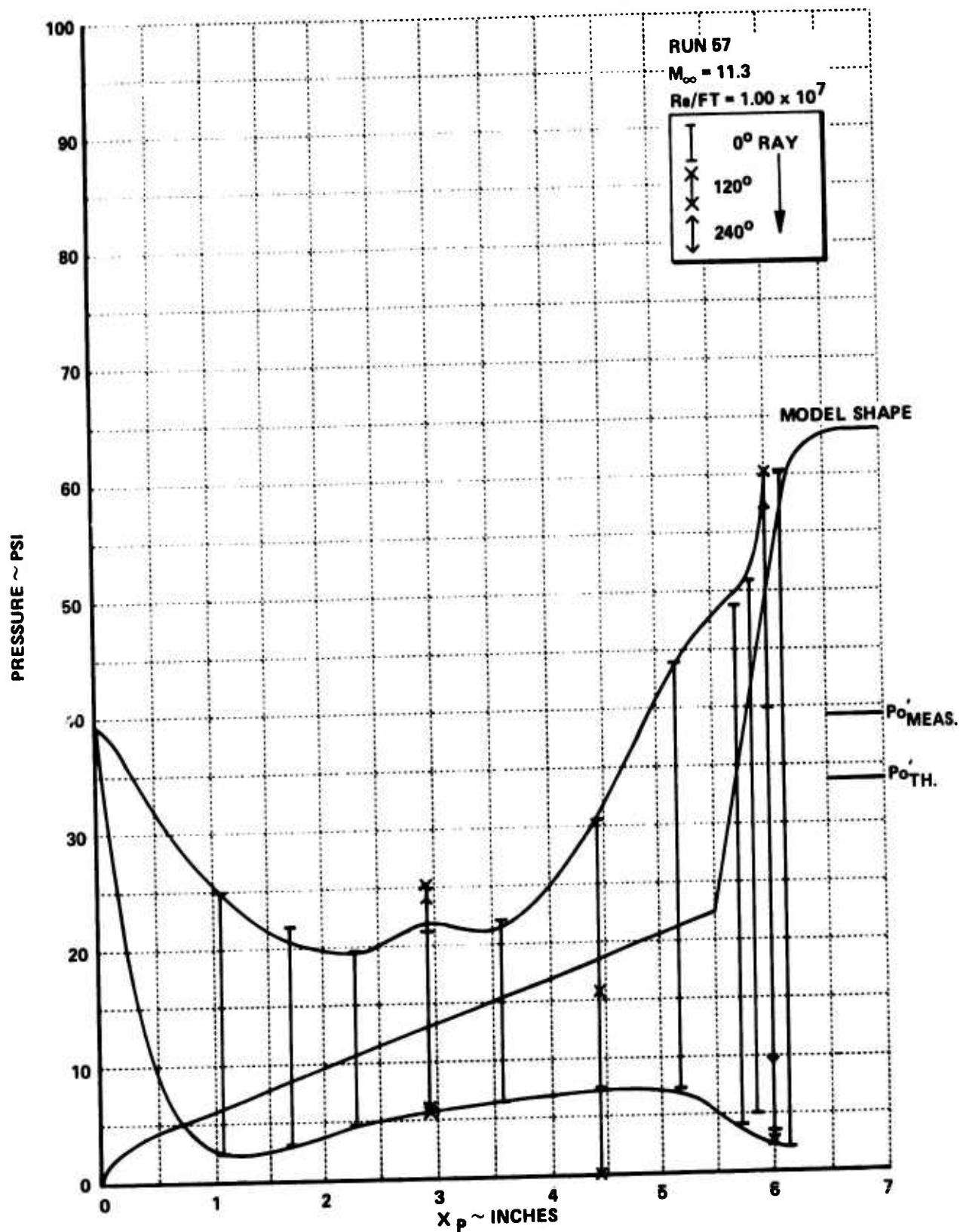


Figure 60b PRESSURE MEASUREMENTS FOR THE E MODE OSCILLATION OVER THE PANT 1 CONFIGURATION AT MACH 11

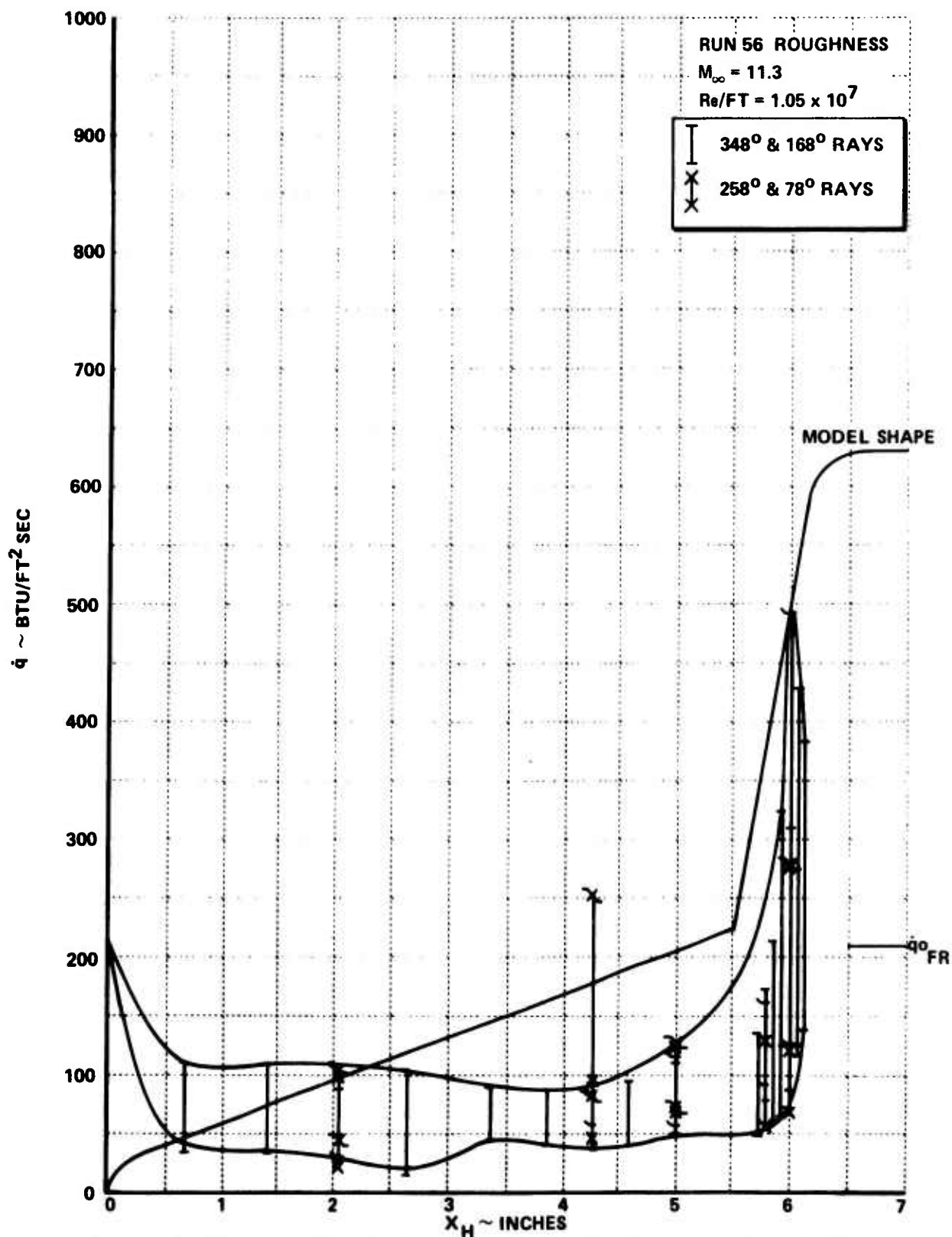


Figure 61a HEAT TRANSFER MEASUREMENTS FOR THE "D" MODE FLOW
 OSCILLATION ON A ROUGH (5 MIL) PANT 1 CONFIGURATION
 AT MACH 11

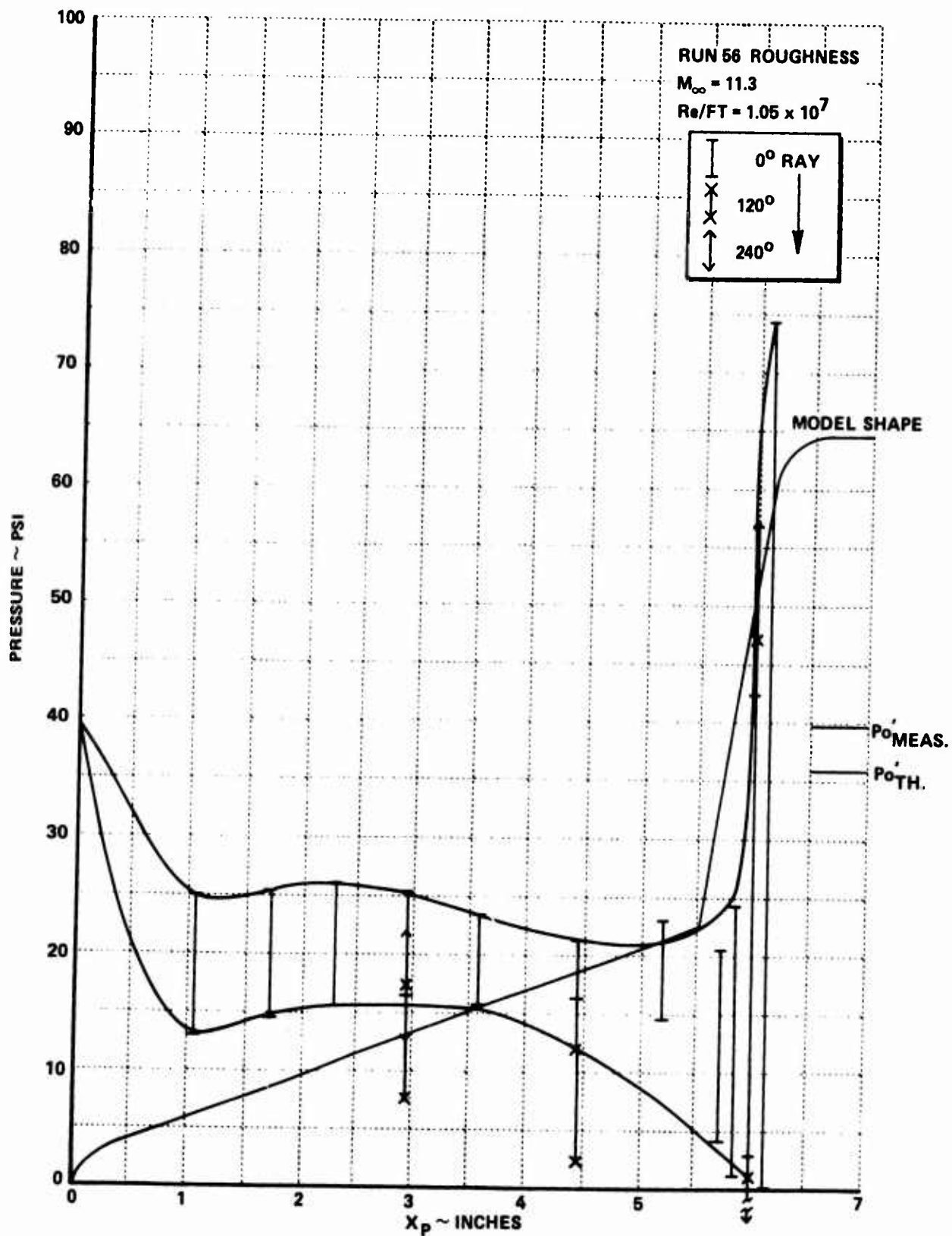


Figure 61b PRESSURE MEASUREMENTS FOR THE "D" MODE FLOW OSCILLATION ON A ROUGH (5 MIL) PANT 1 CONFIGURATION AT MACH 11

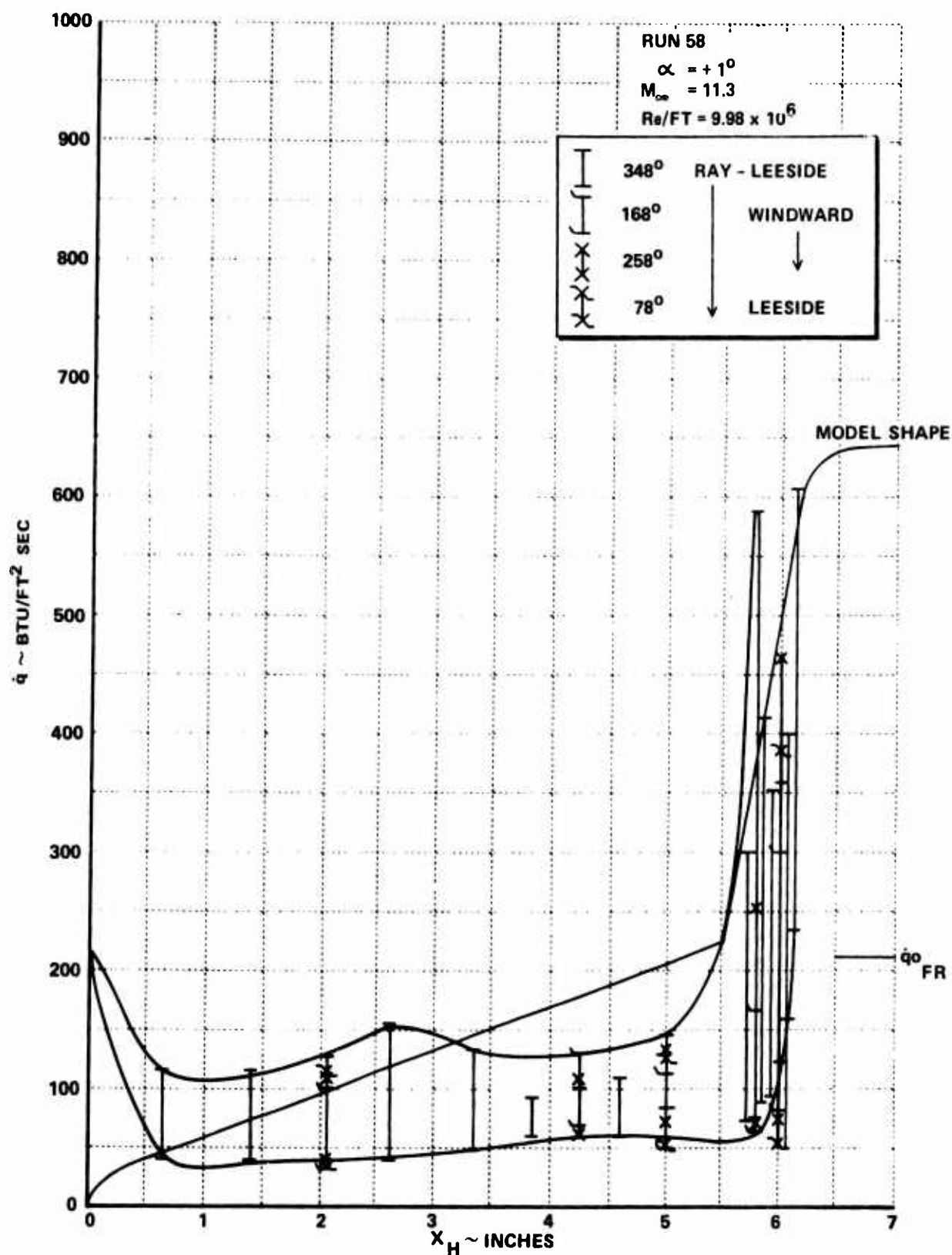


Figure 62a HEAT TRANSFER MEASUREMENTS OVER A SMOOTH PANT 1 CONFIGURATION FOR A 1° ANGLE OF ATTACK AT MACH 11

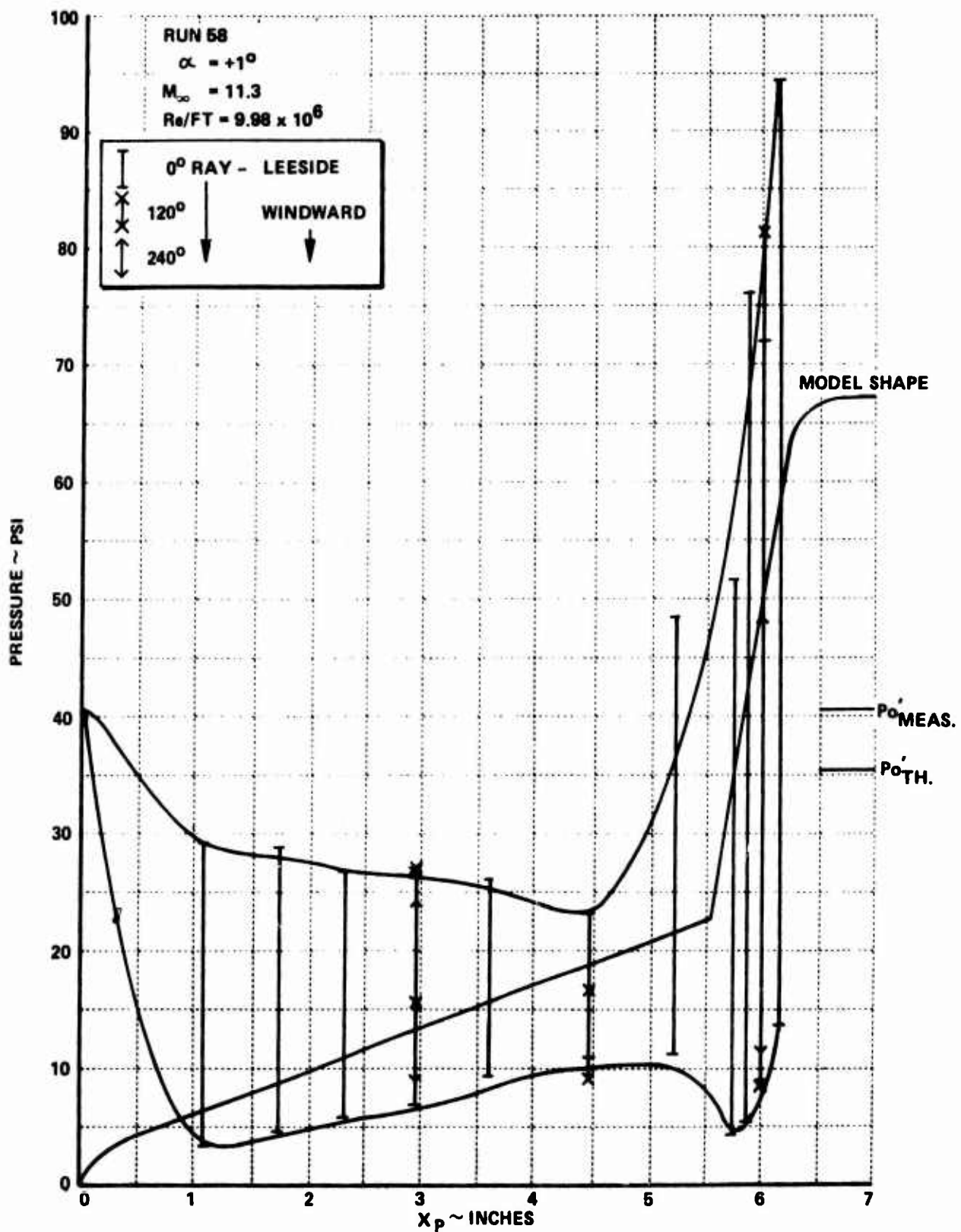


Figure 62b PRESSURE MEASUREMENTS OVER A SMOOTH PANT 1
 CONFIGURATION FOR A 1° ANGLE OF ATTACK AT MACH 11

these modes of oscillation, are similar, but variations of pressure and heating rate though large are smaller than those measured when a full E mode is observed.

The detailed heat transfer distributions on the Pant I show that heat transfer rates up to three times larger than the stagnation point heating levels to the nose tip of the model, or twelve times the heating rate to the stagnation point of a sphere with an equal base diameter, are encountered on the second conical surface of the model. The maximum heating rates are observed at the point of reattachment of the shear layer formed by shock-shock interaction. This reattachment point, which originates just above the cone-cone junction is swept across the face of the model as the separated region grows, forcing outward the position of the shock-shock interaction. Our interest in the D type and asymmetric mode instabilities stem from the fact that these phenomena have been observed in ablation tests where asymmetric ablation has induced nose shapes which are at most equivalent to a symmetric nose tip placed at angle of attack. The asymmetric pressure and heat transfer and pressure loading can play a key role in the survivability and accuracy of high β re-entry vehicles.

Section 4

CONCLUSIONS

A detailed study has been conducted of the aero-thermodynamics of ablated nose shapes at Mach numbers from 8 to 13 and Reynolds numbers up to 80×10^6 based on nose tip diameter. The detailed measurements of heat transfer and pressure which were obtained on blunt elliptic, blunt biconic and triconic nose tip configurations demonstrated the importance of accurately describing the length and characteristics of regions boundary layer transition and relaminarization. The length and properties of the transition region were found to be strongly influenced by the local pressure gradient and the structure of the entropy layer. However while the length of this region (which can exceed that of the preceding laminar run) cannot be predicted, our time-resolved measurements support the intermittency model of turbulence. The heat transfer measurements demonstrated that relaminarization occurred in regions of strong expansions on all the nose shapes tested, yet this phenomena is not modelled in conventional shape-change codes, and is little understood as a basic fluid dynamic effect.

Model roughness was found to have a major effect on the beginning of transition and the length and characteristics of the transition region. Even when the beginning and length of the transition region were specified from experiment, theoretical prediction methods based on the Powers roughness model were found to be in very poor agreement with measurements. Roughness does influence relaminarisation; however, complete relaminarisation can occur in the presence of roughness. Regions of shock wave-boundary layer interaction are observed on mildly indented nose shapes. The large heat transfer rates generated at the base of the shock formed in these regions of viscous interaction provide the mechanism for driving ablating bodies into more highly indented nose configurations.

In the second phase of this investigation, we studied, in detail, the structure and development of attached, separated and unsteady separated flows about highly indented nose shapes. While emphasis here was centered on the high Reynolds number high Mach number regime, measurements also performed on two "highly ablated" nose shapes (Widhopf 1 and 2) under extremely low Reynolds

number conditions, $Re_N = 300$. This study was performed explicitly for the purpose of comparing high frequency heat transfer measurements with calculations made with the Navier-Stokes code devised by Widhopf and Victoria. While we did not find the high frequency oscillation predicted by Widhopf and Victoria over the Widhopf 1 configuration, the mean heat transfer measurements were in excellent agreement with theory. The measurements on the Widhopf 2 configuration exhibited the longitudinal E mode oscillation with a characteristic Strouhal number of 0.17. A first harmonic of this oscillation, an asymmetric D mode, was also observed.

Detailed studies were made, in high Mach number high Reynolds number flows, of the occurrence and structure of flow instabilities occurring on highly indented nose tip configuration of shapes which are believed to be generated under some flight conditions. In the first set of studies, we examined the model configurations and free-stream conditions under which unsteady flows were developed over highly indented nose shape under turbulent flow conditions at Mach numbers from 8 to 13. The oscillation boundaries were determined for smooth highly-indented bodies and expressed in terms of bluntness ratio and the triconic representation. Measurements on selected configurations demonstrated that model roughness is an important parameter and should be explored further. E and D oscillations as well as the asymmetric L mode were observed in these studies. The detailed heat transfer measurements over the AO configuration demonstrated that heat transfer rates of the order ten times the stagnation point value to a sphere of an equal base diameter are generated in the reattachment region on highly indented nose shapes. Surface pressures which exceed the pitot pressure in the free stream are also observed in this region. A small angle of attack was found to induce strong asymmetric oscillations which could induce a significant destabilizing moment. The symmetric E mode oscillation was found to have a Strouhal number between 0.15 and 0.2 for the various indented nose shapes studies, with the asymmetric oscillations occurring at frequencies which were harmonics of the symmetric oscillations. The detailed measurements on the PANT 4 configuration demonstrated that roughness can modify the E mode oscillation and induce asymmetric oscillations causing asymmetric forces of significant proportions. Again extremely large heat transfer rates were generated in the reattachment of these flows.

PART II
EXPERIMENTAL STUDIES OF PARTICLE ENHANCED
HEATING OF NOSE TIP

1. INTRODUCTION

The phenomena which arise when the nose tips of hypersonic re-entry vehicles encounter clouds formed from ice crystals or dust particles are known to be of key importance to nose tip integrity and mission accuracy. While nose tip erosion resulting from particle impact has been a primary concern of the designer, the increase in nose tip heating, relative to the clean air environment, associated with particle rebound, or the ejection of material from the surface of the nose tip can play a critical role in this problem. Recently, it has been recognized that the increased heating associated with simple particle impact and associated chemical reactions is only one ingredient of the augmentation heating problem. Studies in dust tunnels at Boeing¹ and AEDC² have demonstrated that a significant increase in aerodynamic heating is associated with the particle-flow interaction in the stagnation region. While the rebounding particles leave a wake which is convected to the surface, changing the local boundary layer properties, studies by Wilkinson et al at TRW,² made in conjunction with measurements made in the dust tunnels at Boeing and AEDC, have identified bow shock-particle interaction as a key phenomenon. Although the particles must have sufficient momentum to reach the shock, particle size does not appear to strongly influence the mechanism of heating augmentation.

Photographic studies made in the wind tunnels at Boeing and Calspan yielded evidence leading to the identification of some of the detailed aerodynamic mechanisms induced by particle-bow shock interaction. Typical photographs showing a single particle-bow shock interaction are shown in Figures 63 and 64. Here the momentum of the re-bouncing particle is such that only a very small penetration is achieved. Under these circumstances, as we shall see later, a ring vortex is formed, which is subsequently convected to the surface of the nose tip to cause increased heating. The development of the vortex ring as it is convected toward the surface was demonstrated first in a movie sequence (see Figure 65) taken in the Boeing tunnel. The non-planar behavior of the vortex ring in this photographic sequence allows us to observe its expanding toroidal structure, which is convected to the surface in a fraction of a millisecond. While particle-induced vortex generation is an



Figure 63 SHOCK-PARTICLE INTERACTION OVER A BLUNT ELLIPSOID



Figure 64 SHOCK-PARTICLE INTERACTION OVER A BLUNTED CONE

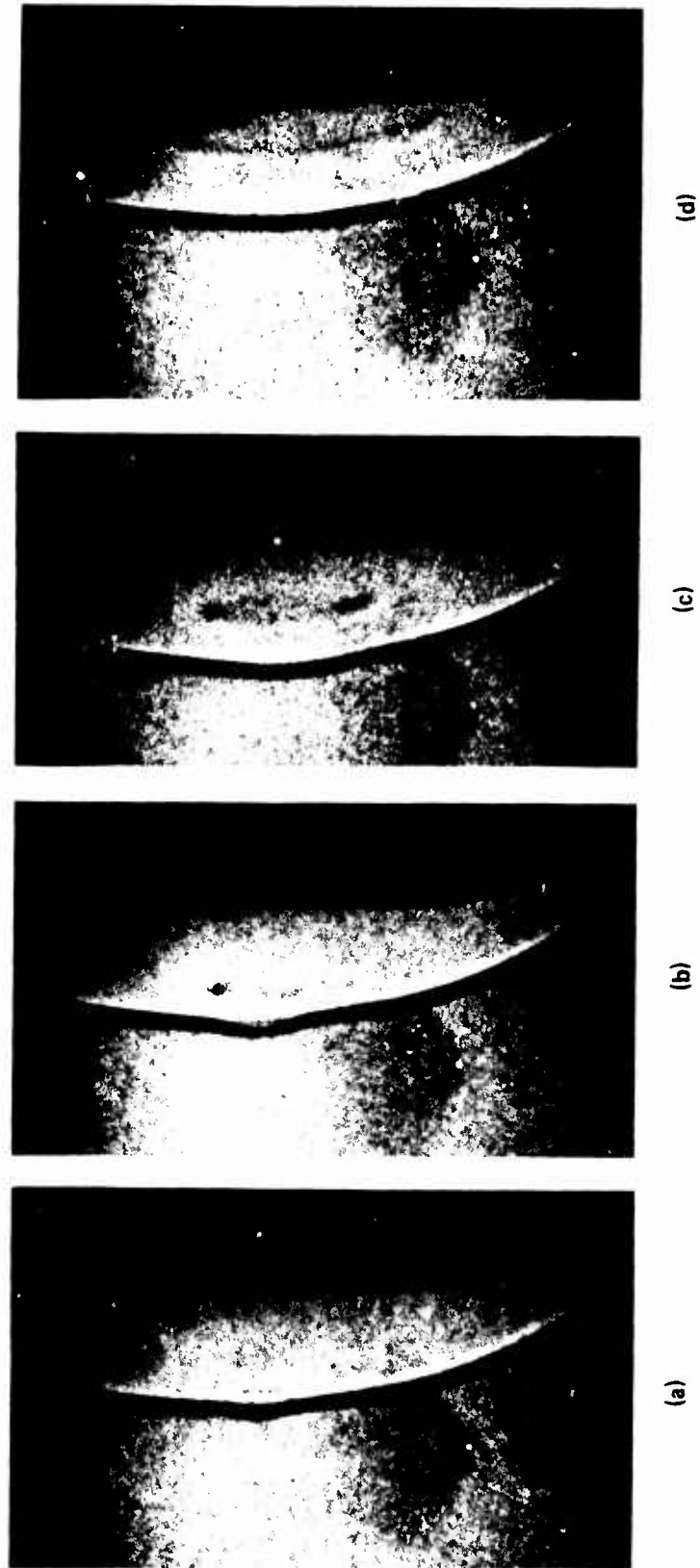


Figure 65 VORTEX GENERATION RESULTING FROM PARTICLE REBOUND,
A SEQUENCE TAKEN IN THE BOEING MACH 6 TUNNEL

intriguing phenomenon which can cause measurable heating augmentation, it is but one of the fluid mechanical mechanisms which result in particle-augmented heating. When the particle has sufficient momentum to penetrate through the bow shock, a shear layer or jet forms at the intersection of the particle and bow shocks which extends to the model surface, presumably causing increased heating.

While earlier studies in dust tunnels demonstrated significant particle-induced heating augmentation, the heat transfer and pressure instrumentation lacked the frequency response to follow discrete interactions. Thus little could be deduced about the detailed mechanisms responsible for increased heating. It was the purpose of the present experimental program to obtain time-resolved measurements of heat transfer and pressure together with high speed movie photographs to establish in detail a quantitative relationship between particle-shock interaction and surface heating augmentation. In the following paper, we will discuss briefly the experimental technique that was employed, and the results obtained, in the studies conducted in the Calspan 48 and 96-inch Shock Tunnels. Following a review of the objectives of the experimental program, we describe the design of the experimental program and the specialized instrumentation developed therein. The results from this program are discussed and the detailed heat transfer and pressure measurements presented. Here, with the aid of high speed schlieren photography we demonstrate that a number of dramatically different flow regimes exist depending upon the mass and launch velocity of the particle, as well as conditions in the free stream. Heat transfer and pressure measurements for these interactions are presented. The conclusions from this study are given together with recommendations for future work.

2. EXPERIMENTAL PROGRAM

2.1 PROGRAM OBJECTIVES

The objective of the studies conducted at Calspan was to delineate the various fluid dynamic mechanisms responsible for heating augmentation, and determine the magnitude of this augmentation as a function of the speed, size

and density of a single particle ejected from the surface, the geometry of the undisturbed flow and the Mach number and Reynolds number of the free stream. Here heat transfer and pressure measurements were required with a high degree of temporal and spatial resolution to enable specific enhancement mechanisms to be isolated. We first wished to demonstrate that a particle fired upstream produces the same type of disturbances observed in the dust tunnel at Boeing where the dust was added to the airflow close to the throat of the tunnel. The earlier studies had suggested that the significant heating augmentation occurred only when the particle possesses sufficient momentum to reach the bow shock. We sought to determine the magnitude of the effect on nose tip heating of the wake shed by the particle as it traversed the shock layer. By launching particles of various sizes, densities and velocities, we wished to determine whether the resulting particle-flow interactions were influenced by particle size. For these flows, we sought to establish the relationship between particle trajectory, body geometry and the instantaneous pressure and heat distribution over a model. Finally, we wished to determine how these results were influenced by Mach number and Reynolds number.

2.2 MODEL AND INSTRUMENTATION

In the experimental studies performed at Calspan, we chose to control the particle trajectory by launching from the model surface rather than adding particles to the free stream as is done in dust tunnels. While this approach gives us the flexibility and control required to perform systematic experimental studies, we were faced with the problem of developing the sophisticated apparatus required to launch particles between 100 and 800 microns in size at velocities between 30 and 300 ft/sec. A major task in this research program was, therefore, devoted to the design and development of a particle launcher system and the high frequency instrumentation required to obtain accurate time-resolved measurements of heat transfer and pressure on the nose shape.

A major consideration in the design of the launcher was the requirement that the launching mechanism caused negligible disturbance to the air-flow in the stagnation region, or create mechanical or electrical interference which

would disturb the output from the delicate high frequency instrumentation on the model surface. For this reason, mechanisms which involved a direct hydraulic launch or created sizable electrical fields were discarded in our initial design studies. After numerous approaches had been explored, we chose a technique which involved impact launching of the particle. A diagram of the impact particle launcher is shown in Figure 66. In this design, we employ two pistons, the second of which has a "cue" mounted in the center of its face, which is placed in contact with the particle to be launched. The first piston is driven down the launch tube when the driver gas (helium) is released behind it through a quick acting valve. The motion of this piston was monitored with photo diodes activated by LED's mounted along the internal surface of the launch tube. The second piston rests in contact with a rubber energy absorption system which acts to restrict its travel, when struck by the first piston, to within 0.50 inches. The particle is launched when the elastic compression wave caused by piston-piston impact travels down and is reflected from the face of the cue. The particle travels through a small cavity in the model, the geometry of which combined with the expansion wave generated as the second piston rebounds, produces a situation in which the pressure disturbance induced by the particle as it exits from the face of the model and traverses the shock layer is effectively the only disturbance produced in the launch process. Again, photo diodes and LED's are used in a measurement scheme to determine the velocity of the second piston. A specially designed inductive-capacitive transducer placed in the exit plane of the model was used to measure directly the exit velocity of the particles when the launcher was calibrated.

The launcher assembly was mounted in a seismic mass which, in turn, was supported within the basic model by a soft rubber suspension system. In this way, the instrumented section was effectively isolated from mechanical disturbances, generated when the launcher was activated. The instrumented section of the model, a schematic diagram of which is shown in Figure 67, contained 80 heat transfer and 28 high frequency pressure gages. Thin film resistance thermometers were used to obtain detailed temporal measurements of surface heat transfer. These gages, which were fabricated by the deposition of a thin platinum film on a pyrex-substrate provide an instantaneous indication of the surface temperature. This quantity can be related to semi-infinite slab theory to the instantaneous

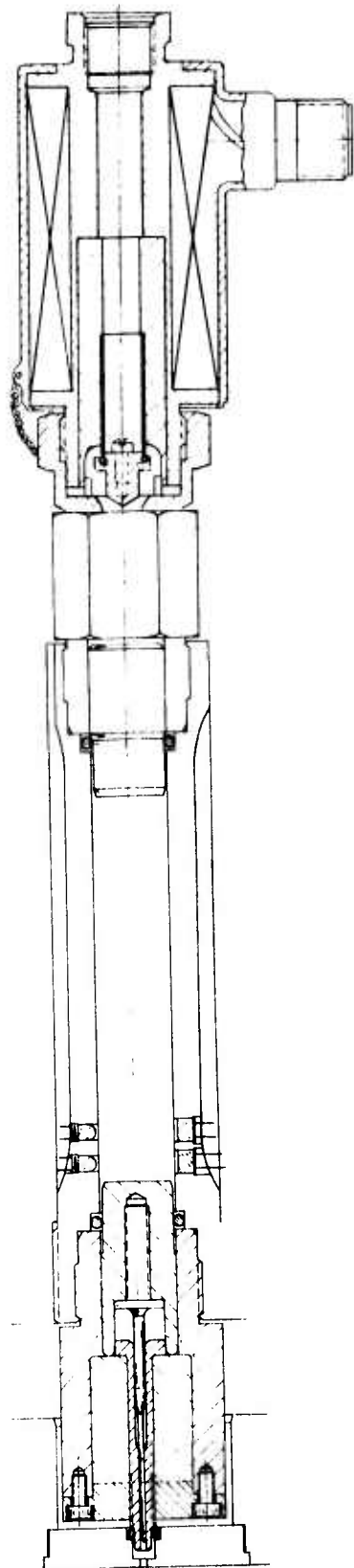


Figure 66 IMPACT PARTICLE LAUNCHER

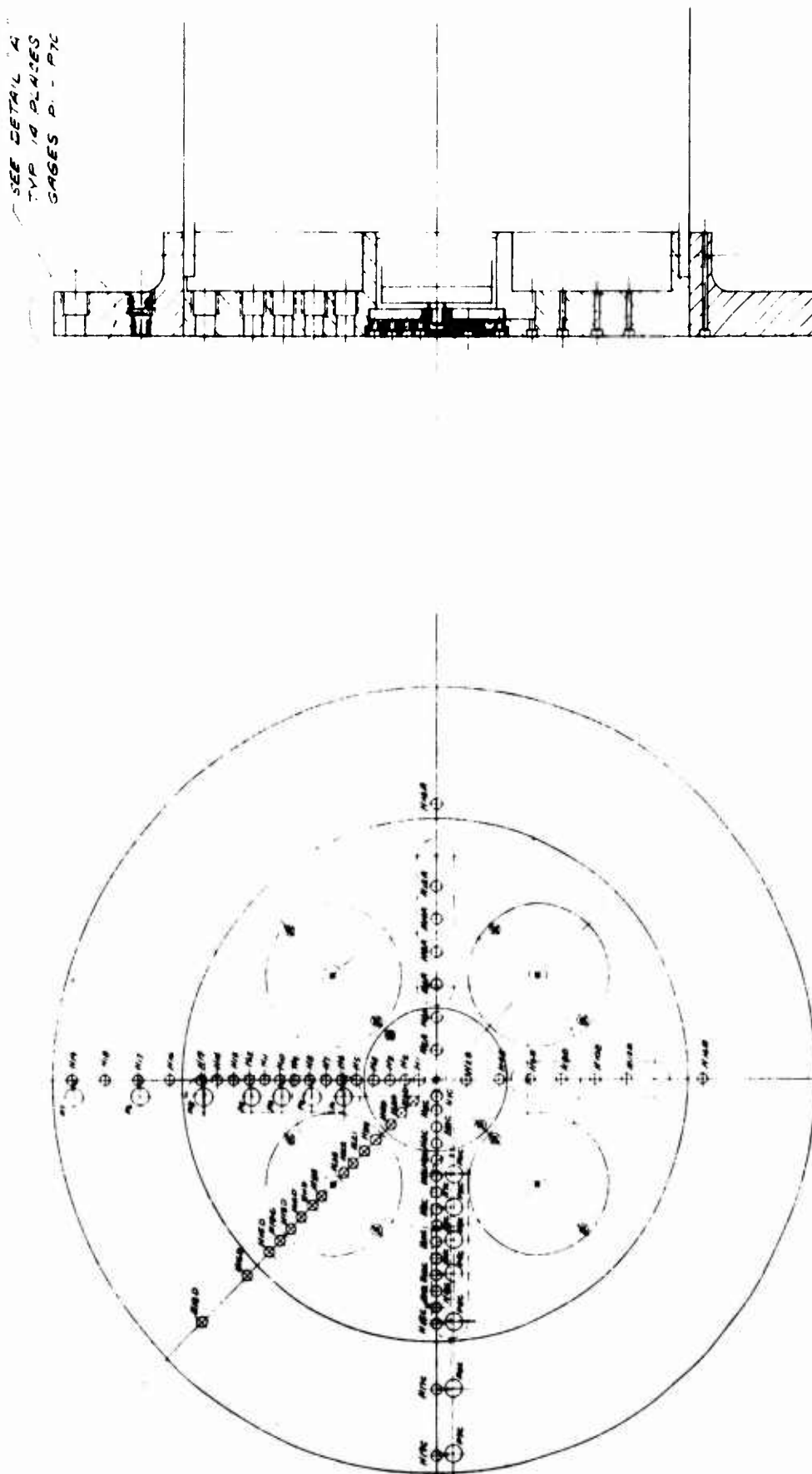


Figure 67 MODEL ASSEMBLY & INSTRUMENTATION NOSE TIP HEATING (SAMSO/AFOSR)

heat transfer rate. Analog networks are attached to each gage output to provide a signal which is directly proportional to the heat transfer rate. Flush mounted piezoelectric pressure transducers with a frequency response up to 200 KHz were used to obtain the temporal variations in pressure resulting from the interaction between particle and flow. In these preliminary studies a flat-faced cylindrical shape was chosen rather than a hemisphere because it afforded us the maximum shock layer thickness and thereby the maximum resolution with high speed cinematography. The basic configuration had a diameter of 6.0 inches; however, a removable ring enabled us to extend the diameter to 9.0 inches. The gages were positioned so that a high density of instrumentation was concentrated in one quadrant of the model, while the balance of instrumentation was distributed symmetrically about the model axis. In this way, we obtained detailed measurements on two mutually perpendicular axes, while retaining the ability to track asymmetric disturbances across the face of the model. Both steel and silica spherical balls, with dimensions between 100 and 500 microns were selected to be launched in the experimental program. The size and density of the particle and the velocity of the launch were chosen with the aid of a simple numerical code so that the particle penetrated specified distances relative to the position of the shock at each free stream condition. Here we sought to understand the various mechanisms which create heating enhancement for the different flow regimes encountered, as well as determining whether particle size is an important factor in this phenomena.

2.3 EXPERIMENTAL FACILITIES

The experimental programs were conducted in Calspan's 48-inch and 96-inch Hypersonic Shock Tunnels (Ref. 3). The operation of these tunnels can be shown simply with the aid of the wave diagram which permits the high pressure air in the driver section to expand into the driven section, and in so doing, generates a normal shock which propagates through the low pressure air. A region of high temperature, high pressure air is produced between this normal shock front and the gas interface between the driver and driven gas, often referred to as the contact surface. When the primary or incident shock strikes the end of the driven section, it is reflected leaving a region of

almost stationary high pressure heated air. This air is then expanded through a nozzle to the desired free stream conditions in the test section.

The duration of the flow in the test section is controlled by the interactions between the reflected shock, the interface, and the leading expansion wave generated by the non-stationary expansion process occurring in the driver section. At Calspan, we normally control the initial conditions of the gases in the driver and driven sections so that the gas interference becomes transparent to the reflected shock, as shown in Figure 80a; thus, there are no waves generated by interface-reflected shock interaction. This is known as operating under "Tailored-Interface" conditions. Under this condition, the test time is controlled by the time taken for the driver-driven interface to reach the throat, or the leading expansion wave to deplete the reservoir of pressure behind the reflected shock; the flow duration is said to be either driver gas limited or expansion limited, respectively. Figure 80b shows the flow duration in the test section as a function of the Mach number of the incident shock. Here it can be seen that for operation at low M_1 , running times of over 25 milliseconds can be obtained with a long driver section.

3. RESULTS AND DISCUSSION

The heat enhancement studies at Calspan were conducted in the 48" and 96" shock tunnels at Mach numbers from 6.5 to 16.3 and Reynolds numbers from 1×10^6 to $30 \times 10^6/\text{ft}$. During the course of this work, 22 runs were made; a listing of these runs is shown in Table 6. In this investigation, we made detailed spatially and temporally resolved measurements of heat transfer and pressure over the face of the flat-ended cylinder shown in Figure 67. The trajectory of the particles launched from the model were varied through the choice of particle size, density and launch velocity to examine the effect of these parameters on the mechanism and magnitude of enhancement heating. The Mach number and Reynolds number of the free stream, as well as free stream velocity and model diameter, were varied to examine how transition on the model and in the free shear layer influences augmentation heating.* Here, we also sought to establish whether "Strouhal number scaling" could be applied to those flows in which gross instabilities were observed to occur.

*Test conditions given in Table 7

Table 6

TEST MATRIX FOR CALSPAN PROGRAM

RUN NO.	M_{∞}	Re /ft. $\times 10^{-6}$	D_B (in.)	d_p /MAT'L (μ)	V_{po} (ft./sec.)	$X_{MAX.}$ (in.)
1	16.3	1.00	9	800/SIL	130	11
2	12.5	2.09	9	800/SIL	130	N/A
3	12.5	1.99	9	800/SIL	130	8.1
4	12.6	2.14	9	800/SIL	130	13
5	12.6	2.06	9	350/SIL	300	9.3
6	12.6	2.05	9	650/SIL	50	5.8
7	12.6	2.03	9	450/SIL	50	5.8
8	12.5	1.94	9	250/SIL	50	5.7
9	RUN ABORTED					
10	12.9	4.45	9	800/SIL	140	12.3
11	6.38	2.34	9	800/STL	80	N/A
12	6.38	2.54	9	NONE	NONE	NONE
13	6.37	2.35	9	NONE	80	NONE
14	CENTERBODY CLOSED EARLY					
15	6.39	2.53	9	800/STL	80	10.2
16	6.36	2.33	9	850/SIL	110	5.7
17	6.43	6.14	9	800/STL	140	6.5
18	6.45	6.12	9	800/STL	90	9.8
19	6.4	15.5	9	800/STL	120	4.9
20	6.4	6.1	6	800/STL	90	2.8
21	6.4	6.1	6	800/STL	120	N/A
22	6.4	30	6	800/STL	180	4.5

Table 7
TEST CONDITIONS FOR HEATING ENHANCEMENT PROGRAM

RUN NO.	2	3	4	5	6	7	8
ATTACK	0.0	0.0	0.0	0.0	0.0	0.0	0.0
YAW	0.0	0.0	0.0	0.0	0.0	0.0	0.0
ROLL	0.0	0.0	0.0	0.0	0.0	0.0	0.0
M(I)	3.631E+00	3.657E+00	3.627E+00	3.599E+00	3.599E+00	3.62E+00	3.630E+00
P(O)	7.838E+03	7.723E+03	8.078E+03	7.743E+03	7.915E+03	7.803E+03	7.610E+03
H(O)	2.098E+07	2.140E+07	2.102E+07	2.096E+07	2.122E+07	2.122E+07	2.145E+07
T(O)	3.171E+03	3.227E+03	3.177E+03	3.171E+03	3.207E+03	3.207E+03	3.238E+03
M	1.222E+01	1.221E+01	1.224E+01	1.215E+01	1.224E+01	1.226E+01	1.218E+01
J	6.363E+03	6.426E+03	6.370E+03	6.359E+03	6.400E+03	6.402E+03	6.435E+03
T	1.127E+02	1.152E+02	1.126E+02	1.142E+02	1.136E+02	1.133E+02	1.160E+02
P	4.479E-02	4.394E-02	4.585E-02	4.644E-02	4.453E-02	4.331E-02	4.375E-02
Q	4.638E+00	4.590E+00	4.812E+00	4.740E+00	4.677E+00	4.563E+00	4.552E+00
RHO	3.335E-03	3.201E-03	3.416E-03	3.412E-03	3.285E-03	3.207E-03	3.166E-03
MU	9.481E-06	9.689E-06	9.474E-06	9.605E-06	9.557E-06	9.532E-06	9.752E-06
RE/FT.	2.238E+06	2.123E+06	2.297E+06	2.259E+06	2.202E+06	2.154E+06	2.089E+06
PITOT	8.710E+00	8.529E+00	8.940E+00	8.649E+00	8.690E+00	8.480E+00	8.459E+00
T*	9.443E+02	9.569E+02	9.460E+02	9.461E+02	9.557E+02	9.542E+02	9.632E+02
MU*	5.764E-07	5.823E-07	5.771E-07	5.771E-07	5.810E-07	5.804E-07	5.841E-07
SQRT.C*	8.519E-01	8.498E-01	8.516E-01	8.516E-01	8.502E-01	8.504E-01	8.492E-01
H(W)	3.213E+06	3.225E+06	3.219E+06	3.237E+06	3.258E+06	3.237E+06	3.252E+06
T(W)	5.350E+02	5.370E+02	5.360E+02	5.370E+02	5.425E+02	5.390E+02	5.415E+02
P(TS)	4.835E-04	4.835E-04	7.736E-04	4.835E-04	4.835E-04	5.802E-04	5.802E-04

Table 7
TEST CONDITIONS FOR HEATING ENHANCEMENT PROGRAM (CONTINUED)

RUN NO.	10	11	12	13	14	15	16
ATTACK							
YAW	0.0	0.0	0.0	0.0	0.0	0.0	0.0
ROLL	0.0	0.0	0.0	0.0	0.0	0.0	0.0
M(I)	3.726E+00	2.284E+00	2.228E+00	2.250E+00	2.261E+00	2.216E+00	2.278E+00
P(O)	1.013E+04	7.121E+02	4.054E+02	3.833E+02	4.356E+02	4.052E+02	3.904E+02
H(U)	2.210E+07	5.563E+06	5.510E+06	5.679E+06	5.671E+06	5.401E+06	5.559E+06
T(O)	3.353E+03	1.543E+03	1.484E+03	1.512E+03	1.511E+03	1.466E+03	1.542E+03
M	1.251E+01	6.403E+00	6.316E+00	6.340E+00	6.404E+00	6.411E+00	6.400E+00
J	6.536E+03	7.195E+03	7.113E+03	7.151E+03	7.155E+03	7.096E+03	7.144E+03
T	1.134E+02	1.785E+02	1.764E+02	1.783E+02	1.747E+02	1.698E+02	1.756E+02
P	9.604E-02	1.753E-01	1.879E-01	1.739E-01	1.847E-01	1.726E-01	1.865E-01
J	1.054E+01	5.026E+00	5.252E+00	4.897E+00	5.317E+00	4.970E+00	4.779E+00
RMJ	7.106E-05	6.240E-05	6.941E-05	8.183E-05	6.871E-05	6.531E-05	7.824E-05
MU	5.534E-08	1.490E-07	1.472E-07	1.488E-07	1.454E-07	1.419E-07	1.490E-07
RE/FT.	4.869E+06	2.320E+06	2.497E+06	2.283E+06	2.526E+06	2.463E+06	2.202E+06
PILOT	1.960E+01	4.350E+00	4.749E+00	9.091E+00	5.670E+00	5.224E+00	4.874E+00
T*	9.800E+02	5.280E+02	6.150E+02	6.218E+02	6.201E+02	6.105E+02	6.263E+02
MU*	5.404E-07	4.324E-07	4.255E-07	4.290E-07	4.281E-07	4.232E-07	4.324E-07
SURT.C*	8.447E-01	9.081E-01	5.100E-01	5.090E-01	6.042E-01	5.106E-01	5.080E-01
H(W)	3.228E+06	3.231E+06	3.231E+06	3.237E+06	3.242E+06	3.225E+06	3.237E+06
T(W)	5.375E+02	5.380E+02	5.380E+02	5.390E+02	5.365E+02	5.370E+02	5.390E+02
P(TS)	4.835E-04	2.127E-04	7.736E-05	1.160E-04	7.736E-05	7.736E-05	9.570E-05

Table 7
TEST CONDITIONS FOR HEATING ENHANCEMENT PROGRAM (CONTINUED)

RUN NO.	17	18	19	20	21	22
ATTACK	0.0	0.0	0.0	0.0	0.0	0.0
YAW	0.0	0.0	0.0	0.0	0.0	0.0
ROLL	0.0	0.0	0.0	0.0	0.0	0.0
M(I)	2.271E+00	1.265E+00	2.092E+00	2.268E+00	2.120E+00	2.101E+00
P(O)	1.048E+03	1.047E+03	2.012E+03	1.093E+03	1.061E+03	4.387E+03
H(O)	9.841E+06	9.728E+06	9.693E+06	9.776E+06	8.828E+06	8.626E+06
T(U)	1.544E+03	1.526E+03	1.352E+03	1.534E+03	1.372E+03	1.375E+03
M	6.460E+00	6.461E+00	6.541E+00	6.463E+00	6.481E+00	6.615E+00
U	4.195E+03	4.170E+03	3.947E+03	4.181E+03	3.974E+03	3.950E+03
T	1.753E+02	1.753E+02	1.514E+02	1.740E+02	1.564E+02	1.483E+02
P	4.314E-01	4.316E-01	8.068E-01	4.504E-01	4.364E-01	1.724E+00
Q	1.261E+01	1.262E+01	2.419E+01	1.318E+01	1.284E+01	5.285E+01
RHD	2.065E-04	2.090E-04	4.471E-04	2.172E-04	2.342E-04	9.754E-04
MU	1.464E-07	1.447E-07	1.264E-07	1.453E-07	1.310E-07	1.244E-07
RE/FT.	2.416E+06	6.023E+06	1.390E+07	6.244E+06	7.105E+06	3.098E+07
PITOT	2.342E+01	2.344E+01	4.486E+01	2.444E+01	2.382E+01	9.801E+01
T*	6.275E+02	6.221E+02	5.840E+02	6.243E+02	5.892E+02	5.828E+02
MU*	4.314E-07	4.292E-07	4.094E-07	4.303E-07	4.121E-07	4.067E-07
SQRT.C*	9.079E-01	9.087E-01	9.145E-01	9.084E-01	9.138E-01	9.145E-01
H(W)	3.246E+06	3.231E+06	3.237E+06	3.237E+06	3.231E+06	3.237E+06
T(W)	5.405E+02	5.380E+02	5.390E+02	5.390E+02	5.380E+02	5.390E+02
P(TS)	1.160E-04	1.354E-04	9.670E-05	1.354E-04	9.670E-05	5.802E-05

The first set of measurements with the model and launcher combination were designed to calibrate the launcher and determine the extent of the electrical and aerodynamic effects resulting from actuating the launch mechanism. The velocity of the launched particle was determined as a function of the driver pressure and piston velocity by obtaining the lapse time as the particle traversed between two inductive-capacitive pickups placed coaxially at the exit of the launcher. With the sensitivity of the recording equipment set at an order of magnitude greater than required at the lowest heat transfer and pressure levels to be observed we found there were no disturbances when the launcher was actuated firing a particle in a vacuum. Actuating the launcher without a particle during several runs demonstrated that there was no measurable difference in the heating or pressure levels before and after activation or in subsequent runs at the same conditions where the launcher was not operated.

The first objective of the tunnel studies was to define the types of particle-flow interaction leading to heating enhancement. To this end, a series of experiments was performed adjusting the momentum of the particle so that it just touched the bow shock, traveled a short distance beyond it, and reached at least 3 body diameters ahead of the body. Before discussing in detail the changes in flow geometry and heat transfer and pressure distributions which occurred under each of these conditions, it is important to comment on the measurements while the particle was in the shock layer. For the range of particle sizes and launch velocities examined (see above) there was no measurable increase in the heat transfer or pressure on the surface of the model as the particle traversed the shock layer. This finding is in agreement with the results of Wilkinson,² et al, who deduced heating augmentation occurred only when the rebounding particles possessed sufficient momentum for them to reach the bow shock.

3.1 PARTICLE-INDUCED VORTEX HEATING AUGMENTATION

Heating augmentation was first observed to occur for trajectories such that the particle just reached the bow shock. A sequence of photographs showing the small "dimple" which occurs as the particle reaches the bow shock and the

subsequent formation of a toroidal vortex is shown in Figure 68. The abrupt change in shock curvature at the junction between the particle and body shock creates a shear layer which subsequently rolls up into a vortex ring as the particle is driven back into the shock layer. The vortex ring is then convected toward the model expanding in diameter as it approaches the surface. Correlating the heat transfer time histories with the movie sequence reveals that increased heating rates are observed at the model surface over a period of just over 1 millisecond, the time taken for the vortex to traverse the shear layer and expand across the model. As the ring passed over the heat transfer gages, their output increased from 1.5 to 3 times their undisturbed values.

3.2 HEATING AUGMENTATION RESULTING FROM SHOCK-SHOCK INTERACTION AND FLOW SEPARATION

When the particle has sufficient momentum to travel ahead of the ambient bow shock location, very dramatic changes occur in the viscous and inviscid flow fields which can cause heating levels that exceed the ambient by factors of 2 to 4 close to the model axis and 5 to 10 toward the periphery of the disk. For practical purposes, we can divide the phenomena observed into three classes: (1) where the particle travels beyond the bow shock along the axis of symmetry but reaches less than 0.7 body diameters from the model surface, (2) where the particle travels along the axis of symmetry but travels beyond 0.7 body diameter before returning toward the body and (3) where the particle travels off center setting up a highly asymmetric flow pattern.

1. Small Upstream Penetration - A sequence of photographs showing the development of a region of shock-shock interaction leading to heating augmentation resulting from small penetration is shown in Figure 69. Here the momentum on the particle was just sufficient for the particle to reach 0.7 of the body diameter ahead of the model. As the particle moves ahead of the bow shock, the shock wave associated with the particle and the flow behind it interacts with the original bow shock inducing a shear layer at their point of intersection. This shear layer sweeps radially outwards across the face of the model increasing the local heat transfer at its base by as much as a factor



Figure 68 HEATING AUGMENTATION ASSOCIATED WITH PARTICLE-INDUCED RING VORTEX INTERACTION

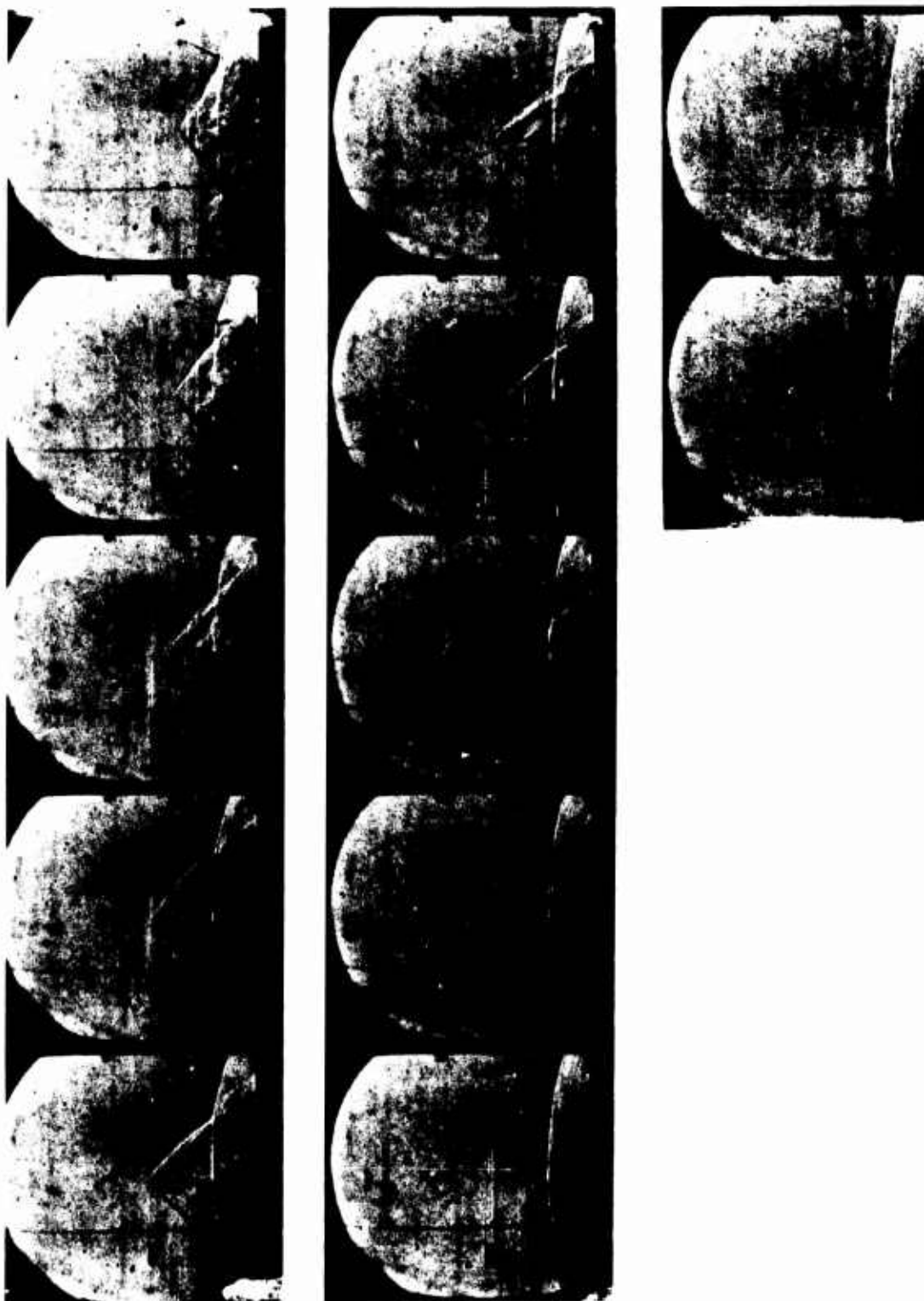


Figure 69 "STABLE" FLOW RESULTING FROM SMALL PENETRATION

of ten. In this sequence, the shear layer reaches the model periphery just as the particle is being driven back to the model surface, and the shear layer then collapses inwards in a quasi-steady fashion, disappearing as the particle re-enters the shock layer. The period of increased heating was just over one millisecond, the time taken for the particle to exit and re-enter the shock layer. Pressure levels just above the pitot level were observed at the base of the shear layer while those within the annulus corresponded roughly with those achieved by compression through the conical shock associated with the particle.

2. Particle Penetrations Beyond One Body Diameter Resulting in Shock Layer Oscillation - When the particle is launched with sufficient momentum for it to reach one body diameter ahead of the body a dramatic change occurs in both the character of the inviscid flow and the pressure and heat transfer on the model surface. Here the entire flow field begins pulsating as demonstrated in the high speed movie sequences shown in Figures 70 and 71. These sequences, which were taken at Mach 6.5 and 1.3 respectively at similar Reynolds number conditions demonstrate considerable similarity in mechanics of oscillation. This oscillation is very similar to pulsating flows* observed over spiked bodies⁴ or highly⁵ indented nose shapes as demonstrated by the movie sequence of these flows shown in Figure 48. The occurrence of these massive pulsations appears independent of particle size and once the particle has reached a body diameter ahead of the surface, the axial motion of the particle is strongly influenced by the flow oscillations. The non-dimensional frequency $\left(\frac{fD}{U}\right)$ was found to lie between 0.17 and 0.19 and appeared relatively independent of Mach number, particle velocity size or penetration, and model size. A Strouhal number of between 0.17 and 0.20 typifies the frequencies encountered over spiked and highly indented bodies, and re-enforces the concept that the basic mechanism is associated with a simple inviscid filling and spilling mechanism. The oscillation is initiated when the shear layer or jet formed by particle/spike shock-bow shock interaction re-attaches to the body surface trapping a conical region of gas. The mass which is being continuously added to this region through the conical shock drives the local stagnation point at the base of the shear layer toward the periphery of the model. This region collapses as the entrapped gas escapes when the shear layer moves off the body, and the sequence begins again with bow shock re-establishing and the particle shock-bow shock interaction

* Termed the E oscillation in this study.

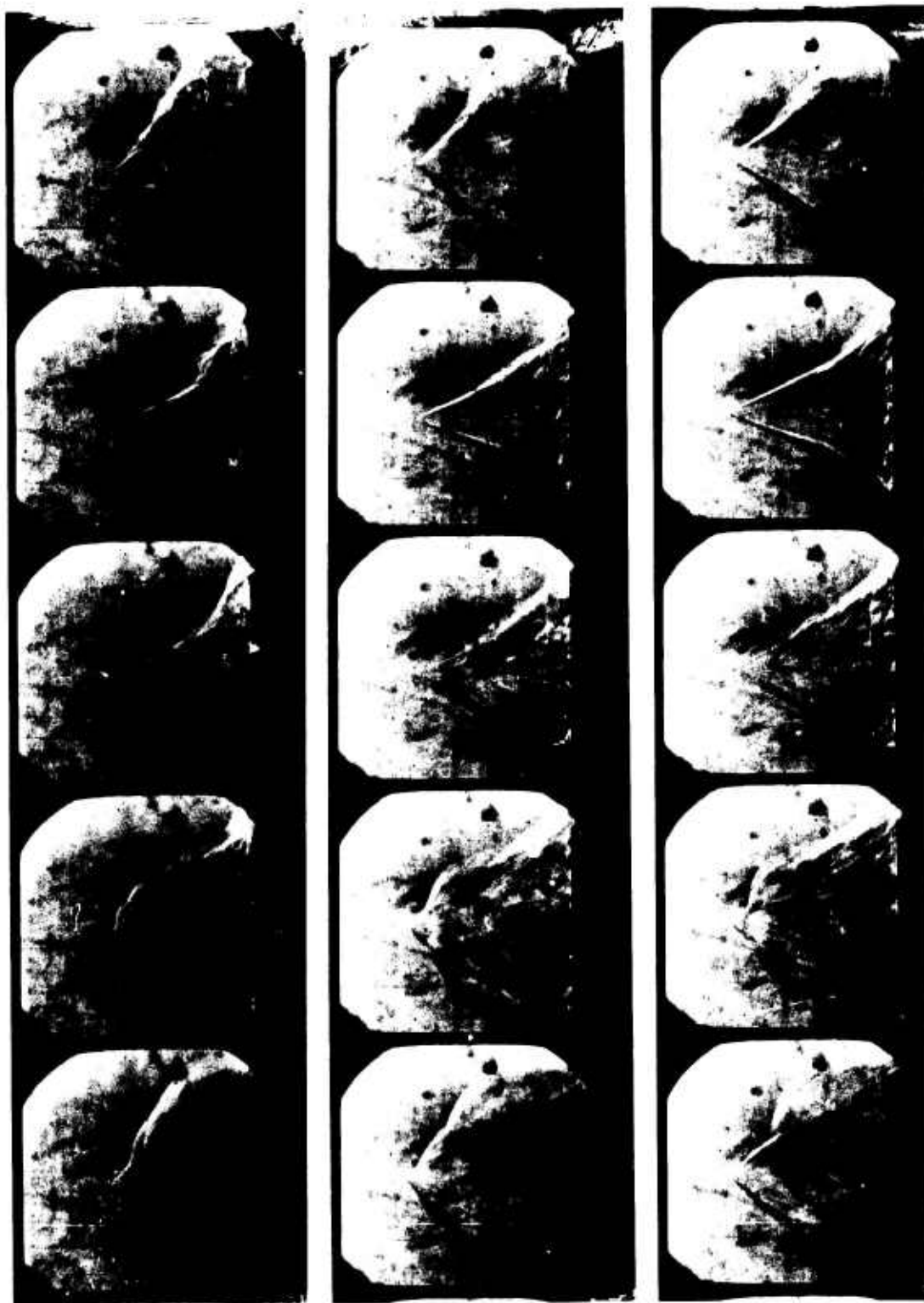


Figure 70 PARTICLE-INDUCED LARGE SCALE OSCILLATION (E) OF FLOW FIELD
(MACH 13)

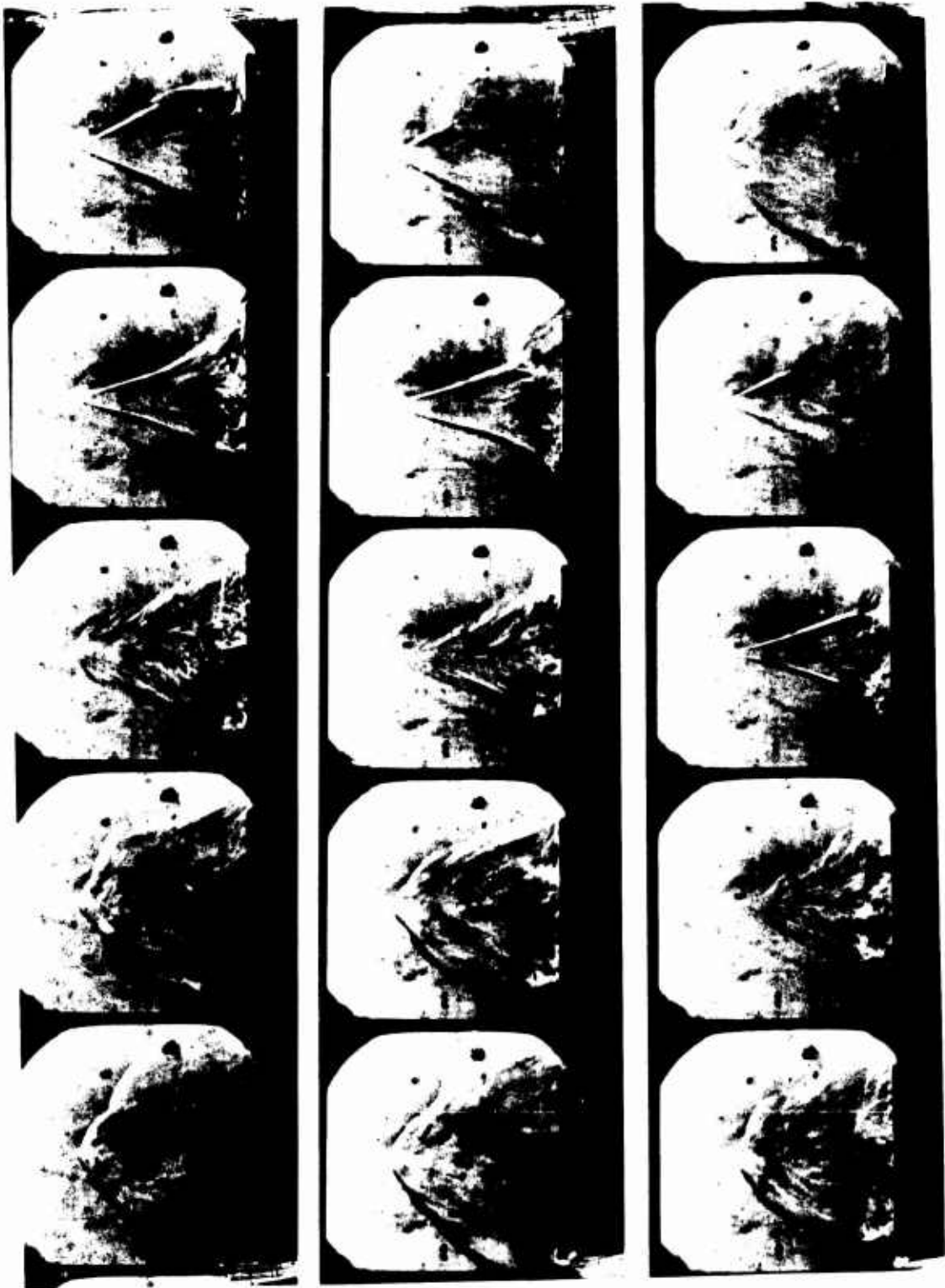


Figure 70 (continued)

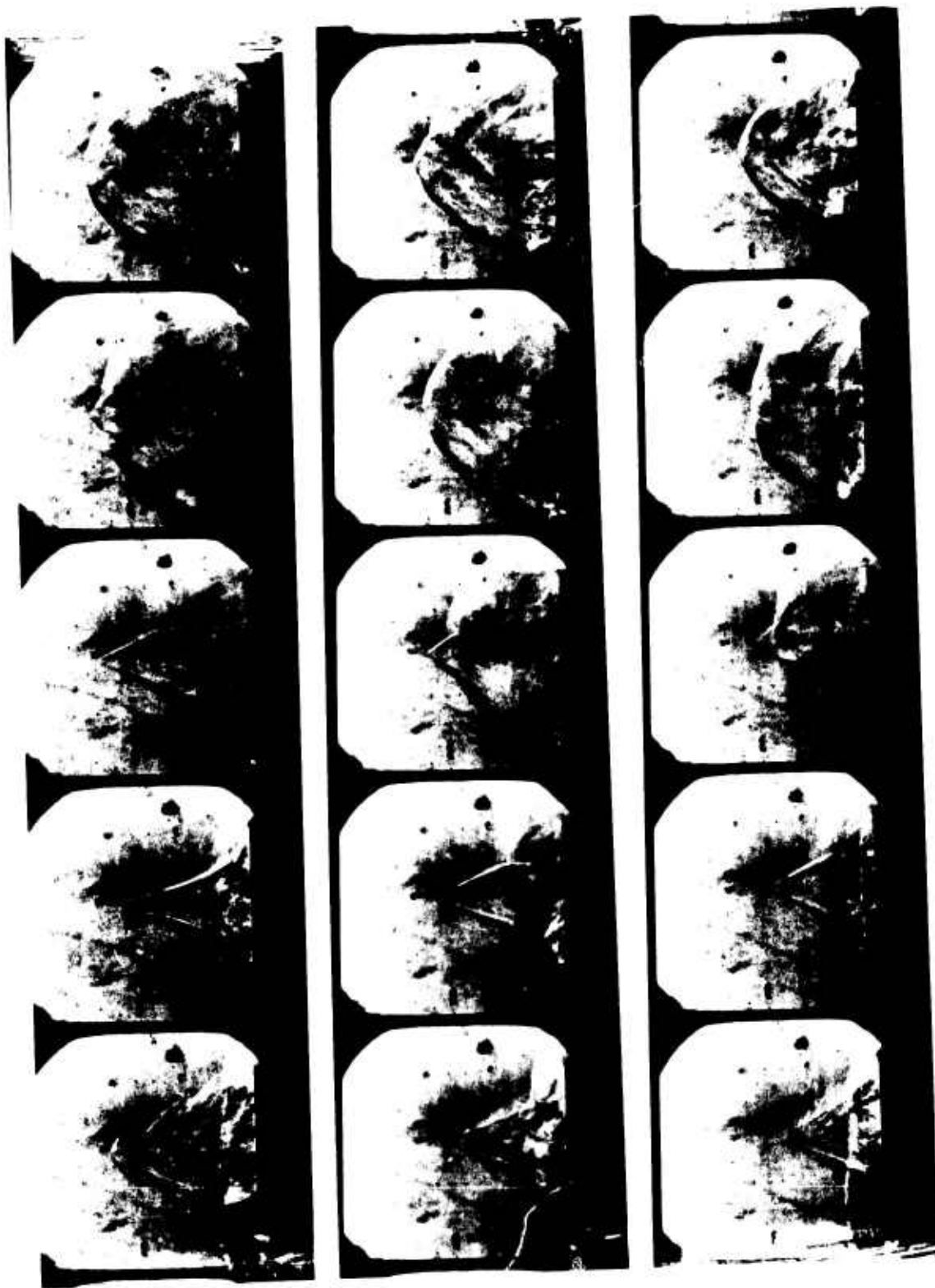


Figure 70 (continue1)

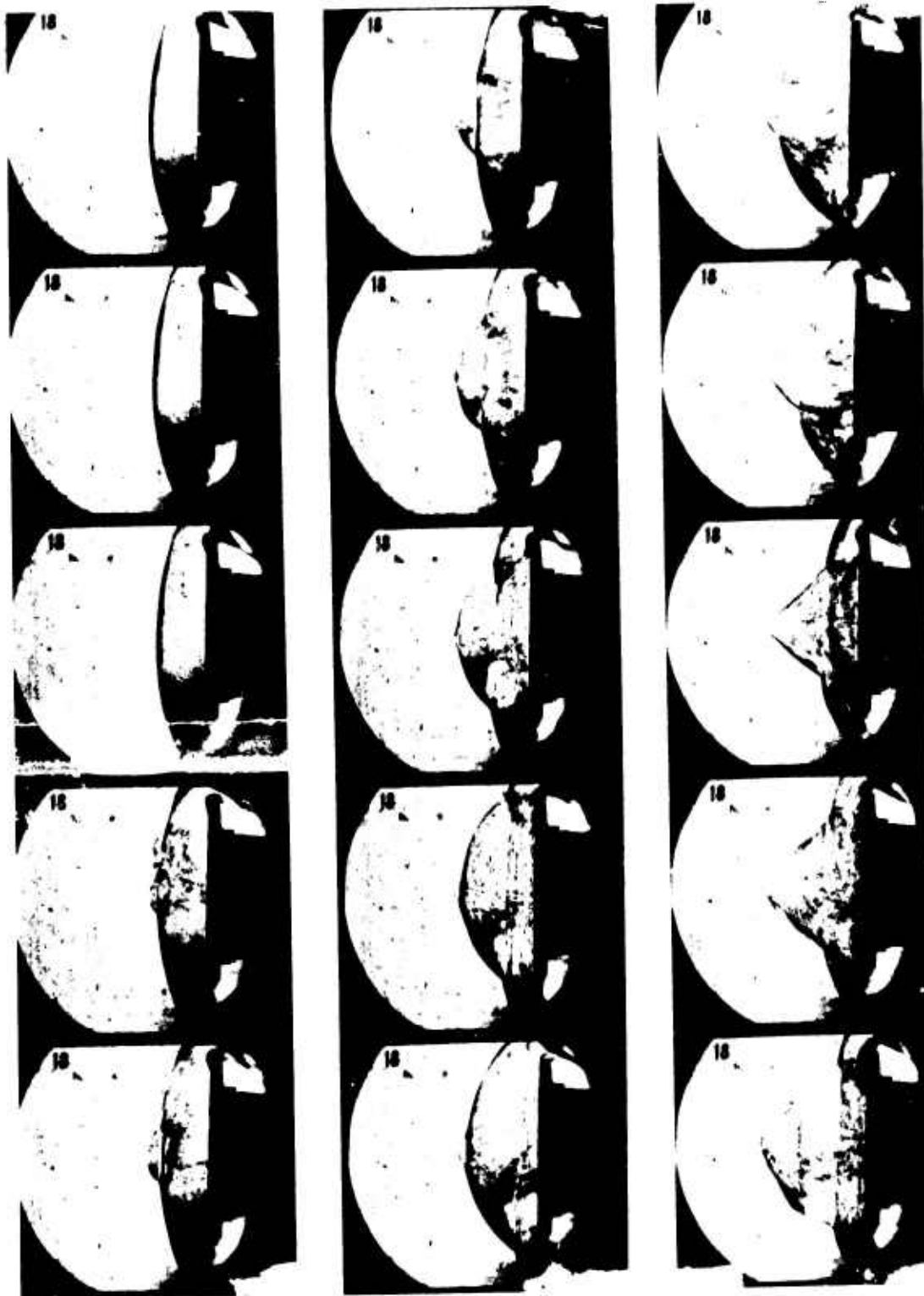


Figure 71 PARTICLE-INDUCED LARGE SCALE OSCILLATION (E) (MACH 6.5)

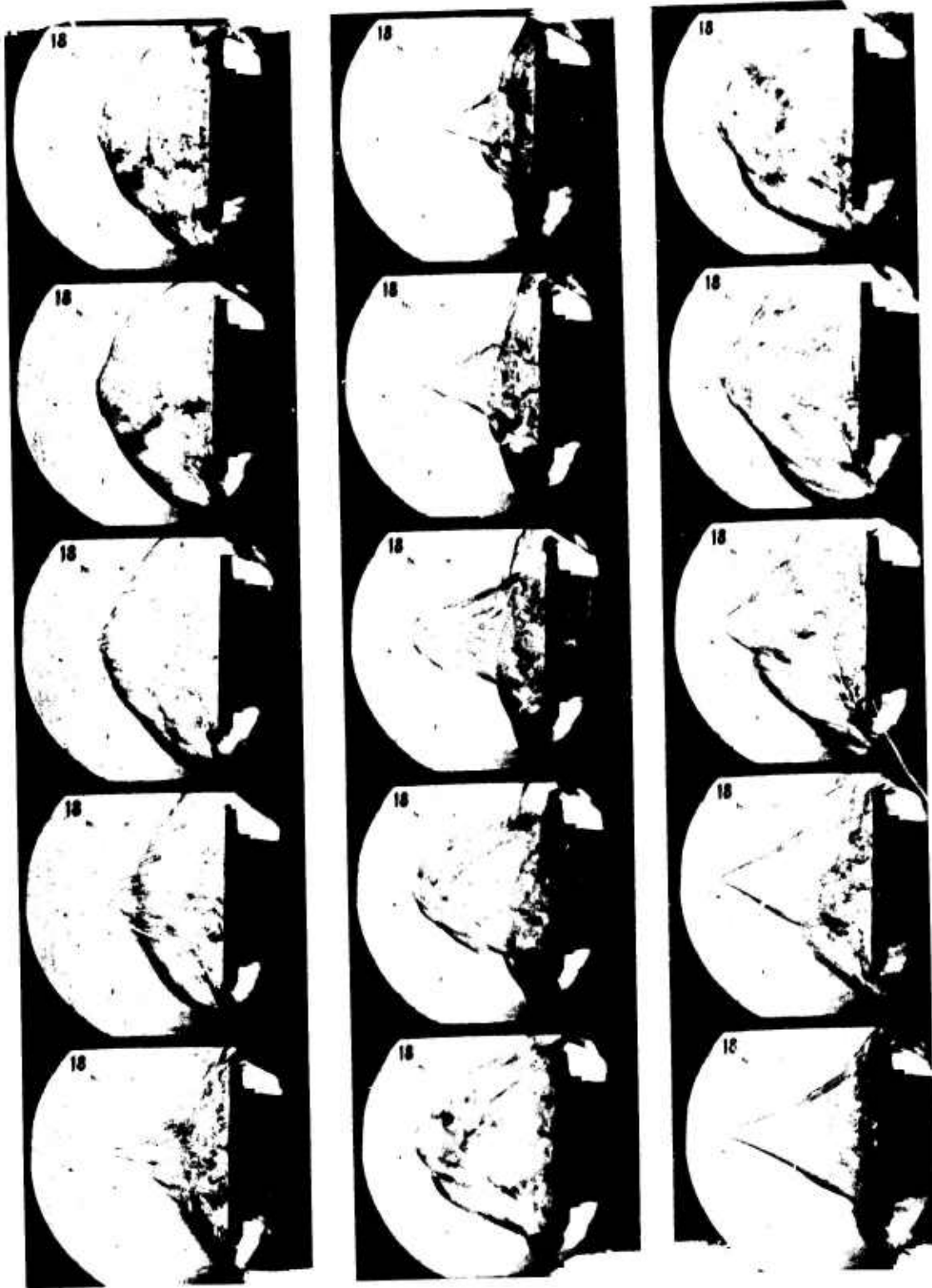


Figure 71 (continued)

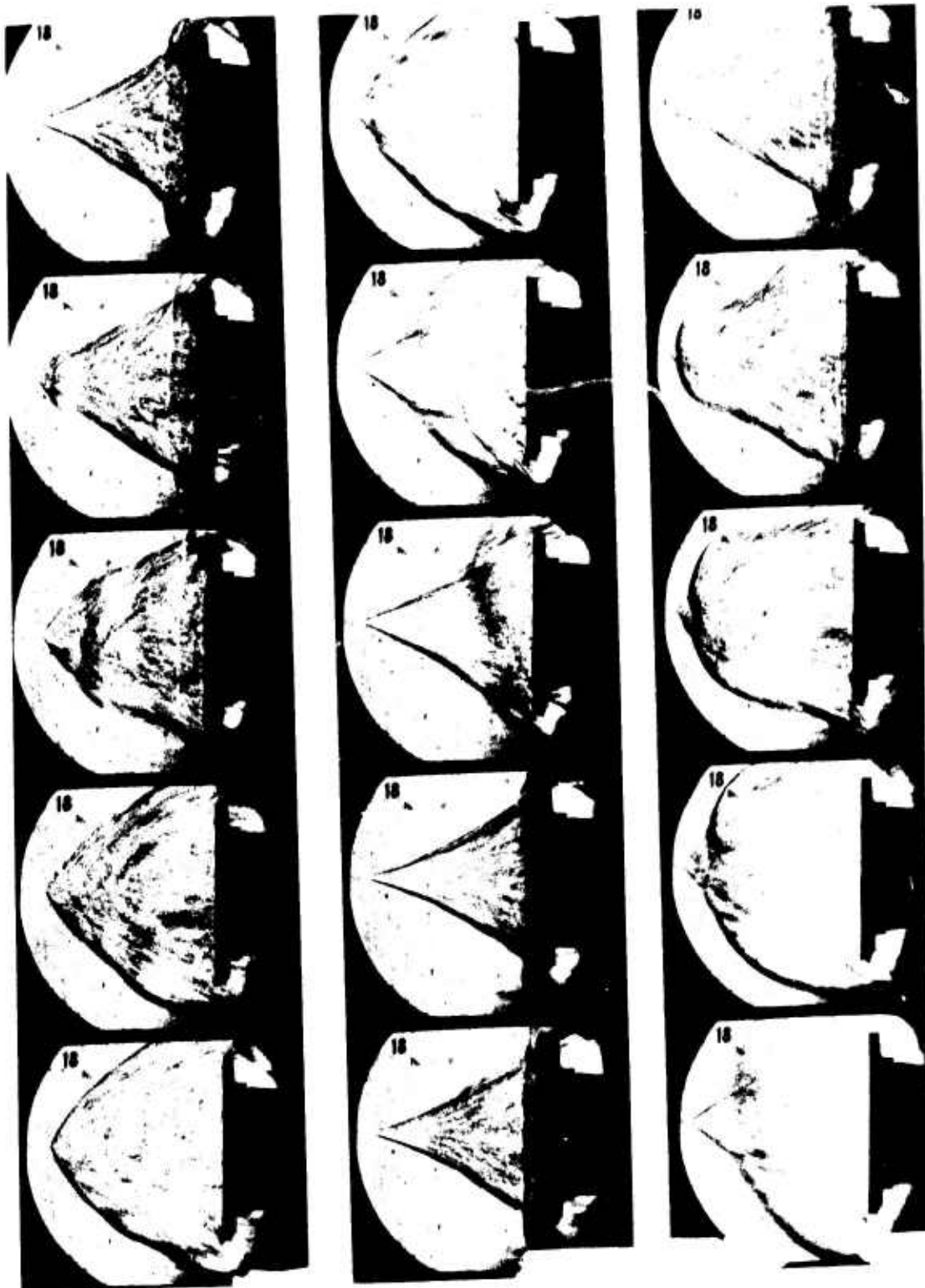


Figure 71 (continued)



Figure 71 (continued)

reforming the shear layer. Perhaps the most intriguing question is why two distinct shock structures, one around the minute particle and a second around the model are not formed at this juncture. Both the pressure and heat transfer records exhibited large excursions from the ambient conditions. A typical record from a thin film heat transfer gage on the face of the model is shown in Figure 72. After the tunnel starting process the gage is exposed to a period of constant heating equal to that observed for the unperturbed flow. The heating rate increases sharply as the particle interacts with the shock and the shear layer sweeps across the face of the model. A decrease in heating occurs as a bulbous shock layer is formed and the flow "collapses" toward the body. This pattern is repeated in a flow oscillation of surprising regularity and persistence. While the heating rates across the model vary with time, the magnitude of the maximum values do not appear sensitive to the exact particle trajectory as can be seen from the measurements made in two runs (shown in Figure 73) at identical free stream conditions but with different particle trajectories. This figure illustrates that the edge of the cylinder experiences the largest heat transfer rates, which can exceed the ambient heating levels by as much as a factor of five. The minimum heating rates fall close to the ambient heating level in the absence of a particle and correspond to the flow condition where the bow shock is collapsing back to the body. A typical variation of the fluctuating surface pressure close to the center of the model for this condition is shown in Figure 74. The maximum levels are roughly equal to the pitot pressure while minimum corresponds to the plateau pressure for conical separated flows over spiked bodies, supporting the postulation that a recirculation region is formed over the model during part of each cycle.

The basic features of particle-induced oscillations at Mach 12 described above were similar to those observed at Mach 6. A photographic sequence showing the E oscillation at this Mach number is shown in Figure 48. The heat transfer distribution for this condition (shown in Figure 75) again indicates that heating is a maximum toward the edge of the cylinder with an augmentation factor of over 5; however, the augmentation factors for the inner gages of approximately 3 are slightly larger than experienced on equivalent gages at the higher Mach number. Increasing the Reynolds number increased the magnitude of

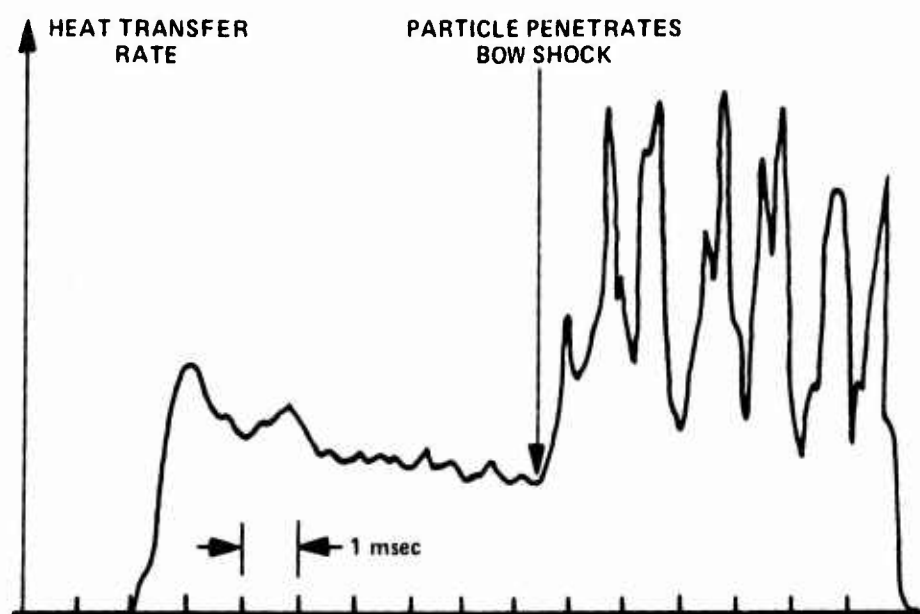


Figure 72 TYPICAL HEAT TRANSFER RECORD FROM THIN FILM GAGES

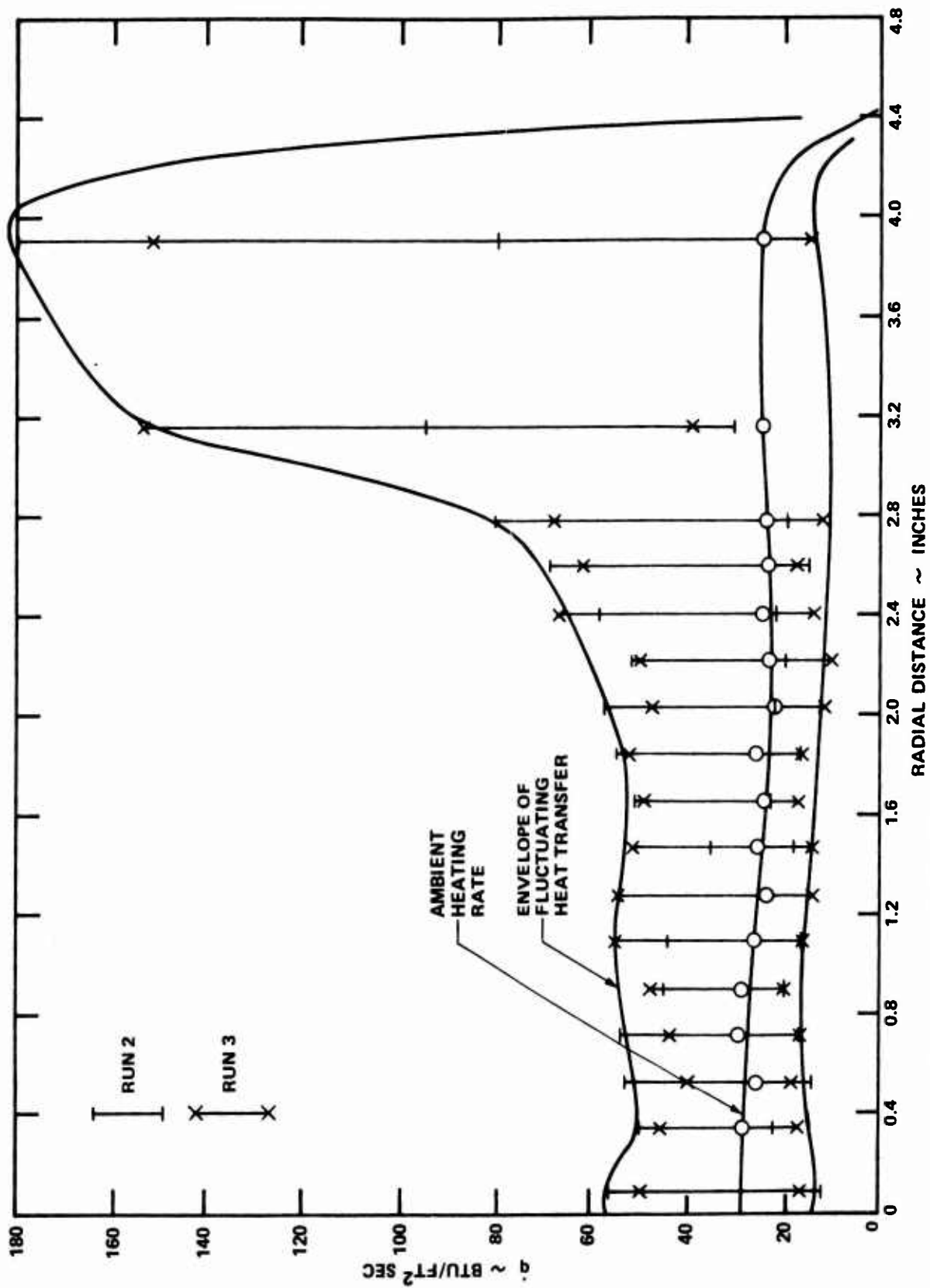


Figure 73 HEAT TRANSFER DISTRIBUTION TO THE FACE OF THE DISC FOR A FULLY OSCILLATING FLOW OVER THE MODEL

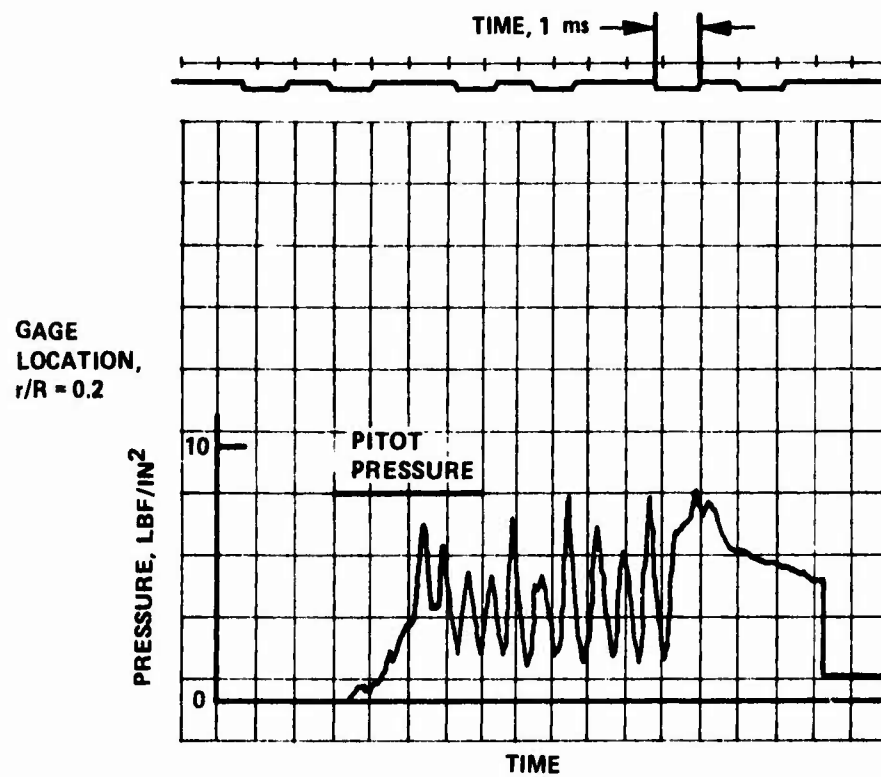


Figure 74 TYPICAL PRESSURE OSCILLOGRAM, RUN 3

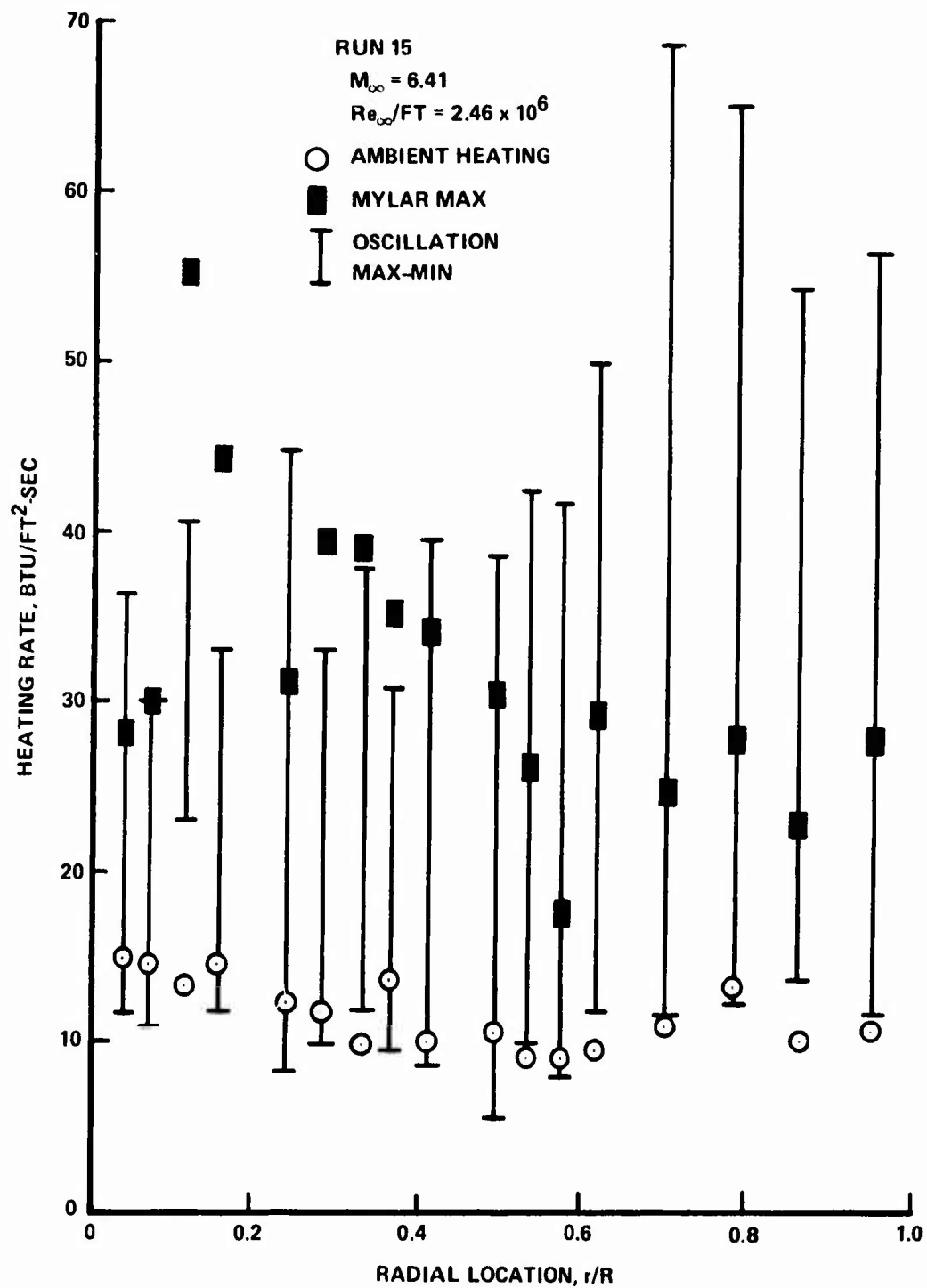


Figure 75 HEAT TRANSFER RATE DISTRIBUTION, RUN 15

heating to the center section of the cylinder (see Figure 76) suggesting that the flow is transitional or turbulent. Shown on Figures 75 and 76 are measurements of the maximum heating levels observed at the beginning of the run when minute particles of the mylar used to seal the throat of the nozzle were convected downstream before bouncing from the face of the model and interacting with the bow shock. These shock-shock interactions produced heating rates which were comparable with those induced in the larger scale oscillation principally because the same mechanism was responsible for the augmentation.

3. Augmentation for Off-Axis Trajectory - Some of the largest augmentation factors measured in the present studies were observed for trajectories where the particle moved off axis as shown in the photographic sequence in Figure 77. Here, because of the asymmetric nature of the motion, the mechanism which caused flow oscillation for the degree of penetration achieved by this particle was not activated. Instead the gas which normally would be trapped within a recirculation region escaped to one side of the model and a non-oscillatory interaction region swept across the model. The maximum heating levels observed on the face of the model are shown in Figure 78. These levels were observed for a period of just under 1 millisecond and the increased heating results from the same type of shock-shock interaction observed for the oscillatory flows. Finally, the photographic sequence shown in Figure 79 provides an example where an oscillation is first observed when the particle initially travels along the axis of symmetry; however, because it moves off axis, an asymmetric flow field results in the spillage of air from one side of the model and the stabilization of the oscillation. The particle is swept downstream and an unperturbed flow re-established over the model. Augmentation factors between 3 and 7 times the unperturbed heating levels are observed for this flow.

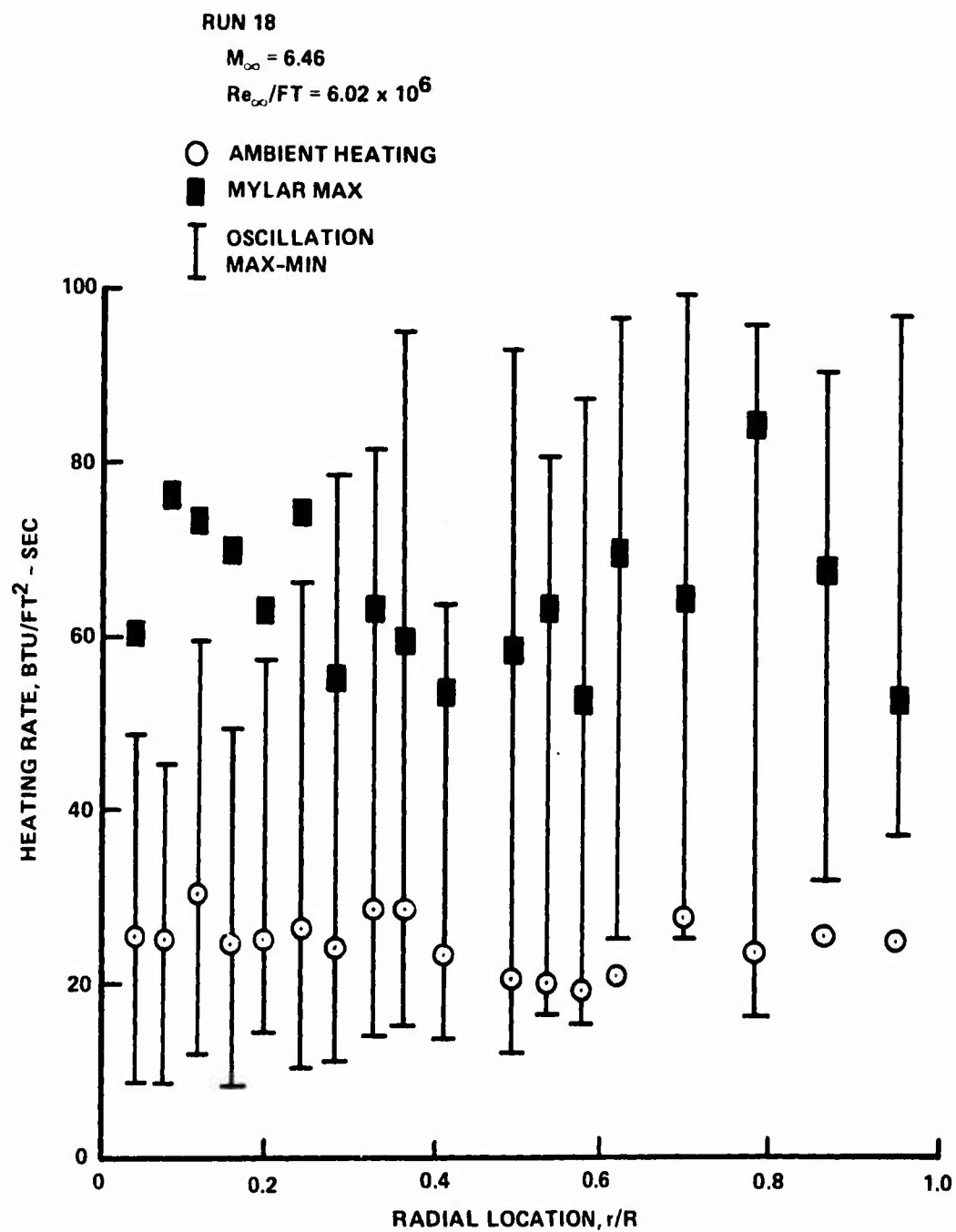


Figure 76 HEAT TRANSFER RATE DISTRIBUTION, RUN 18

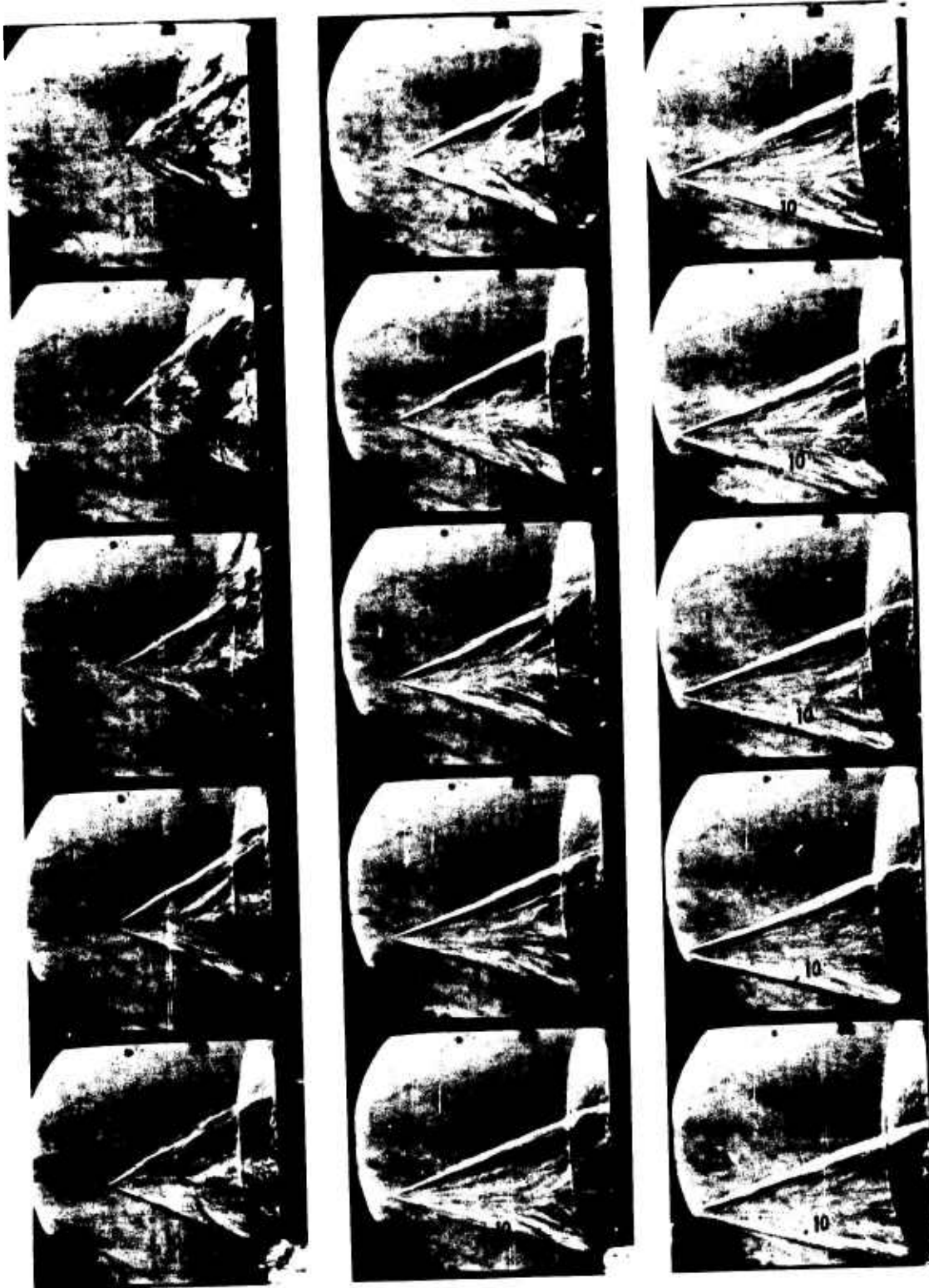


Figure 77 NON-OSCILLATORY FLOW RESULTING FROM OFF-AXIS PARTICLE TRAJECTORY

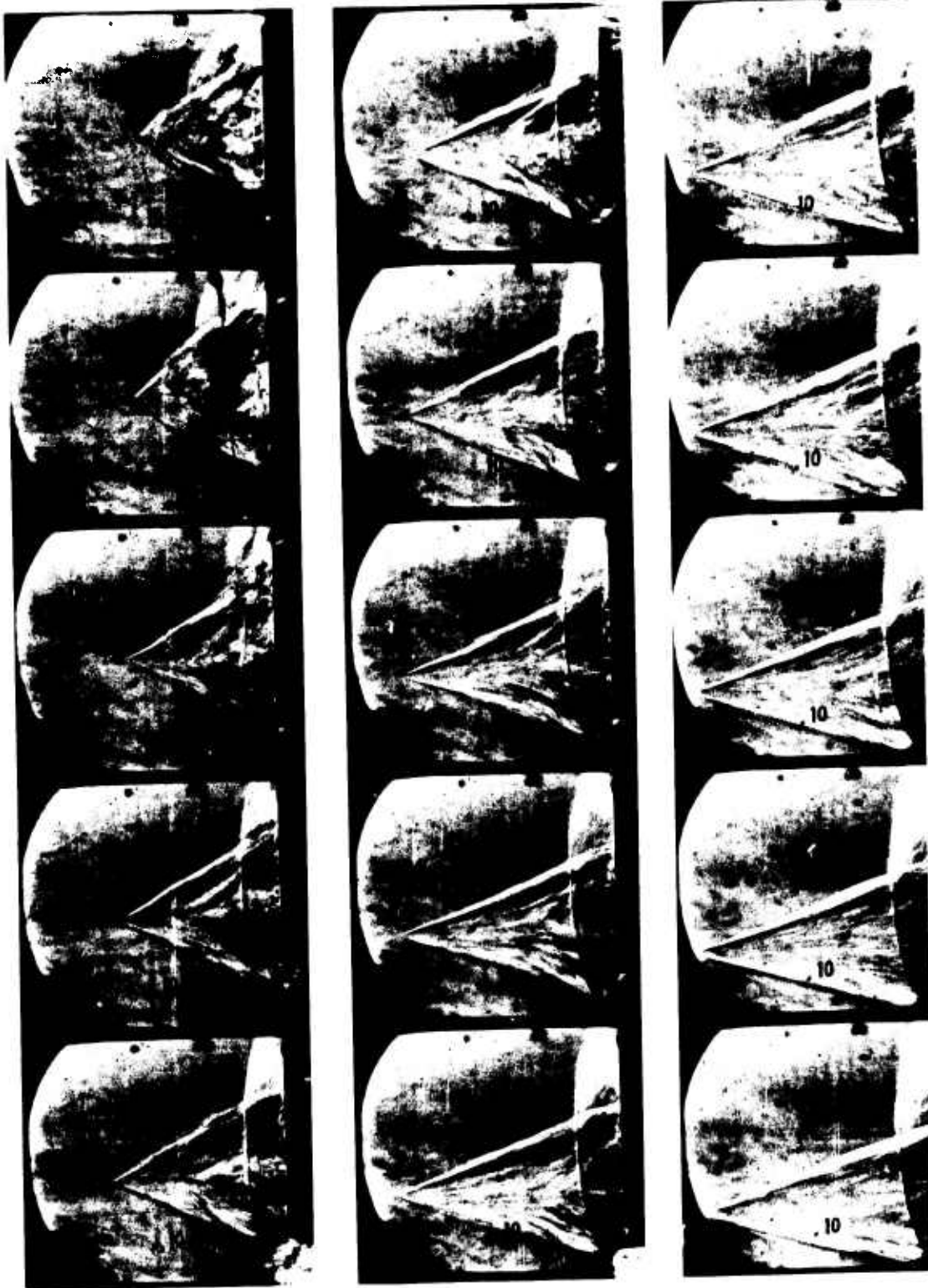


Figure 77 (continued)



Figure 77 (continued)

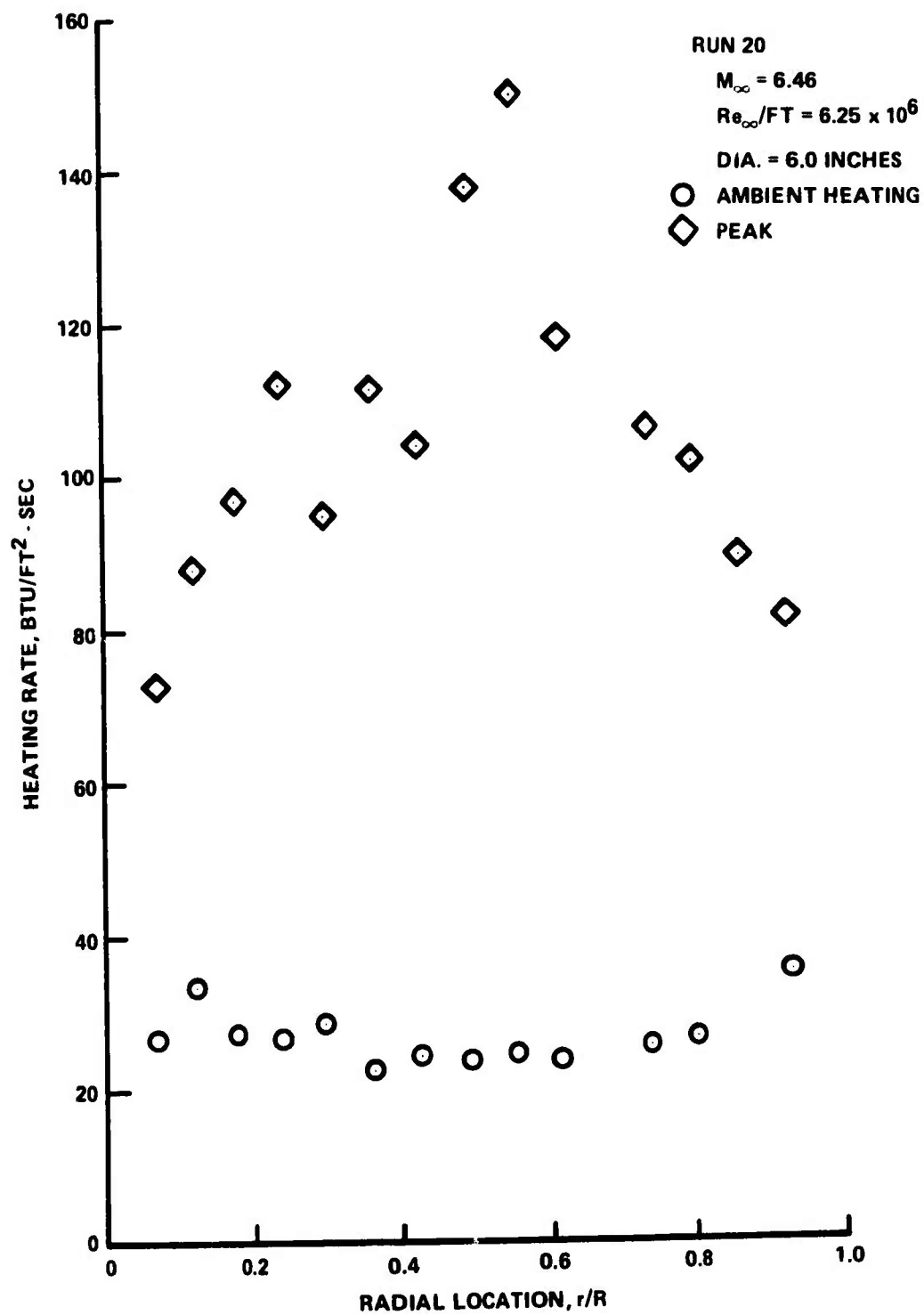


Figure 78 HEAT TRANSFER RATE DISTRIBUTION, RUN 20

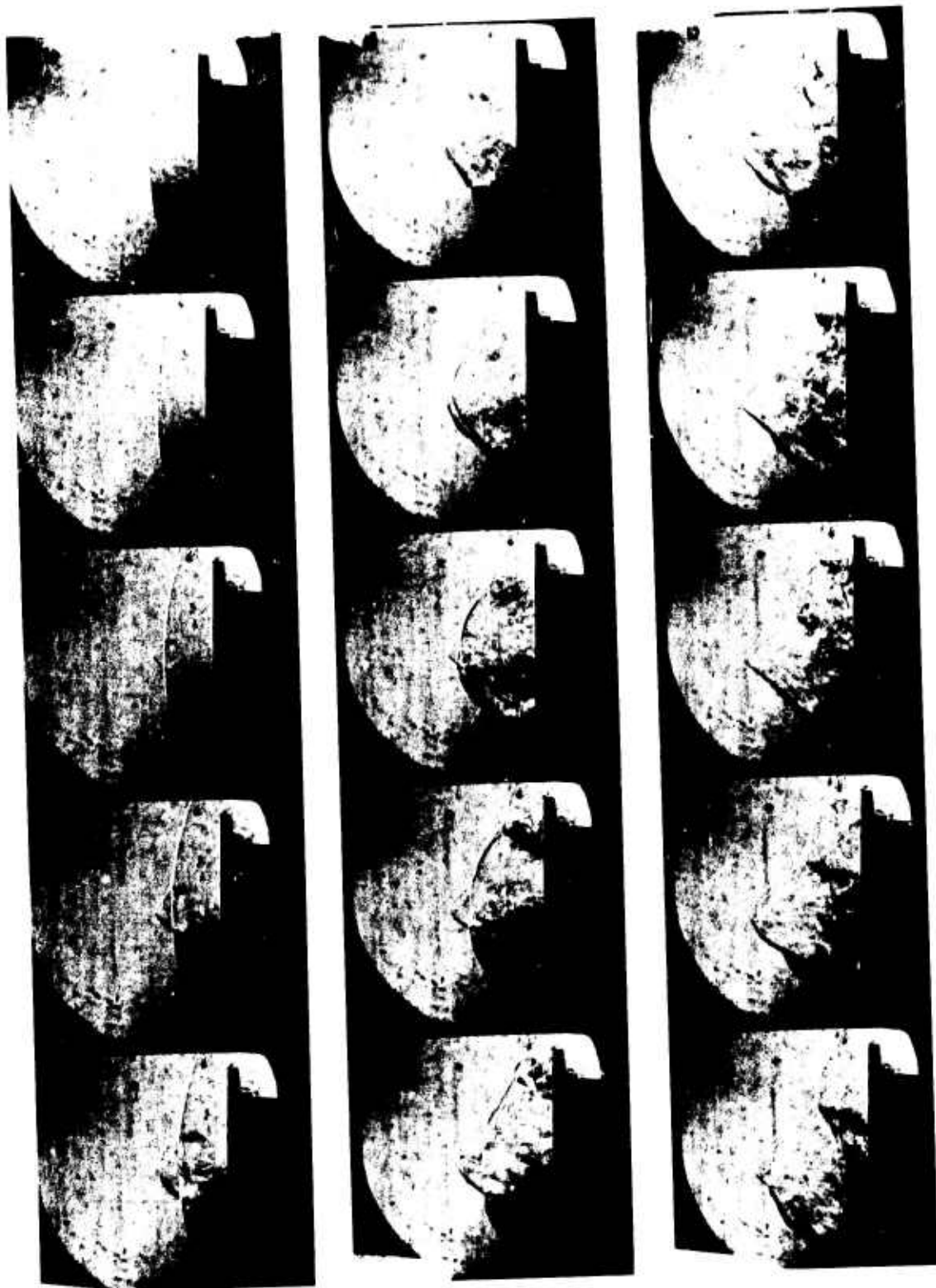


Figure 79 WEAK OSCILLATORY FLOW RESULTING FROM SMALL PENETRATION
AND OFF-AXIS TRAJECTORY

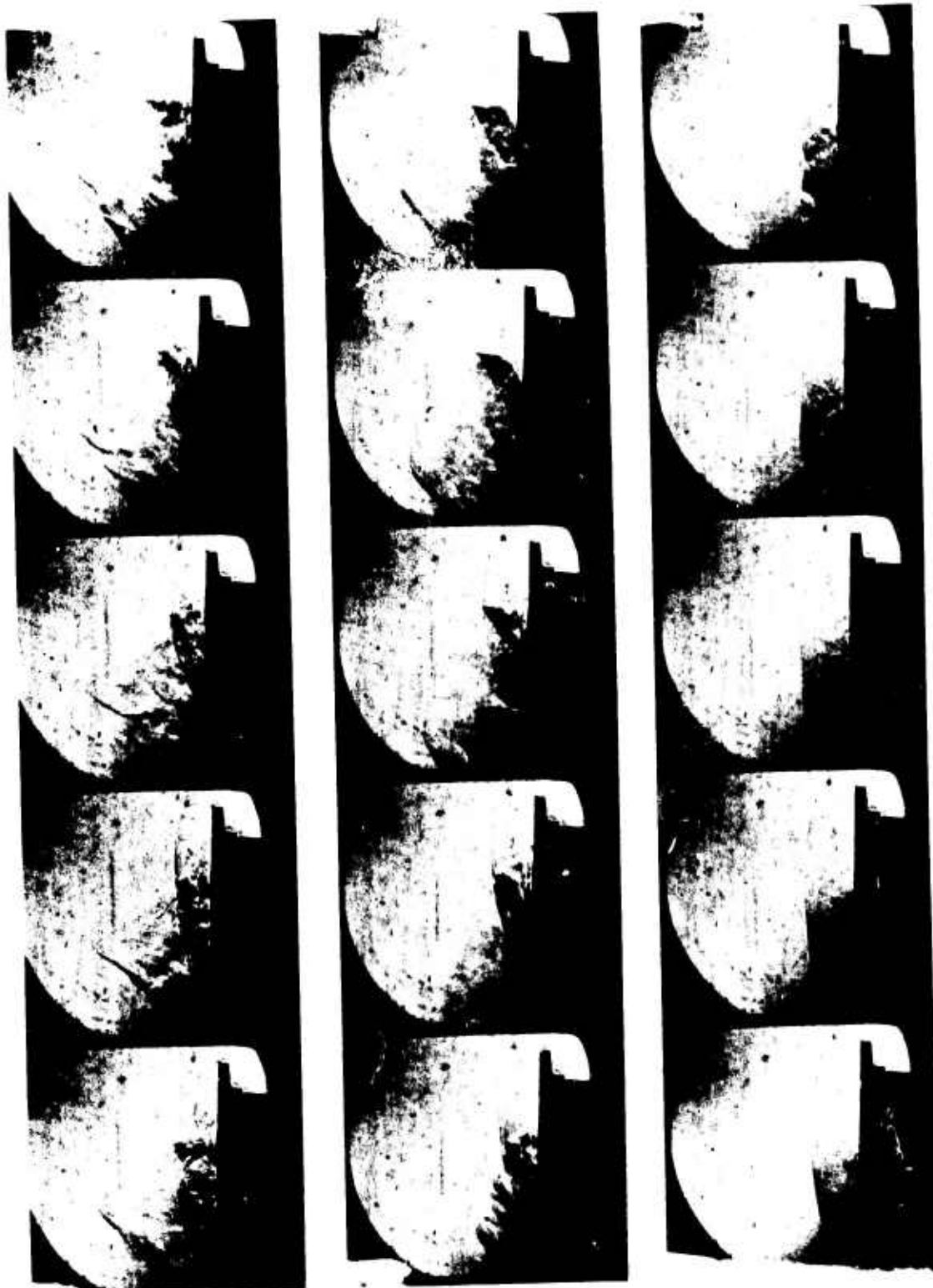


Figure 79 (continued)

3.3 FLUID DYNAMIC MECHANISMS IN AUGMENTATION HEATING

Studying the interaction between a single particle and the shock layer allows us to focus more accurately on the underlying mechanisms responsible of heating augmentation. The movement of a single small particle across the shock layer can be predicted with reasonable accuracy using simple Newtonian concepts employing a drag coefficient determined for free-molecular flows. In our studies with steel and silica particles between 100 and 800 microns in size we were unable to detect heating augmentation associated with interaction between the wake of the particle (in the shock layer) and boundary layer over the model. One might anticipate that the particle wake would increase the vorticity at the edge of the boundary layer increasing the local heating and/or "tripping" the laminar boundary layer in the stagnation region. If such effects were present, they did not create a measurable increase in heating for our system and conditions. The first measurable heating augmentation occurs when the toroidal vortex, formed when the particle causes a minor perturbation of the bow shock, is convected over the model boundary layer. The unsteady changes in the shock curvature in the region of shock-shock interaction are believed responsible for the formation and subsequent "roll-up" of an annular shear layer. The ring vortex so formed expands as it is convected over the body, and the increased heating can be explained in terms of increased vorticity of the edge of the boundary layer. If this vorticity acts to "trip" the originally laminar boundary layer then the heating augmentation can be correspondingly larger. When there is a sustained movement of the particle ahead of the bow shock then the interaction between the shock surrounding the flow field associated with the particle, and the bow shock enveloping the model, creates a shear layer or jet which attaches to the face of the model. The heating rates associated with such interactions have been explored by Holden in spiked body flows⁴ and Edney,⁶ and Keyes and Hains⁷ in regions of shock interference. It seems clear that major augmentation occurs when the "Edney Type IV" or "jet" interaction is established over the model. Until the shear layer is swept to the edge of the model for the first time, the movement of the particle can be predicted by simple drag models; however, when the flow begins to oscillate, the alternate formation and collapse of the recirculation region ahead of the body imposes a system of forces on the particle which makes its motion extremely complex. The

particle travels far beyond the point predicted by applying the simple laws of motion to an isolated particle in the free stream. As discussed earlier, the mechanism of oscillation is controlled primarily by simple inviscid flow considerations and $\frac{fD}{U}$ the non-dimensional frequency remains remarkably uniform at 0.16 and 0.19, figures similar to those obtained for the E oscillation over spiked bodies. Again, the maximum heating is found at the base of the re-attaching jet of shear layer where factors of 3 to 6 times the ambient unperturbed levels are observed. The minimum heating values were just less than those measured in unperturbed flow. Pressures on the flat face were found to vary between values just greater than the pitot pressure to minimums roughly equal to the plateau pressure corresponding to separated flow over the face of the model.

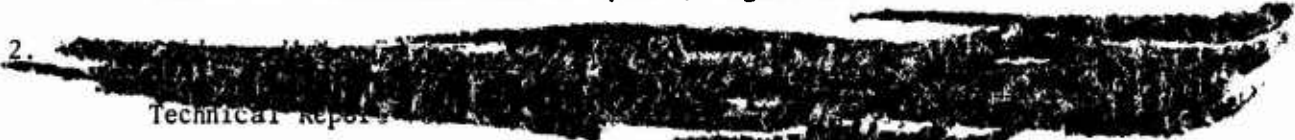
If the particle travels off axis permitting an asymmetric interaction region and asymmetric spillage, then a non-oscillatory interaction region can be observed. While the period of augmented heating is less for these cases, augmentation factors are observed. Again, the major mechanism is interference heating resulting from shock-shock interaction.

4. CONCLUSIONS AND RECOMMENDATIONS

An experimental study has been presented which demonstrates that a single minute particle, launched through the bow shock of a flat-ended cylinder, can induce severe distortions in the bow shock shape, augmenting the heating rates to the model surface by as much as a factor of 8. This investigation identified four distinctly different classes of flow phenomena resulting from particle-shock wave interaction together with temporally and spatially resolved heat transfer and pressure measurements associated with them. The most dramatic of these results when the particle penetrates more than a body diameter beyond the bow shock and massive flow instabilities similar to those encountered over spiked bodies are observed. These studies have identified the principle mechanism of enhancement heating as one associated with the reattachment of a jet/shear layer generated by particle shock-bow shock interaction after the particle has penetrated the bow shock. Future studies should investigate how nose tip

configuration influences the large heating augmentation and flow instabilities observed in the present studies. Measurements should be made to determine particle-induced augmentation over rough models under fully turbulent boundary layers. The studies should be extended to include multiple particle interactions and off-axis launch. Skin friction measurements in addition to the measurements of heat transfer and pressure should be made to better define the flow adjacent to the model surface.

REFERENCES

1. SAMS0-TR-73-272, "Minuteman Hot Structure Heating Augmentation Study - Volume I: Mechanisms and Analyses", August 1973.
2. 
Technical Report
3. Calspan Hypersonic Shock Tunnel, Description and Capabilities, Brochure, 1973.
4. Holden, M.S., "Experimental Studies of Separated Flows at Hypersonic Speeds--Part I: Separated Flows over Axisymmetric Spiked Bodies" AIAA Journal, Vol. 4, No. 4, (April 1966).
5. Holden, M.S., "Studies of Transitional Heating and Flow Instabilities Over Ablated Nose Shapes", Calspan Report Number AB 5646-A1-1, September 1975.
6. Edney, B.E., "Anomalous Heat Transfer and Pressure Distributions on Blunt Bodies in the Presence of an Impinging Shock", The Aeronautical Research Institute of Sweden, Report FFA-115, February 1968.
7. Keyes, J.W. and Hains, F.D., "Analytical and Experimental Studies of Shock Interference Heating in Hypersonic Flows", NASA TN D-7139, May 1973.
8. Wilkinson, H.R., Marcisz, T.J., Gustafson, G.Q., D'Attorre, L., and Bilyk, M.A., "Flow Phenomena in Particle-Induced Convective Heating Augmentation", Report DNA 3799F, 30 January 1976.

Appendix A
EXPERIMENTAL FACILITIES AND MEASUREMENT TECHNIQUES

A.1 EXPERIMENTAL FACILITIES

The experimental programs were conducted in Calspan's 48-inch and 96-inch Hypersonic Shock tunnels (Ref. 14). The operation of these tunnels can be shown simply with the aid of the wave diagram shown in Figure 80a. The tunnel is started by rupturing a double diaphragm which permits the high pressure air in the driver section to expand into the driven section, and in so doing generates a normal shock which propagates through the low pressure air. A region of high temperature, high pressure air is produced between this normal shock front and the gas interface between the driver and driven gas, often referred to as the contact surface. When the primary or incident shock strikes the end of the driven section, it is reflected leaving a region of almost stationary high pressure heated air. This air is then expanded through a nozzle to the desired free stream conditions in the test section.

The duration of the flow in the test section is controlled by the interactions between the reflected shock, the interface, and the leading expansion wave generated by the non-stationary expansion process occurring in the driver section. At Calspan we normally control the initial conditions of the gases in the driver and driven sections so that the gas interface becomes transparent to the reflected shock, as shown in Figure 79; thus, there are no waves generated by interface-reflected shock interaction. This is known as operating under "Tailored-Interface" conditions. Under this condition, the test time is controlled by the time taken for the driver-driven interface to reach the throat, or the leading expansion wave to deplete the reservoir of pressure behind the reflected shock; the flow duration is said to be either driver gas limited or expansion limited, respectively. Figure 80b shows the flow duration in the test section as a function of the Mach number of the incident shock. Here it can be seen that for operation at low M_1 , running times of over 25 milliseconds can be obtained with a long driver section. When run under these latter conditions at high pressures and Reynolds numbers,

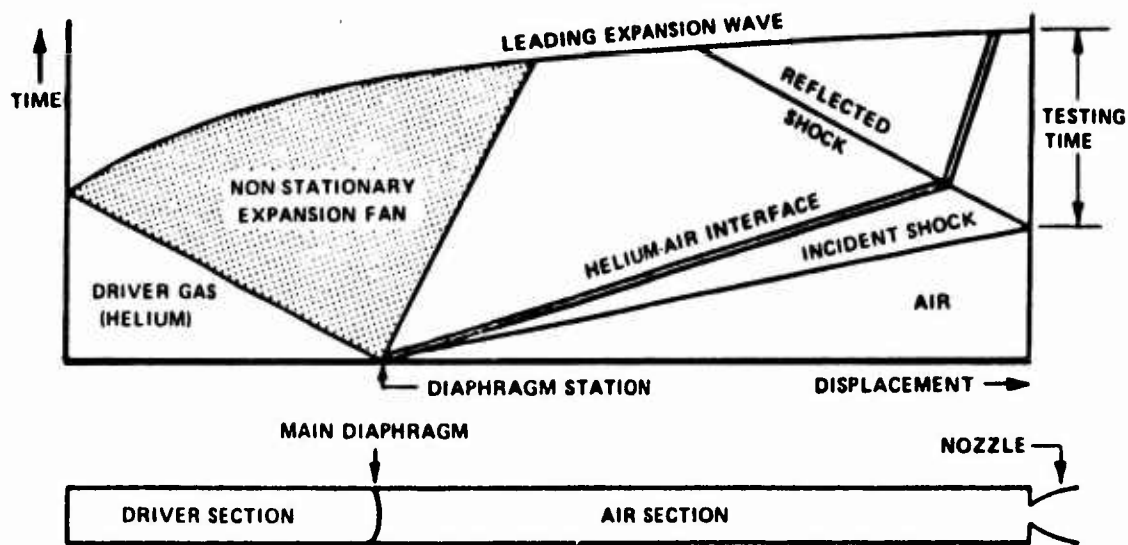


Figure 80a WAVE DIAGRAM FOR TAILORED-INTERFACE SHOCK TUNNEL

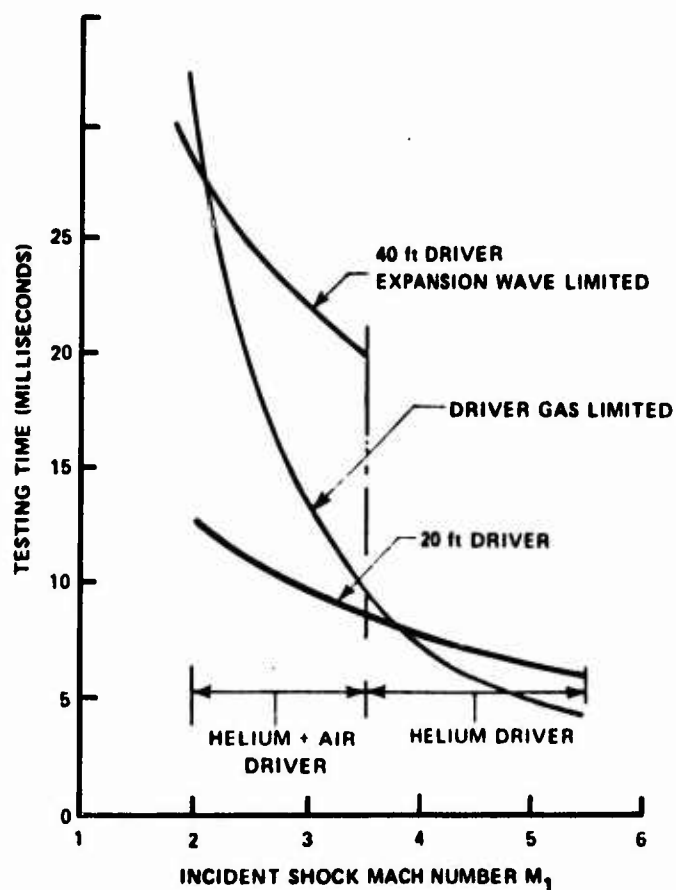


Figure 80b TEST TIME AVAILABLE FOR TAILORED-INTERFACE OPERATION OF 48-INCH SHOCK TUNNEL

the test running times are of the same magnitude or longer than for piston driven tunnels (Ref. 15, 16) with comparable stagnation temperature, and the reservoir conditions and flow quality are superior to piston driven tunnels. This is due to the fact that the test gas has been processed by a simple reflected shock rather than multiple shocks as in piston tunnels. A further consequence is that the free stream conditions can be calculated with far more accuracy in a shock tunnel.

It is interesting to note that if sensitive high frequency instrumentation is to be used in the very severe heating conditions encountered in turbulent interaction regions in hypersonic flow, running times longer than 20 milliseconds present distinct problems because the sensing element can be damaged or destroyed by overheating since it must be placed close to the flow environment.

By running the shock tunnels at low incident shock Mach numbers and high driver pressures, we can generate test conditions in which we can obtain very large Reynolds numbers. The large test core allows us to use models which are at least 3 feet in length. The maximum Reynolds number capabilities of the tunnels are shown in Figure 81. Under these maximum Reynolds number conditions, the location of the end of natural transition on flat plate models as determined from heat transfer and other measurements, is shown in Figure 82.

A.2 MODEL AND FLOW FIELD INSTRUMENTATION

A.2.1 Introduction

To make a meaningful study of regions of unsteady flow over nose-tip configurations, measurements of both the mean and the fluctuating flow field should be obtained. Our studies indicated that to obtain the complete power spectrum for the surface pressure, a frequency response from 200 Hz to 100 kHz was required. The measurements of skin friction and heat transfer in the separation and reattachment regions indicated that a frequency of at

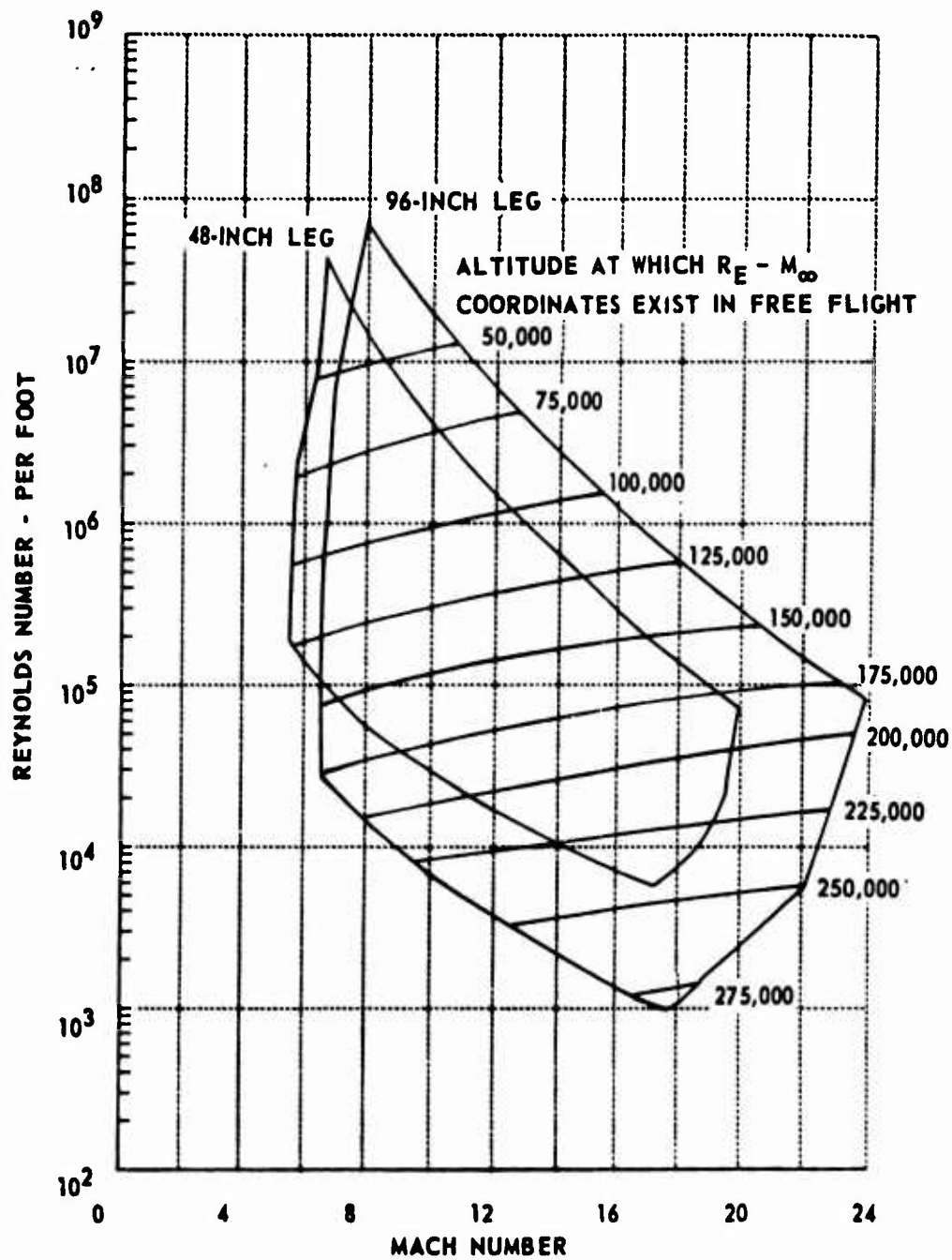


Figure 81 CALSPAN HYPERSONIC SHOCK TUNNEL PERFORMANCE

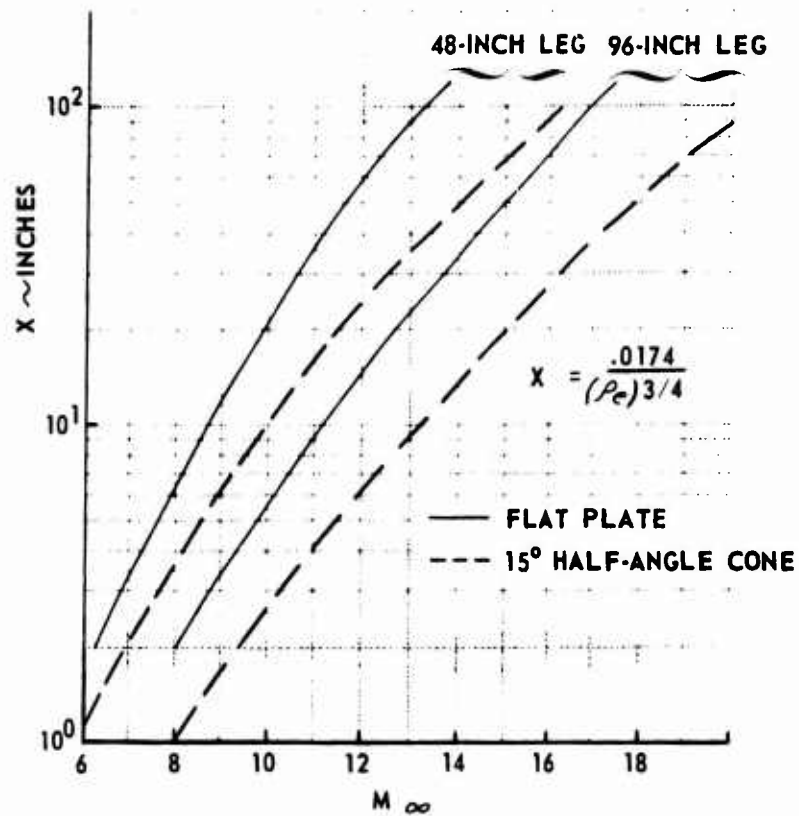


Figure 82 MINIMUM TRANSITION DISTANCE ON SHARP FLAT PLATE MODELS FOR CALSPAN HYPERSONIC SHOCK TUNNELS

least 10 kHz was required to follow the motion of the separation and reattachment points. It is also desirable to make fluctuation measurements through the flow field to help establish the source and mechanism which generated the high level of heat transfer pressure fluctuation observed.

A.2.2 Skin Friction Measurements

In order to define separation and the length of separated regions accurately in separated regions over ablated nose tip shapes, it is important to measure the surface shear. The inherent unsteadiness of these regions also makes it desirable to follow the fluctuations in the wall shear to trace the movement of the separation and reattachment points and hopefully gain some insight into the fluid mechanics of such motions. Our recent studies indicate that a frequency response of at least 10 kHz is required to follow these movements in hypersonic flow.

In axisymmetric regions of viscous interaction, separation is defined as the condition at which the surface is zero at one point only in the interaction region. Because direct measurements of surface shear are difficult to make, pressure distribution, surface pitot, and oil flow measurements have been used to determine separation. Pressure distribution measurements have been shown by Green (Ref. 17) and by Spaid and Frishett (Ref. 18) to be an extremely poor indicator of boundary layer separation in supersonic flow. Holden (Ref. 19) found this technique was even more insensitive at hypersonic speeds. From our studies we have noted that the introduction of a small disturbance into the laminar sublayer beneath the sonic line can cause dramatic effects both in the immediate vicinity and downstream of the disturbance.

On our studies of the separation of turbulent boundary layers in hypersonic flow, we have used a gage (Ref. 20) which directly measures surface shear to indicate the separation condition. A diagram of the skin friction

transducer which we would use in the proposed studies is shown in Figure 83. The transducer consists of a diaphragm which is supported flush with the model surface by two piezo-ceramic beams, which develop a charge when placed in bending by a surface shear on the diaphragm. A third beam is used to provide acceleration compensation; the beams are connected electrically to eliminate thermal, normal, and transverse pressure effects. An FET impedance transform circuit is mounted internally to eliminate cable noise effects at low levels of skin friction. The gage, which has been refined and developed over the past 12 years, has been used to measure very low levels of skin friction encountered in separated regions in low Reynolds number hypersonic flow and more recently very high levels in regions of shock wave-turbulent boundary layer interactions in hypersonic flow. Because of the very severe heating conditions encountered in the latter studies, special care was taken to minimize the heat conduction through the flexures. The very large dynamic loads generated on the transducers during tunnel shutdown when run at the high dynamic pressure conditions used in our studies caused the diaphragms to be torn from the supporting beam. This problem was overcome by careful design of the flexure and by mounting the transducer in the seismic mass-rubber suspension system shown in Figure 83.

A.2.3 Heat Transfer Instrumentation

A knowledge of the heat transfer distribution on nose tips is of great importance because of the very severe heating rates generated in the reattachment region. Almost as important as the severity of reattachment heating is the extremely large heat transfer gradients which occur both in the separation and reattachment regions. Regions of high heat transfer gradient present a problem to the experimenter because they can cause transverse heat conduction problems in the model. This can distort heat transfer distributions and in some cases dramatically reduce the maximum indicated heating. An example which illustrates this feature is given in the report of Hiers and Loubsky (Ref. 21) where they used a thin skin technique to obtain

heat transfer measurements in regions of turbulent viscous layer attachment. They found that the corrections to their measurements were of the same magnitude as the measurements themselves. To reduce transverse heat conduction along the model surface, the model should be made from a non-conducting material; this is incompatible with the thin skin technique unless a segmented model is used. To overcome these problems we use a measurement of heat transfer which relies on sensing the transient surface temperature of a non-conducting model by means of thin-film resistance thermometers. Because the thermal capacity of the gage is negligible, the instantaneous surface temperature of the backing material is related to the heat transfer rate by the classical semi-infinite slab theory. Analog networks are used to convert the outputs of the gages, which are proportional to surface temperature, to a voltage directly proportional to heat transfer. The thin film gage has a frequency response to 1 MHz.

The gages are fabricated on either small pyrex buttons or on contoured inserts, the ability of this technique to make closely spaced measurements in regions of shock impingement is demonstrated in Figure 81.

A.2.4 Surface and Flow Field Pressure Measurements

We employed two types of surface pressure transducers in our shock tunnel studies. The Calspan-designed and constructed lead zirconium titanate piezoelectric pressure transducers (Ref. 22) were used to obtain essentially the mean pressure distribution through the interaction region, though the transducer and orifice combination could follow fluctuations up to 15 kHz. A second flush-mounted transducer, especially designed for high frequency measurements by PCB in Buffalo, was used to obtain surface pressure fluctuation measurements from 200 Hz to 120 kHz. To prevent a resonance, a special mounting system was developed (as shown in Figure 84) to lock the gage firmly into the model. A thin insulating barrier of aluminized mylar was attached to the diaphragm of the transducer to prevent thermal heating effect caused by the large heat transfer rates (over 500 Btu/ft² sec) generated in the reattachment regions.

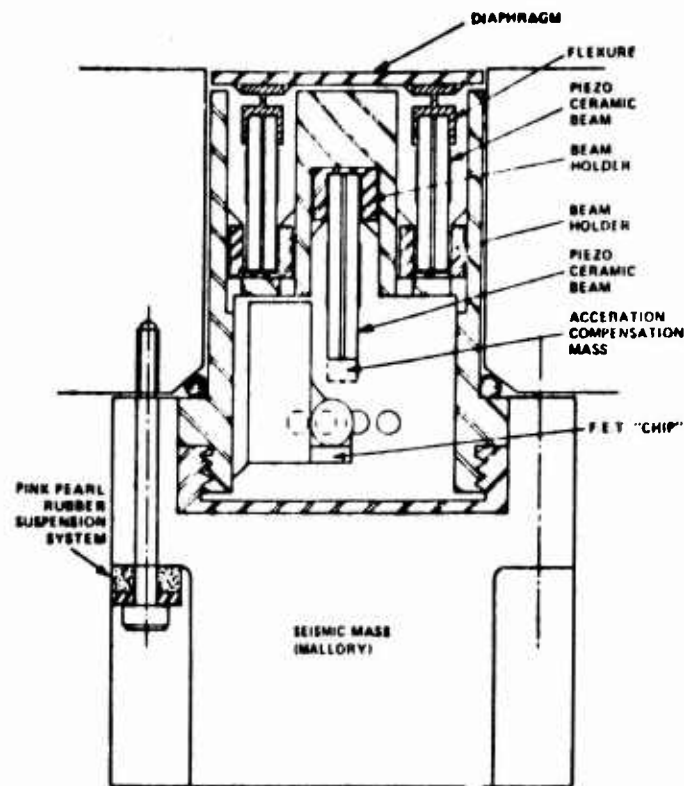
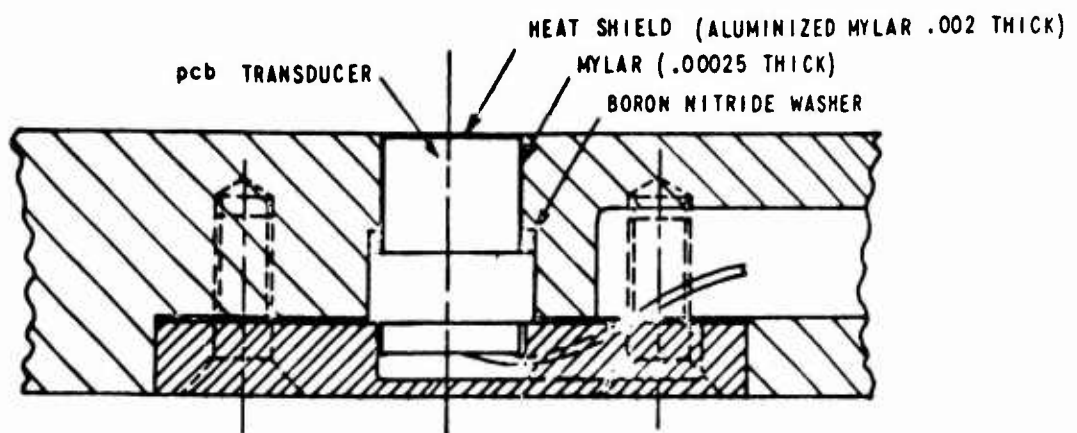


Figure 83 DRAWING OF SECTION THROUGH SKIN FRICTION TRANSDUCER



(a) TYPICAL MOUNTING TECHNIQUE USED IN MODEL

Figure 84 HIGH-FREQUENCY PRESSURE MOUNTING

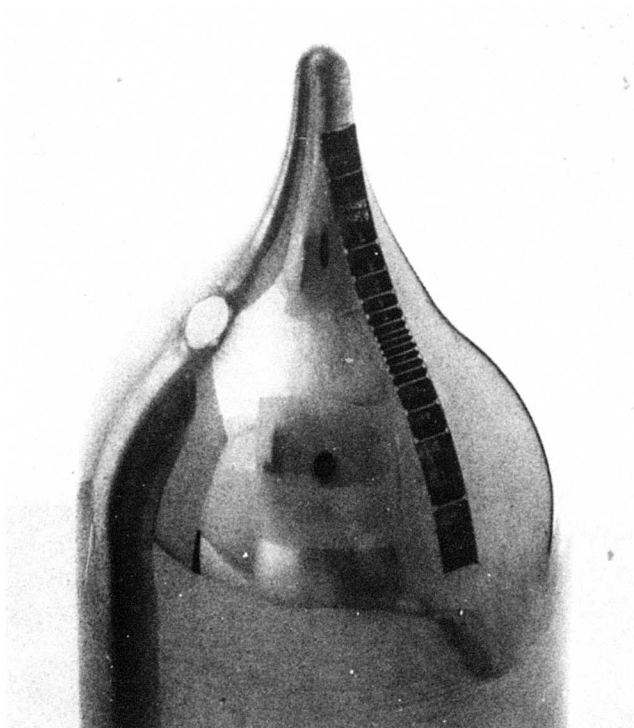
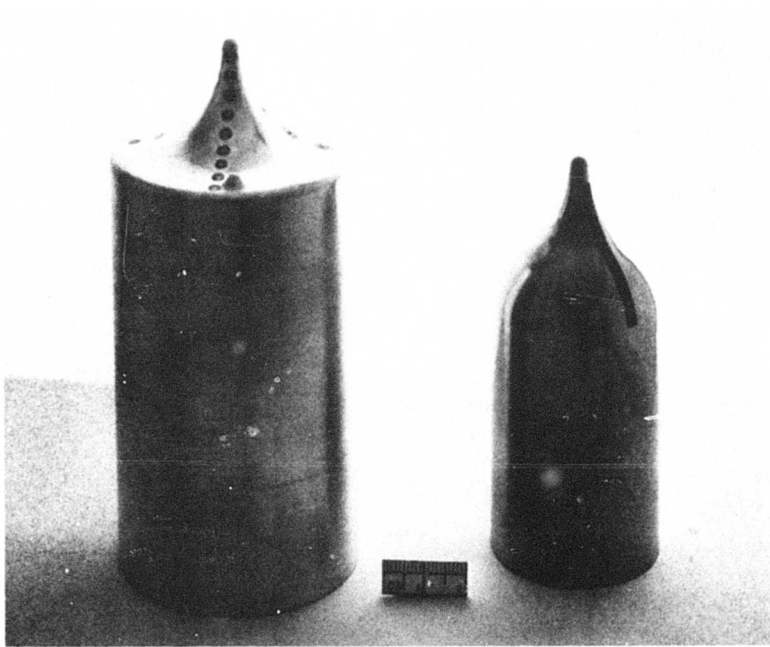


Figure 85 MODELS SHOWING TYPICAL HEAT TRANSFER GAGE INSTALLATION

A.2.5 Data Recording and Processing

The outputs from the transducers are recorded on a NAVCOR (Ref. 14) magnetic drum system and on CEC and AMPEX FM tape recorders, and monitored on oscilloscopes. The NAVCOR system, which can hold 48 channels of data in digital form, is essentially a low frequency response system which will record the mean output of the gages over the running time. The fluctuation measurements will be recorded on the FM tape recorders in analog form and subsequently converted into digital form by the analog-to-digital conversion/data storage system developed at Calspan.

The fluctuation data, in punched card form, are then processed by an existing digital computer program to obtain the statistical properties -- Root Mean Square Pressure, Power- and Cross-Spectra, and Auto- and Cross-Correlation functions.

A.2.6 Single Frame and High Speed Motion Schlieren Photography

A single-pass Schlieren system with a horizontal knife-edge was employed in all of the studies of high Reynolds number, high Mach number flows over ablated nose shapes. However for the studies of the low Reynolds numbers aerodynamics of the Widhopf 1 and 2 nose tips we employed a double-pass system with a high degree of cut-off. Here we used a single frame camera with a microsecond spark to record the event. We used a Red Lake high speed movie camera with speeds of up to 10,000 frames per second to record the flow oscillation occurring about the highly ablated nose shapes and the particle-launch model.

CONCLUSIONS

A unique set of experimental measurements have been reported which demonstrate that a single minute particle launched through the bow shock of a flat-ended cylinder can augment the heating rates to the model surface by as much as a factor of ten. These studies have identified the principal mechanism of enhancement heating as one associated with the reattachment of a jet/shear layer generated by the shock-shock interaction after the particle has penetrated the bow shock. This investigation identified four distinctly different classes of flow phenomena resulting from particle shock-bow shock interaction, together with the heating augmentation levels associated with them. The most dramatic of these is one where a flow instability similar to that encountered over the highly indented nose shapes is observed.

REFERENCES

1. Ko, D. "Use of Linear Stability Theory for the Prediction of Boundary Layer Transition" Presented at the Third Boundary Layer and Shape Change Interchange Meeting Aerospace Report No. TOR-0076 (6550-76)-1 October 1, 1975.
2. Wilcox, D. "Turbulent Model Transition Predictions" Presented at the Third Boundary Layer and Shape Change Interchange Meeting Aerospace Report No. TOR-0076(6550-76)-1 October 1, 1975.
3. Finson, M. "Transitional Boundary Layer Turbulence Model" Presented at the Third Boundary Layer and Shape Change Interchange Meeting Aerospace Report No. TOR-0076(6550-76)-1 October 1, 1975.
4. Demetriades, A., Laderman, A.J. Advanced Penetration Problems Program Final Report, Volume I, SAMSO TR No. 75-51 December 1974.
5. Emmons, H.W. "The Laminar-Turbulent Transition in a Boundary Layer - Part I" J. Aero Sci., Vol 18 No. 7 July 1951.
6. Holden, M.S. "An Experimental Investigation of Turbulent Boundary Layers at High Mach Numbers and Reynolds Numbers" NASA CR-112147, November 1972.
7. Bushnell, D.M., Johnson, C.B., Harvey, W.D. and Feller, W.V. "Comparison of Prediction Methods and Studies of Relaxation in Hypersonic Turbulent Boundary Layers" Turbulent Boundary Layer Conference Proceeding, NASA Langley Research Center, December 1968.
8. Lees, L. "Laminar Heat Transfer over Blunt Nosed Bodies at Hypersonic Flight Speeds" Jet Prop. Vol. 26 #4 (April 1956) pp. 259-269.
9. Cresci, R., MacKenzie, D. and Libby, P. "An Investigation of Laminar, Transitional and Turbulent Heat Transfer on Blunt-Nosed Bodies in Hypersonic Flow" J. Aeron. Sci. Vol. 27 No. 6 June 1960) pp. 401-414.
10. Mirels, H. "Equilibrium Shape of Ablative Nose Tips in Hypersonic Flow" Aerospace Report No. TR-0074(4240-10)-8 November 1973.
11. Crowell, P. "Some Calculations of the Flow over Blunt Biconic Configurations" Private Communication.
12. Mirels, H. "Equilibrium Shape of Ablative Nose Tips in Hypersonic Flow" AF Report No. SAMSO-TR-73-372; also Aerospace Report No. TR-0074(4240-10)-8 November 26, 1973.

13. Bagnynovskii, K.A. and Godunov, S.K. "Difference Schemes for Many-Dimensional Problems" Doklady Akad Nauk U.S.S.R. 115, 431.
14. Powars, C.A. "Passive Nose Tip Technology Program" Interim Report Vol. III Surface Roughness Effects, Part II - Roughness Augmented Heating Data Analysis and Correlation Aerotherm Report 74-96 January 1973.
15. Welsh, W.E. "Shape and Surface Roughness Effects on Turbulent Nose Tip Ablation AIAA Journal Vol. 8 No. 11 November 1970 pp. 1983-1989.
16. Abbott, M.J., et al "Unsteady Flow on Ablated Nosetip Shapes--PANT Series G Test and Analysis Report" Aerotherm Report 73-87, Project 7040 December 1973.
17. Maull, D.J. "Hypersonic Flow over Axially Symmetric Spiked Bodies" J. Fluid Mech. 8 584-592 (1960).
18. Wood, C.J. "Hypersonic Flow over Spiked Cones" J. Fluid Mech. 12 614-624 (1962).
19. Holden, M.S. "Experimental Studies of Separated Flows at Hypersonic Speeds--Part I: Separated Flows over Axisymmetric Spiked Bodies" AIAA Journal, Vol. 4 No. 4 (April 1966).
20. Widhopf, G.F. and Victoria, K.J. "Numerical Solutions of the Unsteady Navier-Stokes Equations for the Oscillatory Flow over a Concave Body" 4th International Conference on Numerical Methods, Boulder Colorado June 1974.
21. Wilkinson, R. "Minuteman H t-Structure Heating Augmentation Study" Vol. 1 Mechanisms and Analyses SAMSO Technical Report No. 73-273 August 1973.
22. "Calspan Hypersonic Shock Tunnel, Description and Capabilities Brochure" March 1973.
23. Needham, D.A., Elfstrom, G.M. and Stollery, J.L. "Design and Operation of the Imperial College Number 2 Hypersonic Gun Tunnel" I.C. Aero Report No. 70-04 May 1970.
24. Enkenhus, K.R. and Parazzoli, C. "The Longshot Free-Piston Cycle--Part I: Theory" vonKarman Inst. for Fluid Dynamics, Technical Note 51 November 1968.
25. Green, J.E. "Interactions Between Shock Waves and Turbulent Boundary Layers" vonKarman Inst. for Fluid Dynamics (Lecture) Report Lecture Series 10 Part 2 January 1969.

26. Spaid, F.W. and Frishnett, J.C. "Incipient Separation of a Supersonic Turbulent Boundary Layer Including the Effects of Heat Transfer" AIAA Paper November 1971.
27. Holden, M.S. "Shock Wave-Turbulent Boundary Layer Interaction in Hypersonic Flow" AIAA Preprint No. 72-74.
28. MacArthur, R.C. "Contoured Skin Friction Transducer" Calspan Report No. AN-2403-Y-1 August 1967.
29. Hiers, R.S. and Loubsky, W.J. "Effects of Shock-Wave Impingement on the Heat Transfer on a Cylindrical Leading Edge" NASA TN D-3859 February 1967.
30. Martin, J.F., Duryea, G.R. and Stevenson, L.M. "Instrumentation for Force and Pressure Measurements in a Hypersonic Shock Tunnel, Advances in Hypervelocity Techniques" Calspan Report No. 113 (Plenum Press, 1962).

DISTRIBUTION LIST FOR CALSPAN REPORT NO. AB-5646-A-1

Air Force Wright Aeronautical
Wright Patterson AFB, Ohio 45433
Attn: Capt. T. Heinrichs (1)
E. G. Brown-Edwards (1)

Air Force Office of Scientific Research
1400 Wilson Blvd.
Arlington, Virginia 20330
Attn: M. Rogers (1)

Arnold Eng. Dev. Center
AFSC, USAF
Arnold Air Force Station
Tennessee 37389
Attn: G. Norfleet (1)

Naval Surface Weapons Center
Silver Spring, Maryland 20910
Attn: D. Reda (1)

DCW Industries
13534 Valley Vista Blvd.
Sherman Oaks, CA 91403
Attn: D. Wilcox (1)

Flow Research Inc.
5959 West Century Blvd. Suite 912
Los Angeles, CA 90045
Attn: D. Ko (1)

General Electric Corp.
3198 Chestnut Street
Philadelphia, PA 19101
Attn: A. Martellucci (1)
D. Brant (1)

Jet Propulsion Laboratory
Gas Dynamics Section
4800 Oak Grove Dr.
Pasadena, CA 91103
Attn: J. M. Kendall (1)
L. Mack (1)

Lockheed Missiles and Space Co.
Continental Bldg. Suite 445
101 Continental Blvd.
El Segundo, CA 90245
Attn: T. R. Fortune (1)
B. Smith (1)

SAMSO
Los Angeles Air Force Station
Los Angeles, CA 90009
Attn: Maj. McCormack/RSSE (1)
Maj. L. Hudack/RSSE (1)
Capt. A. T. Hopkins/RSSE (1)
Lt. E. Taylor/RSSE (1)
Capt. D. Jackson (1)

Institute for Defense Analysis
Science and Technology Div.
400 Army-Navy Drive
Arlington, VA 22202
Attn: H. P. Liepman (1)

Aerotherm/Accurex Corp.
485 Clyde Ave.
Mt. View, CA 94040
Attn: R. M. Kendall (1)

Avco Systems Div.
201 Lowell Street
Wilmington, Mass. 01852
Attn: A. Pallone (1)
B. Reeves (1)

McDonnell-Douglas Corp.
5301 Bolsa Avenue
Huntington Beach, CA 92647
Attn: A. Garblik (1)

PDA, Inc.
Esplanade I, Suite 204
3001 Red Hill Avenue
Costa Mesa, CA 92626
Attn: J. MacDonald (1)

Aeronutronic-Ford
Space and Reentry Systems
Ford Road
Newport Beach, CA 92663
Attn: A. Demetriades (1)
C. White (1)

Physical Sciences, Inc.
18 Lakeside Office Park
Wakefield, Mass. 01880
Attn: M. Finson (1)

DISTRIBUTION LIST (Cont'd)

Department of Aerospace Engineering
University Park
University of Southern California
Los Angeles, CA 90007
Attn: J. Laufer (1)

HQ SAMSO
Los Angeles AFS
P. O. Box 92960
Worldway Postal Center
Los Angeles, CA 90009

RSN (1)
RSR (1)
RSMM/Maj. Brown (1)

RSSR/Capt. Vercruyse (1)
RSDR/Lt. Loga (1)
RSGAA/Mr. Owens (Ltrs of Transmittal
Only)

Air Force Wright Aeronautical Laboratory
Wright-Patterson Air Force Base, Ohio
Ohio 45433
MXS/Attn: M. Buck (1)
K. Stetson (1)

SAMSO/MNNR
Norton AFB, CA 92409
Attn: Maj. Jackson (1)

Aerospace Corporation
P. O. Box 92957
Attn: Mr. W. Portenier (5)
Los Angeles, CA 90009

Navy Department
Strategic Systems Project Office
Washington, DC 20360
Attn: SP-272 (1)

Defense Documentation Center (2)
Cameron Station
Alexandria, VA 22314

Air University Library
Maxwell AFB, AL 36112
Attn: AUL 3T-64-316 (1)

Lockheed Missiles and Space Co.
1111 Lockheed Way
Sunnyvale, CA 94088
Attn: C. Thompson (1)

TRW
1 Space Park
Redondo Beach, CA
Attn: G. Gustafson (1)

PDA
1740 Garry Avenue
Santa Ana, CA 92705
Attn: P. Crenshaw (1)

SAI
1200 Prospect St.
LaJolla, CA 92037
Attn: K. Victoria (1)
R. Dirling (1)

Aeronautical Research Associates of
Princeton, Inc.
50 Washington Road
Princeton, NJ 08540 (1)

Advanced Technology Laboratories, Inc.
400 Jericho Turnpike
Jericho, NY 11753 (1)

Polytechnic Institute of Brooklyn
Department of Aerospace Engineering
and Applied Mechanics
Route 110, Farmingdale, NY 11735 (1)

California Institute of Technology
Department of Engineering and
Applied Science
Pasadena, CA 91109 (1)

California Institute of Technology
Graduate Aeronautical Laboratories
Pasadena, CA 91109 (1)

University of California
Division of Aeronautical Sciences
ATTN: Professor Maurice Holt
Berkeley, CA 94720 (1)

Case Western University
School of Engineering
University Circle
Cleveland, OH 44106 (1)

DISTRIBUTION LIST (Cont'd)

Cornell University
College of Engineering
ATTN: Professor E. L. Resler
Ithaca, NY 14850 (1)

Hydronautics, Inc.
Pindell School Road
Laurel, MD 20810 (1)

Georgia Institute of Technology
Department of Mechanical Engineering
ATTN: Professor Novak Zuber
Atlanta, GA 30332 (1)

Illinois Institute of Technology
Department of Mechanical and
Aerospace Engineering
Chicago, IL 60616 (1)

The Johns Hopkins University
Department of Mechanics
Baltimore, MD 21218 (1)

The Martin Company
RIAS Division
ATTN: Dr. S. H. Maslen
1450 South Rolling Road
Baltimore, MD 21227 (1)

Massachusetts Institute of Technology
Department of Aeronautics
and Astronautics
Cambridge, MA 02139 (1)

University of Texas at Austin
Applied Research Laboratories
Austin, TX 78712 (1)

New York University
Department of Aeronautics and
Astronautics
University Heights
Bronx, NY 10453 (1)

North American Rockwell Corporation
Science Center/Aerospace and
Systems Group
ATTN: Dr. N. D. Malmuth
1049 Camino Dos Rios
Thousand Oaks, CA 91360 (1)

Princeton University
Forrestal Research Center
Gas Dynamics Laboratory
Princeton, NJ 08540 (1)

Princeton University
Department of Aeronautical Engineering
Princeton, NJ 08540 (1)

Rutgers - The State University
Department of Mechanical and
Aerospace Engineering
New Brunswick, NJ 08903 (1)

Stanford University
Department of Aeronautics and
Astronautics
Stanford, CA 94305 (1)

Stanford University
Department of Mechanical Engineering
Stanford, CA 94305 (1)

University of Southern California
Department of Aerospace Engineering
University Park
Los Angeles, CA 90007 (1)

University of Toronto
Institute for Aerospace Studies
Toronto 5, Canada (1)

Professor William O. Criminale
University of Washington
Department of Oceanography
Seattle, WA 98105 (1)

Virginia Polytechnic Institute and
State University
Department of Aerospace Engineering
ATTN: Dr. G. R. Inger
Blacksburg, VA 24061 (1)

University of Notre Dame
Department of Aeronautical Engineering
Notre Dame, IN 46556 (1)

Professor Erik Mollo-Christensen
Massachusetts Institute of Technology
Department of Meteorology
Cambridge, Mass. 02139 (1)

DISTRIBUTION LIST (Cont'd)

Mr. I. E. Garrick
Langley Research Center
Officer of Director for Center
Development
Hampton, VA 23365 (1)

Professor Carl Kaplan
The Johns Hopkins University
Department of Mechanics
Baltimore, MD 21218 (1)

FOREIGN

Tel Aviv University
Department of Aerodynamics
ATTN: Professor I. J. Wygnanski
Tel Aviv, Israel (1)

Technion Research and Development
Foundation
Department of Aeronautical Engineering
ATTN: Professor J. Rom
Haifa, Israel (1)

von Karman Institute for Fluid Dynamics
Hypersonic Laboratory
ATTN: Dr. J. J. Ginoux
Rhode-Saint-Genese, Belgium (1)

Institut de Mecanique Statistique
de la Turbulence
ATTN: Professor A. Favre
12, Avenue General Leclerc
13-Marseille (3e) - France (1)

UNCLASSIFIED

SECURITY CLASSIFICATION OF THIS PAGE (When Data Entered)

REPORT DOCUMENTATION PAGE		READ INSTRUCTIONS BEFORE COMPLETING FORM
1. REPORT NUMBER TR-76-1066	2. GOVT ACCESSION NO.	3. RECIPIENT'S CATALOG NUMBER 9
4. TITLE (and Subtitle) STUDIES OF TRANSITIONAL FLOW, UNSTEADY SEPARATION PHENOMENA AND PARTICLE INDUCED AUGMENTATION HEATING ON ABLATED NOSE TIPS.		5. PERFORMING ORG. REPORT NUMBER -AB-5834-A-1 ✓
7. AUTHOR(s) MICHAEL S. HOLDEN		8. CONTRACT OR GRANT NUMBER(s) F44620-75-C-0019
9. PERFORMING ORGANIZATION NAME AND ADDRESS CALSPAN CORPORATION P O BOX 235 BUFFALO, NEW YORK 14221		10. PROGRAM ELEMENT, PROJECT, TASK AREA & WORK UNIT NUMBERS 681307 9781-03 61192F
11. CONTROLLING OFFICE NAME AND ADDRESS AIR FORCE OFFICE OF SCIENTIFIC RESEARCH/NA BLDG 410 BOLLING AIR FORCE BASE, D C 20332		12. REPORT DATE 1976 Oct 1975
14. MONITORING AGENCY NAME & ADDRESS (if different from Controlling Office) 12 198p.		13. NUMBER OF PAGES 177
		15. SECURITY CLASS. (of this report) UNCLASSIFIED
16. DISTRIBUTION STATEMENT (of this Report) Approved for public release; distribution unlimited. 16 AF-9781 17 978103		
17. DISTRIBUTION STATEMENT (of the abstract entered in Block 20, if different from Report) 18 AFOSR 19 TR-76-1066		
18. SUPPLEMENTARY NOTES 14 CALSPAN- AB-5646-A-1		
19. KEY WORDS (Continue on reverse side if necessary and identify by block number) BLUNT BODY TRANSITION ON BLUNT BODIES TRANSITIONAL HEATING ROUGHNESS HEATING PARTICLE AUGMENTED HEATING HYPERSONIC FLOW. SEPARATED FLOW UNSTEADY FLOW PRESSURE HEAT TRANSFER PARTICLE/SHOCK WAVE INTERACTION		
20. ABSTRACT (Continue on reverse side if necessary and identify by block number) This report describes the results of two distinct studies of the aerodynamic heating of nose tips. In PART 1 of these studies we examined experimentally the development of laminar, transitional and turbulent boundary layers over ablated nose shapes at Mach numbers from 8 to 13 for Reynolds numbers up to 80×10^6 based on model diameter. Two groups of models were employed in this study, blunt elliptic, blunt biconic and triconic models were used in the first phase of this investigation where the greatest emphasis was placed on examining the length and structure of the transition region and the parameters which influence it. The		

second phase of this study was devoted to examining the flow over "highly ablated" nose shapes, over which flow separation and gross flow instabilities occurred. Here we studied how nose tip configuration, roughness and model incidence, as well as the Mach number and Reynolds number of the free stream, influenced the occurrence and structure of large scale periodic instabilities. These studies demonstrated the strong effect of pressure gradient and roughness on the length and characteristics of the transition region. In turn these parameters, along with nose tip geometry, strongly influence the occurrence of flow instabilities over highly-indented nose shapes. In PART II of this investigation, we studied, in detail, the generation of disturbances in the stagnation region of the flow as a particle, which comes from the model surface, interacts with the bow shock. Here we were primarily interested in gaining a knowledge of the magnitude and mechanism of heating enhancement. These studies which were conducted at Mach 6 and 13, demonstrated that there was little heating enhancement as the particle (between 100 and 800 microns in size) transversed the shock layer; however heating levels between 3 and 10 times the stagnation point value can be generated as the particle penetrates the bow shock. Four distinctly different flow regimes were found to exist for different penetration distances and particle trajectories. Of these the most dramatic is one where a flow instability similar to that encountered over the highly indented nose shapes is observed.

* - as indicated in Part II
xx was studied

were studied in detail.